TECHNISCHE
UNIVERSITÄT
MÜNCHEN

WALTHER-
MEISSNER-
INSTITUT

BAYERISCHE
AKADEMIE DER
WISSENSCHAFTEN

Nanomechanical Hybrid Systems

Matthias Pernpeintner

Dissertation

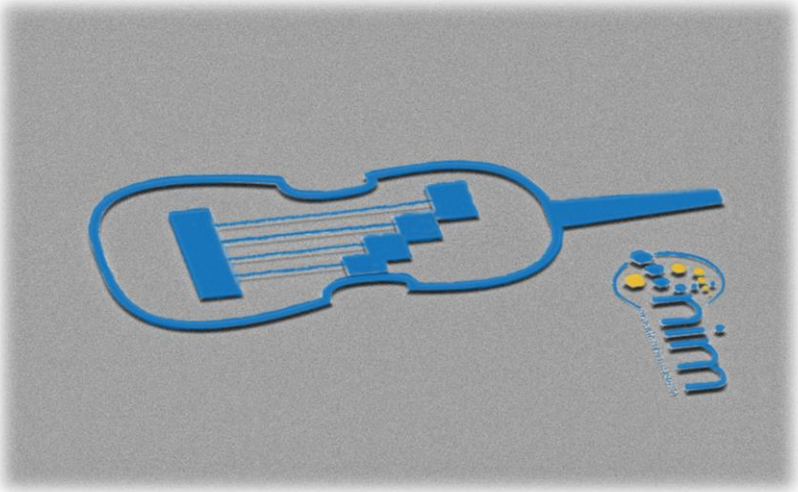

TECHNISCHE UNIVERSITÄT MÜNCHEN

Lehrstuhl E23 für Technische Physik

Walther-Meißner-Institut für Tieftemperaturforschung
der Bayerischen Akademie der Wissenschaften

Nanomechanical hybrid systems

Matthias Elmar Maria Pernpeintner

Vollständiger Abdruck der von der Fakultät für Physik der Technischen Universität München zur Erlangung des akademischen Grades eines

Doktors der Naturwissenschaften

genehmigten Dissertation.

Vorsitzender:	Prof. Dr. W. Zwerger
Prüfer der Dissertation:	1. Prof. Dr. R. Gross
	2. Prof. Dr. J. J. Finley

Die Dissertation wurde am 17.06.2016 bei der Technischen Universität München eingereicht und durch die Fakultät für Physik am 25.07.2016 angenommen.

Abstract

Nanomechanical systems are promising candidates for the realization of highly precise sensing devices as well as for testing fundamental quantum mechanics and for applications in quantum information processing and storage. One of the outstanding characteristics of tensile stressed nanomechanical beams, cantilevers or membranes is their high mechanical quality factor, enabling precise frequency measurement and long coherence times. The integration of nanomechanical resonators into hybrid systems allows combining these properties with additional functionality or enhanced control of the mechanics via external parameters.

In this thesis, nanomechanical resonators interacting with magnetic or electrical degrees of freedom are investigated. We use tensile stressed nanomechanical beams which we couple to a magnetic thin film or a superconducting coplanar waveguide microwave resonator.

First, we present fabrication and basic characterization of tensile stressed silicon nitride and aluminium nanobeams and determine their relevant material properties. Besides, we derive a theoretical description of the mechanics of multilayer nanobeams and verify it by comparing model predictions to experimental findings. Next, we present a magnetomechanical hybrid system consisting of a tensile stressed silicon nitride nanoresonator covered with a thin cobalt or nickel film. In a proof-of-principle experiment, we demonstrate that this platform can be used to probe magnetostriction in thin films via its impact on the mechanics.

Turning to circuit electromechanics, we fabricate and characterize a device in which a pure silicon nitride nanobeam is integrated into a superconducting niobium microwave resonator. This hybrid system features high quality factors in both the mechanical and the microwave resonator and thus allows for the sensitive study of damping mechanisms in silicon nitride at low temperatures. Besides, we present a circuit electromechanical device consisting of a tensile stressed aluminium nanobeam and an aluminium microwave resonator. We characterize the microwave and the mechanical resonator and show sideband cooling of the fundamental mechanical mode. Additionally, we investigate electromechanically induced transparency and thus demonstrate backaction of the mechanics on the microwave resonator. The presented all-aluminium platform allows for the integration of transmon qubits and thus constitutes an important step towards circuit electromechanics in the quantum regime. We propose protocols that allow ground state cooling, mechanical state preparation and three-body entanglement in a similar circuit electromechanical device and present first steps towards its experimental implementation.

In conclusion, the results of this thesis are useful, e. g., for the realization of sensing devices, for the investigation of magnetoelastic properties of thin films and for the study of mechanical damping in nanoresonators. Besides, we open the path for fundamental tests of quantum mechanics with circuit electromechanical systems and for possible applications of nanomechanical beam resonators in quantum information processing and storage.

Zusammenfassung

Nanomechanische Systeme sind vielversprechende Kandidaten für die Realisierung hochpräziser Sensoren, für das Studium grundlegender Quantenphänomene und für Anwendungen in der Prozessierung und Speicherung von Quanteninformation. Eine der herausragenden Eigenschaften zugverspannter Nanoresonatoren ist ihre hohe mechanische Güte, was eine genaue Messung ihrer Resonanzfrequenz und lange Kohärenzzeiten ermöglicht. Nanomechanische Hybridsysteme verbinden diese Vorteile mit zusätzlicher Funktionalität oder erlauben die Kontrolle mechanischer Eigenschaften mithilfe externer Parameter.

Diese Arbeit beschäftigt sich mit nanomechanischen Resonatoren, die mit magnetischen oder elektrischen Freiheitsgraden wechselwirken. Wir nutzen hierfür zugverspannte Nanobalken, die an einen magnetischen Dünnfilm oder an einen supraleitenden Mikrowellenresonator im koplanaren Wellenleiterdesign gekoppelt sind.

Im ersten Teil der Arbeit werden die Fabrikation und die grundlegende Charakterisierung von zugverspannten Siliziumnitrid- und Aluminium-Nanobalken vorgestellt und deren wichtigste Materialparameter bestimmt. Wir leiten außerdem eine theoretische Beschreibung der Mechanik von mehrlagigen Nanobalken her und verfizieren sie durch Vergleich mit experimentellen Ergebnissen. Ferner untersuchen wir ein magnetomechanisches Hybridsystem auf der Basis eines zugverspannten Siliziumnitrid-Nanobalkens, der mit einem Cobalt- oder Nickel-Dünnfilm bedeckt ist. In einem Grundlagenexperiment weisen wir nach, dass dieser Aufbau dazu benutzt werden kann, Magnetostriktion in einem Dünnfilm mit Hilfe mechanischer Messgrößen zu untersuchen.

Der zweite Teil der Arbeit behandelt das Gebiet der Schaltkreis-Elektromechanik. Wir zeigen die Fabrikation und Charakterisierung eines reinen Siliziumnitrid-Nanobalkens, der in einen supraleitenden Niob-Mikrowellenresonator integriert ist. Aufgrund seiner hohen mechanischen und elektrischen Güte eignet sich eine derartige Probe zur Untersuchung der Dämpfungsmechanismen in Siliziumnitrid bei tiefen Temperaturen. Des Weiteren untersuchen wir ein Hybridsystem, das aus einem zugverspannten Aluminiumbalken und einem Aluminium-Mikrowellenresonator aufgebaut ist. Wir charakterisieren den mechanischen und den Mikrowellenresonator und demonstrieren Seitenbandkühlung der fundamentalen Schwingungsmode des Nanobalkens. Wir untersuchen ferner elektromechanisch induzierte Transparenz und weisen damit eine Rückwirkung der mechanischen Schwingung auf den Mikrowellenresonator nach. Das gezeigte aluminiumbasierte Hybridsystem ermöglicht die Integration von Transmon-Quantenbits und stellt damit einen wichtigen Schritt hin zu Schaltkreis-Elektromechanik im Quantenlimes dar. Wir entwickeln Protokolle zur Reali-

sierung von Grundzustandskühlung, Präparation mechanischer Zustände und Dreikörper-Verschränkung in solch einem elektromechanischen System und zeigen erste Schritte hin zur experimentellen Implementierung.

Die Ergebnisse dieser Arbeit können z. B. für die Realisierung nanomechanischer Sensoren, für die Bestimmung magnetoelastischer Eigenschaften in Dünnfilmen und für die Untersuchung von Dämpfungsmechanismen in Nanoresonatoren von Nutzen sein. Darüberhinaus ebnen sie den Weg für Experimente zu den Grundlagen der Quantenmechanik auf der Basis von Schaltkreis-Elektromechanik und für mögliche Anwendungen nanomechanischer Balkenresonatoren in der Quanteninformationsverarbeitung und -speicherung.

Contents

Abstract I

Zusammenfassung III

1 Introduction 1

2 Nanomechanical resonators 5
2.1 Equation of motion . . . 6
2.2 Thermal motion . . . 7
2.3 Duffing nonlinearity . . . 8

3 Characterization of silicon nitride and aluminium nanobeam resonators 11
3.1 Fabrication of pure silicon nitride and aluminium beams . . . 11
3.1.1 Silicon nitride nanobeams . . . 11
3.1.2 Aluminium nanobeams . . . 12
3.2 Experimental setup for room temperature mechanical spectroscopy . . . 13
3.2.1 Optical laser interferometry . . . 13
3.2.2 Measurement setup . . . 15
3.3 Silicon nitride nanobeams . . . 16
3.4 Aluminium nanobeams . . . 18
3.5 Summary . . . 19

4 Mechanics of homogeneous and multilayer nanobeams 21
4.1 Mechanics of a nanobeam with homogeneous cross-section . . . 21
4.1.1 Forces acting on an infinitesimal volume element . . . 21
4.1.2 Relation between bending moment and displacement curvature . . . 23
4.1.3 Equation of motion and resonance frequency . . . 24
4.1.4 Approximations for resonance frequency and beam shape . . . 25
4.1.5 Comparison of the full numerical solution to approximated results . . . 27
4.1.6 Effective mass . . . 27
4.1.7 Geometric nonlinearity . . . 29
4.2 Double-layer beam – out-of-plane vibrational mode . . . 30
4.3 Double-layer beam – in-plane vibrational mode . . . 31
4.3.1 Vibrational in-plane motion . . . 33

4.3.2 Torsional motion . . . 33
4.3.3 Torsion, elongation and bending energy . . . 34
4.4 Comparison with experimental data . . . 35
4.4.1 Sample and experimental setup . . . 35
4.4.2 Measurement results and comparison to multilayer beam theory . . . 36
4.4.3 Torsional motion associated to the in-plane mode . . . 37
4.5 Summary . . . 38

5 Magnetostriction sensing with a nanomechanical beam 39
5.1 Sample fabrication . . . 40
5.2 Experimental setup . . . 41
5.2.1 Optical free beam interferometer in an electromagnet . . . 41
5.2.2 Measurement setup and coordinate system . . . 44
5.3 Model connecting mechanical resonance frequency changes to magnetostriction . . . 44
5.3.1 Magnetostrictive strain in a free-standing magnetic thin film . . . 45
5.3.2 Magnetoelastic stress in a magnetic thin film on top of a substrate . . . 46
5.3.3 Effective stress in the double-layer nanobeam . . . 47
5.4 Experimental results . . . 48
5.4.1 Magnetostriction of a cobalt thin film . . . 48
5.4.2 Magnetostriction of a nickel thin film . . . 51
5.4.3 Stress-to-frequency conversion and estimated measurement sensitivity 56
5.5 Summary . . . 57

6 Circuit nano-electromechanics 59
6.1 Fundamental concepts in cavity opto- and electromechanics . . . 59
6.2 Circuit nano-electromechanics with superconducting CPW resonators . . . 64
6.2.1 Microwave resonators . . . 64
6.2.2 Capacitive coupling . . . 67
6.3 Detection of mechanical motion, frequency noise calibration and determination of the coupling rate . . . 68
6.4 Sideband cooling of mechanical motion . . . 69
6.5 Electromechanically induced transparency . . . 70

7 Circuit nano-electromechanics with a non-metallized nanobeam 73
7.1 Sample layout and fabrication . . . 74
7.2 Modeling of the dielectric electromechanical coupling . . . 75
7.2.1 Electric field distribution and electromechanical coupling . . . 75
7.2.2 Impact of geometry . . . 76
7.3 Experimental setup . . . 77
7.4 Experimental results . . . 78
7.4.1 Characterization of microwave cavity and mechanical resonator . . . 78
7.4.2 Frequency noise calibration . . . 80
7.4.3 Determination of the coupling rate via Duffing nonlinearity . . . 81
7.5 Temperature dependence of the mechanical quality factor . . . 82
7.6 Estimated mass sensitivity . . . 84

7.7 Summary 84

8 Circuit nano-electromechanics with an aluminium nanobeam 87
8.1 Sample fabrication 87
8.2 A priori estimation of the electromechanical coupling 89
8.3 Cryogenic setup 90
8.4 Experimental results 90
8.4.1 Characterization of the microwave resonator 91
8.4.2 Characterization of the nanobeam resonator 92
8.4.3 Determination of the electromechanical vacuum coupling 94
8.4.4 Sideband cooling of mechanical motion 95
8.4.5 Electromechanically induced transparency 97
8.5 Steps towards circuit electromechanics in the quantum regime 98
8.5.1 Inductive coupling between a microwave resonator and a nanobeam 101
8.5.2 Coupling of a transmon qubit to a circuit electromechanical hybrid system 103
8.5.3 Three-body interactions in an electromechanical resonator-qubit hybrid system 103
8.6 Summary 105

9 Summary and Outlook 107

A Analytical approximation of the resonance frequency of a tensile stressed nanobeam including bending effects 111

B Lorentzian response spectrum with complex background 113

C Effective length of a nanobeam integrated in a CPW microwave resonator 115

D Temperature dependence of the resonance frequency of a tensile stressed nanobeam 117
D.1 Annealing of an aluminium beam 118
D.2 Cooling an aluminium beam to mK temperatures 118

Bibliography 119

List of Publications 129

Acknowledgments 131

Chapter 1

Introduction

In the past decades, micro- and nanomechanical resonators have gained enormous importance in science and industrial applications. Whereas centimeter- to meter-sized mechanical resonators have been used for a long time (in form of mechanical clocks or tuning forks, for instance), the development of micro- and nanofabrication techniques, starting in the 1960s, provided the means to scale down the size of mechanical resonators and greatly extend their range of applications [1]. Apart from serving as frequency reference (e. g. quartz crystals in a watch), micromechanical resonators are widely employed as sensing devices. Micromechanical vibrating accelerometers and gyroscopes, e. g., are commonly used in smartphones [2], route guidance systems [3], electronic stability control in cars [4] or for the detection of a free fall in a variety of electronic devices [5]. In a lot of technical applications and consumer electronics, where ultimate sensitivity is not required, such microelectromechanical systems (MEMS) serve as compact, low-cost and low-energy consuming sensing devices [6, 7].

From a scientific point of view, the integration of micromechanical resonators has pushed the sensitivity of various analytic tools in physics and material science: Micromechanical cantilevers are the key element of atomic force microscopy (AFM) and scanning tunneling microscopy (STM) and allow for the precise investigation of surface texture, topography and defects [8]. Recently, cantilever resonators have been employed for the mechanical manipulation and read-out of spin qubits in diamond [9], nanoscale magnetic resonance imaging [10] and for the investigation of forces and folding behaviour of proteins [11]. Moving on to nanoscale mechanical resonators, sensitivity can even be increased. One of the most fascinating perspectives of nanoscale mechanical resonator sensing devices is the detection and identification of single molecules or even atoms in a gas or an aerosol [12–14]. To this end, a doubly-clamped nanostring resonator – a tensile stressed nanobeam or a carbon nanotube – is placed in a flow of highly diluted gas molecules/atoms. If a particle hits the nanoresonator and sticks to it, the mass of the nanostring changes, resulting in a shift of its resonance frequency. So the adsorption of a molecule/atom can be detected by continuously monitoring the resonance frequency of the high-Q nanoresonator. In an ultrahigh vacuum environment and at low temperature (4 K), mass sensitivities down to the yoctogram range have been demonstrated, corresponding to the mass of a single proton [14]. Even if such systems are still in the stage of fundamental research, in future applications similar devices could serve, e. g., as sensors for the analysis of gases and de-

tection of toxins or explosives, providing a quick and low-cost alternative to conventional mass spectroscopy [15–17].

Apart from these perspectives in sensing applications, micro- and nanomechanical resonators have become a promising tool for the investigation of fundamental questions in quantum mechanics and possible applications in quantum information processing and storage. Integrating a micro/nanomechanical resonator into an optical cavity or a microwave circuit allows to precisely control and read out the motion of the mechanical element [18]. This idea led to the emergence of the fields of cavity optomechanics and, derived from this, circuit electromechanics [19].

Cavity opto- and electromechanical systems combine the excellent mechanical properties of tensile stressed, low-loss mechanical resonators with the controllability and the sensitivity of the readout techniques developed for optical cavities or microwave resonators. For the latter, a natural choice are superconducting resonators due to their ultralow damping rates [18, 20, 21]. Such circuit electromechanical hybrid devices, consisting of a nanomechanical resonator and a superconducting microwave resonator, can be combined with other degrees of freedom (e. g. qubits/artificial atoms) for enhanced state control or excitation transfer experiments [22, 23].

Recently, important steps towards experiments with mechanical systems in the quantum regime have been taken. It is possible to cool single modes of a MHz mechanical resonator to the quantum ground state and to prepare them in a squeezed vacuum state, where one of the quadratures of mechanical motion is reduced below the standard quantum limit [24, 25]. Furthermore, entanglement of mechanical motion with a microwave state in a circuit electromechanical hybrid system was demonstrated, a key ingredient for possible applications in quantum information processing and storage [26].

From a quantum application perspective, mechanical resonators are a promising candidate for the conversion of single optical to microwave photons and vice versa [27]. Whereas the direct photon-photon interaction is weak, a mechanical element that is strongly coupled to both an optical and a microwave cavity can serve as a transducer for quantum information stored in optical or microwave photons. First experiments towards the realization of this idea have already been published [28, 29].

In this thesis, we investigate high-Q nanomechanical resonators embedded in magnetomechanical or circuit electromechanical hybrid devices. We use tensile stressed nanobeam resonators, fabricated from a silicon nitride or aluminium thin film, and couple them to a magnetic thin film or a superconducting microwave circuit, respectively. In the first case, the magnetomechanical coupling allows to control the mechanical properties via external magnetic fields or to operate the nanobeam resonator as a sensor for magnetoelastic effects. Regarding the circuit electromechanical devices, we demonstrate control and read-out of the nanobeam motion via the microwave circuit and show backaction effects of the mechanics on the microwave resonator. Besides, we report on theoretical and experimental progress towards the integration of a transmon qubit into a circuit electromechanical device, enabling single phonon control and novel state preparation protocols.

Chapter 2 lays the foundations for the mathematical description of nanomechanical resonators. We use an effective one-dimensional oscillator model to describe the vibrational motion of a tensile stressed nanobeam resonator. We derive the amplitude spectrum of thermal motion and the response spectrum in the non-linear regime of high displacement, which will be an important tool in the experiments later.

In Chap. 3, we discuss the fabrication and characterization of pure silicon nitride and aluminium nanobeams and determine their relevant material parameters. This is the basis for the integration of nanobeams into more complex hybrid systems. For this purpose, usually multilayer nanobeams are employed, fabricated of a stack of two or more thin film layers. We derive a comprehensive description of the mechanics of multilayer nanobeams in Chap. 4. In particular, we show that the vibrational modes of such multilayer nanobeams can be described similar to the motion of homogeneous beams by introducing effective material parameters. Knowing the relations between these effective parameters and the bare material properties of the individual layers allows to tailor the properties of multilayer nanobeams and to study material properties in multilayer hybrid systems.

An application of a double-layer nanobeam used for sensing purposes is given in Chap. 5. Here we present a platform which allows to quantitatively investigate magnetostriction in a ferromagnetic thin film. The presented technique is based on a tensile stressed silicon nitride nanobeam covered with a magnetic thin film. We use the interaction between magnetization and elastic properties to determine the magnetostriction constants of the magnetic thin film by resonance spectroscopy of the nanobeam motion.

The last part of this thesis discusses the topic of circuit electromechanics. Chapter 6 introduces the fundamental concepts of circuit electromechanics and gives a brief overview of the experimental realization based on superconducting coplanar waveguide (CPW) microwave resonators. In Chaps. 7 and 8, we present two approaches towards circuit electromechanics, where a nanobeam resonator is coupled to a CPW microwave resonator. First, we integrate a pure silicon nitride nanobeam into a niobium microwave resonator (Chap. 7). We present the fabrication process, characterize the hybrid system and determine the electromechanical vacuum coupling. As an alternative approach, promising in particular for quantum applications, we combine a tensile stressed aluminium nanobeam with an aluminium CPW microwave resonator (Chap. 8). We show basic characterization measurements and demonstrate sideband cooling of the mechanical motion and electromechanically induced transparency (EMIT), an interference effect similar to optomechanically induced transparency. Finally, we provide an outlook on ongoing experimental work at the Walther-Meißner-Institut regarding circuit electromechanics in the quantum regime.

Chapter 2

Nanomechanical resonators

For many applications, the motion of nanomechanical resonators, like nanobeams, cantilevers or membranes, can formally be treated as a one-dimensional, damped and (nearly) harmonic oscillator. Consequently, the description of the mechanics of the three-dimensional body can be reduced to a single degree of freedom, as illustrated in Fig. 2.1, by introducing effective parameters like effective mass, damping rate and potential. In case of small displacements, this effective potential is nearly harmonic, and nonlinearities can be taken into account via perturbation theory.

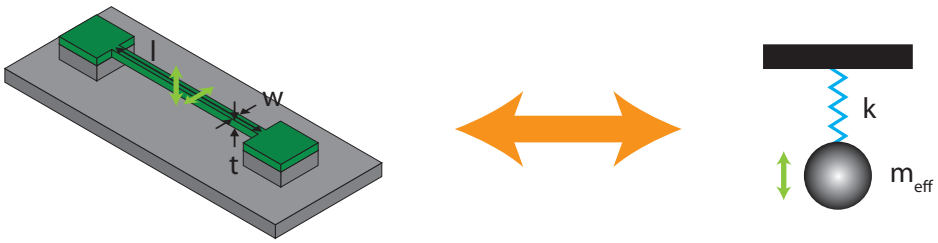

Figure 2.1: Schematic illustration of a doubly-clamped nanobeam resonator with length l, width w and thickness t. Its vibrational motion, indicated by the light green arrows, can be described in a one-dimensional oscillator model with stiffness k and effective mass m_{eff}.[1]

In this chapter, we briefly review the fundamental relations which are used to describe nanomechanical resonators within the above mentioned one-dimensional model with effective parameters. In Chap. 4, we will derive these effective parameters for a doubly-clamped, tensile stressed nanobeam, which will be investigated throughout this thesis. Thereby we will prove the validity of the one-dimensional model.

[1] We assume the modes of the nanobeam to be uncoupled (which is usually the case), so they can be described as effectively independent one-dimensional resonators with respective parameters k, m_{eff} and Γ_{m}.

2.1 Equation of motion

The equation of motion of a one-dimensional damped harmonic oscillator with external coherent drive is given by

$$\ddot{x} + \Gamma_\mathrm{m}\dot{x} + \frac{k}{m_\mathrm{eff}}x = \frac{F_0}{m_\mathrm{eff}}\exp(-i\Omega t)\ . \tag{2.1}$$

Here, x is the displacement and Γ_m, k, m_eff, F_0 and $\Omega/2\pi$ denote the damping rate, the effective spring constant, the effective mass, the driving force and the drive frequency, respectively.

With the ansatz $x(t) = x_0\exp(-i\Omega t)$, we obtain the complex steady-state solution

$$x_0 = \frac{F_0/m_\mathrm{eff}}{(\Omega_\mathrm{m}^2 - \Omega^2) - i\Gamma_\mathrm{m}\Omega}\ , \tag{2.2}$$

where we have defined the angular resonance frequency $\Omega_\mathrm{m} = \sqrt{k/m_\mathrm{eff}}$. The *quality factor* of the resonance is defined as

$$Q := \frac{\Omega_\mathrm{m}}{\Gamma_\mathrm{m}}\ .$$

For a highly tensile-stressed nanobeam, the resonance frequency of the n-th vibrational mode is [30]

$$\Omega_{\mathrm{HTS},n} = \frac{n\pi}{l}\sqrt{\frac{\sigma_0}{\rho}}\ , \tag{2.3}$$

where l, σ_0 and ρ denote the length, prestress and density of the nanobeam. A comparison with the generic relation $\Omega_\mathrm{m} = \sqrt{k/m_\mathrm{eff}}$ shows that the prestress σ_0 acts as an effective stiffness of the resonator while the density ρ replaces the effective mass m_eff.

For typical tensile-stressed nanobeams, the resonance frequency can be written more precisely by taking into account bending effects to first order[2]:

$$\Omega_{\mathrm{TS},n} = \Omega_{n,\mathrm{HTS}}\frac{l\sqrt{\sigma_0 A}}{l\sqrt{\sigma_0 A} - 2\sqrt{EI}}\ . \tag{2.4}$$

Here, A, E and I are the cross-section, Young's modulus and the area moment of inertia of the beam. The latter is given by $I_\mathrm{ip} = w^3 t/12$ for in-plane and $I_\mathrm{oop} = wt^3/12$ for out-of-plane vibrational modes [31,32], and w and t denote the width and thickness of the beam, respectively.

In experiments, usually the squared magnitude and the phase of the displacement x_0 are measured. The first is given by

$$|x_0|^2 = \frac{F_0^2/m_\mathrm{eff}^2}{(\Omega_\mathrm{m}^2 - \Omega^2)^2 + \Gamma_\mathrm{m}^2\Omega^2} \approx \left(\frac{F_0/m_\mathrm{eff}}{2\Omega_\mathrm{m}}\right)^2 \frac{1}{(\Omega_\mathrm{m} - \Omega)^2 + \Gamma_\mathrm{m}^2/4}\ .$$

The approximation is valid for $\Gamma_\mathrm{m} \ll \Omega_\mathrm{m}$, which is satisfied for all mechanical resonators studied in this thesis. Thus, for these resonators, the response spectrum has Lorentzian lineshape.

The phase of the mechanical response relative to the drive can be written as

$$\varphi = \arg(x_0) = \arctan\left(\frac{\Gamma_\mathrm{m}\Omega_\mathrm{m}}{\Omega_\mathrm{m}^2 - \Omega^2}\right) \approx \arctan\left(\frac{\Gamma_\mathrm{m}}{2(\Omega_\mathrm{m} - \Omega)}\right)\ . \tag{2.5}$$

[2]Please see Chap. 4 for a detailed derivation of Eq. 2.4 and a comparison to the approximation of a highly tensile-stressed beam.

As can be seen in Fig. 2.2, the derivative $\mathrm{d}\varphi/\mathrm{d}\Omega$ reaches its maximum in resonance, where

$$\frac{\mathrm{d}\varphi}{\mathrm{d}\Omega}\left(\Omega = \Omega_\mathrm{m}\right) = \frac{2}{\Gamma_\mathrm{m}} \,. \tag{2.6}$$

Especially for high-Q resonators ($\Gamma_\mathrm{m} \ll \Omega_\mathrm{m}$), the resonance frequency can therefore be

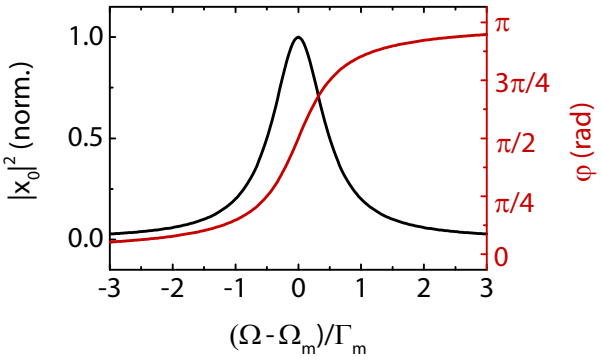

Figure 2.2: Lorentzian amplitude spectrum of mechanical motion. The squared magnitude $|x_0|^2$, normalized to $|x_{0,\mathrm{max}}|^2 := (F_0/(m_\mathrm{eff}\Omega_\mathrm{m}\Gamma_\mathrm{m}))^2$, is plotted in black, the phase φ in red. Note that, due to the minus sign in the ansatz $x(t) = x_0 \exp(-i\Omega t)$, a positive φ corresponds to a phase lag of the mechanical response relative to the drive.

measured precisely by monitoring the phase of the response function. We will make use of this in Chap. 5, where we investigate magnetostrictive resonance frequency shifts in nanobeam resonators covered with a magnetic thin film.

2.2 Thermal motion

Even without an externally applied coherent drive, the modes of a nanomechanical resonator are excited due to thermal energy. In experiments, this *Brownian motion* is commonly utilized to calibrate the read-out of the mechanical amplitude. We therefore derive the relation between the temperature of the nanobeam resonator and its thermal motion amplitude.

According to the equipartition theorem [33], the energy of a system in thermal equilibrium with its environment is $k_\mathrm{B}T/2$ per degree of freedom, where k_B is the Boltzmann constant and T the temperature of the bath. In case of a nanomechanical resonator with effective mass m_eff and resonance frequency $\Omega_\mathrm{m}/2\pi$, the thermal energy can therefore be expressed by [34]

$$\frac{1}{2}k_\mathrm{B}T = \frac{1}{2}m_\mathrm{eff}\Omega_\mathrm{m}^2\overline{x_\mathrm{th}^2} \,. \tag{2.7}$$

Here, $\overline{x_\mathrm{th}^2}$ is the mean squared displacement of the nanobeam and related to the mechanical motion spectrum via

$$\overline{x_\mathrm{th}^2} := \int_0^\infty S_\mathrm{xx}(\Omega)\frac{\mathrm{d}\Omega}{\pi} \,, \tag{2.8}$$

where we have introduced the (single-sided) amplitude spectrum of the mechanical resonator $S_\mathrm{xx}(\Omega)$, given in units of m^2/Hz [21, 34, 35]. Please note that this is a spectrum in terms of angular frequency Ω and related to the (bare) frequency spectrum by $S_\mathrm{xx}(\Omega) = S_\mathrm{xx}(f)/2\pi$ with the frequency $f = \Omega/2\pi$.

For a high-Q resonator ($\Gamma_\mathrm{m} \ll \Omega_\mathrm{m}$) in thermal equilibrium with its environment, the amplitude spectrum has a Lorentzian lineshape and can be written as [34]

$$S_{xx}(\Omega) = \left(\frac{F_\mathrm{th}(\Omega)/m_\mathrm{eff}}{2\Omega_\mathrm{m}}\right)^2 \frac{1}{(\Omega-\Omega_\mathrm{m})^2 + \Gamma_\mathrm{m}^2/4} , \tag{2.9}$$

where $F_\mathrm{th}^2(\Omega)$ is the thermal driving force spectrum, given in units of force^2/bandwidth, i.e. $[F_\mathrm{th}^2(\Omega)] = \mathrm{N}^2/\mathrm{Hz}$. Substituting Eq. 2.9 into Eq. 2.8 and assuming a frequency-independent thermal force spectrum in the vicinity of the mechanical resonance, $F_\mathrm{th}^2(\Omega) \approx F_\mathrm{th}^2(\Omega_\mathrm{m})$, we get

$$\overline{x_\mathrm{th}^2} = \frac{F_\mathrm{th}^2(\Omega_\mathrm{m})}{2m_\mathrm{eff}^2\Gamma_\mathrm{m}\Omega_\mathrm{m}^2} .$$

Together with the equipartition theorem (Eq. 2.7), we obtain the thermal driving force [34]

$$F_\mathrm{th}^2(\Omega_\mathrm{m}) = 2m_\mathrm{eff}\Gamma_\mathrm{m}k_\mathrm{B}T .$$

Inserting this into Eq. 2.9 finally leads to the calibrated mechanical response spectrum, which relates the system temperature to the displacement via

$$S_{xx}(\Omega) = \frac{k_\mathrm{B}T}{2\Omega_\mathrm{m}^2 m_\mathrm{eff}} \frac{\Gamma_\mathrm{m}}{(\Omega-\Omega_\mathrm{m})^2 + (\Gamma_\mathrm{m}/2)^2} . \tag{2.10}$$

Owing to the small effective mass and the high quality factor of tensile stressed nanomechanical resonators, their thermal motion can often be detected even at mK temperatures. This provides an easy way for calibrating the mechanical displacement spectrum and determining the absolute displacement for a given driving force. We will make use of this technique in Chaps. 3, 7 and 8.

2.3 Duffing nonlinearity

Whereas for small displacement the motion of a nanobeam can well be described as a damped harmonic oscillator, nonlinear effects modify the dynamics of the beam for high amplitude states [36, 37]. In general, different mechanisms contribute to this nonlinear behaviour. For tensile stressed nanobeams, on which we will focus in this thesis, the dominating contribution is the *geometric nonlinearity* the origin of which will be discussed in Sec. 4.1.7. To account for it, we add a cubic term to the equation of motion 2.1, leading to the *Duffing equation* [36, 38]

$$\ddot{x}(t) + \Gamma_\mathrm{m}\dot{x}(t) + \Omega_\mathrm{m}^2 x(t) + \alpha x^3(t) = \frac{F_0}{m_\mathrm{eff}} \exp(-i\Omega t) .$$

The *Duffing nonlinearity* α is related to material properties of the nanobeam by [37, 39][3]

$$\alpha = \pi^4 \frac{E}{4l^4\rho} > 0 . \tag{2.11}$$

[3] In literature, sometimes the relation $\alpha = \pi^4(E + \frac{3}{2}\sigma_0)/(4l^4\rho)$ is given, where σ_0 denotes the prestress of the nanobeam; but as usually $\sigma_0 \ll E$, the contribution of the prestress to the nonlinearity α can safely be neglected.

Here, E and ρ denote Young's modulus and the mass density of the nanobeam, respectively. The amplitude spectrum of a Duffing oscillator is given by the implicit equation [38]

$$\left[\Gamma_\mathrm{m}^2 + 4\left(\Omega - \Omega_\mathrm{m} - \frac{3}{8}\frac{\alpha}{\Omega_\mathrm{m}}x_0^2\right)^2\right] x_0^2 = \frac{F_0^2}{m_\mathrm{eff}^2\Omega_\mathrm{m}^2}\,. \tag{2.12}$$

For a weak external drive, the response function of the Duffing oscillator is nearly a Lorentzian around the resonance frequency $\Omega_\mathrm{m}/2\pi$. For increasing drive power, however, the maximum of the amplitude spectrum $x_{0,\mathrm{max}}$ shifts to higher frequencies Ω_eff, as illustrated in Fig. 2.3. This behavior is summarized as backbone curve [38]

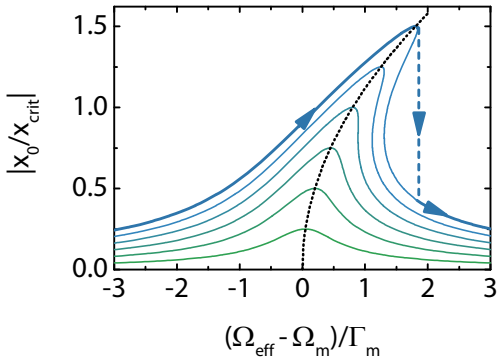

Figure 2.3: Amplitude spectrum of a Duffing oscillator. For amplitudes exceeding the critical amplitude x_crit, the response spectrum is bistable. When sweeping the frequency over the resonance from left to right, one accesses the high-amplitude state as illustrated by the blue arrows. The maxima of the amplitude spectra follow the backbone curve indicated by the red dotted line.

$$x_{0,\mathrm{max}}^2 = \frac{8}{3}\frac{\Omega_\mathrm{m}}{\alpha}\left(\Omega_\mathrm{eff} - \Omega_\mathrm{m}\right). \tag{2.13}$$

If $x_{0,\mathrm{max}}$ exceeds the so-called critical amplitude $x_\mathrm{crit} = (4/3)^{3/2}\sqrt{\Gamma_\mathrm{m}\Omega_\mathrm{m}/\alpha}$, the Duffing oscillator enters a bistable regime so that for a small frequency range below Ω_eff, there are two stable and one metastable amplitude states (where the latter cannot be accessed experimentally). When sweeping the drive frequency over the resonance from low to high frequencies, the nanobeam remains in the high-amplitude state up to Ω_eff, jumping down to lower amplitudes for $\Omega > \Omega_\mathrm{eff}$, as illustrated in Fig. 2.3 (dashed blue line). This allows to experimentally determine Ω_eff as a function of the applied driving force F_0. For a more detailed discussion of the Duffing oscillator, please see Refs. [21, 38, 40].

In this thesis, we will employ the Duffing nonlinearity to gain information about the mechanical properties of the nanobeam (Chap. 4) and to determine the beam motion amplitude when the material parameters are known (Chap. 7).

Chapter 3

Characterization of silicon nitride and aluminium nanobeam resonators

3.1 Fabrication of pure silicon nitride and aluminium beams

The fabrication of doubly-clamped nanobeam resonators is based on a process developed at the chair of Prof. J. Kotthaus at LMU Munich. This process has been modified within the scope of this thesis to allow the integration with magnetic materials and superconducting microwave circuits: To investigate the interaction of mechanics with magnetic degrees of freedom (see Chap. 5), we use Si_3N_4/ferromagnet bilayer nanobeams, whereas for circuit nano-electromechanics, we fabricate pure Si_3N_4 beams in a niobium microwave circuit (Chap. 7) and pure aluminium beams in an aluminium microwave circuit (Chap. 8).

In this chapter, we introduce the fabrication process for pure Si_3N_4 and aluminium nanobeams and present measurements which allow to characterize the mechanical properties of the nanobeams such as the prestress σ_0 and Young's modulus E.

3.1.1 Silicon nitride nanobeams

The fabrication of tensile stressed Si_3N_4 nanobeams starts with a commercial silicon wafer on which 100 nm of tensile stressed Si_3N_4 have been deposited, as illustrated in Fig. 3.1a (i). Using electron beam lithography and negative resist, the nanobeams and rectangular clamping pads are patterned on the chip (ii). The pattern is transferred to the Si_3N_4 in an anisotropic Ar/SF_6 reactive ion etching (RIE) step (iii). A subsequent isotropic RIE step (SF_6 only) releases the nanobeams from the substrate (iv). The sample is cleaned with hot acetone and remover, if necessary.

Figure 3.2 shows a scanning electron microscope (SEM) image (top view and tilted view) of a typical Si_3N_4 nanobeam. Here, we have etched approximately 500 nm into the silicon substrate to release the nanobeam. Due to the comparatively high acceleration voltage $U_{\mathrm{EHT}} = 20\,\mathrm{kV}$ used here, the underetched parts of the Si_3N_4 film can be identified as they appear as bright areas along the clamping pads of the nanobeam (in particular in Fig. 3.2b). Besides, the tilted SEM image reveals the ridge below the Si_3N_4 nanobeam as a residue of the isotropic RIE process.

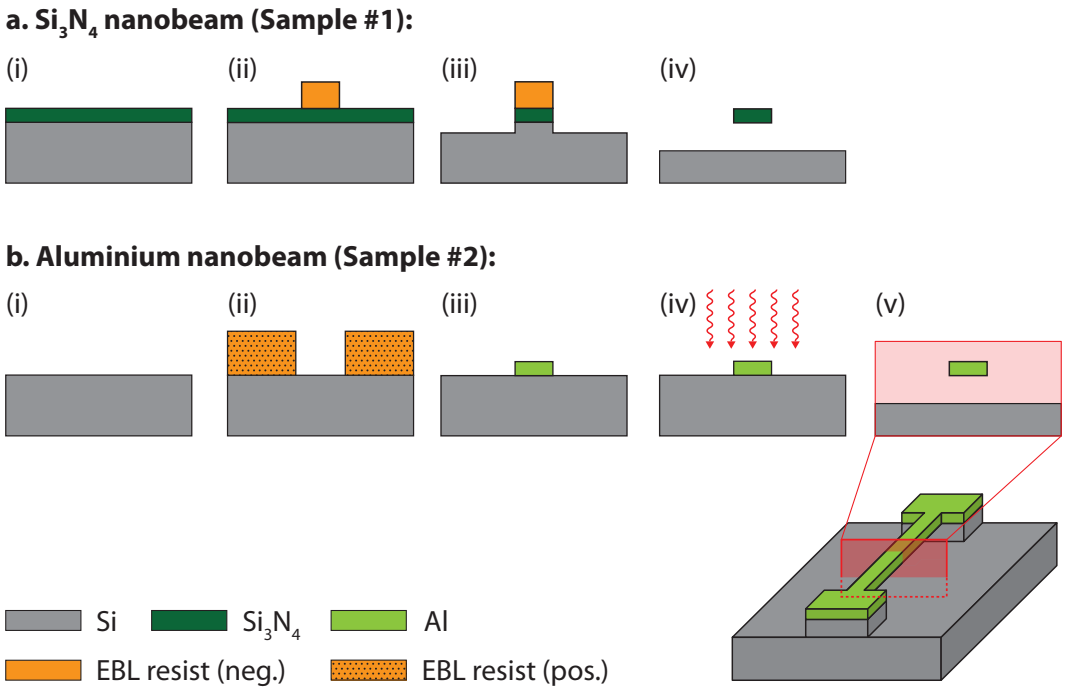

Figure 3.1: Schematic of the fabrication processes of (a) Si_3N_4 and (b) aluminium nanobeam resonators on a silicon substrate.

3.1.2 Aluminium nanobeams

We use a blank commercial silicon wafer as a substrate [Fig. 3.1b, (i)] and define the inverse pattern (nanobeam and clamps) with electron beam lithography and positive resist (ii). A 100 nm thin aluminium film is deposited on the chip using electron beam evaporation, followed by a lift-off step (iii). In order to generate a tensile stress in the aluminium film, the sample is annealed at 350 °C in vacuum for 30 min (iv). As a last step, we release the beam with an isotropic RIE process (v).

Figure 3.3a shows a scanning electron microscopy (SEM) image of a typical aluminium nanobeam. To illustrate the effect of annealing on the stress in the aluminium thin film, we have fabricated an aluminium nanobeam sample without the annealing step (see Fig. 3.3b). Obviously there is a compressive stress in the evaporated aluminium film, resulting in a buckled nanobeam. The fabrication of high-Q nanobeam resonators in the MHz frequency range, however, requires a tensile stressed aluminium film. We therefore apply the annealing step, which releases the compressive stress and generates a modest tensile stress instead. For aluminium nanobeams, this tensile stress can be further increased by cooling the sample to low temperatures due to the large difference in the thermal expansion coefficient of aluminium and the silicon substrate. We will discuss this in more detail in Chap. 8.

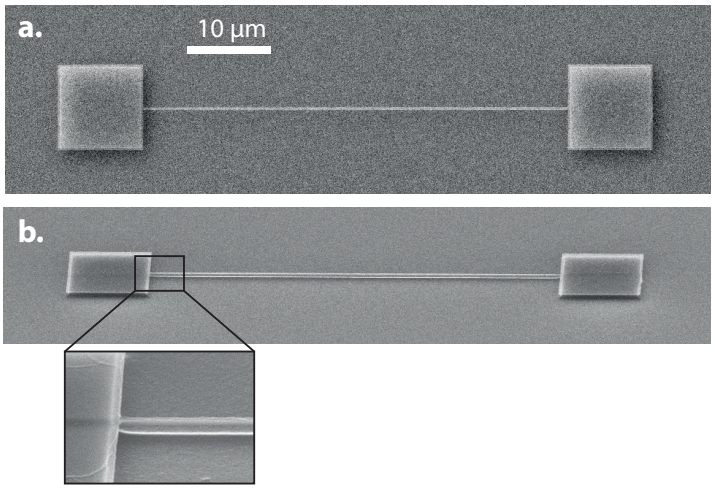

Figure 3.2: SEM images of a 50 µm long and 290 nm wide Si_3N_4 nanobeam, fabricated as described in Sec. 3.1.1. **a.** Top view. **b.** Tilted view (tilt angle: 60°). To take these images, a comparatively high acceleration voltage $U_{EHT} = 20\,kV$ was used, which allows to clearly identify the underetched parts of the Si_3N_4 film along the borders of the clamping pads.

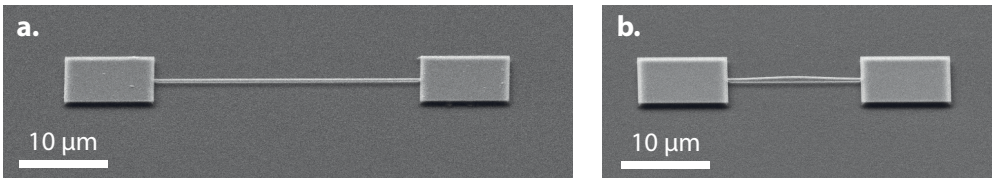

Figure 3.3: **a.** SEM image (at a tilt angle of 60°) of a 30 µm long and 340 nm wide, tensile stressed aluminium nanobeam, made from an annealed 100 nm thick film of e-beam evaporated aluminium. **b.** SEM image of an aluminium beam where the annealing step has been left out, resulting in a buckled beam shape caused by compressive prestress.

3.2 Experimental setup for room temperature mechanical spectroscopy

In the past decades, several techniques for the experimental investigation of the motion of nanomechanical resonators have been developed. While electrically conducting nanobeams can be driven and measured using magnetomotive forces [41], for insulating nanobeams a dielectric drive and read-out scheme has been developed. Here, we use optical interferometry to detect the nanobeam motion, while driving it with a piezoelectric actuator. This method is versatile in the sense that it does not require electrical contacts on the sample and can be applied to both insulating and conducting nanobeams.

3.2.1 Optical laser interferometry

To characterize our nanomechanical beam resonators, an optical free space laser interferometer (*IFM 1*) was developed, designed and installed at the WMI (see Fig. 3.4a,b). It provides a quick and easy way to characterize the nanobeam samples and therefore plays

an important role for the control of fabrication parameters and pre-characterization of nanoelectromechanical or magnetomechanical hybrid systems.

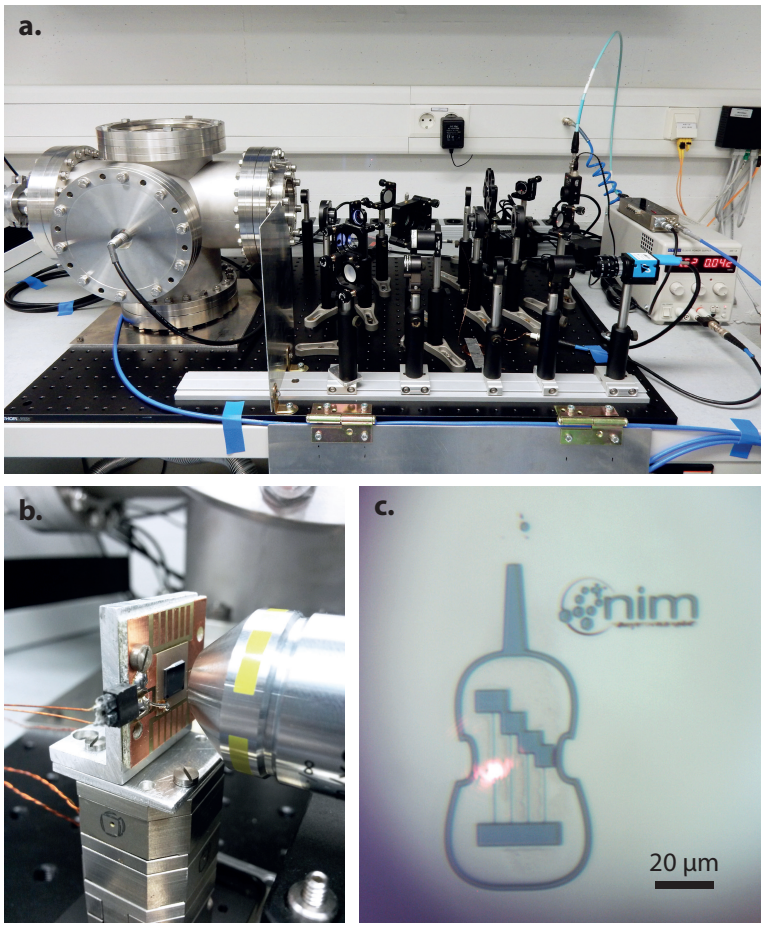

Figure 3.4: **a.** Photograph of the optical laser interferometer. **b.** Detailed view of the sample mounted inside the vacuum chamber. **c.** Live microscope image of a Si_3N_4 nanobeam sample. The laser spot is focused on one of the nanobeam resonators to detect its mechanical motion.

Figure 3.5 shows a schematic of the interferometry setup. A HeNe laser ($\lambda = 673\,\text{nm}$) with an output power of 2.3 mW is filtered and focused on the sample with a 10x or 20x objective. The reflected light is analyzed using a fast photodetector (*Thorlabs DET10A*, bandwidth 1 GHz). Before being incident on the nanobeam, the originally linearly polarized laser light is converted to circularly polarized light using a $\lambda/4$ plate. This ensures that the reflected light intensity is independent of the relative orientation of the nanobeam and the polarization axis[1]. The reflected laser light transits the $\lambda/4$ plate again and therefore the circular polarization is converted back to a linear polarization, which is perpendicular to the polarization of the incoming laser beam. In this way, we efficiently couple the reflected laser light onto the photodetector using a polarizing beam splitter.

[1] As the laser wavelength λ is similar to the width of typical nanobeams (100 to 500 nm), the reflected light amplitude and phase can depend on the angle between nanobeam and polarisation direction in case of linearly polarized light. To avoid this, we use circularly polarized light.

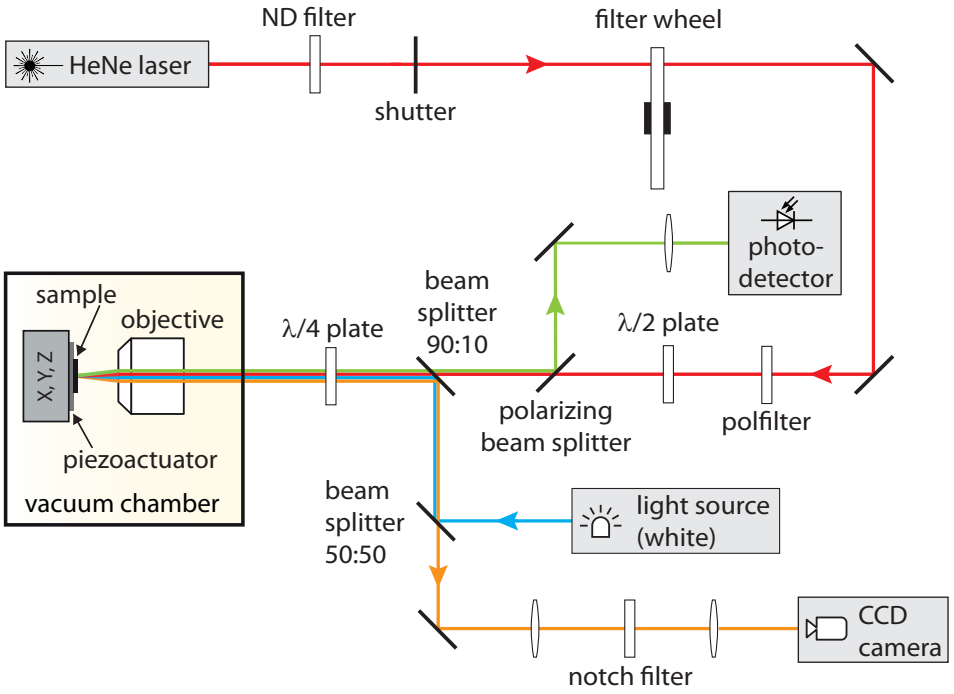

Figure 3.5: Schematic of the free beam interferometer shown in Fig. 3.4. The sample is mounted on a piezopositioner and located in a vacuum chamber to avoid gas damping. The laser beam is focused on a nanobeam resonator, and the reflected light is analyzed with a photodetector. An integrated optical microscope allows to monitor and adjust the position of the laser spot on the sample.

The sample, mounted on a piezoelectric actuator to excite the nanobeam resonance, can be positioned in all three spatial directions (x, y, z) with an *Attocube* piezopositioner. To avoid gas damping [42,43], the sample is operated in a vacuum chamber ($p < 10^{-4}$ mbar).

In order to control the position of the laser spot on the sample, an optical microscope is integrated into the laser interferometer. This allows a simple and fast positioning and focusing of the laser spot on the nanobeam. For an exemplary microscope image, see Fig. 3.4c.

3.2.2 Measurement setup

Figure 3.6 schematically shows the measurement setup (including the RF spectroscopy components) which was used to investigate the motion of pure Si_3N_4 and aluminium nanobeams and to pre-characterize nanomechanical hybrid samples.

To excite the motion of the nanobeam with a time-dependent force $F_0 \exp(-i\Omega t)$, the output of a vector network analyzer (VNA, *Rohde&Schwarz ZVA 8* or *ZVB 8*) is connected to the piezoactuator on which the sample is mounted. The reflected laser light, which is modulated by the nanobeam motion, is converted to a photovoltage signal, amplified (*Femto DHPVA-200*) and measured with the VNA. Sweeping the VNA frequency over the resonance frequency of the nanobeam allows investigating the response spectrum of the respective mode and extracting e. g. its resonance frequency and linewidth.

To measure the thermal motion spectrum of the undriven mechanical resonator, the VNA is replaced by a spectrum analyzer (*Rohde&Schwarz FSV*). We use this to calibrate the interferometric read-out as derived in Sec. 2.2, which allows to convert the measured photovoltage to the absolute displacement of the nanobeam.

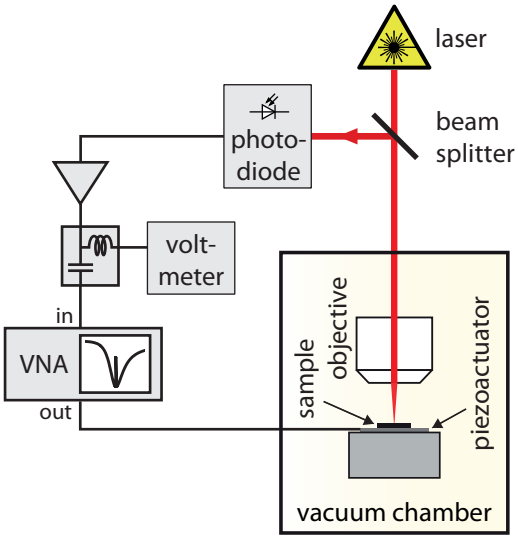

Figure 3.6: Setup used for the characterization of nanobeam resonators with the optical laser interferometer shown in Fig. 3.4. For reasons of clarity, the optics have been strongly simplified in this schematic.

3.3 Silicon nitride nanobeams

In this section, we show experimental data of a pure Si_3N_4 nanobeam fabricated from a $t = 100\,\mathrm{nm}$ thin tensile stressed Si_3N_4 film on a silicon substrate, as detailed above (*Sample #1*). The beam length and width is $l = 60\,\mu\mathrm{m}$ and $w = 550\,\mathrm{nm}$, respectively. By measuring the thermal motion spectrum of the beam, we can calibrate the interferometric readout, i. e. we can determine the constant of proportionality relating the measured photovoltage to the amplitude of the beam motion. Additionally, the measured resonance frequency allows to calculate the prestress along the beam axis. Second, we measure the response spectrum of the driven nanobeam as a function of drive power in the nonlinear regime (i. e. for high amplitudes) to determine the Duffing parameter α and Young's modulus E of the beam.

Figure 3.7 shows the thermal motion spectrum of the fundamental out-of-plane mode, measured at room temperature ($T = 293\,\mathrm{K}$), together with the square root of the Lorentzian fit according to Eq. 2.10. From the experimental data, we extract a photovoltage amplitude of $\sqrt{S_{\mathrm{UU}}^{\mathrm{max}}} = 0.73\,\mu\mathrm{V}/\sqrt{\mathrm{Hz}}$, corresponding to a thermal motion amplitude of $\sqrt{S_{\mathrm{xx}}^{\mathrm{max}}} = 3.5\,\mathrm{pm}/\sqrt{\mathrm{Hz}}$ at the resonance frequency. The calibration factor, which allows to convert a measured photovoltage to a mechanical displacement, is therefore given by $C := \sqrt{S_{\mathrm{xx}}/S_{\mathrm{UU}}} = 11.3\,\mathrm{pm}/\mu\mathrm{V}$.

In Fig. 3.8a, the amplitude spectrum of the driven mechanical motion is plotted for a weak driving force, from which we extract the resonance frequency $\Omega_{\mathrm{m}}/2\pi = 4.485\,\mathrm{MHz}$

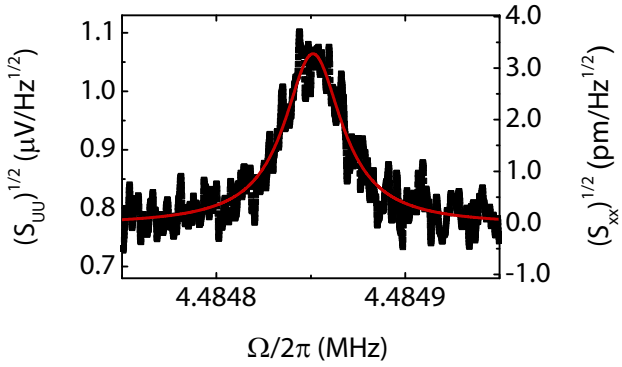

Figure 3.7: Thermal motion spectrum of the fundamental out-of-plain mode of Sample #1 (Si_3N_4 nanobeam). From the Lorentzian fit according to Eq. 2.10, the calibration factor relating the maximum measured photovoltage to the mechanical displacement of the nanobeam can be extracted.

and the linewidth[2] $\Gamma_m/2\pi = 28.6\,\mathrm{Hz}$, corresponding to a quality factor $Q = \Omega_m/\Gamma_m = 1.57 \times 10^5$. This value is slightly lower than expected (cf., e. g., Ref. [44]), which we attribute to linewidth broadening due to a slight thermal instability of the resonance frequency during the measurement.

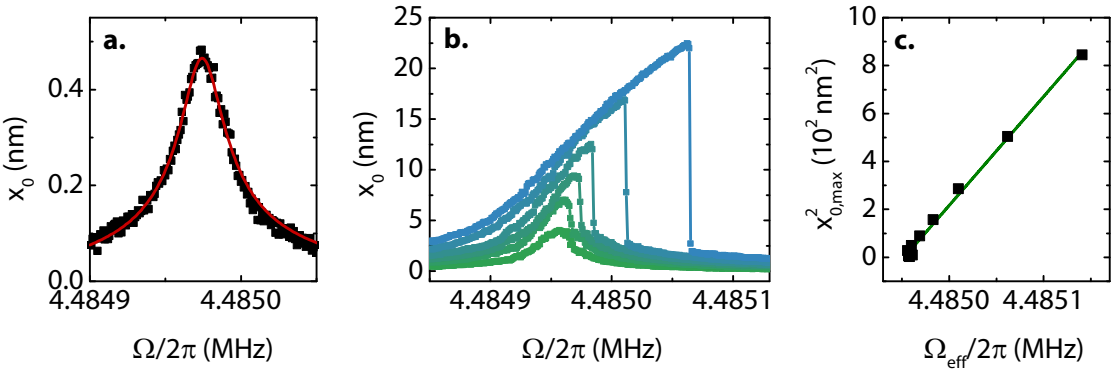

Figure 3.8: a-b. Amplitude spectrum of the fundamental out-of-plain mode of Sample #1 for (a) weak ($U_{piezo} = 0.2\,\mathrm{mV_{rms}}$) and (b) increasing drive power ($U_{piezo} = 1.7$ to $9.4\,\mathrm{mV_{rms}}$). The red line is a Lorentzian fit to the experimental data. **c.** Maximum of the amplitude spectra versus effective resonance frequencies for various driving strengths (backbone curve), extracted from the spectra shown in (b). The green line is a linear fit, which allows to extract Young's modulus according to Eq. 2.13.

To determine Young's modulus of the Si_3N_4 beam, we increase the drive power to access the Duffing regime of the resonator (see Sec. 2.3). Figure 3.8b shows the amplitude spectrum for drive voltages between 1.7 and $9.4\,\mathrm{mV_{rms}}$, applied to the piezoactuator. We observe the expected shift of the effective resonance frequency for increasing drive power and the emerging bistable region, where the amplitude jumps at the effective resonance frequency. As we are sweeping the drive frequency from lower to higher values in our experiments, we always access the upper branch of the bistable region (see Sec. 2.3). For a comparison of frequency up- and downsweeps, please see Ref. [40].

[2] Throughout this thesis, *linewidth* always means the full width at half maximum (FWHM).

In Fig. 3.8c, the square of the peak amplitude $x^2_{0,\mathrm{max}}$ is plotted versus the effective resonance frequency $\Omega_{\mathrm{eff}}/2\pi$. According to Eq. 2.13, the slope of this so-called *backbone curve* is related to the Duffing nonlinearity α, for which we find $\alpha = 1.2 \times 10^{26}\,\mathrm{m^{-2}s^{-2}}$. Using Eq. 2.11, we obtain the Young's modulus $E_{\mathrm{SiN}} = 162\,\mathrm{GPa}$. This is significantly reduced compared to the literature value for spatially homogeneous Si_3N_4 thin films $E_{\mathrm{SiN,film}} = 300\,\mathrm{GPa}$ [45], but in good agreement with experimental values found for highly-stressed Si_3N_4 nanoresonators [39, 44].

Using the experimentally determined Young's modulus, Eq. 2.4 and the density of Si_3N_4, $\rho_{\mathrm{SiN}} = 2600\,\mathrm{kg/m^3}$ [46], we can calculate the tensile stress from the measured resonance frequency and obtain $\sigma_0 = 732\,\mathrm{MPa}$, which is in good agreement with previously measured values from similar Si_3N_4 films [39, 44, 47].

3.4 Aluminium nanobeams

Similar to Sample #1, a $l = 30\,\mu\mathrm{m}$ long tensile stressed aluminium nanobeam (*Sample #2*) with cross-section $w \times t = 340\,\mathrm{nm} \times 100\,\mathrm{nm}$ has been characterized at room temperature to determine its material parameters. Figure 3.9a,b shows the amplitude spectrum of the fundamental out-of-plane mode in the linear (weak drive) and nonlinear (increasing drive power) regime, respectively. From these data, we extract the resonance frequency $\Omega_{\mathrm{m}}/2\pi = 4.177\,\mathrm{MHz}$, the linewidth $\Gamma_{\mathrm{m}}/2\pi = 520\,\mathrm{Hz}$ ($Q = 8.0 \times 10^3$) and the nonlinearity $\alpha = 5.3 \times 10^{26}\,\mathrm{m^{-2}s^{-2}}$. We proceed as above and obtain the Young's modulus $E_{\mathrm{Al}} = 47.3\,\mathrm{GPa}$ and the prestress $\sigma_0 = 159\,\mathrm{MPa}$. Again, the experimentally determined Young modulus is lower than the literature value for bulk aluminium $E_{\mathrm{Al}} \approx 70\,\mathrm{GPa}$ [32]. The values that can be found for thin film aluminium deviate strongly dependent on fabrication parameters (see, e. g., Refs. [48, 49]).

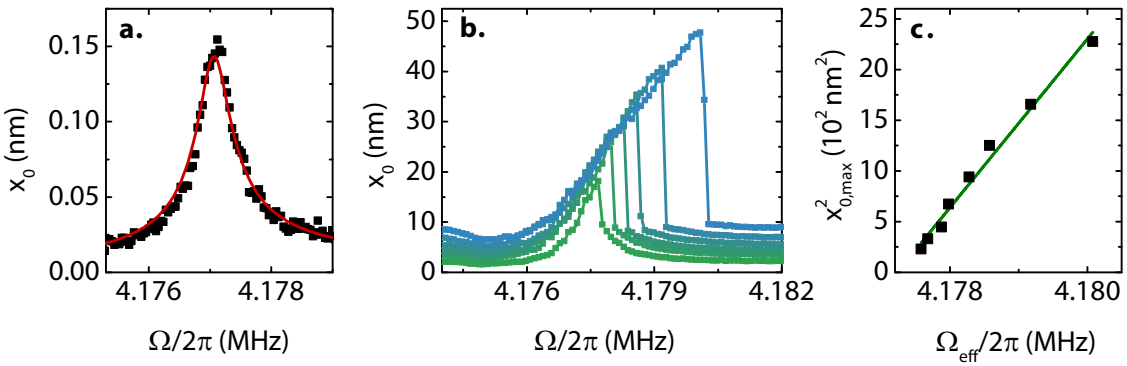

Figure 3.9: a-b. Amplitude spectrum of the fundamental out-of-plain mode of Sample #2 for (a) weak ($U_{\mathrm{piezo}} = 0.7\,\mathrm{mV_{rms}}$) and (b) increasing drive power ($U_{\mathrm{piezo}} = 90$ to $350\,\mathrm{mV_{rms}}$). The red line is a Lorentzian fit to the experimental data. **c.** Maximum of the amplitude spectra versus effective resonance frequencies for various driving strengths (backbone curve), extracted from the spectra shown in (b). The green line is a linear fit, which allows to extract Young's modulus according to Eq. 2.13.

The high damping rate $\Gamma_{\mathrm{m}}/2\pi = 520\,\mathrm{Hz}$, exceeding the one measured for the Si_3N_4 beam by a factor of 18, is caused by defect losses typically occuring in metal (or metallized) nanomechanical resonators at room temperature. It is consistent with previous experiments analyzing the damping rates of metallized Si_3N_4 membranes [50] and

nanobeams [51]. At low temperature, however, these defects freeze out, which significantly reduces the damping rate [52, 53]. In Chap. 8, we will demonstrate this and compare the room temperature and mK damping rates of an aluminium beam integrated in a superconducting circuit.

3.5 Summary

In this chapter, we have introduced the fabrication process of pure Si_3N_4 and aluminium nanobeam resonators on a silicon substrate. Employing optical laser interferometry, we have characterized a 60 µm long Si_3N_4 beam and a 30 µm long aluminium beam, fabricated from tensile stressed Si_3N_4 and aluminium films, respectively. By measuring the thermal motion of the nanobeam resonators, we calibrated the interferometric read-out and determined the amplitude of the beam motion. Analyzing the response spectra of the nanobeam resonators as a function of drive power allowed access to two important material properties, prestress and Young's modulus. Here, we made use of the non-linear Duffing regime of a strongly driven nanobeam. We determined prestress, Young's modulus and damping rates for both Si_3N_4 and aluminium samples and compared the measured quantities to literature values. While Si_3N_4 nanobeams, fabricated from a highly tensile stressed Si_3N_4 thin film, feature high resonance frequencies and excellent damping characteristics even at room temperature, the quality factors of aluminium nanobeams are limited to several thousand at room temperature due to defect losses. Nevertheless, aluminium nanobeams are well suited for the integration into all-aluminium superconducting circuits, as the damping rates are significantly reduced at low temperatures. We will show this in Chap. 8, where we present experimental data of an aluminium nanobeam integrated in a superconducting microwave circuit.

Chapter 4

Mechanics of homogeneous and multilayer nanobeams

Nanomechanical multilayer structures offer the possibility of tailoring the properties of a nanoresonator to a large extent and are therefore ideally suited for integration into hybrid systems [50, 51]. The combination of different materials – often tensile stressed silicon nitride together with a metal thin film – allows realization of excellent mechanical properties together with a good coupling to other degrees of freedom, like microwave circuits [54], magnetic systems [55] or spin currents [56]. We will make use of this idea in Chap. 5, where we form a magneto-mechanical hybrid system by depositing a magnetoelastic thin film onto a nanobeam resonator. The resulting hybrid system can be used to probe magnetostriction via its impact on the mechanical properties of the nanobeam resonator.

This chapter provides a theoretical description of the mechanics of multilayer nanobeams. A thorough understanding of these systems allows to tailor the properties of multilayer nanobeams *a priori* and to infer material properties from experimentally determined quantities.

First, we present an analytical description of the flexural motion of homogeneous, tensile stressed nanobeams and relate the resonance frequency of their vibrational modes to the material properties of the beam. Based on this, we derive an analytical description of the mechanics of multilayer nanobeams and show that the vibrational modes of such beams can be treated similar to the ones of a nanobeam with homogeneous cross-section by introducing effective variables for the relevant material parameters. We compare the predictions of this multilayer beam theory to experimental data and demonstrate good quantitative agreement between experiment and model.

The results presented in this chapter have partly been published in [57].

4.1 Mechanics of a nanobeam with homogeneous cross-section

4.1.1 Forces acting on an infinitesimal volume element

We consider a volume element of the beam with length $\mathrm{d}x$ and cross-sectional area A as indicated in Fig. 4.1. The beam is aligned along the x-axis, the displacement $v(x)$ is in

z-direction. The thickness of the beam (along the z-direction) is denoted t, the width (along $\hat{\mathbf{y}}$) is w[1]. According to standard beam theory [58], the bending of the beam is associated with a shear force $F_\mathrm{s}(x)$ and a torque $M(x)$ (along the y-direction) acting on the infinitesimal volume element depicted in Fig. 4.1b. The net force in z-direction applied to the volume element is then given by $F_\mathrm{bending} = -\frac{\partial F_\mathrm{s}}{\partial x}\mathrm{d}x$. Here, the minus sign is due to the sign convention of Ref. [31], as illustrated in Fig. 4.1b. The net moment on the volume element, $\frac{\partial M}{\partial x}\mathrm{d}x$, is related to the shear force F_s by [31, 58]

$$\frac{\partial M}{\partial x}\mathrm{d}x = F_\mathrm{s}\frac{\mathrm{d}x}{2} + \left(F_\mathrm{s} + \frac{\partial F_\mathrm{s}}{\partial x}\mathrm{d}x\right)\frac{\mathrm{d}x}{2} \approx F_\mathrm{s}\mathrm{d}x\ . \tag{4.1}$$

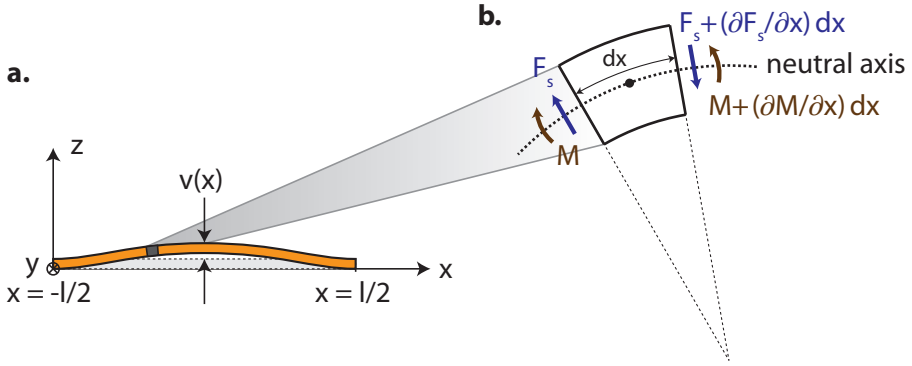

Figure 4.1: a. Definition of the coordinate system used in this chapter. The beam with length l is aligned along the x-direction, the displacement $v(x)$ is in the x-z-plane. **b.** Shear force and torque acting on an infinitesimal volume element, caused by the bending of the beam. We follow the beam sign convention in [31].

For a prestressed beam, there are additional axial forces $F_{\mathrm{ax},1}$ and $F_{\mathrm{ax},2}$ acting on the volume element, as indicated in Fig. 4.2. They are given by

$$\begin{aligned}\mathbf{F}_{\mathrm{ax},1} &= \sigma_0 A(-\cos\varphi_1\hat{\mathbf{x}} + \sin\varphi_1\hat{\mathbf{z}}) \quad \text{and}\\ \mathbf{F}_{\mathrm{ax},2} &= \sigma_0 A(\cos\varphi_2\hat{\mathbf{x}} - \sin\varphi_2\hat{\mathbf{z}}),\end{aligned}$$

where σ_0 is the prestress. The net force due to the prestress is then given by

$$\mathrm{d}\mathbf{F}_\mathrm{prestress} = \mathbf{F}_{\mathrm{ax},2} + \mathbf{F}_{\mathrm{ax},1} = \sigma_0 A\left[(\cos\varphi_2 - \cos\varphi_1)\hat{\mathbf{x}} + (\sin\varphi_1 - \sin\varphi_2)\hat{\mathbf{z}}\right]\ .$$

For small displacement of the beam ($v \ll l$ and $\varphi_{1,2} \ll 1$), we can use the approximations $\cos\varphi_2 - \cos\varphi_1 \approx 0$ and $\sin\varphi_1 - \sin\varphi_2 \approx \varphi_1 - \varphi_2 = \mathrm{d}\varphi$. Furthermore, we have $\mathrm{d}\varphi \approx \mathrm{d}x/r$ and the curvature radius r is given by [59]

$$\frac{1}{r} = \frac{\frac{\partial^2 v}{\partial x^2}}{\left[1 + \left(\frac{\partial v}{\partial x}\right)^2\right]^{3/2}} \approx \frac{\partial^2 v}{\partial x^2}\ .$$

[1]Compared to the previous chapters, we slightly change the nomenclature: The displacement of the beam is now described by v, whereas x, y and z denote spatial coordinates. We restrict our discussion to transverse vibrational modes and can therefore assume $\mathbf{v} \parallel \hat{\mathbf{z}}$.

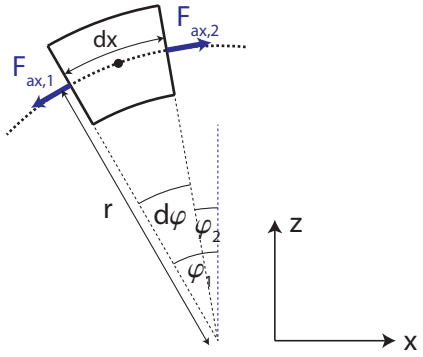

Figure 4.2: Axial force in a prestressed beam.

For the approximation on the right hand side we have used $\partial v/\partial x \ll 1$ for small displacement. With the above approximations we finally get

$$\mathrm{d}\mathbf{F}_{\mathrm{prestress}} = \sigma_0 A \mathrm{d}x \, \frac{\partial^2 v}{\partial x^2} \, \hat{\mathbf{z}}. \tag{4.2}$$

Note that the axial force due to the prestress does not contribute to the bending moment acting on the volume element.

The total force on the volume element, acting in y-direction, is the sum of the axial force due to prestress $\mathrm{d}F_{\mathrm{prestress}}$ and the shear force due to bending $\mathrm{d}F_{\mathrm{bending}} = -\frac{\partial F_{\mathrm{s}}}{\partial x}\mathrm{d}x$.

4.1.2 Relation between bending moment and displacement curvature

As mentioned above, an axial force due to prestress does not cause any bending moment. Therefore, we can neglect the prestress in this subsection and assume $\sigma_0 = 0$.

In order to derive the relation between the bending moment M and the curvature of the beam $\partial^2 v/\partial x^2$, we consider the volume element shown in Fig. 4.3. By definition, the length of the neutral axis $\tilde{r} = \tilde{r}_{\mathrm{nf}}$ does not change under influence of a bending moment, while the other layers of the beam are elongated ($\tilde{r} > \tilde{r}_{\mathrm{nf}}$) resp. compressed ($\tilde{r} < \tilde{r}_{\mathrm{nf}}$). The change in length of such a layer is given by

$$\mathrm{d}x' - \mathrm{d}x = \mathrm{d}x \frac{\tilde{r} - \tilde{r}_{\mathrm{nf}}}{r} \, .$$

This results in a stress [59]

$$\sigma = E \, \frac{\mathrm{d}x' - \mathrm{d}x}{\mathrm{d}x} = E \, \frac{\tilde{r} - \tilde{r}_{\mathrm{nf}}}{r} \, , \tag{4.3}$$

corresponding to the torque

$$\mathrm{d}M = \sigma w \mathrm{d}\tilde{r} (\tilde{r} - \tilde{r}_{\mathrm{nf}}) = E w \mathrm{d}\tilde{r} \, \frac{(\tilde{r} - \tilde{r}_{\mathrm{nf}})^2}{r} \, . \tag{4.4}$$

The total bending moment can be calculated by integration of $\mathrm{d}M$:

$$M = \int_{\tilde{r}=0}^{t} \mathrm{d}M = \int_{\tilde{r}=0}^{t} E w \mathrm{d}\tilde{r} \frac{(\tilde{r} - \tilde{r}_{\mathrm{nf}})^2}{r} \, ,$$

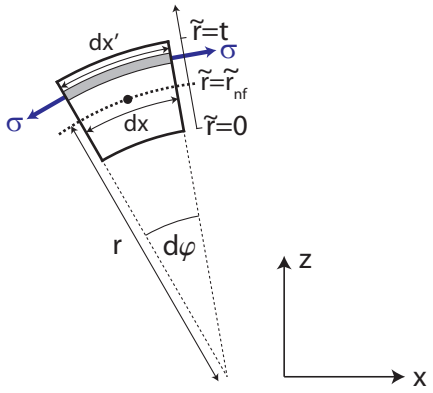

Figure 4.3: Derivation of the relation between torque and curvature of the beam.

where t is the thickness of the beam. In case of a homogeneous beam, the neutral axis is in the center of the beam, $\tilde{r}_{\mathrm{nf}} = t/2$, and we get $M = Ewt^3/(12r)$. Defining the area moment of inertia as $I = wt^3/12$ and using $1/r \approx \partial^2 v/\partial x^2$ yields [32, 59]

$$M = EI\frac{\partial^2 v}{\partial x^2} \,. \tag{4.5}$$

With Eq. 4.1 and $\mathrm{d}F_{\mathrm{bending}} = -\frac{\partial F_{\mathrm{s}}}{\partial x}\mathrm{d}x$, we then obtain the relation

$$\mathrm{d}F_{\mathrm{bending}} = -\frac{\partial^2 M}{\partial x^2}\mathrm{d}x = -EI\frac{\partial^4 v}{\partial x^4}\mathrm{d}x \,. \tag{4.6}$$

4.1.3 Equation of motion and resonance frequency

Using Eqs. 4.2 and 4.6, the total restoring force acting on the infinitesimal volume element can be expressed as

$$\mathrm{d}F_{\mathrm{restoring}} = \mathrm{d}F_{\mathrm{bending}} + \mathrm{d}F_{\mathrm{prestress}} = -EI\,\frac{\partial^4 v}{\partial x^4}\mathrm{d}x + \sigma_0 A\mathrm{d}x\,\frac{\partial^2 v}{\partial x^2} \,. \tag{4.7}$$

This results in the following equation of motion for the transverse vibrational mode of the beam [58, 60]

$$-\,EI\,\frac{\partial^4 v}{\partial x^4} + \sigma_0 A\,\frac{\partial^2 v}{\partial x^2} = \rho A\,\frac{\partial^2 v}{\partial t^2} \,, \tag{4.8}$$

where ρ denotes the mass density of the volume element.

To solve this equation of motion, we first assume a harmonic time dependence $v(x,t) = v(x)\exp(-i\Omega t)$, which leads to the following differential equation for $v(x)$ [58]:

$$-\,EIv^{(4)}(x) + \sigma_0 Av''(x) = -\rho A\Omega^2 v(x) \,. \tag{4.9}$$

The general solution of this differential equation is

$$v(x) = c_1\exp(\alpha x) + c_2\exp(-\alpha x) + c_3\sin(\beta x) + c_4\cos(\beta x) \tag{4.10}$$

with

$$\begin{aligned} \mu_{\pm} &= \frac{\sigma_0 A \pm \sqrt{\sigma_0^2 A^2 + 4EI\rho A\Omega^2}}{2EI} \,, \\ I &= \frac{wt^3}{12} \,, \\ \alpha &= \sqrt{\mu_+} > 0 \text{ , and} \\ \beta &= -i\sqrt{\mu_-} > 0 \,. \end{aligned}$$

For a doubly-clamped beam, the boundary conditions are [32, 58]

$$\begin{aligned} v(x = -l/2) &= 0 \,, \\ v(x = l/2) &= 0 \,, \\ v'(x = -l/2) &= 0 \text{ , and} \\ v'(x = +l/2) &= 0 \,. \end{aligned} \tag{4.11}$$

The application of these boundary conditions to the general solution (4.10) results in a homogeneous system of four linear equations and four variables c_j $(j = 1, 2, 3, 4)$. The determinant of this system of equations has to vanish, which is a necessary condition for the existence of solutions:

$$e^{-\alpha l}\left[\left(\alpha^2 - \beta^2\right)\left(e^{2\alpha l} - 1\right)\sin(\beta l) + 4\alpha\beta e^{\alpha l} - 2\alpha\beta\left(e^{2\alpha l} + 1\right)\cos(\beta l)\right] = 0 \tag{4.12}$$

As α and β are functions of Ω, this condition allows to determine the possible resonance frequencies $\Omega_n/2\pi$ of the beam. In general, there are no analytical solutions to this equation; thus, the resonance frequencies $\Omega_n/2\pi$ have to be determined numerically.

For special cases, however, there are approximations which allow to give an analytical expression for Ω_n. This will be discussed in the next section.

4.1.4 Approximations for resonance frequency and beam shape

In case of a nanobeam with vanishing or dominating stress, one can neglect one of the two contributions on the left hand side of Eq. 4.9 and/or modify the boundary conditions Eq. 4.11, which allows solving the equation of motion analytically. In the following, we will review these approximations and additionally derive a formula for the resonance frequency of a tensile stressed beam which includes bending effects to first order. We show that this expression is suitable to predict the resonance frequency of typical tensile stressed beams precisely and compare all approximations to the full numerical solution.

Unstressed beam *[US]* ($\sigma_0 \approx 0$):

In this case, the second term on the left hand side of Eq. 4.9 vanishes and $\alpha = \beta = (\rho A/EI)^{1/4}\Omega^{1/2}$. Substituting the general solution 4.10 into the set of boundary conditions 4.11 leads to the determinant $\cos(\alpha l)\cosh(\alpha l) - 1 = 0$, the roots of which have to be found numerically: $\alpha_n l = 0, 4.730..., 7.853..., 10.996..., ...$ [32]. Here, n denotes the mode index. The corresponding resonance frequencies are given by

$$\Omega_{\mathrm{US},n} = \sqrt{\frac{EI}{\rho A}}\,\alpha_n^2$$

and the beam shape is described by

$$v_{\mathrm{US},n}(x) = a_n\left(\cos(\alpha_n z) - \cosh(\alpha_n z)\right) + b_n\left(\sin(\alpha_n z) - \sinh(\alpha_n z)\right) \tag{4.13}$$

with $a_n/b_n = 1.018..., 0.999..., 1.000...$ for the first three modes.

Tensile stressed beam with simply-supported ends *[TS-SS]*:
Assuming simply-supported ends instead of fixed, i. e. clamped, ends, the last two equations of the boundary condition 4.11 are replaced by $v''(x = \pm l/2) = 0$. The modified set of boundary conditions is fulfilled by the solution

$$v_{\mathrm{TS-SS}}(x) = v_0 \cos(n\pi x/l)\ . \tag{4.14}$$

With this, the equation of motion 4.8 reduces to [30]

$$\ddot{v}(t) - \left(\frac{n\pi}{l}\right)^2\left[\frac{\sigma_0}{\rho} + \left(\frac{n\pi}{l}\right)^2\frac{EI}{\rho A}\right]v(t) = 0\ . \tag{4.15}$$

The resonance frequencies are therefore given by

$$\Omega_{\mathrm{TS-SS},n} = \frac{n^2\pi^2}{l^2}\sqrt{\frac{EI}{\rho A}}\sqrt{1 + \frac{\sigma_0 A l^2}{n^2 EI\pi^2}}\ . \tag{4.16}$$

.

Highly tensile stressed beam *[HTS]* ($\sigma_0 \gg EI\pi^2/Al^2$):
Here, we can simplify the equation of motion 4.15 further and obtain [30, 37]

$$\ddot{v}(t) - \left(\frac{n\pi}{l}\right)^2\frac{\sigma_0}{\rho}v(t) = 0 \tag{4.17}$$

with the resonance frequency

$$\Omega_{\mathrm{HTS},n} = \frac{n\pi}{l}\sqrt{\frac{\sigma_0}{\rho}}\ . \tag{4.18}$$

This approximation means that we fully neglect the contribution of the bending energy to the equation of motion (first term of the left hand side of Eq. 4.8) and approximate the nanobeam as a flexible string (*nanostring*).

While the nanostring approximation is usually employed when dealing with tensile stressed Si_3N_4 beams, it implicates significant errors of several percent depending on the respective material parameters. This is particularly relevant for the precise investigation of material parameters via resonance frequency measurements. We therefore present an alternative analytical approximation of the resonance frequency of a tensile stressed nanobeam, which includes bending effects to first order. For a complete derivation of this approximation, please see App. A.

Starting from the full determinant (Eq. 4.12), we derive the equation

$$(-1)^n 2\alpha\beta + (\alpha^2 - \beta^2)\sin(\beta l) = 0\ ,$$

which holds for $\sigma_0^2 A \gg 2EI\rho\Omega^2$. With the approximations $\alpha \approx \alpha_0 := \sqrt{\sigma_0 A/EI}$ and $\beta \approx \Omega\sqrt{\rho/\sigma_0}$ (see App. A), this relation can be simplified further:

$$(-1)^n 2\beta + \alpha_0 \sin(\beta l) = 0$$

For the n-th mode, $\beta l \approx n\pi$. Therefore, we can expand $\sin(\beta l)$ around $\beta l \approx n\pi$, which leads to

$$\beta = \frac{n\alpha_0\pi}{\alpha_0 l - 2} \, .$$

Substituting the definition of β into this expression, we finally obtain

$$\Omega_{\mathrm{TS},n} = \frac{n\sigma_0\pi\sqrt{A/\rho}}{l\sqrt{\sigma_0 A} - 2\sqrt{EI}} = \Omega_{n,\mathrm{HTS}} \frac{l\sqrt{\sigma_0 A}}{l\sqrt{\sigma_0 A} - 2\sqrt{EI}} \tag{4.19}$$

with $\Omega_{\mathrm{HTS},n} = (n\pi/l)\sqrt{\sigma_0/\rho}$ as defined above.

Equation 4.19 illustrates that the derived expression is a first order correction to the approximation of a highly tensile stressed beam. Obviously, $\Omega_{n,\mathrm{TS}} > \Omega_{n,\mathrm{HTS}}$. This can easily be understood as the bending contribution to the total energy of the vibrating nanobeam leads to an effective stiffening of the resonator, resulting in an increased eigenfrequency.

In the next section, we will demonstrate that for typical tensile stressed nanomechanical beams, this approximation can reproduce the full numerical solution of Eq. 4.12 much more precisely than the usually employed high-prestress approximation 4.18.

4.1.5 Comparison of the full numerical solution to approximated results

In order to compare the full numerical calculation of beam shape and resonance frequency to the approximations introduced above, we choose the parameters of the tensile stressed Si_3N_4 and aluminium beams (Samples #1 and #2) characterized in Chap. 3.

Figure 4.4a shows the calculated resonance frequency of both in-plane and out-of-plane modes of Sample #1 and #2, using the full numerical solution of Eq. 4.12, the approximation of a tensile stressed beam with included bending effects (*TS*, Eq. 4.19) as well the usually employed approximations of a simply-supported tensile stressed beam (*TS-SS*, Eq. 4.16) and a highly tensile stressed beam (*HTS*, Eq. 4.18). While the latter show significant deviations from the measured resonance frequency values (up to 15%), the approximation *TS* can reproduce the data within $|\Delta\Omega/\Omega| < 0.4\%$. In particular for the determination of material parameters from resonance frequency measurements, it is therefore necessary to take bending effects into account in order to reproduce the resonance frequency correctly.

In Fig. 4.4b, the beam shape of the fundamental in-plane and out-of-plane mode is plotted for Sample #1 (red lines) and #2 (blue lines), together with the limiting cases of a highly prestressed beam and an unstressed, doubly-clamped beam.

4.1.6 Effective mass

In the previous sections, we have treated the nanobeam resonator as a three-dimensional elastic solid and derived the equation of motion, the resonance frequency and the beam shape of the resonator modes. When dealing with nanomechanical resonators integrated in hybrid systems or sensing devices, however, it is more convenient to describe the mechanical resonator as a one-dimensional harmonic oscillator with effective mass m_{eff}, resulting in the equation of motion introduced in Chap. 2:

$$\ddot{x} + \Gamma_{\mathrm{m}}\dot{x} + \Omega_{\mathrm{m}}^2 x = \frac{F_0}{m_{\mathrm{eff}}} \exp(-i\Omega t) \, .$$

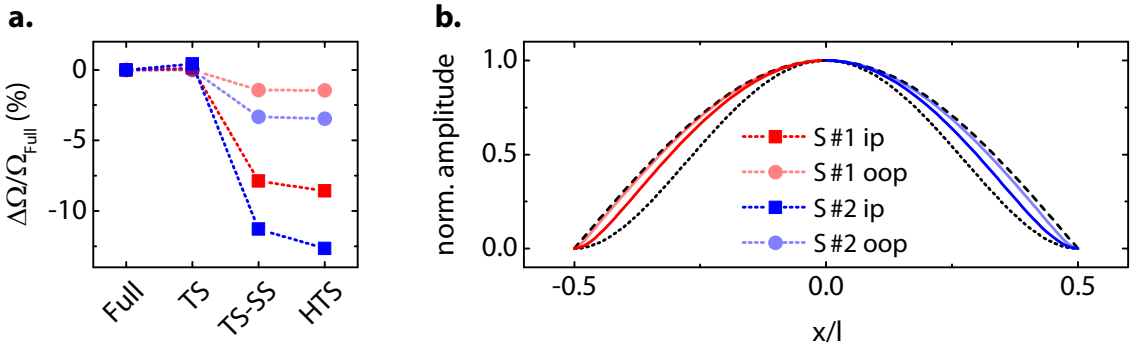

Figure 4.4: **a.** Relative error of the calculated resonance frequency compared to the full numerical solution. *TS*: tensile stressed beam with included bending effects (Eq. 4.19); *TS-SS*: tensile stressed beam with simply-supported ends (Eq. 4.16); *HTS*: highly tensile stressed beam (Eq. 4.18). **b.** Numerically calculated beam shape of the in-plane (ip) and out-of-plane (oop) mode of Sample #1 and #2, compared to the shape of an unstressed (dots) and a highly tensile stressed beam (dashed line). For reasons of clarity, only one half of the axially symmetric beam profile is shown for both Sample #1 and #2.

Here, we have introduced the phenomenological damping term $\Gamma_\mathrm{m}\dot{x}$ and the external driving force $F_0 \exp(-i\Omega t)$.

To determine the effective mass m_eff from the full three-dimensional description presented above, we start with the energy stored in the oscillation of a nanomechanical beam (see Supplementary Information of [44]):

$$\mathcal{U} = \frac{1}{2}\rho w t \Omega_\mathrm{m}^2 \int_{-l/2}^{l/2} \mathrm{d}x\, v^2(x) \tag{4.20}$$

Substituting the numerically calculated (or approximated) beam shape $v(x)$ into Eq. 4.20 allows determining the integral $\int_{-l/2}^{l/2} \mathrm{d}x\, v^2(x)$. Conversely, the total energy of a one-dimensional harmonic oscillator with displacement x_0 is given by

$$\mathcal{U} = \frac{1}{2} m_\mathrm{eff} \Omega_\mathrm{m}^2 x_0^2 \,, \tag{4.21}$$

where we define $x_0 := v(0)$ as the displacement of the center of the beam. Comparing Eqs. 4.20 and 4.21, we obtain

$$m_\mathrm{eff} = \frac{\rho w t}{x_0^2} \int_{-l/2}^{l/2} \mathrm{d}x\, v^2(x) \,. \tag{4.22}$$

Note that the effective mass depends on the mode shape and therefore varies for the different modes of the mechanical resonator.

For a highly tensile stressed beam, the displacement follows $v(x) \propto \cos(n\pi x/l)$ (see Eq. 4.14) and therefore the effective mass $m_\mathrm{eff,HTS}/m = 0.5$ is independent of the mode index n. For an unstressed beam, $m_\mathrm{eff,US}/m = 0.396$ for the fundamental mode ($n = 1$). Here, we have used the beam shape given by Eq. 4.13. The effective mass m_eff of a tensile stressed beam is limited by these two borderline cases, $m_\mathrm{eff,US} < m_\mathrm{eff} < m_\mathrm{eff,HTS}$.

Table 4.1 lists the calculated effective masses of the fundamental in-plane and out-of-plane mode of Sample #1 and #2.

	$m_{\mathrm{eff}}^{\mathrm{ip}}/m$	$m_{\mathrm{eff}}^{\mathrm{oop}}/m$
Sample #1	0.46	0.49
Sample #2	0.45	0.48

Table 4.1: Effective mass of the fundamental in-plane and out-of-plane modes of Sample #1 and #2, relative to their real masses $m_{\mathrm{S}\#1} = 8.6\,\mathrm{pg}$ and $m_{\mathrm{S}\#2} = 2.8\,\mathrm{pg}$.

4.1.7 Geometric nonlinearity

In the above derivation of the prestress-induced restoring force $\mathrm{d}\mathbf{F}_{\mathrm{prestress}}$ on an infinitesimal volume element of the beam (see Sec. 4.1.1), we assumed a constant prestress σ_0 independent of the beam displacement $v(x)$. Hereby, we neglected that a finite displacement elongates the nanobeam and therefore increases the prestress by $\delta\sigma = E\delta l$ (where δl denotes the elongation of the beam). Thus, the restoring force depends on the amplitude state of the nanobeam.

In the following, we will show that this so-called *geometric nonlinearity* leads to an additional term $\alpha v^3(t)$ in the equation of motion. This modified equation of motion is known as the *Duffing equation* [61]. To derive this we employ the approximation of a highly tensile stressed beam[2], as introduced in Sec. 4.1.4.

The length of the displaced nanobeam is given by

$$l' = \int_{-l/2}^{l/2} \sqrt{1 + v'^2(x)}\mathrm{d}x \approx \int_{-l/2}^{l/2} \left(1 + \frac{v'^2(x)}{2}\right) \mathrm{d}x \; .$$

Here we have expanded the square root to first order as $v'(x) \ll 1$. Using the approximation of a highly tensile-stressed beam, $v(x) = v_0 \cos(n\pi x/l)$ (see Sec. 4.1.4), we obtain

$$l' = l\left(1 + \frac{n^2 v_0^2 \pi^2}{4l^2}\right) \; . \tag{4.23}$$

This elongation of the displaced beam increases the tensile stress along the beam axis:

$$\sigma = \sigma_0 + E\frac{l' - l}{l} = \sigma_0 + \frac{n^2 v_0^2 \pi^2 E}{4l^2}$$

Substituting this into the equation of motion of a highly tensile-stressed beam (Eq. 4.17) yields

$$\dot{v}(t) - \left(\frac{n\pi}{l}\right)^2 \frac{\sigma_0}{\rho} v(t) - \frac{n^2 E \pi^4}{4l^4 \rho} v^3(t) = 0 \; .$$

Obviously, the elongation of the displaced beam leads to an additional term in the equation of motion which is proportional to v^3. The constant of proportionality, called *Duffing parameter*, is defined by

$$\alpha := \frac{n^2 E \pi^4}{4l^4 \rho} \; . \tag{4.24}$$

Whereas the Duffing nonlinearity can usually be neglected for small displacement, it leads to an effective resonance frequency shift and a bistable behaviour for large mechanical

[2] The geometric nonlinearity is only a small correction of the harmonic oscillator potential. Therefore, the errors induced by using the highly tensile stressed beam approximation are of second order and therefore negligible.

amplitudes, which they typically occur for strong drive power. Please see Chap. 2 for a detailed discussion of the effects of the Duffing nonlinearity on the behaviour of the mechanical beam.

4.2 Double-layer beam – out-of-plane vibrational mode

Up to now, we have focused on a beam with homogeneous cross-section. Here, we extend the discussion to beams consisting of two or more layers stacked in z-direction. For the sake of clarity, we restrict the following derivation to a system of only two layers with thickness t_A and t_B, as illustrated in Fig. 4.5. The Young's modulus and prestress of these layers are denoted E_A and E_B resp. $\sigma_{0,\mathrm{A}}$ and $\sigma_{0,\mathrm{B}}$. This scheme, however, is rather generic and can therefore be extended to three or more layers easily. In this section, we focus on the discussion of the out-of-plane mode, i. e. the displacement $u(x)$ is along $\hat{\mathbf{z}}$.

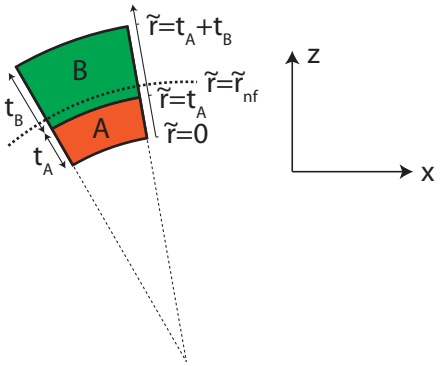

Figure 4.5: Nomenclature for the double-layer beam. The beam consists of two layers A and B with thickness t_A and t_B, stacked in z-direction.

As above, we consider an infinitesimal volume element of the nanobeam as illustrated in Fig. 4.5. Here, the axial force due to prestress is the sum of the forces in the two layers and can therefore (analogously to the derivation in Sec. 4.1.1) be written

$$\mathrm{d}\mathbf{F}_\mathrm{prestress} = \mathrm{d}\mathbf{F}_\mathrm{prestress,A} + \mathrm{d}\mathbf{F}_\mathrm{prestress,B} = (\sigma_{0,\mathrm{A}} w t_\mathrm{A} + \sigma_{0,\mathrm{B}} w t_\mathrm{B}) \mathrm{d}x \frac{\partial^2 u}{\partial x^2} \hat{\mathbf{z}} \,.$$

By defining the effective prestress σ_eff, we can treat the double layer system similar to the homogeneous beam:

$$\mathrm{d}\mathbf{F}_\mathrm{prestress} = \sigma_\mathrm{eff} A \mathrm{d}x \frac{\partial^2 u}{\partial x^2} \hat{\mathbf{z}} \,,$$

with $A = w(t_\mathrm{A} + t_\mathrm{B})$ and

$$\sigma_\mathrm{eff} := \frac{\sigma_{0,\mathrm{A}} t_\mathrm{A} + \sigma_{0,\mathrm{B}} t_\mathrm{B}}{t_\mathrm{A} + t_\mathrm{B}}.$$

The relation between bending moment and beam curvature can be derived analogously to Sec. 4.1.2 considering that E depends on z (resp. $\tilde{r}$) and that the neutral axis is not necessarily located in the center of the beam. To calculate $\tilde{r}_\mathrm{nf}$ for a double-layer beam, we use the fact that the total force acting on the infinitesimal volume element is the sum of the axial force due to prestress and a bending force, as described above. The latter does not stretch the beam, i. e. the stress normal to the beam cross-section due to

elongation/compression (as illustrated in Fig. 4.3) has to vanish when integrated over the cross-section. Using Eq. 4.3, this integral reads for the double-layer beam

$$\int_{\tilde{r}=0}^{t_\mathrm{A}+t_\mathrm{B}} \mathrm{d}\tilde{r}\sigma(\tilde{r}) = \int_{\tilde{r}=0}^{t_\mathrm{A}+t_\mathrm{B}} \mathrm{d}\tilde{r}E(\tilde{r})\frac{\tilde{r}-\tilde{r}_\mathrm{nf}}{r} = 0\,.$$

Solving this for $\tilde{r}_\mathrm{nf}$ yields

$$\tilde{r}_\mathrm{nf} = \frac{E_\mathrm{A}t_\mathrm{B}^2 + 2E_\mathrm{A}t_\mathrm{A}t_\mathrm{B} + E_\mathrm{B}t_\mathrm{A}^2}{2(E_\mathrm{A}t_\mathrm{B} + E_\mathrm{B}t_\mathrm{A})}\,,$$

where we have used $E(\tilde{r}) = E_\mathrm{A}$ for $\tilde{r} < t_\mathrm{A}$ and $E(\tilde{r}) = E_\mathrm{B}$ for $\tilde{r} > t_\mathrm{A}$. As above (cf. Eq. 4.4), the bending moment is given by

$$M = \int_{\tilde{r}=0}^{t_\mathrm{A}+t_\mathrm{B}} \mathrm{d}M = \int_{\tilde{r}=0}^{t_\mathrm{A}+t_\mathrm{B}} E(\tilde{r})w\mathrm{d}\tilde{r}\frac{(\tilde{r}-\tilde{r}_\mathrm{nf})^2}{r}\,.$$

This leads to

$$M = \frac{w\left[E_\mathrm{A}^2t_\mathrm{B}^4 + 2E_\mathrm{A}E_\mathrm{B}t_\mathrm{A}t_\mathrm{B}\left(2t_\mathrm{A}^2 + 3t_\mathrm{A}t_\mathrm{B} + 2t_\mathrm{B}^2\right) + E_\mathrm{B}^2t_\mathrm{A}^4\right]}{12r(E_\mathrm{A}t_\mathrm{B} + E_\mathrm{B}t_\mathrm{A})}\,.$$

Therefore, we can treat the double-layer beam similar to the homogeneous case,

$$M = E_\mathrm{eff}I\frac{\partial^2 u}{\partial x^2}\,,$$

by defining $I = w(t_\mathrm{A} + t_\mathrm{B})^3/12$ and the effective Young's modulus

$$E_\mathrm{eff} = \frac{E_\mathrm{A}^2t_\mathrm{B}^4 + 4E_\mathrm{A}E_\mathrm{B}t_\mathrm{A}^3t_\mathrm{B} + 6E_\mathrm{A}E_\mathrm{B}t_\mathrm{A}^2t_\mathrm{B}^2 + 4E_\mathrm{A}E_\mathrm{B}t_\mathrm{A}t_\mathrm{B}^3 + E_\mathrm{B}^2t_\mathrm{A}^4}{(t_\mathrm{A} + t_\mathrm{B})^3(E_\mathrm{A}t_\mathrm{B} + E_\mathrm{B}t_\mathrm{A})}\,. \tag{4.25}$$

With these effective material parameters, the resulting equation of motion for the double-layer beam reads

$$-E_\mathrm{eff}I\frac{\partial^4 u}{\partial x^4} + \sigma_\mathrm{eff}A\frac{\partial^2 u}{\partial x^2} = \rho_\mathrm{eff}A\frac{\partial^2 u}{\partial t^2}\,, \tag{4.26}$$

where the effective density is given by

$$\rho_\mathrm{eff} = \frac{\rho_A t_\mathrm{A} + \rho_B t_\mathrm{B}}{t_\mathrm{A} + t_\mathrm{B}}\,. \tag{4.27}$$

Equation 4.26 is fully equivalent to Eq. 4.9 if one replaces the material parameters ρ, σ and E by the effective material parameters ρ_eff, σ_eff and E_eff. Hence, the resonance frequency of the out-of-plane mode of a double-layer nanomechanical beam is (analogously to a homogeneous beam) given by Eqs. 4.18 resp. 4.19, employing effective parameters.

4.3 Double-layer beam – in-plane vibrational mode

Similar to the previous section, we investigate a nanobeam consisting of two layers with thickness t_A and t_B stacked in z-direction, as illustrated in Fig. 4.6. Now, we focus on the in-plane vibrational motion of the beam, i. e. the displacement $u(x)$ is along $\hat{\mathbf{y}}$.

Again, we consider an infinitesimal volume element of the nanobeam as illustrated in Fig. 4.6. The restoring forces $\mathrm{d}F_\mathrm{re,A}$ and $\mathrm{d}F_\mathrm{re,B}$ arising from bending and elongation of the two beam layers A and B act on the respective centers of mass of the two layers.

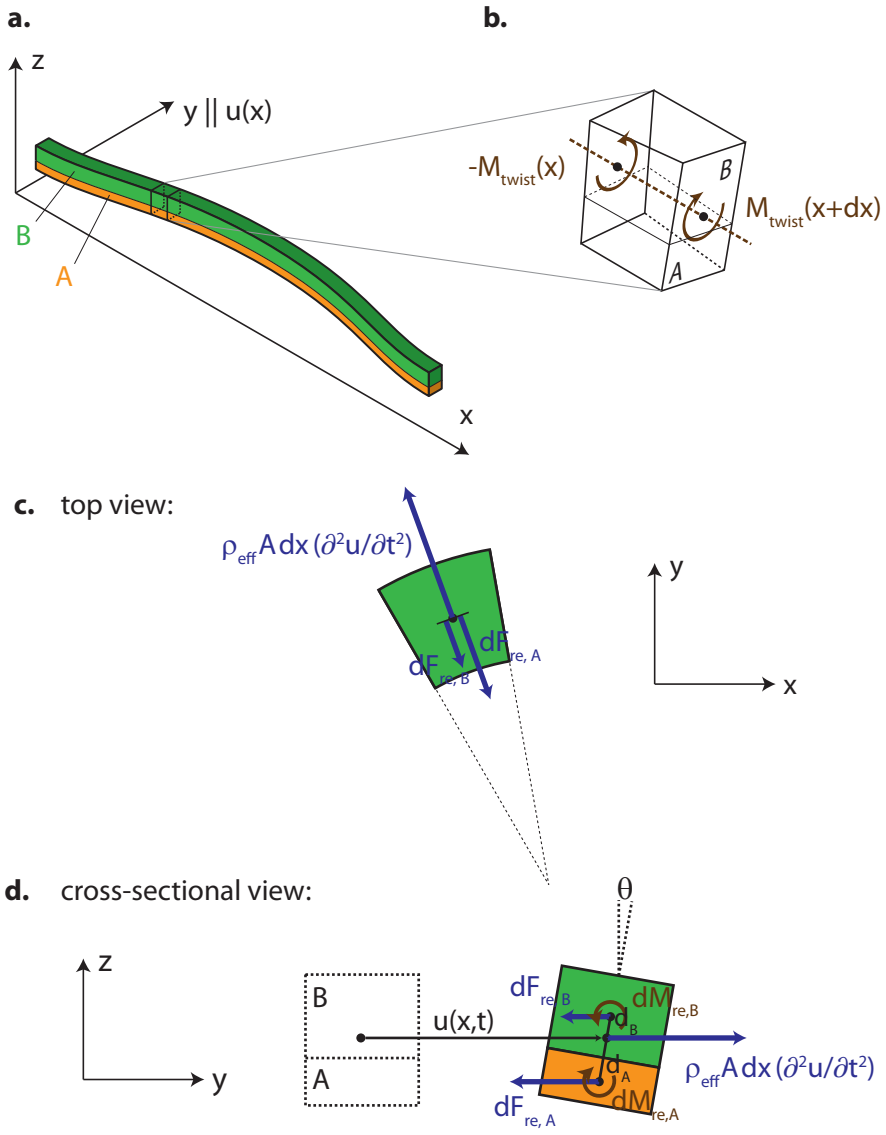

Figure 4.6: **a.** Schematic illustration of the in-plane vibrational motion of the double-layer nanomechanical beam. **b.** Infinitesimal volume element of the beam with dimensions $dx \times b \times (t_\mathrm{A} + t_\mathrm{B})$. Tilt and torsion of the volume element are indicated. **c-d.** Top view and cross-sectional view of the volume element, illustrating the restoring forces and corresponding torques.

The distance between the center of mass of A (B) and the center of mass of the whole volume element is denoted d_A (d_B). As the restoring forces $\mathrm{d}F_{\mathrm{re},i}$ ($i = \mathrm{A}, \mathrm{B}$) do not act on the center of mass of the whole volume element, they induce a torque $\mathrm{d}M_{\mathrm{re},i} = \mathrm{d}F_{\mathrm{re},i} d_i$ along $\hat{\mathbf{x}}$ on the volume element as depicted in Fig. 4.6d. The net torque is then given by $\mathrm{d}M_\mathrm{re} = \mathrm{d}M_\mathrm{re,A} - \mathrm{d}M_\mathrm{re,B}$. This torque induces a tilt (angle θ) of the volume element so that the in-plane vibrational mode is accompanied by an oscillating x-dependent torsion of the double-layer beam.

In the following, we will show that the corresponding tilt angles $\theta(x)$ are small and the torsional energy is about four orders of magnitude smaller than the total energy stored

in the beam vibration. Therefore, the contribution of the beam torsion may be neglected when describing the in-plane motion of the double-layer nanobeam, as shown in more detail in Sec. 4.3.3.

4.3.1 Vibrational in-plane motion

We first focus on the pure vibrational in-plane motion of the double-layer beam neglecting beam torsion. We show that the vibrational in-plane motion of a double-layer beam can be described analogous to that of a homogeneous beam by defining effective material parameters. In the next section, we turn to the torsional degree of freedom and estimate the tilt angle θ of the torsional motion as well as the corresponding energy stored in the torsion of the beam. We use these results to show that the torsional motion can indeed be neglected.

For a double-layer beam, the restoring force acting on the infinitesimal volume element is given by (see Fig. 4.6c)

$$\mathrm{d}F_{\mathrm{re}} = \mathrm{d}F_{\mathrm{re,A}} + \mathrm{d}F_{\mathrm{re,B}} \ ,$$

where $\mathrm{d}F_{\mathrm{re},i} = \mathrm{d}F_{\mathrm{prestress},i} + \mathrm{d}F_{\mathrm{bending},i}$ $(i = \mathrm{A}, \mathrm{B})$ is defined similar to Eq. 4.7. With the effective density $\rho_{\mathrm{eff}} = (\rho_{\mathrm{A}} t_{\mathrm{A}} + \rho_{\mathrm{B}} t_{\mathrm{B}})/(t_{\mathrm{A}} + t_{\mathrm{B}})$ and the beam cross-section $A = w(t_{\mathrm{A}} + t_{\mathrm{B}})$, Newton's second law for the volume element reads

$$\mathrm{d}F_{\mathrm{re,A}} + \mathrm{d}F_{\mathrm{re,B}} = \rho_{\mathrm{eff}} \mathrm{d}x A \frac{\partial^2 u}{\partial t^2} \ .$$

Using Eqs. 4.2 and 4.6 and defining the effective Young's modulus

$$E_{\mathrm{eff}} = \frac{E_{\mathrm{A}} I_{\mathrm{A}} + E_{\mathrm{B}} I_{\mathrm{B}}}{I_{\mathrm{A}} + I_{\mathrm{B}}} = \frac{E_{\mathrm{A}} t_{\mathrm{A}} + E_{\mathrm{B}} t_{\mathrm{B}}}{t_{\mathrm{A}} + t_{\mathrm{B}}}$$

and the effective prestress

$$\sigma_{\mathrm{eff}} = \frac{\sigma_{0,\mathrm{A}} t_{\mathrm{A}} + \sigma_{0,\mathrm{B}} t_{\mathrm{B}}}{t_{\mathrm{A}} + t_{\mathrm{B}}} \ ,$$

the resulting equation of motion for the double-layer beam reads

$$- E_{\mathrm{eff}} I \frac{\partial^4 u}{\partial x^4} + \sigma_{\mathrm{eff}} A \frac{\partial^2 u}{\partial x^2} = \rho_{\mathrm{eff}} A \frac{\partial^2 u}{\partial t^2} \ , \tag{4.28}$$

where $I = I_{\mathrm{A}} + I_{\mathrm{B}}$.

Similar to the case of out-of-plane motion, Eq. 4.28 is fully equivalent to Eq. 4.9 if one replaces the material parameters ρ, σ and E by the effective material parameters ρ_{eff}, σ_{eff} and E_{eff}. Hence, the resonance frequency can be calculated similar to the one of a homogeneous beam using the above defined effective parameters. Note that the definition of the effective Young's modulus is different for in-plane and out-of-plane motion.

4.3.2 Torsional motion

Equation 4.28, which describes the in-plane vibrational motion of a double-layer nanobeam, only holds for small beam torsion $\theta \ll 1$, where the displacement of the two beam layers from the equilibrium position is approximately equal: $u_{\mathrm{A}} \approx u_{\mathrm{B}} = u$. In the following, we will estimate the tilt angle θ of the in-plane beam motion and in this way justify the above assumption.

As illustrated in Figs. 4.6b and d, there are two different types of torque acting on the volume element: First, we have $\mathrm{d}M_{\mathrm{re}} = \mathrm{d}M_{\mathrm{re,A}} - \mathrm{d}M_{\mathrm{re,B}}$ (introduced at the beginning of Sec. 4.3), which arises from the fact that the forces $\mathrm{d}F_{\mathrm{re,A}}$ and $\mathrm{d}F_{\mathrm{re,B}}$ act on the center of mass of the layers A and B and in general do not compensate each other:

$$\mathrm{d}M_{\mathrm{re}} = \mathrm{d}M_{\mathrm{re,A}} - \mathrm{d}M_{\mathrm{re,B}} = \mathrm{d}F_{\mathrm{re,A}} d_{\mathrm{A}} - \mathrm{d}F_{\mathrm{re,B}} d_{\mathrm{B}} \,. \tag{4.29}$$

Second, if the beam is twisted, there is a corresponding torque proportional to $\partial\theta/\partial x$ acting on the cross-section of the beam at x and $x + \mathrm{d}x$. This torque is – similar to $\mathrm{d}\mathbf{M}_{\mathrm{re}}$ – directed along $\hat{\mathbf{x}}$ and given by [32]

$$M_{\mathrm{twist}}(x) = \mu I_{\mathrm{p}} \frac{\partial\theta(x)}{\partial x} \,, \tag{4.30}$$

where I_{p} is the polar moment of inertia and μ the shear modulus. Summing up all torques along $\hat{\mathbf{x}}$ acting on the infinitesimal volume element leads to the equation of motion for the torsional oscillation of the beam (cp. Ref. [32])

$$M_{\mathrm{twist}}(x + \mathrm{d}x) - M_{\mathrm{twist}}(x) + \mathrm{d}M_{\mathrm{re}} = \rho I_{\mathrm{p}} \mathrm{d}x \frac{\partial^2\theta}{\partial t^2} \,.$$

We use Eq. 4.30 and expand $M_{\mathrm{twist}}(x)$ in a Taylor series around x. Together with Eq. 4.29, we then obtain

$$\mu I_{\mathrm{p}} \frac{\partial^2\theta}{\partial x^2} + \frac{\mathrm{d}M_{\mathrm{re}}}{\mathrm{d}x} = \rho I_{\mathrm{p}} \frac{\partial^2\theta}{\partial t^2} \,, \tag{4.31}$$

where

$$\frac{\mathrm{d}M_{\mathrm{re}}}{\mathrm{d}x} = \left(\sigma_{0,A} A_{\mathrm{A}} \frac{\partial^2 u_{\mathrm{A}}}{\partial x^2} - E_{\mathrm{A}} I_{\mathrm{A}} \frac{\partial^4 u_{\mathrm{A}}}{\partial x^4}\right) d_{\mathrm{A}} - \left(\sigma_{0,B} A_{\mathrm{B}} \frac{\partial^2 u_{\mathrm{B}}}{\partial x^2} - E_{\mathrm{B}} I_{\mathrm{B}} \frac{\partial^4 u_{\mathrm{B}}}{\partial x^4}\right) d_{\mathrm{B}} \,. \tag{4.32}$$

The lever arms d_{A} and d_{B} can easily be calculated from the thickness of the two layers t_{A} and t_{B} and the respective densities ρ_{A} and ρ_{B}. Then, the quantities v_{A} and v_{B} are related to the center-of-mass motion u via $u_{\mathrm{A}} = u - d_{\mathrm{A}} \sin\theta$ and $u_{\mathrm{B}} = u + d_{\mathrm{B}} \sin\theta$ as can be seen in Fig. 4.6d. For small θ, we can further approximate $\sin\theta \approx \theta$. For a rough estimation, we assume $\theta(x,t) \propto u(x,t)$ with the proportionality constant $C = \theta/u$ and use the approximate beam displacement $u(x) \approx u_0 \cos(\pi x/l)$ (see Sec. 4.4). Substituting this into Eqs. 4.31 and 4.32 allows determination of the proportionality constant C that fulfils the equation of motion for the torsion (cf. Eq. 4.31) for all x. Finally, this yields the maximum twist angle $\theta(0) = C\,u(0)$ connected with a given beam displacement amplitude $u(0)$.

4.3.3 Torsion, elongation and bending energy

At last we calculate the torsional energy of the fundamental in-plane mode of the beam and compare it to the elongation and bending energy. The amount of energy stored in the torsion of the twisted beam is given by [62]

$$\mathcal{U}_{\mathrm{torsion}} = \int_{-l/2}^{l/2} M_{\mathrm{twist}}(x) \frac{\mathrm{d}\theta}{\mathrm{d}x} \mathrm{d}x \,.$$

Using Eq. 4.30, we find

$$\mathcal{U}_{\mathrm{torsion}} = \mu I_{\mathrm{p}} \int_{-l/2}^{l/2} \left(\frac{\mathrm{d}\theta}{\mathrm{d}x}\right)^2 \mathrm{d}x \,. \tag{4.33}$$

The contributions of elongation and bending to the energy of a displaced nanomechanical beam have been derived by Unterreithmeier *et al.* [44]. These are

$$\mathcal{U}_{\text{elongation}} = \frac{A\sigma_{\text{eff}}}{2}\int_{-l/2}^{l/2}\left(\frac{\partial u}{\partial x}\right)^2 \mathrm{d}x \tag{4.34}$$

and

$$\mathcal{U}_{\text{bending}} = \frac{w^3 t E_{\text{eff}}}{24}\int_{-l/2}^{l/2}\left(\frac{\partial^2 u}{\partial x^2}\right)^2 \mathrm{d}x\,, \tag{4.35}$$

where we have used the effective material parameters σ_{eff} and E_{eff} as justified above. In the next section, we will use Eqs. 4.33–4.35 to demonstrate that indeed the torsional degree of freedom can be neglected when describing the in-plane vibrational motion of typical double-layer nanomechanical beams.

4.4 Comparison with experimental data

To verify the above derived theory of doubly-clamped, multi-layer nanomechanical beams, we compare it to experimental data taken by F. Hocke during his PhD thesis [21] and published in Ref. [57]. The sample has been fabricated by X. Zhou [63]. We will not give a complete overview of this circuit electromechanical hybrid sample (*Sample #3*) and its electromechanical features. Instead, the coupling of the mechanical resonator to the microwave circuit is used only for read-out of the mechanical motion here. For a more detailed discussion of Sample #3, please see Refs. [21, 63].

4.4.1 Sample and experimental setup

Sample #3 consists of a $l = 60\,\mu\text{m}$ long and $w = 140\,\text{nm}$ wide Si_3N_4/niobium nanobeam integrated into a superconducting microwave circuit. The thickness of the nanobeam layers is $t_{\text{SiN}} = 70\,\text{nm}$ and $t_{\text{Nb}} = 130\,\text{nm}$, resulting in an effective mass of $m_{\text{eff}} = 5.4\,\text{pg}$. Here, we have used the relation $m_{\text{eff}} = 0.5\rho_{\text{eff}} lw(t_{\text{SiN}} + t_{\text{Nb}})$ and Eq. 4.27 for the effective density with $\rho_{\text{SiN}} = 2600\,\text{kg}\,\text{m}^{-3}$ [46] and $\rho_{\text{Nb}} = 8570\,\text{kg}\,\text{m}^{-3}$ [64]. [3]

The nanomechanical beam is capacitively coupled to a $\lambda/4$ superconducting coplanar waveguide microwave resonator with a resonance frequency of $\omega_c/2\pi = 6.07\,\text{GHz}$ and a quality factor of $Q \approx 8\,000$. Figure 4.7 shows the simplified experimental setup and a circuit diagram of the sample.

The microwave resonator is driven at its resonance frequency $\omega_c/2\pi$ with low power to minimize backaction on the mechanics. The nanobeam is excited by application of an additional MHz (AC) drive tone from the vector network analyzer (VNA) which is added to the microwave drive with a bias tee. Due to the electromechanical coupling between the microwave cavity and the mechanical resonator, the nanobeam motion induces sidebands in the microwave transmission which are measured using a homodyne detection scheme (see Fig. 4.7). Using frequency noise calibration[4], the height of the observed sidebands can directly be converted into a mechanical amplitude.

The experiment is conducted at a temperature of 400 mK.

[3] The value of m_{eff} differs from the one given in Ref. [57] due to a deviating definition of the effective mass: In Ref. [57], $m_{\text{eff}} = 0.63\rho_{\text{eff}} lw(t_{\text{SiN}} + t_{\text{Nb}})$ was used.

[4] For details on the experimental techniques used in circuit electromechanics, please refer to Chap. 6.

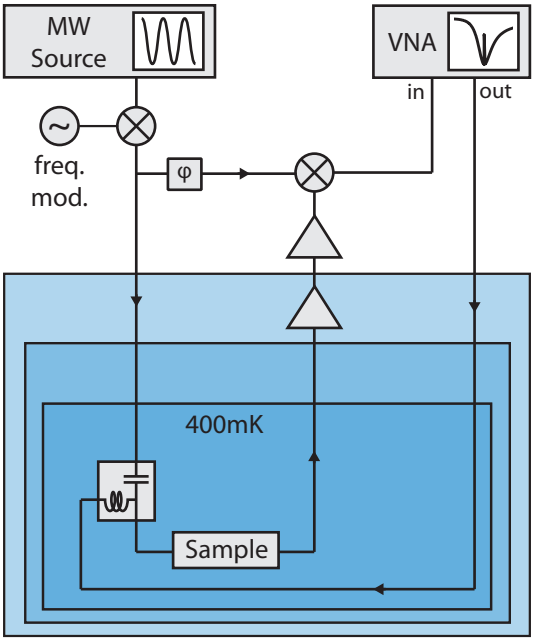

Figure 4.7: Schematic of the experimental setup used for analyzing the vibration characteristics of Sample #3.

4.4.2 Measurement results and comparison to multilayer beam theory

Figure 4.8a shows the measured homodyne signal as a function of the AC drive frequency, for a comparatively weak drive of $P_{\mathrm{ac}} = -100\,\mathrm{dBm}$. We observe a Lorentzian lineshape with a resonance frequency of $\Omega_{\mathrm{m}}/2\pi = 1.45\,\mathrm{MHz}$ and a linewidth of $\Gamma_{\mathrm{m}}/2\pi \approx 15\,\mathrm{Hz}$. Upon increasing the AC drive power, the nanobeam motion enters the non-linear Duffing regime, where the effective resonance frequency shifts as a function of drive power (see Fig. 4.8b). The relation between mechanical amplitude and effective resonance frequency is hereby given by the backbone equation 2.13, which allows to extract the Duffing non-linearity $\alpha = 3.7 \times 10^{25}\,\mathrm{m^{-2}s^{-2}}$ (similar to Secs. 3.3 and 3.4).

Using the experimentally determined resonance frequency $\Omega_{\mathrm{m}}/2\pi$ and Duffing parameter α allows to calculate the effective prestress and Young's modulus, σ_{eff} and E_{eff}, of the nanobeam resonator. In the following, we want to compare the full numerical calculation to the approximation of a tensile-stressed nanobeam (*TS*, see Eq. 4.19) and the widely employed approximation of a highly tensile-stressed beam (*HTS*, see Eq. 4.18).

First, we use Eq. 4.24 to determine E_{eff} from the measured Duffing nonlinearity α and obtain $E_{\mathrm{eff}} = 126\,\mathrm{GPa}$. With this, we can calculate the effective prestress from the measured $\Omega_{\mathrm{m}}/2\pi$ using the full numerical solution of the determinant Eq. 4.12 and obtain $\sigma_{\mathrm{eff}} = 182\,\mathrm{MPa}$. Employing the above mentioned approximations of a tensile stressed or a highly tensile stressed beam, we get $\sigma_{\mathrm{eff,TS}} = 183\,\mathrm{MPa}$ or $\sigma_{\mathrm{eff,HTS}} = 196\,\mathrm{MPa}$, respectively.

For comparison with the above derived multilayer beam theory, we use the material parameters $E_{\mathrm{SiN}} = 160\,\mathrm{GPa}$, $\sigma_{0,\mathrm{SiN}} = 830\,\mathrm{MPa}$ (both experimentally determined for a

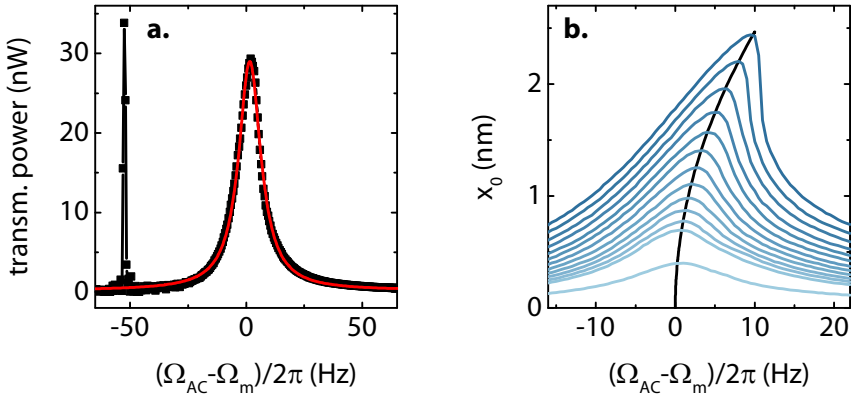

Figure 4.8: **a.** Amplitude spectrum of the fundamental in-plane mode of the nanobeam for low drive power and Lorentzian fit. The peak at $\Omega_{\mathrm{AC}} - \Omega_{\mathrm{m}} = -2\pi \times 50\,\mathrm{Hz}$ is used for calibrating the readout circuit. **b.** Amplitude spectra as a function of drive power (0.1 to 4.0 pW, light to dark blue lines) and fitted backbone curve (black line).

similar sample [44]), $E_{\mathrm{Nb}} = 105\,\mathrm{GPa}$ [32] and an estimated compressive stress in the niobium film of $\sigma_{0,\mathrm{Nb}} \approx -150\,\mathrm{MPa}$[5]. This results in

$$\begin{aligned} E_{\mathrm{eff}} &= 124\,\mathrm{GPa} \quad \text{and} \\ \sigma_{\mathrm{eff}} &= 204\,\mathrm{MPa}\,. \end{aligned}$$

These values are in good agreement with the experimentally determined parameters and thus support the validity of the multilayer beam theory.

4.4.3 Torsional motion associated to the in-plane mode

Next, we verify that the contribution of torsional motion to the in-plane mode is sufficiently small to be neglected. To this end, we calculate the twist angle as derived in Sec. 4.3.2 and obtain $\theta(0) = C\,u(0) = 0.0014°$ for a typical displacement of $u(0) = 1\,\mathrm{nm}$ ($C = 2.43 \times 10^4\,\mathrm{rad/m}$). Here, we have used the lever arms $d_{\mathrm{A}} = 12.3\,\mathrm{nm}$ and $d_{\mathrm{B}} = 87.7\,\mathrm{nm}$, the polar moment of inertia $I_{\mathrm{p}} = 1.54 \cdot 10^{-28}\,\mathrm{m}^{-4}$ [31] and the mean shear modulus $\mu = (\mu_{\mathrm{A}} t_{\mathrm{A}} + \mu_{\mathrm{B}} t_{\mathrm{B}})/(t_{\mathrm{A}} + t_{\mathrm{B}}) = 91\,\mathrm{GPa}$ (as $\mu_{\mathrm{Nb}} = 38\,\mathrm{GPa}$,[6] and $\mu_{\mathrm{SiN}} = 120\,\mathrm{GPa}$ [66]).

Substituting the approximate beam shape $u(x) = u_0 \cos(\pi x/l)$ with $u_0 = 1\,\mathrm{nm}$ and $\theta(x) = C\,u(x)$ into Eqs. 4.33 – 4.35, we find

$$\begin{aligned} \mathcal{U}_{\mathrm{torsion}} &= 1.9 \times 10^{-23}\,\mathrm{J}\,, \\ \mathcal{U}_{\mathrm{elongation}} &= 4.2 \times 10^{-19}\,\mathrm{J}\,, \text{ and} \\ \mathcal{U}_{\mathrm{bending}} &= 1.1 \times 10^{-21}\,\mathrm{J}\,. \end{aligned}$$

Hence, the torsional energy of the in-plane mode is about four orders of magnitude smaller than the total energy $\mathcal{U}_{\mathrm{tot}} = \mathcal{U}_{\mathrm{torsion}} + \mathcal{U}_{\mathrm{elongation}} + \mathcal{U}_{\mathrm{bending}}$. The torsional degree of freedom can therefore safely be neglected when describing the in-plane vibrational motion of the presented double-layer nanomechanical beam.

[5] We cannot directly access the compressive stress in our sputtered niobium films. The assumed stress, however, is consistent with values reported in literature for superconducting Nb thin films deposited by DC magnetron sputtering [65].

[6] This value was calculated from $\mu = E/(2(1+\nu))$ [32] with the Poisson ratio $\nu_{\mathrm{Nb}} = 0.40$ [32] and Young's modulus $E_{\mathrm{Nb}} = 105\,\mathrm{GPa}$ [32].

4.5 Summary

In this chapter, we have given a solid mechanics description of the flexural modes of a prestressed, doubly-clamped nanobeam resonator. We have derived the equations of motion and reduced them to an effective one-dimensional description of an effective mass in a harmonic potential with Duffing nonlinearity. The latter can be attributed to the geometric nonlinearity of a displaced nanobeam.

For practical purposes, the full numerical solution of the equations of motion is inconvenient. We have therefore derived an analytical expression which can reproduce the resonance frequency of a typical tensile-stressed nanobeam within 1% tolerance, much better than the usually employed highly-stressed beam approximation. We have demonstrated this by comparing to experimental parameters of the pure Si_3N_4 and aluminium nanobeam samples presented in Chap. 3.

Based on this, we have shown that a multilayer nanobeam can be treated similar to a beam with homogeneous cross-section when introducing effective material parameters for density, prestress and Young's modulus. This holds for the out-of-plane modes as well as for the in-plane modes. Regarding the latter, there is an additional torsional motion component which, however, can be neglected for typical parameter sets. We have compared the results of this multilayer beam theory to experimental data and demonstrated good quantitative agreement.

These results can be used to extract material parameters from (relatively simple) characterization experiments and in this way investigate material properties of thin films at room temperature or at low temperatures down to mK. Besides, in future experiments, the understanding of the mechanics of multilayer resonators allows to *a priori* tailor the parameters of such systems according to experimental demands.

Chapter 5

Magnetostriction sensing with a nanomechanical beam

Nanomechanical systems are an established platform for mass and force detection. In particular, the high quality factors of their vibrational modes [44] make them ideally suited for high-precision sensing applications in (nano)biology, medicine, chemistry and physics [10, 15, 17, 67, 68]. For example, nanomechanical resonators allow for the detection of DNA molecules [69] and atoms [14], and nanomechanical resonance spectroscopy has been proposed as a versatile tool and extension of conventional spectroscopy techniques in biology and chemistry [70]. In solid state physics, nanomechanical sensors are utilized for the investigation of material properties of thin films [71–73], which often significantly differ from those of bulk materials [74, 75]. One particular aspect is the investigation of externally tunable material properties as discussed in the field of multiferroics [76]. For example, it has been demonstrated that magnetostriction and magnetic anisotropy in a $Ga_{0.948}Mn_{0.052}As$ thin film can precisely be investigated using a nanomechanical beam setup [77].

Here, we extend this concept and present a versatile platform for the experimental investigation of magnetostrictive thin films which uses a doubly-clamped silicon nitride nanobeam covered with a thin layer of the material of interest. This approach allows for the investigation of any magnetostrictive thin film material – conducting as well as insulating – which can be deposited on a Si_3N_4 nanobeam, using e. g. electron beam evaporation, thermal evaporation or sputtering.

In the given sample layout, the magnetic thin film is tightly connected to the underlying nanobeam. An externally applied magnetic field does therefore not cause a measurable deformation of the magnetic film (as for usual magnetostriction measurement techniques); instead, it gives rise to magnetoelastic stress which can be read out by monitoring the resonance frequency of the double-layer nanobeam. This allows to deduce the magnetostriction constants of the thin film (see also [77]).

As a proof-of-principle experiment, we use the presented method to investigate two well-characterized materials, a cobalt and a nickel thin film (both polycrystalline), to allow comparison to literature data obtained with well-established methods.

As the thin film deposition is the last step in the sample fabrication process, the ferromagnetic film is not exposed to etching solution or dry etch reactants, which allows to

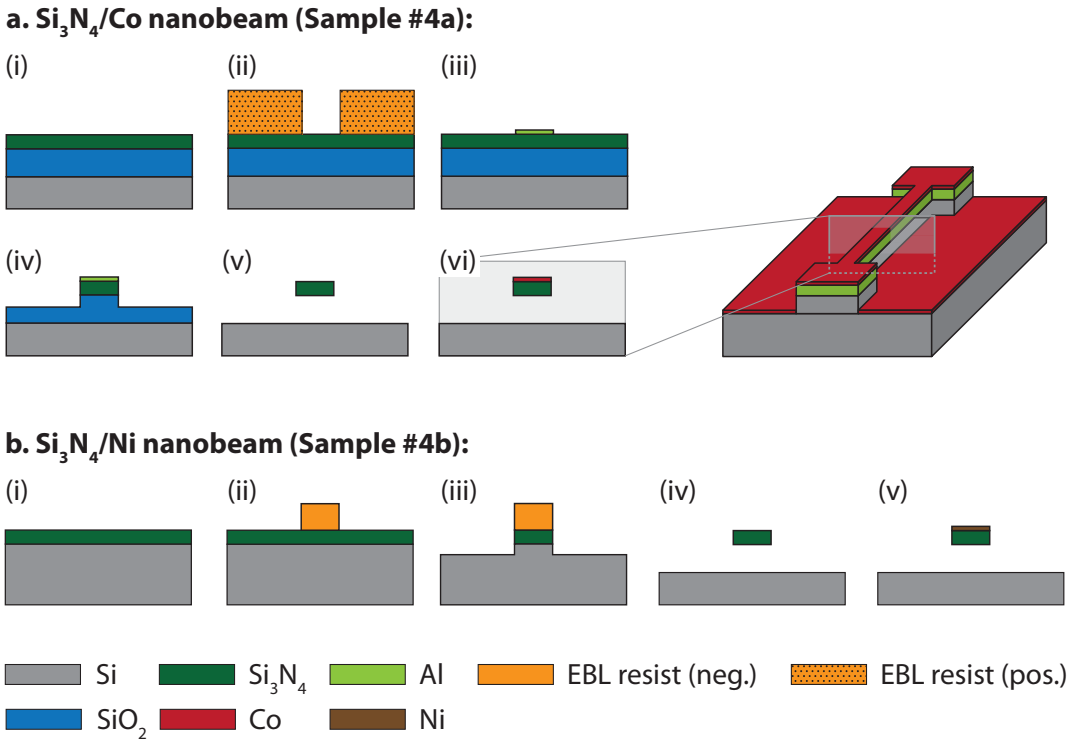

Figure 5.1: Schematic of the fabrication processes of Sample #4a and #4b. The individual steps are explained in the main text.

apply this technique to a broad range of materials. Moreover, the measurement sensitivity is expected to be independent of the film thickness which could be useful for the investigation of very thin magnetostrictive films.

The results shown in the following have partly been published in [78].

5.1 Sample fabrication

The fabrication process of the Si_3N_4/Co sample (*Sample #4a*) starts with a single-crystalline silicon wafer commercially coated with a 200 nm thick thermal oxide and a $t_{SiN} = 90$ nm thick LPCVD (low pressure chemical vapor deposition) highly stressed Si_3N_4 film [Fig. 5.1a (i)]. We use electron beam lithography (ii), aluminium evaporation and lift-off to create an etch mask for the $l = 25\,\mu$m long and $w = 350$ nm wide, doubly-clamped nanomechanical beam (iii). With a reactive ion etching step, we pattern-transfer the structure to the silicon nitride layer (iv). We subsequently remove the aluminium mask and release the nanobeam with buffered hydrofluoric acid (v). Finally, we deposit $t_{Co} = 10$ nm of cobalt on the chip using electron beam evaporation (vi).

The Si_3N_4/Ni sample (*Sample #4b*) is fabricated slightly differently[1]. Similar to Sample #1, we start with a single-crystalline silicon wafer coated with 100 nm of highly tensile-stressed LPCVD Si_3N_4 [Fig. 5.1b (i)]. We pattern the Si_3N_4 nanobeam using electron beam lithography (ii) and an anisotropic RIE step with Ar/SF_6 (iii), followed by an isotropic RIE process with SF_6 only (iv). Lastly, the $t_{Ni} = 10$ nm thick nickel film is deposited using electron beam evaporation (v).

5.2 Experimental setup

5.2.1 Optical free beam interferometer in an electromagnet

The experiments with Sample #4a have been conducted with a fiber interferometer built by Rasmus Holländer during his Bachelor's thesis at the Walther-Meißner-Institut. This setup is described in detail in [79] and will not be discussed here.

Within Peter Jörg's Bachelor's thesis, which I supervised, the setup was redesigned and rebuilt as a free beam interferometer, which is shown in Fig. 5.2. We have used this modified interferometer (*Magnet-IFM*) for the experiments with Sample #4b. In the following, we will give a quick overview of the interferometer setup. For a more detailed description, please see Ref. [80].

The Magnet-IFM consists of a vacuum and an ambient pressure part. The sample and the objective are placed inside a vacuum dipstick (Fig. 5.2a,c), which is positioned between the poleshoes of a *Bruker B-E 10* electromagnet. This electromagnet, providing a homogeneous magnetic field up to 200 mT at the sample position, can be rotated around an axis orthogonal to the magnetic field direction. The angle between the sample and the magnetic field orientation can be controlled over a range of approximately 240°. Most of the optical elements of the interferometer are concentrated in an *interferometer head*, mounted on top of the vacuum dipstick (see Fig. 5.2b). Similar to IFM1, the Magnet-IFM includes an optical microscope which provides a live image of the device under test and thus allows a fast and easy positioning of the laser spot on the sample surface.

The design of the interferometer head is inspired by the layout developed at the chair of Prof. J. Finley (Walter Schottky Institute, TU Munich) [81]. A schematic of the interferometer head is shown in Fig. 5.3.

To keep the weight of the interferometer head low, the laser source, a frequency- and power-stabilized diode laser (*Ondax LM-633-PLR-40*, $\lambda = 633$ nm), is mounted on an additional optical table and connected to the interferometer with an optical single-mode fiber. On the first level of the interferometer head, the laser beam is coupled from the fiber into the optical path of the interferometer using two mirrors and a $\lambda/2$ plate. The latter converts the linear polarization of the laser light into circular polarization. The laser beam is guided through a window into the vacuum dipstick and focused on the sample using a *MellesGriot* lens array (working distance 0.8 mm). The lens array replaces the microscope objective used in typical interferometers (see e. g. Chap. 3). The main reason

[1] We have used different fabrication processes for Sample #4a and Sample #4b for technical reasons only. At the beginning of this work, the fabrication was based on $Si/SiO_2/Si_3N_4$ wafers, where the SiO_2 buffer layer was etched with buffered hydriflouric acid. To make the fabrication process compatible with aluminium structures (see Chap. 8), we moved to Si/Si_3N_4 chips and released the nanobeams by introducing an isotropic RIE step. For simplicity, Sample #4b was fabricated according to this new process even if aluminium was not used on this sample.

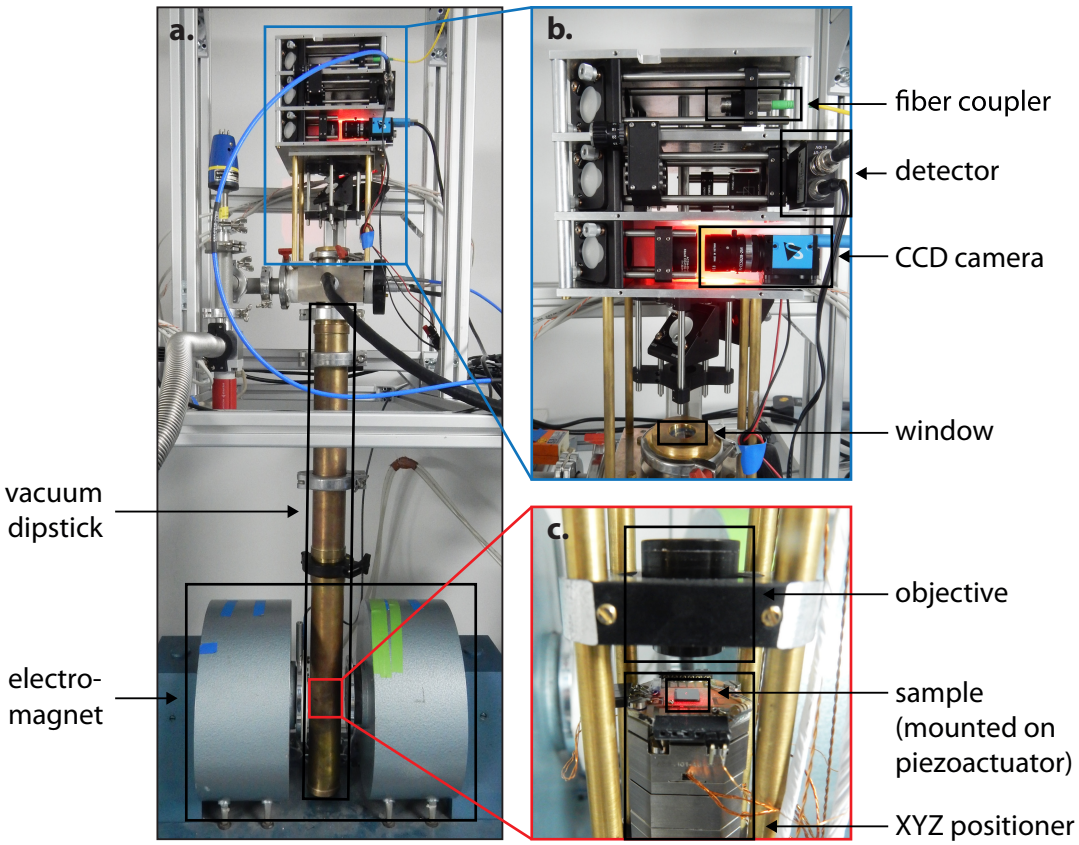

Figure 5.2: Photograph of the magnet free beam interferometer used to investigate Sample #4b. The sample is mounted on a piezoelectric XYZ-positioner (c) and located inside a vacuum tube. The optical elements for the generation and detection of the laser beam as well as the microscope optics are collected in the interferometer head (b) on top of the vacuum dipstick. The vacuum dipstick is placed between the poleshoes of an electromagnet, which can be rotated around its vertical axis (a).

is that the casing of this lens array is made of aluminium and therefore non-magnetic, while standard microscope objectives contain magnetic parts, which would distort both imaging and interferometry in an external magnetic field.

The sample is mounted on an *Attocube XYZ*-positioner which allows to move it relative to the position of the laser spot. The laser light reflected at the sample surface is directed back to the interferometer head and focused on a photodetector (*Thorlabs DET10A*, bandwidth 1 GHz), which is located on the second level of the interferometer head. The third level contains the microscope optics: a LED for illumination of the sample and a CCD camera onto which the sample image is projected. As a light source, we use a super-bright red LED whose emission wavelength $\lambda = 615\,\text{nm}$ is close to the laser wavelength to minimize the focal shift between the microscope image and the laser spot on the sample[2]. A notch filter in front of the CCD camera reduces the intensity of the laser spot on the camera and prevents saturation (or damage) of the CCD. In contrast to IFM1, we here do not use the polarization of the laser light to separate the reflected from the incoming

[2]In contrast to standard microscope objectives, the *MellesGriot* lens array used here is not corrected for focal shifts as it is typically employed for monochromatic laser light.

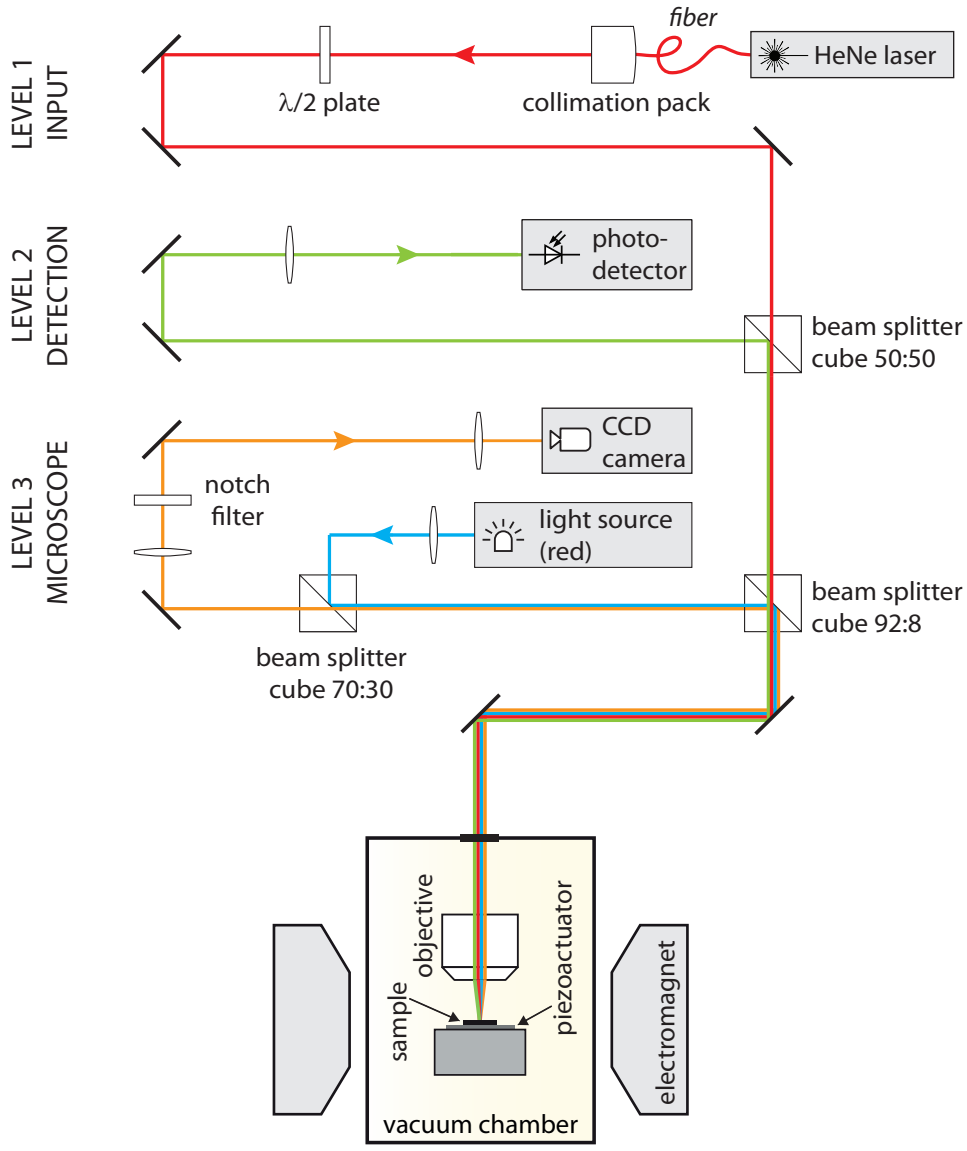

Figure 5.3: Schematic of the free space laser interferometer integrated into a vacuum dipstick for magnetic field measurements (*Magnet-IFM*).

laser light, i. e. we use non-polarizing beam splitters throughout. The reason is that due to the magneto-optical Kerr effect [82] the polarization of the laser light can be rotated after reflection at the surface of a magnetized film. Using a polarizing beam splitter in the optical path would therefore lead to a magnetization-dependent laser intensity on the detector and thus distort the measured signal.

Compared to a fiber interferometer, the Magnet-IFM has several advantages: First, the integrated microscope allows for a fast and easy positioning of the laser spot on the sample surface. Second, the working distance between the sample and the objective is much larger than the fiber-sample distance in a fiber interferometer, which is typically several µm. This prevents damaging of the sample and the optics. Besides, the laser light

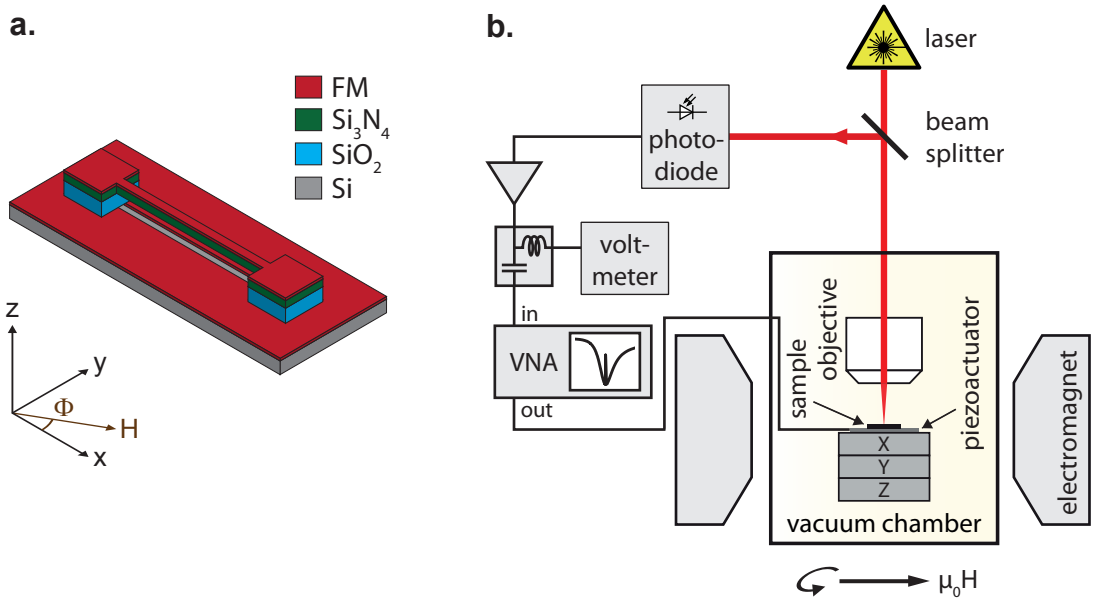

Figure 5.4: **a.** Schematic of Sample #4a/b, a doubly-clamped Si_3N_4 nanobeam (green) covered with a thin ferromagnetic film (dark red). The external magnetic field $\mu_0 H$ is oriented in the sample plane (i. e. the x-y-plane). **b.** Illustration of the experimental setup. A laser beam is focused on the sample and the reflected light is guided to a photodetector. The measured photovoltage is analyzed with a vector network analyzer, whose output is used to drive the nanobeam motion via a piezoelectric actuator. The sample is located in a vacuum chamber to avoid air damping. For reasons of clarity, the optics have been strongly simplified in this schematic.

reflected at the sample surface can effectively be coupled back into the optical path and guided to the photodetector, enabling a more sensitive detection of the nanobeam motion.

5.2.2 Measurement setup and coordinate system

The measurement setup is schematically shown in Fig. 5.4. The experiments are performed at room temperature and in vacuum ($p < 10^{-4}$ mbar) to avoid air damping. Using a piezoelectric actuator onto which the sample is glued, we can resonantly drive the flexural modes of the nanobeam. The beam motion modulates the reflected laser light, which linearly translates into a modulation of the detected photovoltage [83]. Employing signal vector analysis we study the mechanical response of the beam as a function of the applied actuator drive frequency. Additionally, to control the magnetization direction of the nanobeam, we apply a static magnetic field provided by the electromagnet, which we are able to rotate in the sample plane (i. e. the x-y-plane). The azimuthal angle Φ is defined between the external field direction and the main beam axis (see Fig. 5.4a).

5.3 Model connecting mechanical resonance frequency changes to magnetostriction

In this section, we present a model predicting the add-on stress on the magnetic layer caused by the magnetostrictive effect. We start with the magnetostrictive deformation of a

polycristalline free-standing ferromagnetic (FM) film with cylindrical shape and transform the corresponding strain tensor to the xyz-coordinate system (where the x-axis is parallel to the nanobeam). Then we use this result to calculate the magnetoelastic stress in a FM thin film on top of a nanobeam resonator and the induced resonance frequency shift.

5.3.1 Magnetostrictive strain in a free-standing magnetic thin film

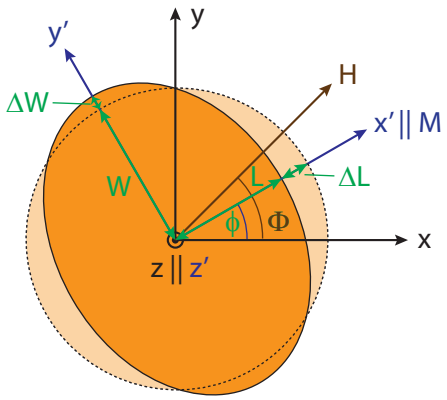

Figure 5.5: Definition of the $x'y'z'$-coordinate system which is rotated by ϕ with respect to the xyz-coordinate system, with $z' \parallel z$. The magnetization is along the x'-axis, while the nanobeam is parallel to the x-axis. Aligning the magnetization in a free-standing magnetostrictive thin film (for illustration purposes we have chosen a cylindrically shaped film here) causes a strain $\lambda_\parallel$ ($\lambda_\perp$) along the x' (y' and z') axis.

First, we consider a free-standing FM thin film, which is centered around the origin of the xyz-coordinate system (the lab system), as illustrated in Fig. 5.5 (dashed circle). In a sufficiently large magnetic field, the FM film is fully magnetized, i. e. all magnetic moments are aligned along the external field direction. Due to magnetostriction, the magnetic film is mechanically deformed along the magnetization direction $\mathbf{M}/M_\mathrm{s}$, which also induces a deformation in both orthogonal directions (dependent on Poisson's ratio), as sketched in Fig. 5.5. The relative contraction/elongation $\epsilon_{\parallel,\perp}$ for the directions along and perpendicular to the magnetization orientation is given by the magnetostrictive constants $\lambda_\parallel$ and $\lambda_\perp$, respectively [84]:

$$\epsilon_\parallel = \frac{\Delta L}{L} = \lambda_\parallel \quad \text{and} \quad \epsilon_\perp = \frac{\Delta W}{W} = \lambda_\perp .$$

For cobalt, iron and nickel, $\lambda_\parallel < 0$ and $\lambda_\perp > 0$.

We define a second coordinate system $x'y'z'$ which is rotated relative to the xyz-system by an angle of ϕ around the z-axis. Here, ϕ denotes the angle between the x-axis and the magnetization direction and Φ is the angle between the x-axis and the external magnetic field orientation, as shown in Fig. 5.5. The $x'y'z'$-coordinate system represents the natural system for the magnetostriction. In this frame of reference, the magnetization $\mathbf{M}$ is along the x'-axis and the magnetostrictive strain tensor is given by

$$\boldsymbol{\epsilon}'_\mathrm{mag} = \begin{pmatrix} \lambda_\parallel & 0 & 0 \\ 0 & \lambda_\perp & 0 \\ 0 & 0 & \lambda_\perp \end{pmatrix} .$$

Using the rotation tensor $\mathbf{R}$, which maps the xyz-coordinate system to the $x'y'z'$-coordinate system,

$$\mathbf{R} = \begin{pmatrix} \cos\phi & -\sin\phi & 0 \\ \sin\phi & \cos\phi & 0 \\ 0 & 0 & 1 \end{pmatrix},$$

we obtain the components of the strain tensor in the xyz-coordinate system of the nanobeam:

$$\begin{aligned} \boldsymbol{\epsilon}_{\text{mag}} &= \mathbf{R}^T \boldsymbol{\epsilon}'_{\text{mag}} \mathbf{R} \\ &= \begin{pmatrix} \lambda_\parallel \cos^2\phi + \lambda_\perp \sin^2\phi & (\lambda_\perp - \lambda_\parallel)\cos\phi\sin\phi & 0 \\ (\lambda_\perp - \lambda_\parallel)\cos\phi\sin\phi & \lambda_\perp \cos^2\phi + \lambda_\parallel \sin^2\phi & 0 \\ 0 & 0 & \lambda_\perp \end{pmatrix}. \end{aligned}$$

5.3.2 Magnetoelastic stress in a magnetic thin film on top of a substrate

In case of a thin magnetic film deposited on a substrate, the shared interface imposes a boundary condition on the FM. More precisely, the geometric dimensions of the FM are fixed in x- and y-direction, which means, the effective strain along these axes vanishes. We describe this by introducing an additional strain $\boldsymbol{\epsilon}_{\text{b}}$ so that the net strain

$$\boldsymbol{\epsilon}_{\text{net}} = \boldsymbol{\epsilon}_{\text{mag}} + \boldsymbol{\epsilon}_{\text{b}}$$

vanishes along the x- and y-direction:

$$\epsilon_{\text{net},x} = \epsilon_{\text{net},y} = 0\,.$$

In a more intuitive picture, magnetostriction changes the equilibrium dimensions of the film. Along the magnetization direction, e. g., the equilibrium length of the film is reduced ($\lambda_\parallel < 0$). However, the boundary conditions require a constant length, which results in a tensile stress in the FM film along the x-axis. Analogously, magnetostriction creates a compressive stress in the FM along the y-direction. Perpendicular to the film plane, the FM is free to expand. Thus, the strain applied by the boundary conditions creates the stress

$$\boldsymbol{\sigma}_{\text{mag}} = \mathbf{C}\,\boldsymbol{\epsilon}_{\text{b}} \tag{5.1}$$

with the elasticity tensor $\mathbf{C}$ [85].

In Voigt notation (see, e. g., Ref. [85]), $\boldsymbol{\epsilon}_{\text{b}}$ is

$$\boldsymbol{\epsilon}_{\text{b}} = \begin{pmatrix} \epsilon_{\text{b},xx} \\ \epsilon_{\text{b},yy} \\ \epsilon_{\text{b},zz} \\ 2\epsilon_{\text{b},yz} \\ 2\epsilon_{\text{b},xz} \\ 2\epsilon_{\text{b},xy} \end{pmatrix} = \begin{pmatrix} \lambda_\parallel \cos^2\phi + \lambda_\perp \sin^2\phi \\ \lambda_\perp \cos^2\phi + \lambda_\parallel \sin^2\phi \\ \epsilon_{\text{b},zz} \\ 0 \\ 0 \\ 2(\lambda_\perp - \lambda_\parallel)\cos\phi\sin\phi \end{pmatrix} \tag{5.2}$$

and the elasticity tensor $\mathbf{C}$ is given by

$$\mathbf{C} = \begin{pmatrix} \lambda+2\mu & \lambda & \lambda & 0 & 0 & 0 \\ \lambda & \lambda+2\mu & \lambda & 0 & 0 & 0 \\ \lambda & \lambda & \lambda+2\mu & 0 & 0 & 0 \\ 0 & 0 & 0 & \mu & 0 & 0 \\ 0 & 0 & 0 & 0 & \mu & 0 \\ 0 & 0 & 0 & 0 & 0 & \mu \end{pmatrix} \tag{5.3}$$

with the shear modulus μ, the Lamé constant $\lambda = (2\mu^2 - E\mu)/(E - 3\mu)$ and Young's modulus E [85, 86].

As the FM film can expand freely in z-direction, the stress component $\sigma_{\mathrm{mag},zz}$ has to vanish. Thus,

$$\epsilon_{\mathrm{b},zz} = \lambda_{\parallel}\left(1 - \frac{E}{2\mu}\right), \tag{5.4}$$

where we have used $\mu = E/(2(1+\nu))$ [85] and $\lambda_{\parallel} = -\nu\lambda_{\perp}$ (as volume magnetostriction can be neglected in first order [84]). Here, ν denotes the Poisson ratio of the magnetostrictive material.

Using Eqs. 5.1–5.4, we obtain the following expression for the stress $\boldsymbol{\sigma}_{\mathrm{mag}}$ in the magnetic film:

$$\boldsymbol{\sigma}_{\mathrm{mag}} = \begin{pmatrix} \sigma_{\mathrm{mag},xx} \\ \sigma_{\mathrm{mag},yy} \\ \sigma_{\mathrm{mag},zz} \end{pmatrix} = -\begin{pmatrix} E\lambda_{\parallel}\cos^2(\phi) \\ E\lambda_{\parallel}\sin^2(\phi) \\ 0 \end{pmatrix}.$$

5.3.3 Effective stress in the double-layer nanobeam

To obtain the effective stress present in the double-layer beam, we take into account the stress in the silicon nitride, σ_{SiN}, as well as in the magnetic thin film, $\boldsymbol{\sigma}^{\mathrm{tot}}_{\mathrm{film}}$. For a double-layer system, the effective stress along the beam direction is given by [51, 57]

$$\sigma_{\mathrm{eff}} = \frac{\sigma_{\mathrm{SiN}} t_{\mathrm{SiN}} + \sigma^{\mathrm{tot}}_{\mathrm{film},x} t_{\mathrm{film}}}{t_{\mathrm{SiN}} + t_{\mathrm{film}}}.$$

Note that the total stress in the magnetic layer contains stress contributions from the fabrication process as well as the magnetoelastic stress, $\boldsymbol{\sigma}^{\mathrm{tot}}_{\mathrm{film}} = \boldsymbol{\sigma}^{0}_{\mathrm{film}} + \boldsymbol{\sigma}_{\mathrm{mag}}$.

For a highly tensile-stressed nanobeam, the resonance frequency of the fundamental flexural mode is well approximated by $\Omega_{\mathrm{res}}/2\pi = (1/2l)\sqrt{\sigma/\rho}$, where σ and ρ denote prestress and density of the nanobeam (see, e. g., Ref. [30]). Using effective values for stress and density of the double-layer beam [51, 57], we obtain

$$\frac{\Omega_{\mathrm{res}}(\phi)}{2\pi} = \frac{1}{2l}\sqrt{\frac{\sigma_{\mathrm{eff}}}{\rho_{\mathrm{eff}}}} = \frac{1}{2l}\sqrt{\frac{\sigma_0 - \sigma_1\cos^2(\phi)}{\rho_{\mathrm{eff}}}}, \tag{5.5}$$

where we have defined $\sigma_0 = (\rho_{\mathrm{SiN}} t_{\mathrm{SiN}} + \sigma^{0}_{\mathrm{film},x} t_{\mathrm{film}})/(t_{\mathrm{SiN}} + t_{\mathrm{film}})$ and $\sigma_1 = E t_{\mathrm{film}} \lambda_{\parallel}/(t_{\mathrm{SiN}} + t_{\mathrm{film}})$.

For $|\sigma_1/\sigma_0| \ll 1$, we can Taylor-expand Eq. 5.5 and obtain for the relative resonance frequency shift

$$\frac{\Delta\Omega_{\mathrm{res}}(\phi)}{\Omega_{\mathrm{res},0}} = \frac{\Omega_{\mathrm{res}}(\phi) - \Omega_{\mathrm{res},0}}{\Omega_{\mathrm{res},0}} = -\frac{\sigma_1}{2\sigma_0}\cos^2(\phi) \tag{5.6}$$

with $\Omega_{\mathrm{res},0}/2\pi = (1/2l)\sqrt{\sigma_0/\rho_{\mathrm{eff}}}$ the resonance frequency at $\phi = 90°$.

We thus expect a $\cos^2(\phi)$-dependence of the resonance frequency as a function of the magnetization direction. By measuring the tuning amplitude $\sigma_1/2\sigma_0$ of the resonance frequency, we can deduce the magnetostriction constants $\lambda_{\parallel}$ and $\lambda_{\perp}$.

5.4 Experimental results

5.4.1 Magnetostriction of a cobalt thin film

In this section, we study magnetostriction in a 10 nm thin polycrystalline cobalt film using Sample #4a. To spectroscopically investigate the sample, we use the fiber interferometer described in [79] and the setup depicted in Fig. 5.4.

Resonance frequency measurements at high magnetic field

First, we measure the resonance frequency of the beam in an external magnetic field of constant magnitude $\mu_0 H = 200\,\mathrm{mT}$, which is above the coercive field and the in-plane anisotropy fields of the Co film. In this regime, the magnetization is, in a good approximation, aligned along the external field direction ($\phi \approx \Phi$). We rotate the external field between $\Phi = -35°$ and 200°, where $\Phi = 0°$ corresponds to $\mu_0\mathbf{H} \parallel \hat{\mathbf{x}}$ (see Fig. 5.5).

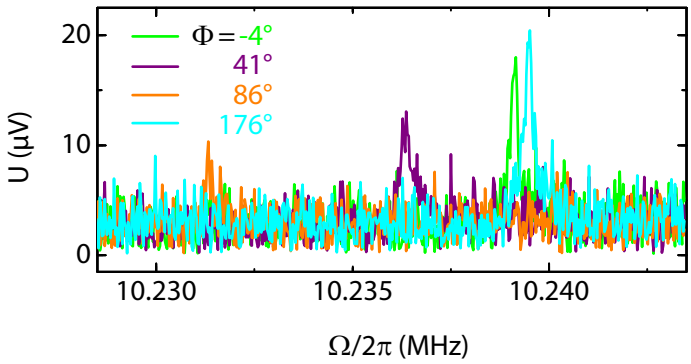

Figure 5.6: Measured photovoltage spectra for an external magnetic field of $\mu_0 H = 200\,\mathrm{mT}$ applied along the nanobeam axis (x-axis) and at an angle of 45°, 90° and 180° to the x-axis. The angle misalignment of 4° is due to the finite angle resolution in the experiment.

Figure 5.6 shows the measured homodyne photovoltage as a function of the drive frequency for four different external field directions $\Phi = -4°, 41°, 86°, 176°$. The drive voltage applied to the piezoactuator is $U_{\mathrm{piezo}} = 7\,\mathrm{mV_{rms}}$. We observe a clear resonance peak corresponding to the fundamental vibrational out-of-plane mode of the nanobeam, whose frequency shifts as a function of the magnetic field orientation. The magnetostrictive frequency shift significantly exceeds the linewidth of the resonance peaks, which is $\Gamma_{\mathrm{m}}/2\pi \approx 300\,\mathrm{Hz}$. In addition to the resonance frequency shift, we observe a variation of the resonance peak amplitude when rotating the external magnetic field vector, as can be seen from Fig. 5.6. We attribute this to a slight translational shift of the sample position in high magnetic fields. In this case the laser spot is not centered on the nanobeam any more, which decreases the detected photovoltage amplitude. The small discrepancy between the

resonance frequency at $\Phi = -4°$ and 176° is due to thermal drift of the resonance frequency during the measurement.

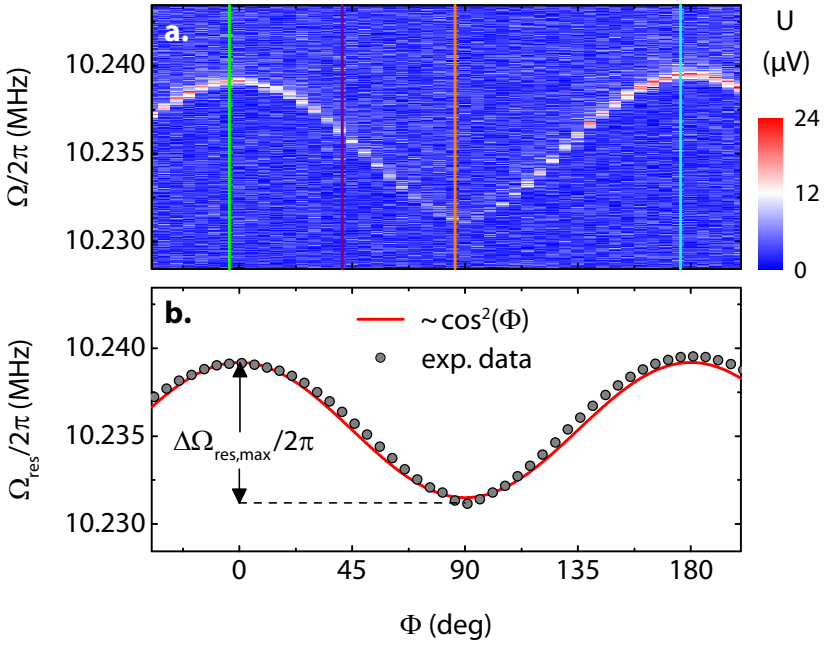

Figure 5.7: Resonance frequency of the fundamental flexural mode as a function of the external magnetic field orientation Φ for $\mu_0 H = 200\,\mathrm{mT}$. **a.** Measured photovoltage U as a function of drive frequency and external field direction. **b.** Fitted resonance frequency $\Omega_{\mathrm{res}}(\Phi)/2\pi$ and expected $\cos^2(\Phi)$ behaviour.

To analyze the observed field orientation dependence in more detail, we measure the amplitude spectrum of the nanobeam as a function of Φ, as shown in Fig. 5.7a. The experimental data confirm the expected 180°-periodicity of the resonance frequency $\Omega_{\mathrm{res}}(\Phi)/2\pi$. From these data we extract the maximum resonance frequency shift $\Delta\Omega_{\mathrm{res,max}} := \Omega_{\mathrm{res}}(0°) - \Omega_{\mathrm{res}}(90°) = 2\pi \times 8.00\,\mathrm{kHz}$ (see Fig. 5.7b). We observe slight deviations between the measured $\Omega_{\mathrm{res}}(\Phi)$ and the expected $\cos^2(\Phi)$ behaviour, especially around $\Phi = 45°$ and 135°. This is quantitatively understood, as the magnetization for these angles Φ is not perfectly aligned in parallel with the applied magnetic field due to the finite shape anisotropy of the nanobeam (see next section for details). Additionally, this quantitative model is compatible with the absence of crystalline magnetic anisotropies in our nanobeam, warranting the assumption of a polycrystalline cobalt film (see Ref. [78]).

To determine the magnetostriction constants $\lambda_{\parallel}$ and $\lambda_{\perp}$ from the experimental data, we first calculate the static prestress σ_0 in the nanobeam. With $\Omega_{\mathrm{res}}(\phi = 90°)/2\pi = (1/2l)\sqrt{\sigma_0/\rho_{\mathrm{eff}}}$, we obtain $\sigma_0 = 892\,\mathrm{MPa}$. Here we have used the effective density $\rho_{\mathrm{eff}} = 3410\,\mathrm{kg\,m^{-3}}$, which we determine from $\rho_{\mathrm{SiN}} = 2800\,\mathrm{kg\,m^{-3}}$ [44] and $\rho_{\mathrm{Co}} = 8900\,\mathrm{kg\,m^{-3}}$ [64] using $\rho_{\mathrm{eff}} = (\rho_{\mathrm{SiN}} t_{\mathrm{SiN}} + \rho_{\mathrm{Co}} t_{\mathrm{film}})/(t_{\mathrm{SiN}} + t_{\mathrm{film}})$ [57]. With Eq. 5.6, the Young's modulus of cobalt $E = 175\,\mathrm{GPa}$ [87] and the relation $\lambda_{\perp} = -\nu\lambda_{\parallel}$, the observed maximum resonance frequency shift of $\Delta\Omega_{\mathrm{res,max}} = 2\pi \times 8.00\,\mathrm{kHz}$ corresponds to a magnetostriction constant of $\lambda_{\parallel} = -79.7 \times 10^{-6}$ ($\lambda_{\perp} = 27.9 \times 10^{-6}$).

To compare these values to literature, we calculate $\lambda_{\parallel}$ and $\lambda_{\perp}$ in polycrystalline magnetically saturated cobalt from the crystal magnetostriction constants $\lambda_{\mathrm{A,B,C,D}}$ as described

in [88] and obtain $\lambda_{\parallel} = -78.4 \times 10^{-6}$ and $\lambda_{\perp} = 27.5 \times 10^{-6}$. This is in very good agreement with the experimentally determined values. Thus we conclude that the proposed method conforms with standard magnetostriction measurement techniques, which e. g. use the bending of a cantilever covered with a thin magnetostrictive film [89–92], and is therefore suitable to quantitatively determine the magnetostriction constants of thin films.

Impact of imperfect magnetization alignment on the resonance frequency shift

To study the deviation of the measured $\Omega_{\mathrm{res}}(\Phi)$ from the expected $\cos^2(\Phi)$ behaviour in more detail, we repeat the above measurement for lower magnetic fields. Whereas for $\mu_0 H = 200\,\mathrm{mT}$ the magnetization $\mathbf{M}$ is roughly aligned along $\mu_0\mathbf{H}$, this is not the case for smaller external fields where magnetic anisotropies significantly contribute to the orientation of the magnetization.

To predict the magnetization direction, we use a Stoner-Wolfarth approach and assume a saturated magnetization state $|\mathbf{M}| = M_{\mathrm{s}}$ (see e. g. Ref. [84]). To determine the equilibrium direction of $\mathbf{M}$ as a function of the external field orientation, we start with the free energy density F_{tot}, containing Zeeman energy density and shape anisotropy. The first is given by $F_{\mathrm{Zeeman}} = -\mu_0 \mathbf{M} \cdot \mathbf{H}$ [84], the latter is $F_{\mathrm{shape}} = (\mu_0/2)\mathbf{M} \cdot \mathbf{N} \cdot \mathbf{M}$, where $\mathbf{N}$ denotes the demagnetization tensor [93]. We approximate the cobalt thin film on the Si_3N_4 nanobeam as an ellipsoid with axis lengths l, w and t_{film}. The corresponding demagnetization tensor has diagonal form with the components $N_{xx} \simeq 0$, $N_{yy} = 0.03$ and $N_{zz} = 0.97$ [94]. Note that we neglect magnetocrystalline anisotropy contributions to F_{tot}, assuming that they average out in a polycrystalline film [95]. The contribution of magnetoelastic energy to F_{tot} is about two orders of magnitude smaller than the contribution of shape anisotropy and can therefore be neglected.

For the present experimental geometry, external magnetic field and magnetization are in the x-y-plane (see Fig. 5.5). Thus, the total free energy density is given by

$$F_{\mathrm{tot}} = -\mu_0 M_{\mathrm{s}} H \cos(\Phi - \phi) + \frac{\mu_0 M_{\mathrm{s}}^2}{2} N_{yy} \sin^2(\phi). \tag{5.7}$$

In Fig. 5.8a-c, we plot the total free energy density as a function of the external magnetic field orientation and the magnetization direction for the parameter values $M_{\mathrm{s}} = 1167\,\mathrm{kA/m}$ (measured by SQUID magnetometry for a similar Co thin film), $N_{yy} = 0.03$ and $\mu_0 H = 200\,\mathrm{mT}$, 100 mT and 25 mT. The minima, which determine the equilibrium magnetization direction, are highlighted by green lines. If the external field significantly exceeds the demagnetization field $\mu_0 H_{\mathrm{demag}} = (\mu_0/2) M_{\mathrm{s}} N_{yy} \approx 22\,\mathrm{mT}$, the magnetization is approximately parallel to the external field, i. e. $\phi \approx \Phi$. Nevertheless, even for $\mu_0 H = 200\,\mathrm{mT}$ there are slight deviations between the calculated energy density minima and the ideal case $\phi = \Phi$ (indicated with the dashed blue line in Fig. 5.8a). For small external fields $\mu_0 H \lesssim \mu_0 H_{\mathrm{demag}}$, the shape anisotropy of the thin cobalt stripe forces the magnetization direction towards the x-axis, as Fig. 5.8c points out.

In Fig. 5.8d, the measured resonance frequency is plotted as a function of the external field orientation Φ for the field strengths $\mu_0 H = 200\,\mathrm{mT}$, 100 mT and 25 mT. The solid lines show the modeled resonance frequency behaviour, based on Eq. 5.6 and the calculated equilibrium magnetization orientation $\phi(\Phi)$. In particular for $\mu_0 H = 200\,\mathrm{mT}$, we observe excellent agreement between the experimental data and the model. For weak magnetic fields, e. g. $\mu_0 H = 25\,\mathrm{mT}$, our simple model explains the resonance frequency shift at

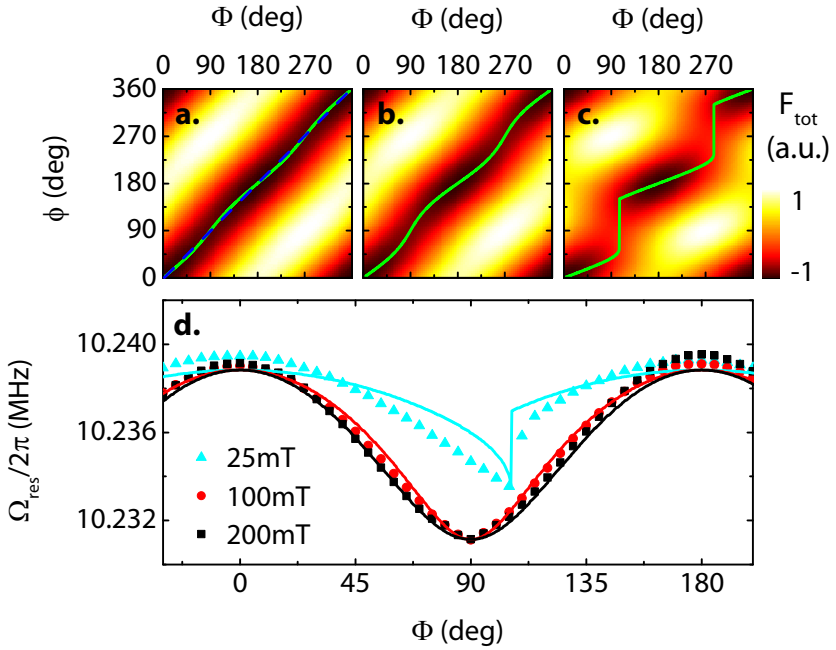

Figure 5.8: a-c. Total free energy density as a function of external magnetic field orientation Φ and magnetization direction ϕ for $\mu_0 H = 200\,\mathrm{mT}$ (a), $100\,\mathrm{mT}$ (b) and $25\,\mathrm{mT}$ (c). The green lines indicate the angle dependence of the free energy density minimum. The colorbar has been rescaled individually for each graph. **d.** Resonance frequency versus external field orientation Φ for various field strengths $\mu_0 H = 200, 100, 25\,\mathrm{mT}$. The symbols represent the experimental data, the modelled resonance frequencies are plotted as solid lines.

least qualitatively, reproducing the switching of the magnetization at $\Phi = 110°$ and the measured maximum frequency shift.

5.4.2 Magnetostriction of a nickel thin film

In this section, we present experimental data for Sample #4b, consisting of a $t_{\mathrm{Ni}} = 10\,\mathrm{nm}$ thin nickel film on a $t_{\mathrm{SiN}} = 100\,\mathrm{nm}$ thin doubly-clamped Si_3N_4 nanobeam resonator ($l = 40\,\mu\mathrm{m}$, $w = 350\,\mathrm{nm}$). Whereas the above measurement has been done with a fiber interferometer [79], we here employ the modified free space interferometer introduced in Sec. 5.2.1. In addition to an improved mechanical stability, the Magnet-IFM allows more efficient coupling of the reflected laser light into the optical path and therefore a higher signal-to-noise ratio.

Mechanical response spectra

Figure 5.9a shows the amplitude spectrum of the nanobeam motion as a function of the external magnetic field direction, with a constant field magnitude $\mu_0 H = 200\,\mathrm{mT}$. We use a piezoactuator voltage of $U_{\mathrm{piezo}} = 22\,\mathrm{mV_{rms}}$, driving the nanobeam motion still in the linear regime. As already observed for Sample #4a, we find a clear modulation of the resonance frequency when rotating the external magnetic field. The observed maximum resonance frequency shift $\Delta\Omega_{\mathrm{res,max}}/2\pi = 1.0\,\mathrm{kHz}$ is significantly smaller than for Sample #4a, but still large compared to the linewidth of the resonance $\Gamma_{\mathrm{m}}/2\pi \approx 325\,\mathrm{Hz}$. Due to the improved mechanical stability of the setup, the signal is clearly visible for all external field

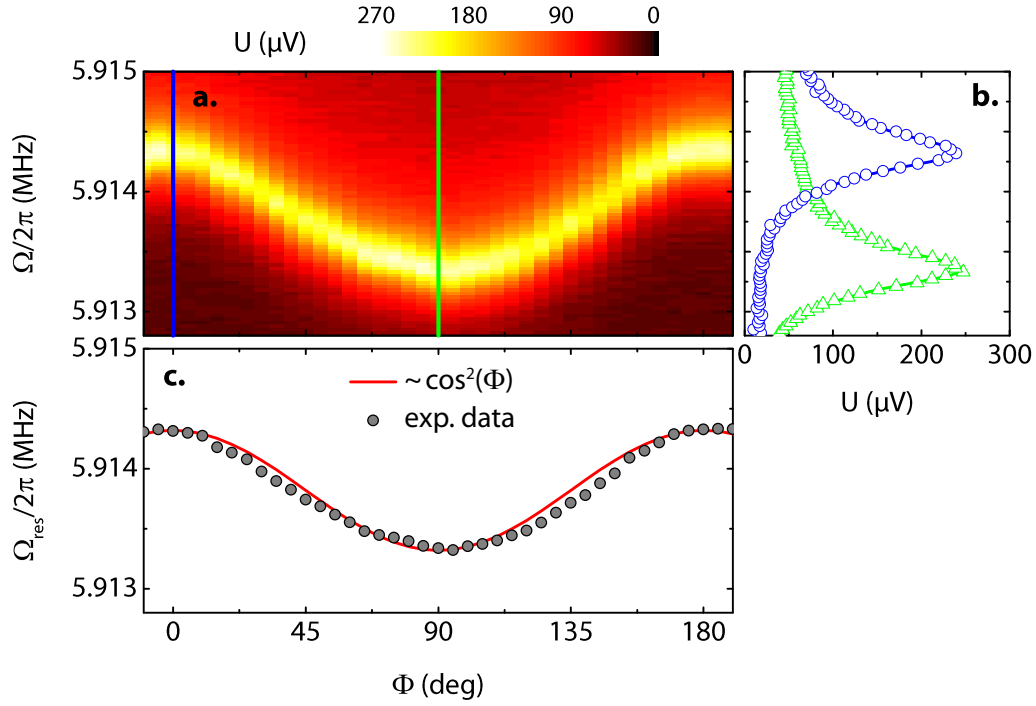

Figure 5.9: **a.** Measured photovoltage as a function of drive frequency Ω/π and external magnetic field orientation Φ for $\mu_0 H = 200\,\mathrm{mT}$. **b.** Mechanical response spectra for $\Phi = 0°$ and 90°, extracted from (a). **c.** Fitted resonance frequency as a function of Φ and expected $\cos^2(\Phi)$-dependence.

directions, as shown in Fig. 5.9b for the two perpendicular orientations $\Phi = 0°$ and 90°. In Fig. 5.9c, the fitted resonance frequency as a function of the magnetic field direction Φ is plotted together with the expected $\cos^2(\Phi)$ dependence. The deviation between the expected and the measured resonance frequency around $\Phi = 45°$ and 135° can be attributed to anisotropy effects in the Ni thin film, causing a small misalignment of the magnetization vector $\mathbf{M}$ relative to the externally applied field $\mu_0\mathbf{H}$. We have already discussed this issue in detail in Sec. 5.4.1.

To determine the magnetostriction constants of the Ni film, we proceed similarly to Sec. 5.4.1. From the minimum resonance frequency $\Omega_{\mathrm{res}}(\Phi = 90°)/2\pi = 5.913\,32\,\mathrm{MHz}$, we determine the prestress in the Si_3N_4/Ni nanobeam, $\sigma_0 = 710\,\mathrm{MPa}$. Here we have used the effective density $\rho_{\mathrm{eff}} = 3170\,\mathrm{kg\,m^{-3}}$, which we calculate from $\rho_{\mathrm{SiN}} = 2600\,\mathrm{kg\,m^{-3}}$ [46], $\rho_{\mathrm{Ni}} = 8900\,\mathrm{kg\,m^{-3}}$ [96] and the thickness of the Si_3N_4 and Ni films given above.

With Eq. 5.6, Young's modulus of nickel $E \approx 200\,\mathrm{GPa}$ [97] and the observed maximum resonance frequency shift of $\Delta\Omega_{\mathrm{res,max}}/2\pi = 1.00\,\mathrm{kHz}$, we find $\lambda_{\parallel} = -13.2 \times 10^{-6}$. This deviates significantly from the literature value $\lambda_{\parallel}^{\mathrm{Ni}} = -38 \times 10^{-6}$ [98].

To investigate this inconsistency in more detail, we measure the saturation magnetization of the Ni film using SQUID magnetometry. We find $M_{\mathrm{s}} = 291\,\mathrm{kA/m}$, which is severely reduced compared to values reported for other Ni thin films ($M_{\mathrm{s}}^{\mathrm{Ni\ film}} = 370\,\mathrm{kA/m}$ [99]) or for bulk nickel ($M_{\mathrm{s}}^{\mathrm{Ni\ bulk}} = 485\,\mathrm{kA/m}$ [100]). This could be explained by a partial oxidization of the film which would also deteriorate the magnetoelastic properties of the film. Besides, in literature different values for Young's modulus of Ni thin films can be found [49, 101, 102]. So we cannot exclude that Young's modulus of our Ni film modulus

deviates from the assumed value $E = 200\,\mathrm{GPa}$, and this would also affect the calculated magnetostriction constant. Thus, further analysis of the magnetic and elastic properties of the Ni film is necessary in order to understand the origin of the small magnetoelastic coupling in this film.

In addition to the resonance frequency shift, we analyze linewidth and amplitude of the measured mechanical response spectra as shown in Fig. 5.10. This was not possible for the experiment with Sample #4a because of an insufficient signal-to-noise ratio. We find a

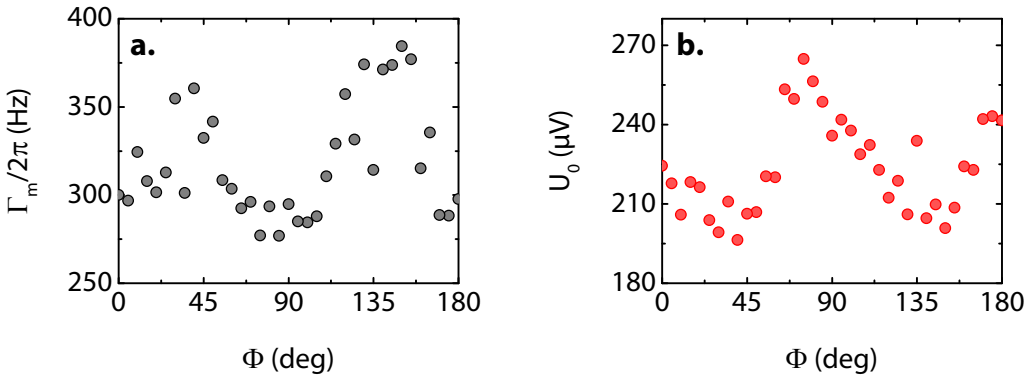

Figure 5.10: **a.** Fitted linewidth and **b.** photovoltage amplitude as a function of the external magnetic field direction Φ.

90°-periodicity of linewidth and amplitude as a function of the magnetic field orientation Φ. While the linewidth is minimal at $\Phi = 0°$, 90° and 180° and increases by approximately 25% around $\Phi = 45°$ and 135°, the amplitude of the Lorentzian response function, U_0, shows the inverse behaviour.

To explain the observed Φ-dependence of the measured linewidth Γ_m, various contributions have been considered. However, we could not find a quantitative explanation of the experimental findings yet. In the following, we briefly discuss two damping mechanisms that might contribute to the observation of a Φ-dependent linewidth and compare them to the experimental results.

First, as the magnetic thin film is electrically conducting, its motion in a static magnetic field induces eddy currents due the Lorentz force. The orientation of these currents is perpendicular to the magnetic field direction Φ. The high aspect ratio between width and length of the magnetic "nanowire" on top of the Si_3N_4 beam suggests an anisotropic conductivity of the magnetic film, thus causing a Φ-dependent damping channel. This contribution, however, would exhibit a 180°-periodicity, similar to the geometry of the sample. Therefore, it cannot be the dominating damping mechanism observed in our experiment.

An alternative approach to explain the measured Φ-dependence of Γ_m is the assumption of magnetoelastic damping. The basic idea is that the time-dependent strain in the ferromagnet caused by the mechanical motion of the nanobeam leads to an oscillation of the equilibrium orientation of the magnetization due to the inverse magnetostrictive effect. This periodic re-alignment of the magnetization direction is subject to damping, which contributes to the total damping of the Si_3N_4/FM nanoresonator. This mechanism can reproduce the 90°-periodicity of the damping as a function of Φ, as we will show

in the following. Quantitatively, however, this damping contribution is several orders of magnitude smaller than the observed effect.

Magnetoelastic damping model

We start with the free energy density of the ferromagnetic thin film (Eq. 5.7), which we extend by a magnetoelastic contribution:[3]

$$F_{\mathrm{tot}}(\Phi,\phi,\epsilon_{xx}) = -\mu_0 H_0 M_{\mathrm{s}} \cos(\Phi-\phi) + \frac{\mu_0 M_{\mathrm{s}}^2}{2} N_{yy} \sin^2\phi + b_1 M_{\mathrm{s}} \epsilon_{xx}(t) \cos^2\phi \; .$$

Here, the magnetoelastic coupling constant is $b_1 = -3\lambda_{\mathrm{s}}\mu$ (with the magnetostriction constant λ_{s} and the second Lamé constant μ) [99], and we assume a dominating xx-component of the strain, caused by the elongation of the displaced nanobeam (see Sec. 4.1.7). Its time-dependence is given by $\epsilon_{xx}(t) = \epsilon_{xx}^0 \cos(\Omega_{\mathrm{m}} t)$ and its amplitude is related to the maximum displacement x_0 and the length l of the nanobeam via

$$\epsilon_{xx}^0 = \frac{x_0^2 \pi^2}{4 l^2} \; .$$

Here, we have used Eq. 4.23 and $\epsilon_{xx} = (l' - l)/l$, where l' (l) is the length of the displaced (undisplaced) beam.

For a given external field orientation Φ_0, the magnetization direction ϕ minimizes the free energy density:

$$\frac{\partial F_{\mathrm{tot}}}{\partial \phi}(\Phi_0, \phi_0, 0) = 0 \; . \tag{5.8}$$

The dynamic strain $\epsilon_{xx}(t)$ leads to an oscillation of the magnetization direction ϕ around ϕ_0 according to $\phi(t) = \phi_0 + \delta\phi \cos(\Omega_{\mathrm{m}} t)$, where $\delta\phi$ is given by

$$\frac{\partial F_{\mathrm{tot}}}{\partial \phi}(\Phi_0, \phi_0 + \delta\phi, \epsilon_{xx}^0) = 0 \; . \tag{5.9}$$

Note that, as the mechanical resonance frequency $\Omega_{\mathrm{m}} \sim$ MHz is about three orders of magnitude smaller than the ferromagnetic resonance (FMR) frequency ($\omega_{\mathrm{FMR}} \sim$ GHz), we assume the magnetization to follow the strain immediately, i. e. the magnetization is always aligned so that it minimizes the free energy density F_{tot}.

From Eqs. 5.8 and 5.9, we can derive $\delta\phi$ as a function of ϵ_{xx}^0. To this end, we Taylor-expand $\partial F_{\mathrm{tot}}/\partial\phi$ around $\phi = \phi_0$ and $\epsilon_{xx} = 0$. In case of a sufficiently high external magnetic field $\mu_0 H_0$, we can assume $\phi_0 \approx \Phi_0$ and $\mu_0 H_0 \gg \mu_0 M_{\mathrm{s}} N_{yy}$, $2 b_1 \epsilon_{xx}^0$ and obtain the relation [103]

$$\delta\phi = \frac{b_1 \epsilon_{xx}^0 \sin(2\Phi_0)}{\mu_0 H_0} \; . \tag{5.10}$$

Thus, $\delta\phi$ shows a 180°-periodic behaviour as a function of Φ_0. The modulation of the magnetization direction is typically small: For our Si_3N_4/Ni sample and a displacement of $x_0 = 1\,\mathrm{nm}$, we obtain $\delta\phi_{\max} \equiv \delta\phi(\Phi_0 = 45°) \sim 1° \times 10^{-5}$.

The oscillation of the magnetization direction can formally be treated as an effective magnetic driving field, in analogy to the discussion in Ref. [104]. This allows determination of the magnetoelastic damping contribution using a standard Gilbert damping approach.

[3] So far, we have neglected the magnetoelastic energy contribution as it is small compared to the Zeeman and anisotropy energy.

The total damping rate of the mechanical motion of the Si_3N_4/FM nanobeam resonator can be written as [105]

$$\Gamma_\mathrm{m} = \Gamma_\mathrm{m,el} + \Gamma_\mathrm{m,mag}$$

with the elastic damping rate $\Gamma_\mathrm{m,el}$ and the magnetoelastic damping contribution $\Gamma_\mathrm{m,mag}$. The latter can be defined as

$$\Gamma_\mathrm{m,mag} = \frac{P_\mathrm{diss,mag}}{\mathcal{U}} \ ,$$

where $P_\mathrm{diss,mag}$ denotes the power dissipated by the continuous re-alignment of the magnetization and $\mathcal{U}$ the energy stored in the nanobeam motion.

Assuming that the elastic energy highly exceeds the magnetic energy, $\mathcal{U}$ is given by (see Eq. 4.21)

$$\mathcal{U} = \frac{1}{2} m_\mathrm{eff} \Omega_\mathrm{m}^2 x_0^2 \sim 10^{-18}\,\mathrm{J} \ .$$

The magnetoelastic power dissipation can be calculated similar to the ansatz given in Ref. [104],

$$P_\mathrm{diss,mag} = \frac{\mu_0 \Omega_\mathrm{m} V}{2} H_0^2 \delta\phi^2 \mathrm{Im}(\chi_{xx}(\Omega_\mathrm{m})) \ ,$$

with the volume of the magnetic layer V and the susceptibility tensor χ, whose relevant component is given by $\mathrm{Im}(\chi_{xx}(\Omega)) = \gamma\mu_0 M_\mathrm{s} \alpha(\Omega/\omega_\mathrm{FMR})$ [105]. Here, γ and α denote the gyromagnetic ratio and the Gilbert damping parameter, respectively. With Eq. 5.10, we obtain

$$P_\mathrm{diss,mag} = \frac{\alpha\gamma V M_\mathrm{s} b_1^2 (\epsilon_{xx}^0)^2}{2} \left(\frac{\Omega_\mathrm{m}}{\omega_\mathrm{FMR}}\right)^2 \sin^2(2\Phi_0) \ . \tag{5.11}$$

As $\sin^2(2\Phi_0) = (1-\cos(4\Phi_0))/2$, the resulting magnetoelastic damping $\Gamma_\mathrm{m,mag} \propto P_\mathrm{diss,mag}$ reproduces the experimentally determined 90°-dependence as a function of the external field orientation Φ_0.

Using typical parameters, we find the magnitude of the calculated energy dissipation to be $P_\mathrm{diss,mag} \sim 10^{-25}\,\mathrm{W}$. The estimated magnetoelastic damping rate is therefore $\Gamma_\mathrm{m,mag} = P_\mathrm{diss,mag}/\mathcal{U} \sim 2\pi \times 10^{-7}\,\mathrm{Hz}$, which is about ten orders of magnitude smaller than expected. Experimentally, we find $\Gamma_\mathrm{m,mag}^\mathrm{exp} \equiv \Gamma_\mathrm{m}(\Phi_0 \approx 45°) - \Gamma_\mathrm{m}(\Phi_0 \approx 0°) \approx 2\pi \times 60\,\mathrm{Hz}$.

So far, we could not resolve this discrepancy. The theoretically predicted magnetoelastic damping is small mainly due to the low mechanical resonance frequency $\Omega_\mathrm{m} \ll \omega_\mathrm{FMR}$, which enters Eq. 5.11 as a square. Possibly there are low-frequency damping mechanisms which are not covered by the presented Gilbert damping ansatz. On the experimental side, further measurements are required to verify (and quantify) the observed magnetization-dependent damping contribution. Here, cross-check experiments with metallic, non-magnetic thin films could allow separating current-induced and magnetoelastic damping contributions.

Sensitive detection of the magnetoelastic frequency shift using the phase

So far, we have extracted the resonance frequency shift of the nanobeam from amplitude spectra measured at various magnetic field orientations. Here, the resonance frequency uncertainty is given by approximately half the mechanical linewidth $\delta\Omega_\mathrm{res} \approx \Gamma_\mathrm{m}/2 \approx 2\pi \times 160\,\mathrm{Hz}$. This is sufficient for the characterization of the presented 10 nm thick cobalt and nickel films. For the investigation of ultrathin films or films with small magnetoelastic coupling, however, the measurement sensitivity can be improved by using a phase-locked

loop (PLL) measurement of the resonance frequency, utilizing the steep slope of the phase of the response spectrum φ as a function of the drive frequency $\Omega/2\pi$ (see Chap. 2).

In the following, we briefly estimate the sensitivity of such a PLL measurement. To this end, we measure the phase spectrum of the nanobeam resonance as a function of the magnetic field orientation Φ. Figure 5.11 shows two of the measured spectra, for $\Phi = 0°$ and $90°$.[4] To determine the resonance frequency shift, we read off the frequency at the phase

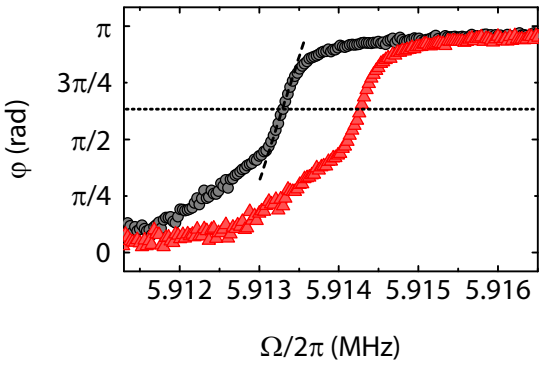

Figure 5.11: Phase φ of the mechanical response as a function of the drive frequency $\Omega/2\pi$ for two different external magnetic field orientations $\Phi = 0°$ (red) and $90°$ (black). Around $\varphi_0 = 1.99$ (indicated by the dashed line), the slope of the measured phase spectra is maximal, which allows to precisely detect resonance frequency shifts.

$\varphi_0 = 1.99$, where the slope of the $\varphi(\Omega)$ curve is maximal. The resonance frequency measurement uncertainty is then given by $\delta\Omega'_{\mathrm{res}} = (\mathrm{d}\varphi/\mathrm{d}\Omega)^{-1}\delta\varphi$. Here, $\delta\varphi$ denotes the phase measurement uncertainty. Using $\delta\varphi \approx 0.02\,\mathrm{rad}$ and $\mathrm{d}\varphi/\mathrm{d}(\Omega/2\pi) \approx 6.8 \times 10^{-3}\,\mathrm{rad/Hz}$, extracted from Fig. 5.11, we calculate $\delta\Omega'_{\mathrm{res}}/2\pi \approx 3\,\mathrm{Hz}$. This is an improvement by a factor 50 compared to $\delta\Omega_{\mathrm{res}}$. In the next section, we will use this to calculate the magnetostriction measurement sensitivity, regarding in particular the investigation of ultrathin films.

5.4.3 Stress-to-frequency conversion and estimated measurement sensitivity

In contrast to cantilever-based experiments, where magnetostriction causes a bending of the mechanical element, the present approach uses a prestressed, doubly-clamped nanobeam where the magnetoelastic stress modifies the total stress along the beam axis and therefore changes the resonance frequency of the beam. This stress-to-frequency conversion allows for an effective determination of the magnetostriction constants via a frequency measurement which does not rely on a quantitative measurement of the beam displacement (as it is the case for cantilever-based techniques). The high quality factor of prestressed Si_3N_4 nanobeam resonators [44] therefore allows to precisely investigate magnetostriction in thin films.

[4] As the response spectra are asymmetric, caused by superposition of a complex background, the measured phase spectra are somewhat deformed compared to the expected arctan-behaviour (see Eq. 2.5). This, however, does not affect the sensitivity of the resonance frequency measurement because the maximum slope $\mathrm{d}\varphi/\mathrm{d}(\Omega/2\pi)$, extracted from the experimental data, is very similar to the theoretical expectation $2/\Gamma_{\mathrm{m}}$ (see Eq. 2.6).

Although the presented method only allows to experimentally access one stress direction (i. e. the stress component along the beam direction), it can be particularly useful for the investigation of very thin (or nanopatterned) magnetostrictive films with a high precision. The reason is that, as we will show in the following, the experimental uncertainty of the calculated magnetostriction constants does not necessarily increase for decreasing film thickness as it is the case for cantilever-based measurement techniques.

To illustrate this, we first calculate the stress-frequency gauge factor, i. e. the change of the resonance frequency of the beam as a function of the stress variation. For Sample #4a, this is

$$\frac{\Delta\Omega_{\mathrm{res}}}{\sigma_{\mathrm{mag},x}} = -\frac{\Omega_{\mathrm{res},0}t_{\mathrm{film}}}{2\sigma_0(t_{\mathrm{SiN}}+t_{\mathrm{film}})} = 2\pi \times 0.57\,\mathrm{Hz/kPa}.$$

Assuming a frequency measurement precision of $\delta\Omega_{\mathrm{res}} \approx \Gamma_{\mathrm{m}}/2$ (with the linewidth of the resonance Γ_{m}), this allows to resolve a stress variation of $\delta\sigma_{\mathrm{mag},x} = 0.26\,\mathrm{MPa}$. This corresponds to an experimental uncertainty in the parallel magnetostriction constant of $\delta\lambda_{\parallel} = \delta\sigma_{\mathrm{mag},x}/E = 1.5 \times 10^{-6}$. Using a phase-locked loop (PLL) to track the resonance frequency of the beam, however, would increase the frequency resolution significantly, allowing an uncertainty $\delta\lambda_{\parallel}$ well below 10^{-6} as estimated in Sec. 5.4.2. This is comparable to other methods [77, 89, 90, 92], even though the thickness of our magnetostrictive films is only 10 nm. In particular, reducing the film thickness further does not necessarily reduce the measurement precision. This is due to the fact that the quality factor of a highly stressed Si_3N_4 beam covered with a thin film typically strongly depends on the film thickness. For Si_3N_4/Au nanobeams, it has been shown recently that the inverse quality factor is proportional to the film thickness for Au layers between 10 nm and 100 nm as the damping in a highly prestressed silicon nitride film is much lower than in the Au film [51]. Therefore, for very thin magnetostrictive films on a highly prestressed Si_3N_4 beam, the resonance frequency measurement uncertainty is proportional to the film thickness, $\delta\Omega_{\mathrm{res}} \propto t_{\mathrm{film}}$. In first approximation, the uncertainty $\delta\lambda_{\parallel} \propto \delta\sigma_{\mathrm{mag},x} = 2\delta\Omega_{\mathrm{res}}\sigma_0(t_{\mathrm{film}} + t_{\mathrm{SiN}})/(\Omega_{\mathrm{res},0}t_{\mathrm{film}})$ is thus independent of the film thickness (assuming $t_{\mathrm{film}} \ll t_{\mathrm{SiN}}$). This characteristic makes the proposed technique an ideal platform for the investigation of magnetostriction in thin and ultrathin films.

5.5 Summary

In this chapter, we have proposed a method to quantitatively investigate magnetostriction in thin films. To this end we used a Si_3N_4 nanomechanical resonator covered with a thin magnetostrictive film. By measuring the resonance frequency of the fundamental vibrational mode of the beam as a function of an external magnetic field, we could deduce the magnetoelastic stress along the beam direction and hence the magnetostriction constants $\lambda_{\parallel}$ and $\lambda_{\perp}$. Compared to previously reported methods, the proposed technique does not rely on a quantitative measurement of the mechanical displacement but utilizes a resonance frequency shift caused by magnetostriction. Besides, it offers a measurement precision which is independent of the film thickness. This enables the investigation of ultrathin magnetostrictive films and paves the way to studying magnetostriction as a function of the film thickness. The proposed technique can be applied to any conducting or insulating material which can be deposited on a Si_3N_4 nanobeam via, e. g., electron beam evaporation, thermal evaporation or sputtering. The material under investigation

does not have to be etch-resistent as it is deposited on the nano-resonator as last step of the sample fabrication process.

Chapter 6

Circuit nano-electromechanics

In this chapter, we introduce the basic ideas and concepts of circuit nano-electromechanics. Most of them have originally been developed for cavity optomechanical systems and later been adapted for circuit electromechanics. In both fields, a mechanical degree of freedom is coupled to a photon cavity; while in cavity optomechanics optical or near-infrared photons are used, circuit electromechanical systems operate at frequencies in the GHz range.

For a comprehensive review of the field of cavity opto/electromechanics, please see Refs. [19,106,107]. This chapter focuses on the concepts and relations that will be relevant for the experimental chapters 7 and 8.

6.1 Fundamental concepts in cavity opto- and electromechanics

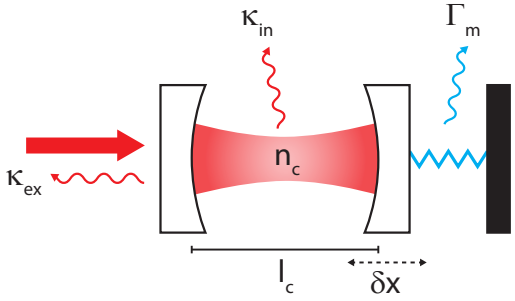

Figure 6.1: Schematic illustration of a cavity optomechanical system. One of the mirrors of a Fabry-Pérot cavity is free to move, which results in a displacement-dependent cavity resonance frequency. The curly arrows indicate the loss channels of the system: the internal and external loss rate of the cavity, κ_{in} and κ_{ex}, and the damping rate of the mechanical system Γ_{m}.

We start with the cavity optomechanical hybrid system depicted in Fig. 6.1. A Fabry-Pérot cavity consisting of two parallel mirrors is coupled to an additional mechanical degree of freedom by connecting one of the mirrors to a spring. The length of the cavity, and thus its resonance frequency, depends on the displacement δx of this mechanical element. For a cavity with length l_{c} and resonance frequency $\omega_{\mathrm{c}}/2\pi$, the frequency shift is $\delta\omega_{\mathrm{c}} = -\omega_{\mathrm{c}} \cdot \delta x / l_{\mathrm{c}}$.

Conversely, the photons in the cavity transfer momentum to the movable mirror, resulting in a radiation pressure force acting on the mechanical resonator [19],

$$F_{\mathrm{rp}} = \frac{\hbar\omega_{\mathrm{c}}\bar{n}_{\mathrm{c}}}{l_{\mathrm{c}}} ,$$

where $\bar{n}_{\mathrm{c}}$ is the average number of photons in the cavity. Thus, there is a mutual coupling of the optical and mechanical degree of freedom which can be used to read out or manipulate the mechanics via the optical cavity and vice versa. The investigation of these interaction effects has lead to the development of the field of cavity optomechanics [19, 106, 108].

The idea of cavity optomechanics can be transferred to the microwave domain by coupling a microwave resonator to a mechanical degree of freedom. In this thesis, we use a superconducting coplanar waveguide (CPW) resonator into which we integrate a nanobeam mechanical resonator as demonstrated, e. g., in Refs. [18, 54]. Massel *et al.* have realized a similar system with a lumped element microwave resonator instead of a CPW resonator [109]. Alternative approaches are based on a drum or membrane mechanical resonator coupled to a lumped element microwave resonator [20] or a membrane inside a three-dimensional microwave cavity [110]. Recently, a graphene membrane has been employed as a mechanical resonator in a circuit electromechanical device, featuring a particularly small mass and therefore high sensitivity to external perturbations [111]. All these systems can be reduced to the schematic representation Fig. 6.1 and are therefore covered by standard cavity opto/electromechanics theory.

In order to describe the electromechanical interaction in such systems quantitatively, we start with the generic Hamiltonian [19, 21]

$$\hat{H} = \hbar\omega_{\mathrm{c}}(x)\left(\hat{a}^{\dagger}\hat{a} + \frac{1}{2}\right) + \hbar\Omega_{\mathrm{m}}\left(\hat{b}^{\dagger}\hat{b} + \frac{1}{2}\right) + \hat{H}_{\mathrm{d}} ,$$

where $\omega_{\mathrm{c}}/2\pi$ and $\Omega_{\mathrm{m}}/2\pi$ are the resonance frequencies of the microwave and the mechanical resonator, respectively, $\hat{a}^{\dagger}$ and $\hat{a}$ ($\hat{b}^{\dagger}$ and $\hat{b}$) are the photon (phonon) creation and annihilation operators and $\hat{H}_{\mathrm{d}}$ describes the microwave drive. The resonance frequency of the microwave cavity[1], $\omega_{\mathrm{c}} = \omega_{\mathrm{c}}(x)$, depends on the displacement of the mechanical element x, which is related to the ladder operators $\hat{b}$ and $\hat{b}^{\dagger}$ via

$$\hat{x} = x_{\mathrm{zpm}}(\hat{b}^{\dagger} + \hat{b}) .$$

Here, we have defined the quantum mechanical zero-point motion of the nanomechanical resonator [19]

$$x_{\mathrm{zpm}} = \frac{\hbar}{\sqrt{2m_{\mathrm{eff}}\Omega_{\mathrm{m}}}} . \tag{6.1}$$

As the electromechanical coupling is typically weak, we can Taylor-expand $\omega_{\mathrm{c}}(x)$ around the equilibrium position of the mechanical resonator, $x = 0$, and obtain

$$\omega_{\mathrm{c}}(x) = \omega_0 + \frac{\partial\omega_{\mathrm{c}}}{\partial x}\, x + \dots . \tag{6.2}$$

[1] Throughout this thesis, we use the term *microwave cavity* as a synonym for *microwave resonator*. Even if, in its literal sense, a microwave cavity is a three-dimensional box resonator, we use this expression here for consistency with most of the literature in the field of circuit electromechanics and for reasons of clarity (as it avoids confusion between the microwave and the mechanical resonator).

Defining the coupling parameter $G = \partial\omega_c/\partial x$ and substituting Eq. 6.2 into the Hamiltonian leads to

$$\hat{H} = \hbar\omega_0\left(\hat{a}^\dagger\hat{a} + \frac{1}{2}\right) + \hbar\Omega_m\left(\hat{b}^\dagger\hat{b} + \frac{1}{2}\right) + \hbar G x_{zpm}\,\hat{a}^\dagger\hat{a}\left(\hat{b}^\dagger + \hat{b}\right) + \hat{H}_d\,.$$

Similar to cavity optomechanics, we can define the radiation pressure force acting on the mechanical element as

$$F_{rp} = -\frac{\partial H}{\partial x} = -\hbar G\bar{n}_c\,, \tag{6.3}$$

where we have used the average photon number $\bar{n}_c = \langle\hat{a}^\dagger\hat{a}\rangle$. Analogously, the average number of phonons in the mechanical resonator is given by $\bar{n}_m = \langle\hat{b}^\dagger\hat{b}\rangle$.

To analyze the backaction of the microwave photons on the motion of the mechanical resonator caused by the radiation pressure force Eq. 6.3, we introduce the mechanical susceptibility χ. It is defined by $\chi(\Omega) := \delta x(\Omega)/\delta F(\Omega)$ and describes the displacement response of the nanobeam, δx, to an external force δF.

For an undisturbed harmonic oscillator, χ is given by (cf. Chap. 2, Eq. 2.2)

$$\chi(\Omega)^{-1} = m_{eff}\left(-\Omega^2 + \Omega_m^2 - i\Gamma_m\Omega\right),$$

where m_{eff}, $\Omega_m/2\pi$ and $\Gamma_m/2\pi$ denote the effective mass, the resonance frequency and the linewidth of the mechanical resonator. To account for the radiation pressure force Eq. 6.3, the susceptibility has to be modified according to

$$\chi(\Omega)^{-1} = m_{eff}\left(-\Omega^2 + \left(\Omega_m^2 + \frac{k_{ba}(\Omega)}{m_{eff}}\right) - i\Omega\left(\Gamma_m + \Gamma_{ba}(\Omega)\right)\right)\,.$$

Here, k_{ba} and Γ_{ba} describe backaction-induced modifications of spring constant and damping rate of the mechanical resonator [19, 21], given by

$$\begin{aligned} k_{ba} &= \hbar G^2\bar{n}_c\left(\frac{\Delta+\Omega}{(\Delta+\Omega)^2+(\kappa/2)^2} + \frac{\Delta-\Omega}{(\Delta-\Omega)^2+(\kappa/2)^2}\right) \quad \text{and} \\ \Gamma_{ba} &= \frac{\hbar G^2\bar{n}_c}{m_{eff}\Omega}\left(\frac{\kappa/2}{(\Delta+\Omega)^2+(\kappa/2)^2} - \frac{\kappa/2}{(\Delta-\Omega)^2+(\kappa/2)^2}\right)\,. \end{aligned}$$

Thus, the mechanical element can still be described as a damped harmonic oscillator with an effective angular resonance frequency Ω_{eff} and an effective damping rate Γ_{eff}. For frequencies close to the mechanical eigenfrequency, $\Omega \approx \Omega_m$, and weak backaction – which is the case for typical cavity opto/electromechanical systems – we obtain

$$\Omega_{eff} \approx \Omega_m + g_0^2\bar{n}_c\left(\frac{\Delta+\Omega_m}{(\Delta+\Omega_m)^2+(\kappa/2)^2} + \frac{\Delta-\Omega_m}{(\Delta-\Omega_m)^2+(\kappa/2)^2}\right) \quad \text{and} \tag{6.4}$$

$$\Gamma_{eff} \approx \Gamma_m + 2g_0^2\bar{n}_c\left(\frac{\kappa/2}{(\Delta+\Omega_m)^2+(\kappa/2)^2} - \frac{\kappa/2}{(\Delta-\Omega_m)^2+(\kappa/2)^2}\right)\,. \tag{6.5}$$

Here, we assume a coherent microwave drive at the frequency $\omega_d/2\pi$ and define $\Delta = \omega_d - \omega_c$ as the detuning of the drive tone with respect to the cavity resonance frequency[2]. Additionally, we have introduced the *electromechanical vacuum coupling rate* $g_0 = G\,x_{zpm}$,

[2] Strictly speaking, the resonance frequency of the microwave cavity is shifted by the presence of the nanobeam resonator: $\omega_c = \tilde{\omega}_c + G\bar{x}$. Here, $\tilde{\omega}_c$ is the (undisturbed) resonance frequency of the bare microwave cavity and $\bar{x}$ is the static displacement of the nanobeam. The frequency shift $\omega_c - \tilde{\omega}_c$, however, is small in typical circuit electromechanical systems and will therefore be neglected in the following.

which serves as a figure of merit for cavity opto/electromechanical systems as we will show later.

In the following, we briefly discuss the physical origin of Eqs. 6.4 and 6.5 and their implications on experiments with circuit electromechanical systems. Following [21, 35], we distinguish between three qualitatively different cases, depending on the detuning Δ.

Undetuned drive ($\Delta = 0$): In this case, the backaction on the mechanics vanishes, leading to an undisturbed resonance frequency and damping, $\Gamma_{\mathrm{eff}} = \Gamma_{\mathrm{m}}$ and $\Omega_{\mathrm{eff}} = \Omega_{\mathrm{m}}$. This result can be understood as follows:

Due to the interaction between microwave and mechanical resonator, microwave drive photons can undergo scattering events in which a phonon is created or annihilated. In case of phonon generation, the energy of the scattered photon is reduced by $\hbar\Omega_{\mathrm{m}}$ (*Stokes process*), whereas in case of phonon annihilation, the energy of the scattered photon is increased by $\hbar\Omega_{\mathrm{m}}$ (*anti-Stokes process*).

This is similar to inelastic light scattering *(Raman scattering)*, where incoming photons are scattered with phonons in a solid. When measuring the transmission spectrum of the microwave resonator, Stokes and anti-Stokes processes lead to the generation of sidebands, shifted by $\pm\Omega_{\mathrm{m}}$ relative to the microwave cavity resonance frequency (see Fig. 6.2).

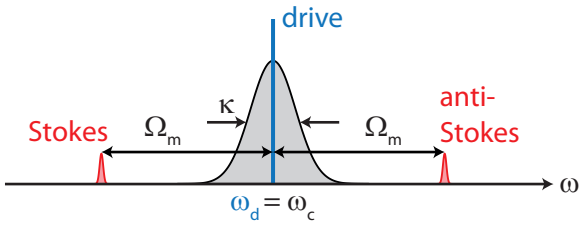

Figure 6.2: Schematic of Stokes and anti-Stokes sidebands for an undetuned drive ($\Delta = 0$, i. e. $\omega_{\mathrm{d}} = \omega_{\mathrm{c}}$). The density of states, defined by the microwave cavity, is equal for Stokes and anti-Stokes peak, thus the net phonon number is unchanged[3]. This configuration allows for a quantum non-demolition measurement of the state of mechanical motion.

If the drive tone is centered at the cavity resonance, the density of states, defined by the microwave cavity, is equal for Stokes and anti-Stokes peaks, so that the rates of Stokes and anti-Stokes processes are equal[3]. The number of phonons in the mechanical resonator is therefore not changed by the electromechanical interaction.

This configuration can be used for a quantum non-demolition measurement of the mechanical excitation state and for the determination of the electromechanical coupling g_0, as we will show in Sec. 6.3.

Red-detuned drive ($\Delta < 0$): According to Eq. 6.5, a red-detuned drive tone induces a linewidth broadening of the mechanical resonance, which is maximal at $\Delta = -\Omega_{\mathrm{m}}$ *(optimum red-detuning)*. This additional damping channel results from the imbalance

[3] More precisely, the ratio of the rates of anti-Stokes and Stokes processes for an undetuned microwave drive is given by the Boltzmann factor $\exp(-\hbar\Omega_{\mathrm{m}}/k_{\mathrm{B}}T)$, which is close to one for typical parameters $\Omega_{\mathrm{m}}/2\pi \simeq 1 \ldots 10\,\mathrm{MHz}$ and $T \simeq 50\,\mathrm{mK}$ [85].

of the rates of Stokes and anti-Stokes processes, as Fig. 6.3 illustrates: For a red-detuned drive, the density of states in the microwave cavity is larger at $\omega_\mathrm{d} + \Omega_\mathrm{m}$ than at $\omega_\mathrm{d} - \Omega_\mathrm{m}$, favoring anti-Stokes processes rather than Stokes processes. In particular, for an ideally red-detuned drive ($\Delta = -\Omega_\mathrm{m}$), the frequency of the anti-Stokes photons matches the cavity resonance frequency (where the density of states is maximal), while the Stokes process is strongly suppressed. Hence, the rate of anti-Stokes scattering events dominates, resulting in a net annihilation of phonons. This can be viewed as an additional loss channel of the mechanical system leading to an effective linewidth broadening.

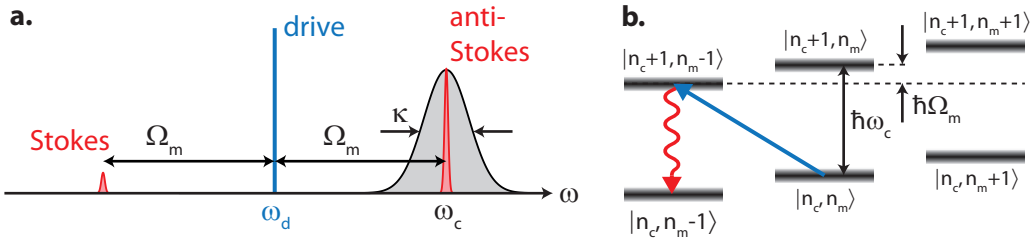

Figure 6.3: a. Schematic of Stokes and anti-Stokes sidebands for an ideally red-detuned drive ($\Delta = -\Omega_\mathrm{m}$, i. e. $\omega_\mathrm{d} = \omega_\mathrm{c} - \Omega_\mathrm{m}$). The anti-Stokes process dominates, as the density of states, defined by the microwave cavity, is maximal at $\omega_\mathrm{d} + \Omega_\mathrm{m}$. The Stokes peak is strongly suppressed, as $\Omega_\mathrm{m} \gg \kappa$ (resolved sideband regime). **b.** Energy level scheme, illustrating the dominating anti-Stokes process. Drive photons with energy $\hbar\omega_\mathrm{d}$ (depicted by the blue arrow) are converted to cavity photons ($\hbar\omega_\mathrm{c}$) by annihilation of phonons ($\hbar\Omega_\mathrm{m}$). This configuration thus allows cooling of the mechanical subsystem.

A red-detuned microwave drive can be employed to transfer excitations from the mechanical to the microwave resonator and in this way cool the mechanical resonator. The ability to depopulate the mechanical resonator via electromechanical interactions is one of the key features in cavity opto/electromechanics and a prerequisite for experiments in the quantum regime. We will give a quantitative description of sideband cooling in Sec. 6.4.

Blue-detuned drive ($\Delta > 0$): For a blue-detuned drive, the effective damping rate Γ_eff is reduced due to phonon creation in the dominating Stokes process (see Fig. 6.4). For sufficiently large $g_0^2\bar{n}_\mathrm{c}$, the effective damping rate Γ_eff can even vanish, resulting in a self-oscillation of the mechanical resonator. In this regime, where the intrinsic mechanical damping is overcompensated by the electromechanically induced phonon generation rate, phonon lasing has been demonstrated [21, 112, 113].

Within the scope of this thesis, we will focus on circuit electromechanical experiments with an undetuned or ideally red-detuned drive. In particular, we use the quantum non-demolition measurement configuration to characterize the mechanical resonator via its interaction with the microwave resonator, calibrate the readout circuit and determine the electromechanical coupling rate. Using an ideally red-detuned drive, we demonstrate sideband cooling and electromechanically induced transparency, an interference effect that will be discussed in Sec. 6.5.

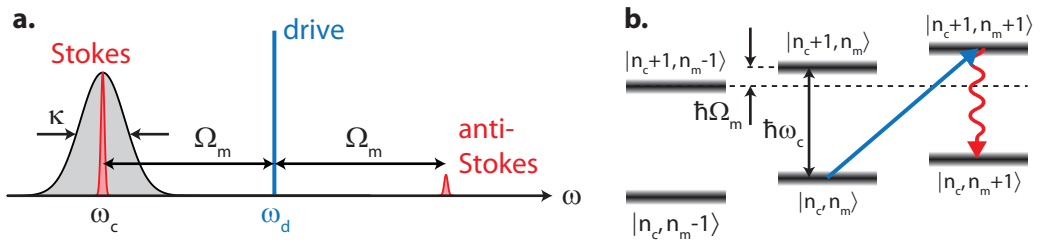

Figure 6.4: **a.** Schematic of Stokes and anti-Stokes sidebands for an ideally blue-detuned drive ($\Delta = \Omega_\mathrm{m}$, i. e. $\omega_\mathrm{d} = \omega_\mathrm{c} + \Omega_\mathrm{m}$). The Stokes process dominates, as the density of states, defined by the microwave cavity, is maximal at $\omega_\mathrm{d} - \Omega_\mathrm{m}$. The anti-Stokes peak is strongly suppressed, as $\Omega_\mathrm{m} \gg \kappa$ (resolved sideband regime). **b.** Energy level scheme, illustrating the dominating Stokes process. Drive photons with energy $\hbar\omega_\mathrm{d}$ (depicted by the blue arrow) are converted to cavity photons ($\hbar\omega_\mathrm{c}$) by generation of phonons ($\hbar\Omega_\mathrm{m}$). This configuration thus allows to amplify the mechanical motion.

Before we give a more detailed quantitative description of these techniques and experiments, we introduce our approach to realize circuit electromechanics with superconducting coplanar waveguide resonators and present some basic relations regarding microwave resonators which are necessary to model the circuit electromechanical hybrid system.

6.2 Circuit nano-electromechanics with superconducting CPW resonators

In this thesis, we investigate circuit nano-electromechanical systems consisting of a superconducting coplanar waveguide resonator with an integrated tensile stressed nanomechanical beam. This approach allows the combination of the high quality factors of both the microwave circuit and the mechanical resonator. The mechanical resonance frequencies are in the low MHz regime. We design the mechanical resonance frequencies to exceed the total loss rate of the microwave resonator, so that our circuit electromechanical devices operate in the resolved sideband regime, enabling e. g. efficient sideband cooling or electromechanically induced transparency.

6.2.1 Microwave resonators

We employ a coplanar waveguide (CPW) microwave resonator fabricated from a superconducting aluminium or niobium thin film deposited on a highly resistive silicon substrate. We use $\lambda/2$ or $\lambda/4$ resonators (length l_c) that are capacitively coupled to an input/output or transmission line, as depicted in Fig. 6.5. In an equivalent circuit picture, a CPW resonator can be seen as an LC circuit (see Fig. 1b) with impedance $Z_0 = \sqrt{L_\mathrm{l}/C_\mathrm{l}}$, where L_l and C_l denote the inductance and capacitance per length of the resonator line [114].

$\lambda/2$ resonator, measured in transmission: The resonance frequency of a $\lambda/2$ CPW resonator is given by

$$\omega_c = \frac{1}{\sqrt{L_n C}} \tag{6.6}$$

with the effective capacitance $C = C_\mathrm{l} l_\mathrm{c}/2$, the effective inductance $L_n = 2L_\mathrm{l} l_\mathrm{c}/(n^2\pi^2)$ and the mode index n [114].

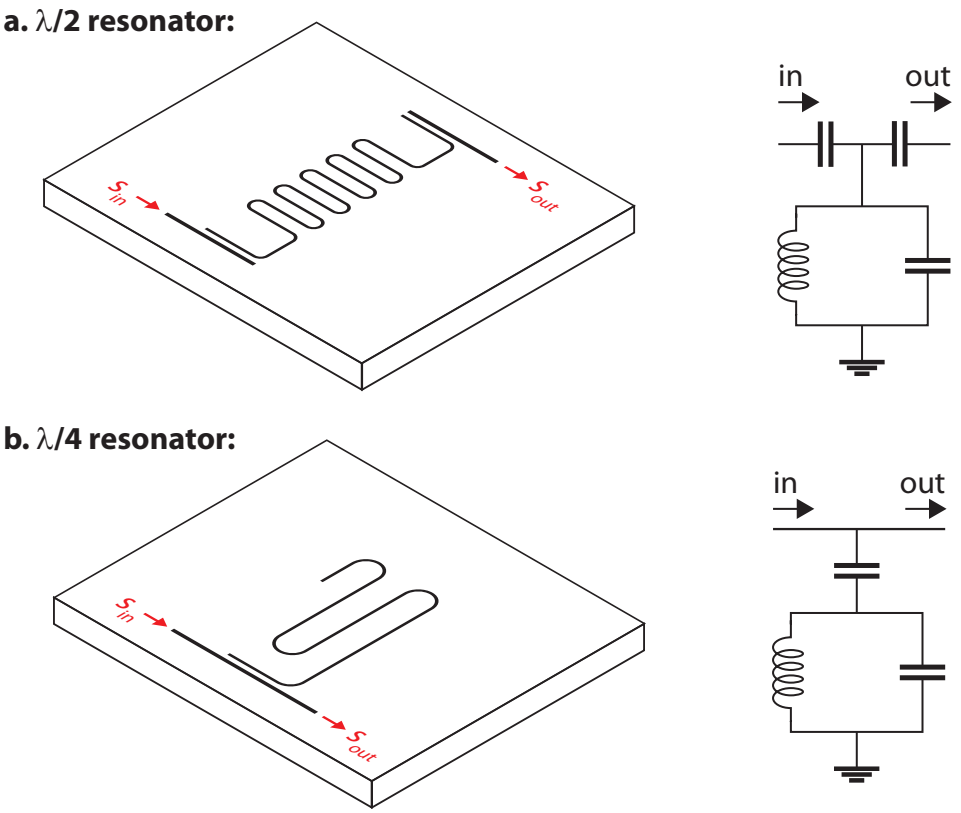

Figure 6.5: Design and equivalent circuit of superconducting coplanar waveguide resonators. **a.** $\lambda/2$ resonator coupled to an input and an output microwave line. **b.** $\lambda/4$ resonator coupled to a transmission line. The impedance of the input, output and transmission lines is $50\,\Omega$.

To experimentally investigate a $\lambda/2$ resonator capacitively coupled to a microwave circuit as sketched in Fig. 6.5a, we apply a microwave tone to the input line and measure the power transmission through the sample, which is defined as $T := |s_{\rm out}/s_{\rm in}|^2$. Here, $s_{\rm in}$ and $s_{\rm out}$ denote the (complex) voltage amplitude of the incoming and outgoing microwave signal, respectively.

In this configuration, the power transmission spectrum of the microwave circuit is given by the Lorentzian [115, 116]

$$T(\omega) = \frac{\kappa_{\rm ex}\kappa/4}{(\omega-\omega_{\rm c})^2 + (\kappa/2)^2}\ , \tag{6.7}$$

which is maximal at the resonance frequency $\omega_{\rm c}/2\pi$ and vanishes for $|\omega - \omega_{\rm c}| \gg \kappa$. Here, we have defined the external damping rate $\kappa_{\rm ex}$ which describes the loss of microwave photons due to the coupling to the input and output line [114]:

$$\kappa_{\rm ex} = 2\omega_{\rm c}^2 R_{\rm L} \frac{C_{\rm c}^2}{C} \tag{6.8}$$

with the coupling capacitance[4] C_c and the load $R_\mathrm{L} = 50\,\Omega$. The internal damping rate caused by two-level state losses, quasiparticle losses and eddy current losses (cf. Ref. [117]) can be written as [114]

$$\kappa_\mathrm{in} = \frac{\alpha l_\mathrm{c}}{Z_0 C} \,,$$

where α is the damping constant per length. The total damping rate, which equals the full width at half maximum (FWHM) of the measured transmission peak, is then $\kappa = \kappa_\mathrm{in} + \kappa_\mathrm{ex}$.

$\lambda/4$ resonator, measured in absorption: The resonance frequency of a $\lambda/4$ resonator can, similar to the previous case, be written as

$$\omega_c = \frac{1}{\sqrt{L_n C}} \tag{6.9}$$

by defining the effective capacitance and inductance as $C = C_\mathrm{l} l_\mathrm{c}/2$ and $L_n = 8 L_\mathrm{l} l_\mathrm{c}/(n^2\pi^2)$.

In the experiment presented in Chap. 8, we capacitively couple a $\lambda/4$ resonator to a microwave transmission line, as shown in Fig. 6.5b. For this configuration, the power transmission follows [21, 116]

$$T(\omega) = 1 - \frac{(\kappa/2)^2 - (\kappa_\mathrm{in}/2)^2}{(\omega - \omega_\mathrm{c})^2 + (\kappa/2)^2} \,. \tag{6.10}$$

In resonance ($\omega = \omega_\mathrm{c}$), we obtain

$$T(\omega_\mathrm{c}) = \left(\frac{\kappa_\mathrm{in}}{\kappa}\right)^2 \,. \tag{6.11}$$

This allows extraction of the internal and external damping rate from linewidth and insertion loss of a measured transmission spectrum.

Under experimental conditions, the transmission spectrum of microwave resonators often shows significant deviations from the ideal Lorentzian lineshape. These deviations can be attributed to impedance mismatches and discontinuities in the microwave lines [118–120]. We therefore fit a modified Lorentzian to the experimental data, which phenomenologically covers these effects by introducing a constant complex background. Please see App. B for details.

The average number of microwave photons in the cavity $\bar{n}_\mathrm{c}$ is related to the drive power by [21]

$$\bar{n}_\mathrm{c} = \frac{P_\mathrm{d}}{\hbar\omega_\mathrm{d}} \frac{\kappa_\mathrm{ex}/2}{(\kappa/2)^2 + \Delta^2} \,, \tag{6.12}$$

where ω_d denotes the angular frequency of the drive, $\Delta = \omega_\mathrm{d} - \omega_\mathrm{c}$ its detuning from the cavity resonance and P_d the drive power at the sample input. The latter is related to the output power of the microwave source, P_source, by

$$P_\mathrm{d} = \mathrm{Att} \cdot P_\mathrm{source} \,, \tag{6.13}$$

where Att is the signal attenuation along the microwave input line between microwave source and sample.

[4] We assume symmetric coupling to the input and output line, i. e. two equal coupling capacitors with capacitance C_c each.

6.2.2 Capacitive coupling

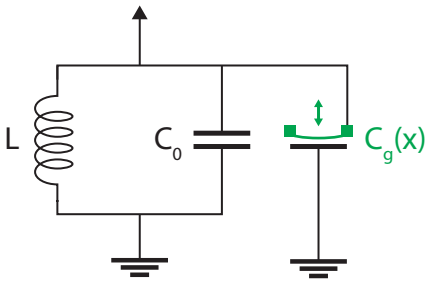

Figure 6.6: Equivalent circuit diagram of a microwave resonator with an embedded mechanical degree of freedom, forming a circuit electromechanical hybrid system.

In order to implement an electromechanical coupling, we integrate a nanomechanical beam resonator into a CPW microwave resonator so that the capacitance of the microwave resonator depends on the displacement of the nanobeam, as sketched in Fig. 6.6:

$$C(x) = C_0 + C_\mathrm{g}(x) \ ,$$

where C_0 and $C_\mathrm{g}(x)$ are the static and dynamic part of the capacitance, respectively, and x denotes the displacement of the nanobeam. In Chaps. 7 and 8, we will present two different approaches to experimentally realize such a capacitive coupling.

In this section, we focus on the relation between $C_\mathrm{g}(x)$ and the coupling parameter G. Later this will be useful to estimate the electromechanical coupling *a priori* and verify the experimentally determined coupling rates.

Assuming $C_\mathrm{g} \ll C_0$, we can expand Eq. 6.6 (or 6.9) to first order in C_g/C_0 and obtain for the disturbed resonance frequency of the microwave resonator

$$\omega_\mathrm{c}(x) = \omega_0 \left(1 - \frac{C_g(x)}{2C_0}\right) \ ,$$

where we have defined $\omega_0 = 1/\sqrt{L_n C_0}$.

The electromechanical coupling parameter $G = \partial\omega_\mathrm{c}/\partial x$ is therefore given by

$$G = -\frac{\omega_0}{2C_0}\frac{\partial C_\mathrm{g}(x)}{\partial x} \ . \tag{6.14}$$

In order to identify C_0 in Eq. 6.14, we use the expressions for Z_0, C and L_n, given in Sec. 6.2.1, and obtain for a $\lambda/2$ resonator

$$G = -\frac{Z_0\omega_0^2}{n\pi}\frac{\partial C_\mathrm{g}(x)}{\partial x} \ . \tag{6.15}$$

Analogously, we calculate for a $\lambda/4$ resonator

$$G = -\frac{2Z_0\omega_0^2}{n\pi}\frac{\partial C_\mathrm{g}(x)}{\partial x} \ . \tag{6.16}$$

The derivative $\partial C_\mathrm{g}(x)/\partial x$ depends on the geometry of the sample and has to be calculated numerically using finite element modeling. We will demonstrate this below for both circuit electromechanical hybrid samples presented in Chap. 7 and 8.

For typical sample geometries, the finite element model yields $\partial C_\mathrm{g}(x)/\partial x \approx 0.02 \ldots 20\,\mathrm{aF/nm}$. Using $Z_0 = 50\,\Omega$ and $\omega_\mathrm{c}/2\pi \simeq 6\,\mathrm{GHz}$ therefore results in a typical coupling strength of $G \simeq 0.1 \ldots 100\,\mathrm{kHz/nm}$.

6.3 Detection of mechanical motion, frequency noise calibration and determination of the coupling rate

As described in Sec. 6.1, an undetuned microwave drive can be used to read out the excitation state of the mechanical resonator via the microwave resonator without backaction on the mechanics. This also allows calibrating the microwave readout circuit and determining the electromechanical coupling g_0, as we will show in the following.

If the mechanical resonator is in equilibrium with its environment at temperature T, the average number of thermally excited phonons is [19]

$$\bar{n}_\mathrm{m} = \frac{k_\mathrm{B} T}{\hbar \Omega_\mathrm{m}} \tag{6.17}$$

and its thermal motion spectrum is given by Eq. 2.10, which we reproduce here to facilitate reading:

$$S_\mathrm{xx}(\Omega) = \frac{k_\mathrm{B} T}{2\Omega_\mathrm{m}^2 m_\mathrm{eff}} \frac{\Gamma_\mathrm{m}}{(\Omega - \Omega_\mathrm{m})^2 + (\Gamma_\mathrm{m}/2)^2} \,. \tag{6.18}$$

Due to the electromechanical coupling, a beam displacement δx induces a frequency shift $\delta\omega_\mathrm{c} = G\,\delta x$ of the microwave resonator. The mechanical motion spectrum S_xx therefore translates into a frequency fluctuation spectrum $S_{\omega\omega} = G^2 S_\mathrm{xx}$ of the microwave cavity. In a homodyne detection scheme, these frequency fluctuations lead to the generation of sidebands at $\omega_\mathrm{d} \pm \Omega_\mathrm{m}$. The measured power spectrum of these sidebands is related to the frequency fluctuation spectrum via $S_\mathrm{PP} = (2K(\Omega)/\Omega^2) S_{\omega\omega}$, where the *transfer function* $K(\Omega)$ covers the effects of signal attenuation and amplification in the microwave output line of the cryostat and the down-conversion of the microwave photons for homodyne detection.[5] The factor 2 takes into account that we measure single-sided power spectra [21,35].

Technically, $K(\Omega)$ can be calculated from the microwave input power, the mixer down-conversion characteristics and the internal and external damping rate of the microwave cavity [21]. This, however, requires precise knowledge of the microwave attenuation and amplification along the signal path, which is usually not available. Instead, we use *frequency noise calibration* to determine $K(\Omega)$ experimentally [35]. To this end, we apply a known frequency modulation to the cavity drive tone, leading to an additional modulation sideband peak in the measured homodyne transmission spectrum. For a monochromatic frequency modulation $S_{\omega\omega} = (1/2)\Omega_\mathrm{dev}^2(\delta(\Omega - \Omega_\mathrm{mod}) + \delta(\Omega + \Omega_\mathrm{mod}))$, the measured power spectrum is [35]

$$S_\mathrm{PP}^\mathrm{mod} = \frac{\Omega_\mathrm{dev}^2}{2\Omega_\mathrm{mod}^2} \cdot \frac{K(\Omega_\mathrm{mod})}{\mathrm{ENBW}} \,, \tag{6.19}$$

where ENBW denotes the detection bandwidth of the spectrum analyzer, $\Omega_\mathrm{mod}/2\pi$ the modulation frequency and $\Omega_\mathrm{dev}/2\pi$ the modulation depth (i. e. the maximum frequency deviation). When choosing $\Omega_\mathrm{mod} \approx \Omega_\mathrm{m}$, Eq. 6.19 allows determining $K(\Omega_\mathrm{m}) \approx K(\Omega_\mathrm{mod})$ from the measured calibration peak height $S_\mathrm{PP}^\mathrm{mod}$.

Having calculated $K(\Omega_\mathrm{m})$, the measured sideband height of thermal motion of the nanobeam can be used to determine the coupling rate g_0. To this end, we substitute Eqs. 6.1 and 6.17 into Eq. 6.18 and get

$$S_\mathrm{xx}(\Omega_\mathrm{m}) = \frac{8\bar{n}_\mathrm{m} x_\mathrm{zpm}^2}{\Gamma_\mathrm{m}} \,.$$

[5] Please note that $K(\Omega)$ depends on the microwave drive power, $K(\Omega) \propto P_\mathrm{d}$.

With $S_{\mathrm{PP}}(\Omega) = (2G^2K(\Omega)/\Omega^2)S_{\mathrm{xx}}(\Omega)$ and $g_0 = G\,x_{\mathrm{zpm}}$, we obtain the relation between the sideband power and the electromechanical vacuum coupling rate

$$\frac{1}{2}S_{\mathrm{PP}}(\Omega_{\mathrm{m}})\Gamma_{\mathrm{m}} = 4g_0^2\frac{K(\Omega_{\mathrm{m}})\bar{n}_{\mathrm{m}}}{\Omega_{\mathrm{m}}^2}\,. \tag{6.20}$$

This equation allows determination of g_0 from the measured power spectral density $S_{\mathrm{PP}}(\Omega_{\mathrm{m}})$ of the sidebands of thermal motion. To calculate g_0 directly from the sideband height of thermal motion and the calibration peak, we substitute Eq. 6.19 into Eq. 6.20 and solve for g_0:

$$g_0^2 = \frac{\Omega_{\mathrm{dev}}^2\Gamma_{\mathrm{m}}}{16\bar{n}_{\mathrm{m}}\mathrm{ENBW}}\frac{S_{\mathrm{PP}}(\Omega_{\mathrm{m}})}{S_{\mathrm{PP}}^{\mathrm{mod}}}\,. \tag{6.21}$$

6.4 Sideband cooling of mechanical motion

As mentioned above, an optimally red-detuned drive tone can be utilized to annihilate phonons from the mechanical resonator and thus reduce its motion. To analyze sideband cooling quantitatively, we define the effective mode temperature T_{eff} of the nanobeam by [21]

$$T_{\mathrm{eff}} = \frac{\hbar\Omega_{\mathrm{m}}\bar{n}_{\mathrm{m}}}{k_{\mathrm{B}}}$$

in analogy to Eq. 6.17.

In case of an ideally red-detuned drive, the dominating anti-Stokes process annihilates phonons from the mechanical system, resulting in a reduced steady-state phonon number. Due to a finite coupling to the environment, the mechanical system is repopulated with thermal phonons, limiting the minimum attainable phonon number.

The steady-state phonon number $\bar{n}_{\mathrm{m}}$ for a system driven on the red sideband depends on the rates of Stokes and anti-Stokes processes as well as on the damping rate of the mechanical resonator and the ambient temperature. In the limit of small coupling $g_0 \ll \kappa$, which is fulfilled for typical circuit electromechanical systems, and a significant cooling rate (this is the case for $\Gamma_{\mathrm{eff}} \gg \Gamma_{\mathrm{m}}$), $\bar{n}_{\mathrm{m}}$ is given by [21, 121]

$$\bar{n}_{\mathrm{m}} \approx \frac{\Gamma_{\mathrm{m}}}{\Gamma_{\mathrm{eff}}}\frac{k_{\mathrm{B}}T}{\hbar\Omega_{\mathrm{m}}} + \frac{A^+}{A^-}\,, \tag{6.22}$$

where we have defined the rates of Stokes and anti-Stokes processes, A^+ and A^-, by

$$A^{\pm} = \frac{g_0^2\bar{n}_{\mathrm{c}}\kappa}{(\Delta \mp \Omega)^2 + (\kappa/2)^2}\,.$$

Note that A^+ and A^- are related to the effective damping rate Γ_{eff} by $\Gamma_{\mathrm{eff}}(\Omega_{\mathrm{m}}) = \Gamma_{\mathrm{m}} + A^- - A^+$ (cf. Eq. 6.5). In the resolved sideband regime ($\Omega_{\mathrm{m}} \gg \kappa$), we have $A^- \gg A^+$ and therefore

$$\Gamma_{\mathrm{eff}} \approx \Gamma_{\mathrm{m}} + \frac{4g_0^2\bar{n}_{\mathrm{c}}}{\kappa} = \Gamma_{\mathrm{m}}(1 + C)\,, \tag{6.23}$$

where we have introduced the electromechanical cooperativity

$$C = \frac{4g_0^2\bar{n}_{\mathrm{c}}}{\Gamma_{\mathrm{m}}\kappa} = \frac{4g^2}{\Gamma_{\mathrm{m}}\kappa}\,. \tag{6.24}$$

The right-hand side of Eq. 6.23 reveals that the coupling to the (comparatively lossy) microwave cavity opens an additional damping channel for the mechanics, resulting in a linewidth broadening and phonon depopulation via the microwave cavity.

In the resolved sideband regime ($\Omega_\mathrm{m} \gg \kappa$), the minimum attainable phonon number is, according to Eq. 6.22, given by

$$\bar{n}_\mathrm{m}^\mathrm{min} \approx \frac{\kappa^2}{16\Omega_\mathrm{m}^2} \ll 1 \,. \tag{6.25}$$

Thus, cavity electromechanical systems operating in the resolved sideband regime can in principle be cooled to the ground state using the electromechanical interaction and a red-detuned microwave drive, independent of ambient temperature and coupling strength. In practice, however, Johnson noise and sideband noise of the microwave drive tone counteract the cooling mechanism. Therefore a low environment temperature together with a sufficiently high electromechanical coupling is necessary to cool a MHz mechanical resonator to its ground state [21, 121, 122].

6.5 Electromechanically induced transparency

Investigating a cavity opto/electromechanical system with two-tone spectroscopy allows the observation of electromechanically induced transparency or absorption (EMIT/EMIA), two effects based on the interference of electromechanically generated anti-Stokes/Stokes photons with an additional microwave probe tone.

In case of an ideally red-detuned drive tone ($\Delta \simeq -\Omega_\mathrm{m}$), e. g., the interaction between microwave drive photons and phonons leads to the generation of anti-Stokes photons at $\omega_\mathrm{d} + \Omega_\mathrm{m} \simeq \omega_\mathrm{c}$, as discussed in the previous section. When applying an additional weak coherent microwave tone to probe the cavity transmission around ω_c (see Fig. 6.7), the anti-Stokes photons interfere destructively with the probe photons, which manifests as an effective transparency of the microwave circuit for probe photons at $\omega_\mathrm{d} + \Omega_\mathrm{m}$. The width of the transmission window is determined by the effective mechanical damping rate, given by Eq. 6.5. The electromechanical hybrid system therefore acts as a tunable and extremely narrow bandpass filter for microwave photons.

In case of a blue-detuned drive tone, the Stokes process dominates and the Stokes photons interfere constructively with the probe tone at $\omega_\mathrm{p} \simeq \omega_\mathrm{d} - \Omega_\mathrm{m}$. This results in an additional absorption of the probe tone at $\omega_\mathrm{d} - \Omega_\mathrm{m}$, as demonstrated e. g. in [112].

A detailed quantitative description of EMIT and EMIA, based on the full Hamiltonian of the coupled circuit electromechanical system, is given in [21]. Here, we only review the final result, relating the power transmission T of the probe tone to the probe frequency $\omega_\mathrm{p} = \omega_\mathrm{d} + \Omega$ and the drive detuning $\Delta = \omega_\mathrm{d} - \omega_\mathrm{c}$. For a $\lambda/4$ resonator, capacitively coupled to a transmission line (as discussed in Sec. 6.2.1), we obtain

$$T = \left| 1 - \frac{\kappa_\mathrm{ex}/2}{-i(\Delta + \Omega) + \kappa/2 + \frac{g_0^2 \bar{n}_\mathrm{c}}{-i(\Omega - \Omega_\mathrm{m}) + \Gamma_\mathrm{m}/2}} \right|^2 .$$

In case of an ideally red-detuned drive tone ($\Delta = -\Omega_\mathrm{m}$), the transmission at cavity resonance $\omega_\mathrm{p} = \omega_\mathrm{c}$ simplifies to

$$T_0 = \left| \frac{1 - \kappa_\mathrm{ex}/\kappa + C}{1 + C} \right|^2 , \tag{6.26}$$

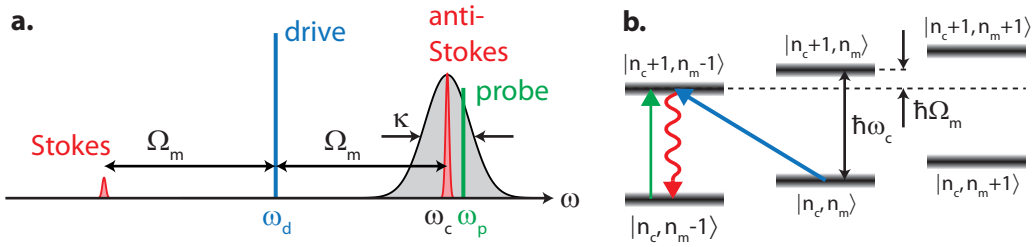

Figure 6.7: Two-tone spectroscopy with an ideally red-detuned drive (*EMIT configuration*). **a.** A strong drive tone (at $\omega_\mathrm{d} = \omega_\mathrm{c} - \Omega_\mathrm{m}$) generates anti-Stokes photons at ω_c which interfere destructively with a weak probe tone applied around the cavity resonance frequency, $\omega_\mathrm{p} \approx \omega_\mathrm{c}$. This leads to a transmission window around ω_c, whose width is given by the effective mechanical damping rate Γ_eff. **b.** Energy level scheme, illustrating the dominating anti-Stokes process. Drive photons (blue arrow) with energy $\hbar\omega_\mathrm{d}$ are converted into cavity photons ($\hbar\omega_\mathrm{c}$) by annihilation of phonons ($\hbar\Omega_\mathrm{m}$). The scattered photons interfere destructively with the weak probe tone (green arrow).

where we have used the cooperativity C as defined in Eq. 6.24.

In Chap. 8, we will demonstrate EMIT in a sample consisting of an aluminium CPW microwave resonator coupled to an aluminium nanomechanical beam.

Chapter 7

Circuit nano-electromechanics with a non-metallized nanobeam

In typical circuit nano-electromechanical devices, a metallized mechanical resonator is capacitively coupled to a superconducting microwave resonator [18, 20, 54]. In such devices the mechanical motion modulates the capacitance of the microwave resonator, allowing efficient coupling of both subsystems. This scheme enables, e. g., sensitive measurement of mechanical motion [18], ground state cooling [20] or the control of microwave signals [54].

To realize even higher coupling strengths, piezoelectric sandwich-like resonators have been integrated into superconducting microwave circuits. This open the path for state transfer experiments between a superconducting qubit and a mechanical resonator via a microwave resonator used as a bus for quantum information [22]. These mechanical resonators, however, suffer from relatively small quality factors prohibiting resolved sideband experiments.

In this chapter, we present an alternative approach towards circuit nano-electromechanics based on a pure, i. e. non-metallized, nanobeam that is coupled to a superconducting microwave resonator via dielectric forces. Even if the expected coupling is comparatively small, this approach is promising for the realization of high quality factors of both the mechanical and the microwave resonator as it avoids any additional dissipation due to metallization of the mechanical resonator [51, 123–125]. We here extend previous work at the chair of Prof. J. Kotthaus, where the dielectric coupling of non-metallized Si_3N_4 nanoresonators has been established as an alternative transduction and control scheme for high-Q nano-electromechanical systems [126, 127]. While for the temperature range between 10 and 300 K, conventional copper microstrip cavities have been employed for the read-out of mechanical motion [46], we here use a superconducting CPW resonator, providing a more sensitive read-out due to its higher quality factor.

First, we present the sample layout and the fabrication steps of this dielectrically coupled circuit nanoelectromechanical hybrid device. Next we calculate the electric field distribution in the coupling area which allows to *a priori* estimate the expected electromechanical coupling. Having introduced the experimental setup, we characterize the device and calibrate the readout circuit via frequency noise calibration. We determine the electromechanical coupling rate by utilizing the nonlinear Duffing response of the nanobeam.

Regarding the potential use of this platform as a sensing device, we estimate the mass sensitivity of this hybrid system.

The main results presented in this chapter have been published in [128].

7.1 Sample layout and fabrication

The dielectrically coupled nano-electromechanical device (*Sample #5*) consists of four superconducting $\lambda/2$ CPW microwave resonators which are capacitively coupled to an input and an output microwave line. One of these resonators is dielectrically coupled to a doubly-clamped, highly tensile-stressed Si_3N_4 nanobeam, as shown in Fig. 7.1a-c. The nanobeam is located between the CPW center line and ground plane with a gap of $s = 150\,\text{nm}$ between beam and electrodes. The capacitance between these electrodes depends on the displacement of the nanobeam. The microwave resonator can therefore be modeled as an LC equivalent circuit [Fig. 7.1d], where part of the capacitance depends on an additional mechanical degree of freedom (the displacement of the nanobeam).

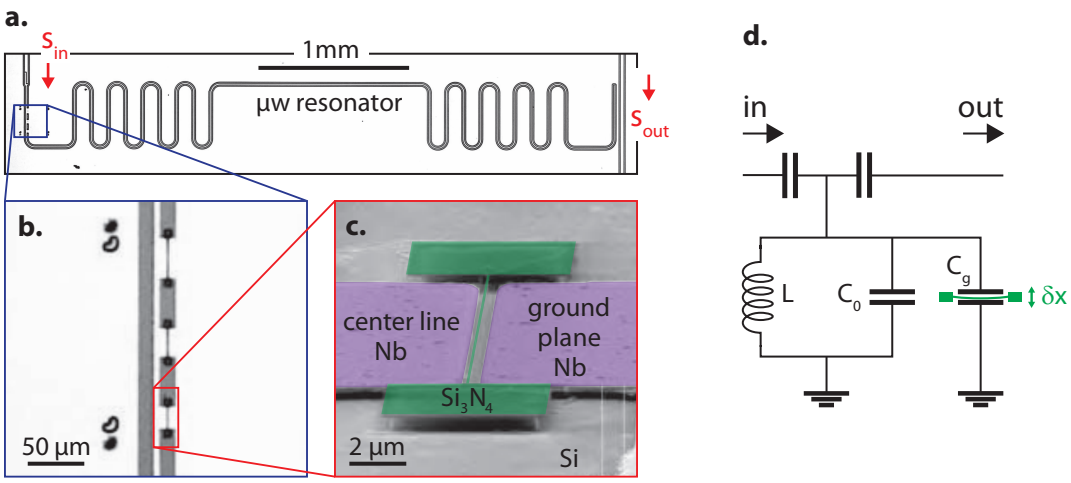

Figure 7.1: a-b. Optical micrograph, **c.** false color scanning electron micrograph and **d.** equivalent circuit diagram of the Si_3N_4/Nb circuit nano-electromechanical hybrid sample (*Sample #5*).

The sample is fabricated on a single-crystalline silicon wafer coated with 400 nm of thermal oxide (SiO_2) and 100 nm of highly tensile-stressed LPCVD (low pressure chemical vapor deposition) silicon nitride (Si_3N_4) [Fig. 7.2(i)]. First, a $l = 20\,\mu\text{m}$ long and $w = 170\,\text{nm}$ wide nanobeam as well as supporting clamping rectangles are defined using e-beam lithography (ii) and covered with aluminium (iii) serving as an etch mask. Next, the unprotected silicon nitride and approximately 100 nm of SiO_2 are removed by an anisotropic SF_6 reactive ion etching (RIE) step (iv). In this way, we align the lower surface of the beam (i. e. the SiO_2-Si_3N_4 interface) approximately with the upper surface of the niobium film deposited later on. With a second e-beam lithography step (v) followed by aluminium sputtering and lift-off (vi), we define a small rectangularly-shaped protective cover for the Si_3N_4 beam and its vicinity. Then, a 100 nm thick niobium film is deposited

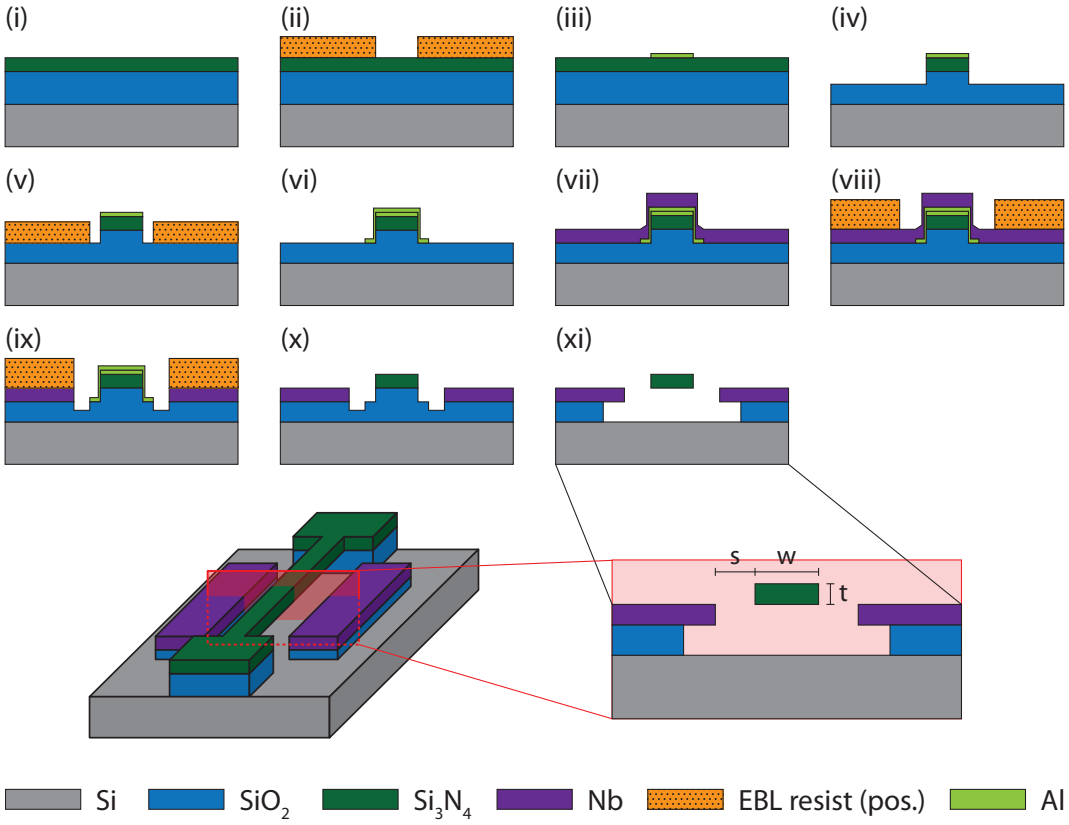

Figure 7.2: Schematic of the fabrication process of Sample #5. For details, please refer to the main text.

by magnetron sputtering (vii). Subsequently, the microwave resonator and its input and output line are patterned by a third e-beam lithography (viii) and a second RIE step (ix). The resist and the aluminium coating are removed with acetone, potassium hydroxide and Piranha, i. e. a mixture of hydrogen peroxide and sulphuric acid (x). Finally, we release the silicon nitride beam using buffered hydrofluoric acid (xi).

7.2 Modeling of the dielectric electromechanical coupling

7.2.1 Electric field distribution and electromechanical coupling

To understand the electromechanical coupling mechanism and to estimate the coupling rate *a priori*, we use a COMSOL 2D model representing the cross-section of the sample at the position of the nanobeam, as depicted in Fig. 7.3a (cf. Ref. [126]). We calculate the electric field distribution, using the geometry parameters of the sample as given above and the dielectric constants of silicon, silicon oxide and silicon nitride, $\epsilon_{\mathrm{Si}} = 11.7$ [129], $\epsilon_{\mathrm{SiO}} = 3.9$ [130] and $\epsilon_{\mathrm{SiN}} = 7.5$ [130]. The niobium is assumed to be a perfect conductor, while silicon, silicon oxide and silicon nitride are modeled as perfect insulators. We further assume a static potential difference between ground plane ($\Phi = 0$) and center line ($\Phi = \Phi_0 > 0$) of the microwave resonator.

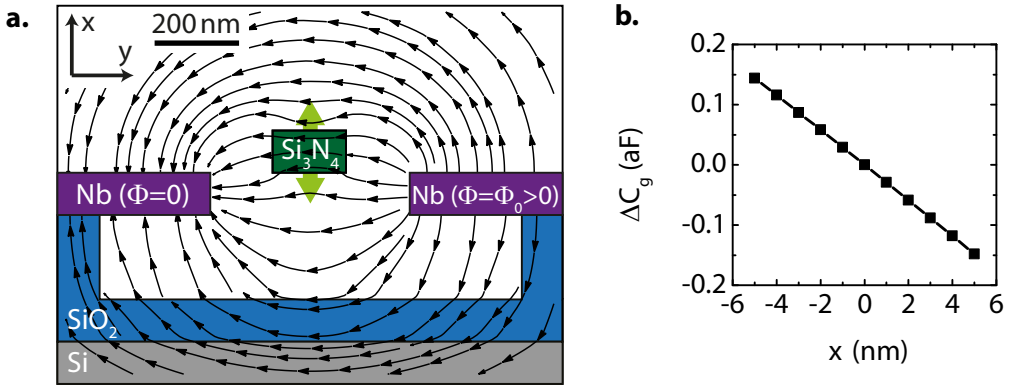

Figure 7.3: **a.** Two-dimensional static COMSOL model to simulate the electromechanical coupling. The black arrows indicate the electric field strength and direction, resulting from an electrostatic potential difference Φ_0 between the niobium electrodes. The light green arrow illustrates the dynamic displacement of the nanobeam (not to scale). **b.** Calculated capacitance change, $\Delta C_g(x_0) := C_g(x_0) - C_g(0)$, as a function of the beam displacement x_0.

In Fig. 7.3, the calculated electric field distribution is plotted. As expected, the presence of the Si_3N_4 nanobeam modifies the electric field between the center line and the ground plane of the microwave resonator due to its high dielectric constant. From the field distribution, we determine the capacitance per length, c_g, between the Nb electrodes. Using the effective length $l_{\text{eff}} = 0.613l$ of the nanobeam, which accounts for the shape of the displaced beam (see App. C), we obtain $C_g = l_{\text{eff}} c_g = 1.37\,\text{fF}$ for the capacitance in the surrounding of the nanobeam. In Fig. 7.3b, the change of this capacitance, ΔC_g, for a small (static) out-of-plane beam displacement x_0 is plotted. This allows to numerically determine $\partial C_g/\partial x_0 = 29.2\,\text{zF/nm}$.

With this, we can estimate the electromechanical coupling, as derived in Sec. 6.2.2. Using Eq. 6.15, the designed impedance $Z_0 = 70\,\Omega$ of the microwave resonator and the measured resonance frequency $\omega_c/2\pi = 5.67\,\text{GHz}$, we estimate the coupling $G/2\pi = 132\,\text{Hz/nm}$.

With an effective mass $m_{\text{eff}} = 0.43\,\text{pg}$ and the mechanical resonance frequency $\Omega_m/2\pi = 13.952\,\text{MHz}$ (see below), we calculate the zero-point motion of the nanobeam, $x_{\text{zpm}} = 37\,\text{fm}$, and thus obtain the electromechanical vacuum coupling $g_0/2\pi = 4.8\,\text{mHz}$.

7.2.2 Impact of geometry

For sensing applications, a high electromechanical coupling is beneficial because is enables a fast and precise readout of the nanobeam motion via the microwave resonator. In the following, we therefore briefly discuss how the coupling depends on the beam dimensions and on the gap size between the niobium electrodes and the beam.

According to Eq. 6.15, the coupling G is proportional to the variation of the capacitance with the beam displacement, $\partial C_g/\partial x$. Fig. 7.4 shows the calculated $\partial C_g/\partial x$ as a function of the beam thickness t, the beam width w and the gap size s. For each of these three figures, we have varied one of the parameters t, w and s, while fixing the other two parameters to the values given in Sec. 7.1.

As expected, $\partial C_g/\partial x$ increases with the thickness of the nanobeam, as a larger t implies a larger volume of the dielectric in an otherwise unchanged capacitor (see Fig. 7.4a). The

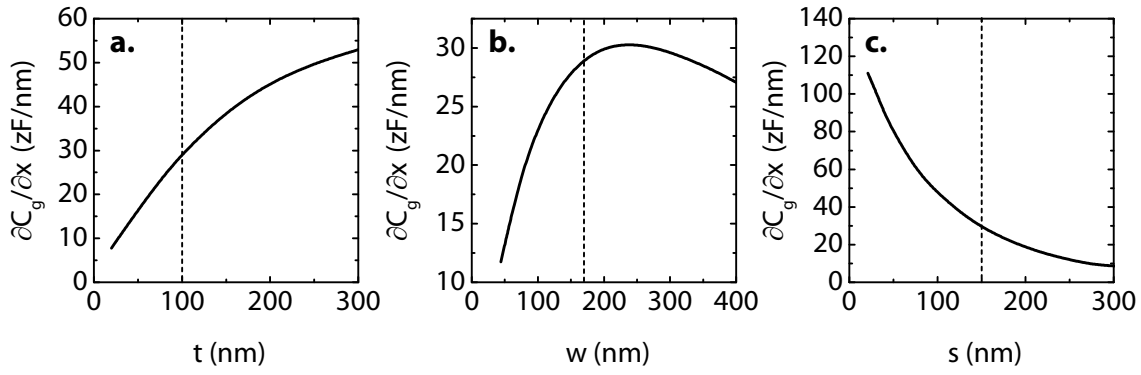

Figure 7.4: Change of the capacitance with beam displacement, $\partial C_g/\partial x$, as a function of (a) the beam thickness, (b) the beam width and (c) the gap size. The dashed lines indicate the thickness (width, gap size) of Sample #5.

effect, however, saturates at large t because the electric field vanishes far away from the Nb electrodes.

Varying the width of the nanobeam instead of the thickness, as plotted in Fig. 7.4b, shows that there is an optimum width around 240 nm. The reason is that for small w, the volume of the dielectric beam is small and so its effect on the capacitance. For large w, however, the capacitance between the Nb electrodes shrinks as their distance is given by $w + 2s$ (here, we have fixed s to 150 nm). The actual nanobeam width realized in our experiment is close to the optimum value.

The most effective way of increasing the electromechanical coupling is to decrease the gap size, as Fig. 7.4c illustrates. The fabrication of such a system with a gap size below 100 nm, however, is challenging, as all the fabrication steps shown above have to be carefully adjusted and aligned with respect to each other.

An alternative approach to increase the electromechanical coupling is to increase the impedance $Z_0 = \sqrt{L_l/C_l}$ of the microwave resonator, as $G \propto Z_0$. This can be achieved by replacing the CPW resonator by a lumped element resonator (see, e. g., Refs. [20, 109]).

7.3 Experimental setup

To experimentally characterize Sample #5, we employ the homodyne measurement setup depicted in Fig. 7.5. The chip, placed inside a gold-plated copper box, is mounted at the mixing chamber stage of a home-made wet dilution refrigerator ("Kermit", *Cryostat #1*) and connected to an input and an output microwave line. The microwave resonator is driven by a microwave source (*Agilent E8267D*) at its resonance frequency $\omega_c/2\pi$ with an estimated microwave power of 2.5 nW (−56 dBm) at the device input. The output microwave signal is amplified with a cryogenic low-noise HEMT (high-electron-mobility transistor) amplifier (*Low Noise Factory, LNC4_8A*) and a room temperature broadband low-noise amplifier (LNA, *Kuhne BB 202 A*). The sample is mounted on a piezoelectric actuator (manufacturer: *PI Ceramic*) driven by the output of a vector network analyzer (VNA, *Rohde&Schwarz ZVA 8*). This allows us to excite the fundamental flexural mode of the nanobeam to a high amplitude state. For phase sensitive detection with the VNA, the microwave signal is downconverted using an I-Q-demodulator (*Marki IR0408LC2Q*). A

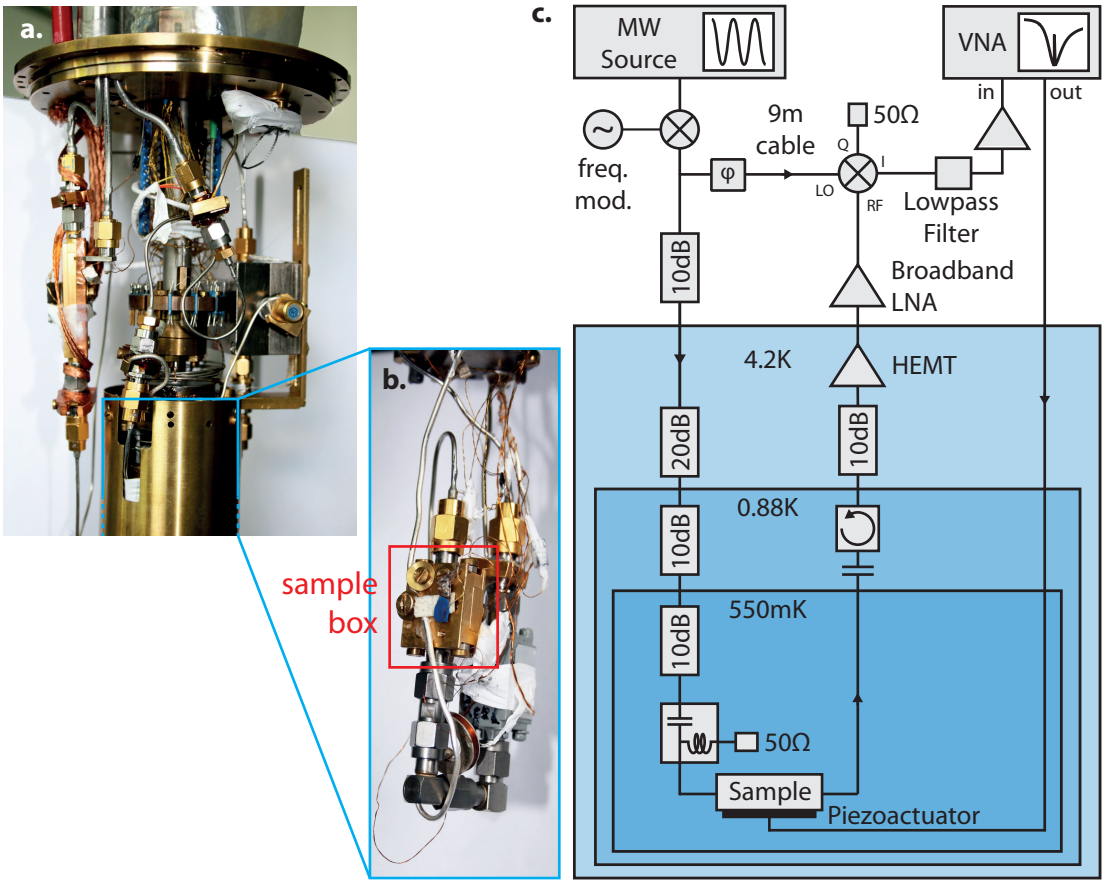

Figure 7.5: a-b. Photograph of the inset of Cryostat #1 (4 K stage and below). **c.** Schematic illustration of the experimental setup and the microwave circuitry inside Cryostat #1. The signal from the microwave source is split up into a drive tone for the superconducting microwave resonator and a reference tone. The drive tone is attenuated within the cryostat and capacitively coupled to the superconducting microwave resonator. The sample output signal is amplified, down-converted, filtered and detected with a vector network analyzer that drives the piezoelectric actuator on which the sample is mounted. The photos (a) and (b) have been taken from Ref. [21].

phase shifter (*ATM PNR P1607*) is used to adjust the phase in a way that the homodyne signal measured at the VNA is maximal corresponding to the quadrature response of the device.

7.4 Experimental results

7.4.1 Characterization of microwave cavity and mechanical resonator

First we spectroscopically investigate the response spectrum of the microwave resonator to determine resonance frequency and linewidth of its fundamental mode. To this end, we employ a vector network analyzer (VNA) connected to the microwave input and output lines of the cryostat and measure the microwave transmission through the sample as a function of the probe frequency. All following experiments were carried out at a temperature of 550 mK.

Figure 7.6a shows an overview of the transmission spectrum of Sample #5. It features four distinct resonance peaks corresponding to the four $\lambda/2$ microwave resonators on the chip, operated in transmission. In the following, we focus on the microwave resonator at $\omega_c/2\pi = 5.67\,\mathrm{GHz}$, into which the nanobeam resonator is integrated.

Figure 7.6b depicts the transmission spectrum around ω_c, which we use to determine the linewidth $\kappa/2\pi = 749\,\mathrm{kHz}$ of the microwave resonator. By design, the microwave resonator is coupled critically to the input and output lines, i. e. $\kappa_{in} \approx \kappa_{ex} \approx \kappa/2$.

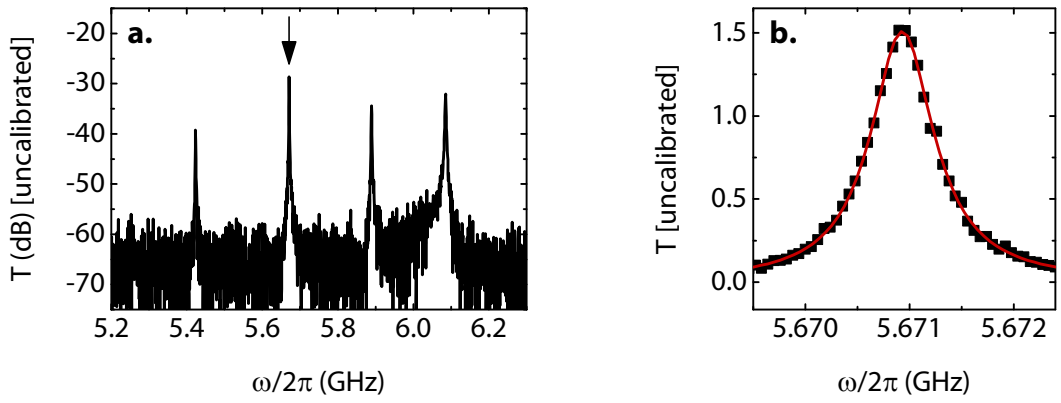

Figure 7.6: **a.** Uncalibrated transmission spectrum of Sample #5, containing four superconducting CPW microwave resonators with frequencies between 5.4 and 6.1 GHz. The arrow indicates the resonator at 5.67 GHz which is coupled to a Si_3N_4 nanobeam. **b.** Detailed view of the transmission spectrum of the microwave resonator at 5.67 GHz. The probe power at the sample input is 5.0 pW (−83 dBm).

To experimentally characterize the mechanical resonator embedded in the microwave circuit, we employ the homodyne measurement setup depicted in Fig. 7.5 as described in the previous section.

When driving the microwave cavity and exciting the beam with the piezoactuator simultaneously, the microwave drive tone with frequency $\omega_d/2\pi$ is modulated by the beam's motion, resulting in the generation of sidebands at $\omega_d \pm \Omega_m$. The corresponding frequency fluctuation amplitude is given by $\delta\omega_c = G\,x_0$ [35], where G is the electromechanical coupling and x_0 the mechanical amplitude. In the homodyne setup employed here, the sidebands of mechanical motion are mapped to the frequency $\Omega_m/2\pi$ and the measured down-converted signal is given by [35]

$$P_{\mathrm{hom}}(\Omega) = \frac{2K(\Omega)}{\Omega^2}\,\delta\omega_c^2 = \frac{2K(\Omega)G^2}{\Omega^2}x_0^2$$

with the oscillation frequency of the beam $\Omega/2\pi$ and the transfer function $K(\Omega)$.

Note that we here drive both the nanobeam and the microwave resonator simultaneously and measure the response of the nanobeam as a function of the RF drive applied to the actuator. Therefore, the measured quantity P_{hom} is not a spectral power, but the absolute sideband power (unit: Watt) induced by the resonantly driven nanobeam. This is in contrast to the usually applied sideband spectroscopy of thermal motion (see Sec. 6.3), where the observable is a power spectrum S_{PP} in units of power/frequency.

Figure 7.7 shows the down-converted spectroscopy signal of the silicon nitride nanobeam when excited in the linear (weak driving) regime. Here, the nanobeam follows

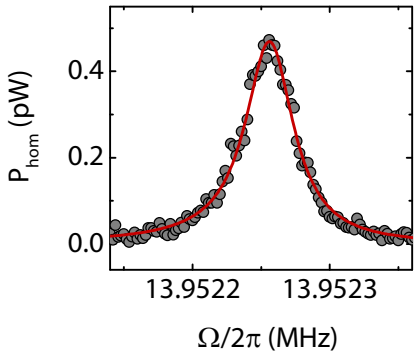

Figure 7.7: Power spectrum of the weakly driven nanomechanical beam ($U_{\mathrm{piezo}} = 35\,\mu\mathrm{V_{rms}}$), measured with the homodyne setup depicted in Fig. 7.5. The red line is a Lorentzian fit to the experimental data.

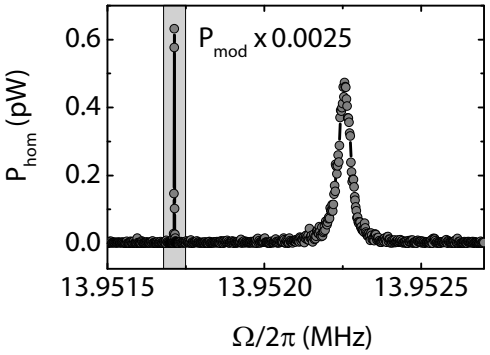

Figure 7.8: Homodyne power spectrum for a weak external drive ($U_{\mathrm{piezo}} = 35\,\mu\mathrm{V_{rms}}$) using a frequency-modulated cavity drive tone. The sideband peak at $\Omega_{\mathrm{mod}}/2\pi = 13.9517\,\mathrm{MHz}$ is scaled by a factor of 0.0025. Analyzing the height of this calibration sideband peak allows to determine the transfer function $K(\Omega_{\mathrm{m}})$.

the behavior expected for a harmonic oscillator. At $T \approx 550\,\mathrm{mK}$, we find an eigenfrequency $\Omega_{\mathrm{m}}/2\pi = 13.95225\,\mathrm{MHz}$ of the nanobeam with a linewidth of $\Gamma_{\mathrm{m}}/2\pi = 29\,\mathrm{Hz}$ corresponding to a quality factor of $Q = 480\,000$. This quality factor exceeds those of comparable nanobeams with niobium metallization [21] by more than a factor of three.

7.4.2 Frequency noise calibration

Next we determine the transfer function $K(\Omega)$ which relates the measured sideband power to the mechanically induced frequency fluctuation $\delta\omega_{\mathrm{c}}$. To this end, we apply a frequency-modulated drive tone with a well-known modulation depth $\Omega_{\mathrm{dev}}/2\pi = 4.2\,\mathrm{kHz}$ at a frequency $\Omega_{\mathrm{mod}}/2\pi$ near the mechanical resonance frequency (see Fig. 7.8). Measuring the corresponding sideband height P_{mod}, we can determine the transfer function[1] $K(\Omega_{\mathrm{mod}}) = P_{\mathrm{mod}}\Omega_{\mathrm{mod}}^2/(2\Omega_{\mathrm{dev}}^2)$ and obtain $K(\Omega_{\mathrm{m}}) \approx K(\Omega_{\mathrm{mod}}) = 1.2\,\mathrm{mW}$.

[1] To derive this relation from Eq. 6.19, we use $P_{\mathrm{mod}} = \mathrm{ENBW}\cdot S_{\mathrm{PP}}^{\mathrm{mod}}$, where ENBW denotes the detection bandwidth of the VNA.

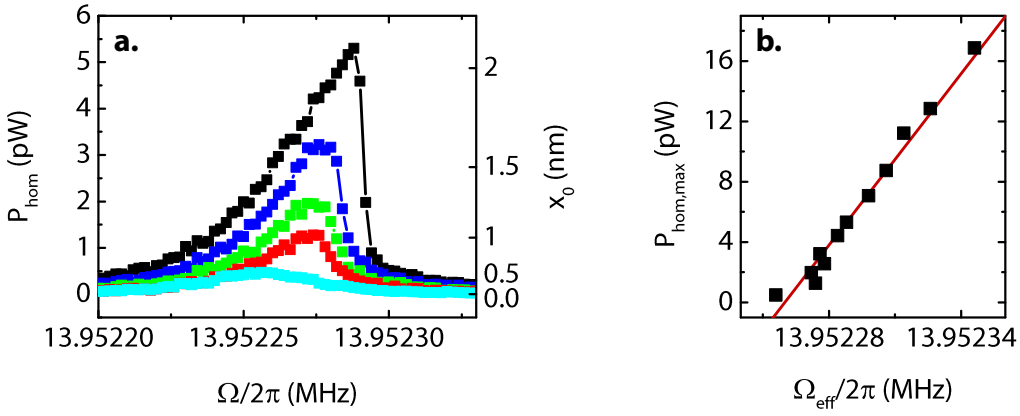

Figure 7.9: **a.** Homodyne power spectrum (left axis) resp. mechanical amplitude spectrum (right axis) of the nanobeam for varying external drive power ($U_{\mathrm{piezo}} = 35$ to $89\,\mu\mathrm{V_{rms}}$). The amplitude scale (on the right) is based on the amplitude calibration described in the main text. **b.** Maximum homodyne power as a function of the effective resonance frequency. The red line is a linear fit to the experimental data – the so-called backbone curve – according to Eq. 7.1.

7.4.3 Determination of the coupling rate via Duffing nonlinearity

To determine the coupling rate g_0, usually the sidebands of thermal motion of the nanobeam are measured. Comparing the sideband height to the displacement of the nanobeam, which can be calculated from the sample temperature, allows determining the coupling g_0, as derived in Sec. 6.3.

Here, the coupling is too small to resolve the thermal motion of the nanobeam. We therefore use an alternative way to access the coupling g_0, which is based on the Duffing nonlinearity of the strongly driven beam.

In the previous chapters, we have already made use of the nonlinear behaviour of tensile stressed nanobeams to determine the prestress and Young's modulus of the beam via its response spectrum. This relies on the fact that the Duffing parameter α, which can be determined from spectroscopy measurements, is related to material properties of the nanobeam.

Here, we reverse this scheme and calculate the Duffing nonlinearity directly from well-known material parameters of the pure Si_3N_4 nanobeam. Comparing this to the observed resonance frequency shift for strong drive allows to relate the measured sideband height (in units of power) to absolute displacement and thus determine the coupling g_0.

To calculate the Duffing nonlinearity α, we use Eq. 2.11, the length of the nanobeam $l = 20\,\mu\mathrm{m}$, the literature values $E = 160\,\mathrm{GPa}$ [44], $\sigma = 830\,\mathrm{MPa}$ [44], $\rho = 2600\,\mathrm{kg/m^3}$ [46] and obtain $\alpha = 9.4 \times 10^{27}\,\mathrm{m^{-2}s^{-2}}$.

Next, we measure the response of the nanobeam motion, P_{hom}, as a function of the piezo drive frequency $\Omega/2\pi$ for various driving strengths, as plotted in Fig. 7.9a. From these data, we extract the effective resonance frequency $\Omega_{\mathrm{eff}}/2\pi$ and the maximum of the homodyne power spectrum $P_{\mathrm{hom,max}}$ for each applied drive voltage U_{piezo}, leading to Fig. 7.9b.

To compare this to the expected backbone curve, we rewrite the backbone curve Eq. 2.13 as

$$P_{\mathrm{hom,max}} = \frac{16}{3}\frac{\Omega_{\mathrm{m}}}{\alpha}\frac{K(\Omega_{\mathrm{m}})G^2}{\Omega_{\mathrm{m}}^2}\left(\Omega_{\mathrm{eff}} - \Omega_{\mathrm{m}}\right) \ , \tag{7.1}$$

where we have used the relation $P_{\mathrm{hom}} = (2K(\Omega)G^2/\Omega^2)x_0^2$.

Thus, we can determine the coupling G from the slope of the linear fit in Fig. 7.9b and obtain $G/2\pi = 312\,\mathrm{Hz/nm}$. The electromechanical vacuum coupling rate is $g_0 = G\,x_{\mathrm{zpf}} = 2\pi \times 11.5\,\mathrm{mHz}$ with the zero-point motion of the beam $x_{\mathrm{zpm}} = \sqrt{\hbar/2m_{\mathrm{eff}}\Omega_{\mathrm{m}}} = 37\,\mathrm{fm}$.

Compared to a similar nano-electromechanical hybrid system with a metallized beam [54], the coupling is about two orders of magnitude smaller here, as it solely relies on the dielectric interaction between nanobeam and niobium electrodes.

7.5 Temperature dependence of the mechanical quality factor

As demonstrated in several studies before, the quality factor of nanomechanical resonators strongly depends on temperature [52, 53, 73, 131]. In particular, two-level defects, which significantly contribute to the overall damping at room temperature, freeze out at low temperatures [73]. In this section, we compare the mK quality factor of the nanobeam motion to values measured at room temperature and at liquid helium temperature and check the observed trend against expectations.

To determine the room temperature quality factor of the fundamental out-of-plane mode of the nanobeam, the sample has been pre-characterized in an optical laser interferometry setup similar to the one sketched in Fig. 3.5. We find a resonance frequency of $\Omega_{\mathrm{m}}^{\mathrm{RT}}/2\pi = 13.955\,\mathrm{MHz}$ and a linewidth of $\Gamma_{\mathrm{m}}^{\mathrm{RT}}/2\pi = 349\,\mathrm{Hz}$, corresponding to a quality factor of $Q_{\mathrm{m}}^{\mathrm{RT}} \approx 40\,000$. Compared to similar nanobeams fabricated at the chair of Prof. J. Kotthaus before [44], the quality factor is slightly reduced. We attribute this to damage of the Si_3N_4 nanobeam during the second RIE step (Fig. 7.2i), in which we used a sputtered aluminium coating to protect the Si_3N_4. Presumably, the aluminium film was too thin, especially at the edges of the nanobeam, so that the Si_3N_4 was exposed to the argon ions used for the etching process of the microwave resonator.

The quality factor at liquid helium temperature was measured in the setup described in Sec. 7.4.1, with the circulation of the ^{3}He/^{4}He mixture of the dilution fridge switched off. We find the resonance frequency $\Omega_{\mathrm{m}}^{4\mathrm{K}}/2\pi = 13.952\,\mathrm{MHz}$ and the linewidth $\Gamma_{\mathrm{m}}^{4\mathrm{K}}/2\pi = 97\,\mathrm{Hz}$ ($Q_{\mathrm{m}}^{4\mathrm{K}} \approx 144\,\mathrm{k}$).

In Fig. 7.10, the quality factor is plotted for all three studied temperatures. We observe a strongly increasing Q at low temperatures, which can roughly be described by a $Q \propto \sqrt{T}$ behaviour over the whole temperature range from $T = 0.5$ to $300\,\mathrm{K}$. This agrees with predictions by Seoánez *et al.*, who theoretically investigated defect-related damping mechanisms in doubly-clamped nanobeams and found a dominating $Q \propto \sqrt{T}$ behaviour at low temperature, caused by relaxation absorption of biased two-level systems (TLS) [132]. Experiments with doubly-clamped gold nanobeams confirmed this temperature dependence for temperatures between 30 and 500 mK [133]. In contrast, for aluminium nanobeams, $Q \propto 1/T$ has been observed at low temperatures ($T \lesssim 1\,\mathrm{K}$) [52, 53]. Still, to our best knowledge, no data covering the full temperature range from room temperature

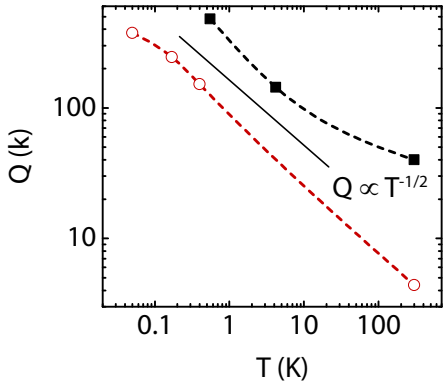

Figure 7.10: Quality factor of mechanical motion for three different temperatures: 550 mK, 4.2 K and room temperature (black squares). The dashed line is a guide to the eye and the solid line depicts a $T^{-1/2}$-behaviour. For comparison, the red circles show the temperature dependence of the quality factor of a comparable aluminium nanobeam integrated in a circuit electromechanical hybrid device (Sample #6). This device will be discussed in detail in Chap. 8.

down to mK have been reported for doubly-clamped nanobeam resonators. In particular, for Si_3N_4 nanobeams the temperature range below 4 K has not been studied yet. Faust *et al.* studied the temperature-dependent damping in tensile stressed Si_3N_4 nanobeams between 4 K and 350 K and found a comparatively weak, non-monotonic temperature dependence, which is attributed to coupling to TLS [73].

The presented platform can be useful to study the damping mechanisms at low temperature and clarify their temperature dependence. Certainly, a more detailed experimental investigation of the damping as a function of temperature will be necessary to substantiate the few data points plotted in Fig. 7.10.

Compared to other materials, silicon nitride features particularly high quality factors (see, e. g., Refs. [42,44,71]). To illustrate this, we have added the measured quality factor of a comparable aluminium nanobeam as a function of temperature to Fig. 7.10. The response spectrum of the aluminium nanobeam resonator has been investigated via its coupling to a microwave circuit. We will discuss this device in Chap. 8 in detail. The measured quality factor of the aluminium nanobeam shows a similar temperature dependence (see also Ref. [52]), but is shifted to lower values compared to the Si_3N_4 nanobeam.

The exceptionally high quality factors of Si_3N_4 nanoresonantors are based on the fact that Si_3N_4 thin films can be fabricated with high intrinsic prestress. The tensile stress in the Si_3N_4 does not significantly affect the damping rate of mechanical motion, Γ_m, but strongly increases the resonance frequency $\Omega_m/2\pi$, resulting in a high quality factor $Q = \Omega_m/\Gamma_m$. Due to the high impedance mismatch between the discrete long-wavelength vibrational modes of the resonator and high-frequency bulk phonon states, acoustic radiation losses into the beam clamps are highly suppressed. Thus, for highly stressed Si_3N_4 nanobeams with large aspect ratio, intrinsic losses are the dominant damping mechanism [44,71]. They are caused by surface defects [134] as well as by bulk defects due to the amorphous nature of the material [73]. The microscopic mechanisms, however, are still subject to investigation.

The presented hybrid platform, in which a high-Q microwave circuit is employed to sensitively read out mechanical motion, can be useful for studying damping in Si_3N_4 at temperatures between several mK and 4 K. Extending the work of Faust *et al.* [73], this could provide further insight into the damping mechanisms in Si_3N_4 and open the path to ultra-high-Q nanomechanical beam resonators.

7.6 Estimated mass sensitivity

For sensing applications, the response of the nanobeam resonator to externally induced changes of its mechanical properties is of particular interest. This can, e. g., be a change of its mass, caused by attaching a particle to the nanobeam, which results in a shift of the resonance frequency of the beam. This concept allows for the detection and identification of particles in a gas flow, for instance.

Even if the presented platform should be understood as a proof-of-principle experiment, we briefly estimate the mass sensitivity of the device.

Adding a point mass δm to the nanobeam will induce a shift of the resonance frequency [14]

$$\frac{\delta\Omega_\mathrm{m}}{\Omega_\mathrm{m}} = \frac{2\delta m}{m_\mathrm{eff}} \,.$$

The factor 2 is due to the fact that we assume the additional mass to be located at the center of the beam, where the displacement and therefore its contribution to the total energy of the oscillation is maximal.

The frequency resolution is given by half of the linewidth of the weakly driven beam, in our case $\Gamma_\mathrm{m}/2 = 14.5\,\mathrm{Hz}$. With the values given above for resonance frequency and effective mass, $\Omega_\mathrm{m}/2\pi = 13.952\,\mathrm{MHz}$ and $m_\mathrm{eff} = 0.43\,\mathrm{pg}$, respectively, we obtain a mass sensitivity of $\delta m = 0.44\,\mathrm{ag}$. This corresponds to the mass of approximately 10^4 carbon atoms.

To optimize the mass sensitivity of nanomechanical sensing devices, usually low-weight resonators, like carbon nanotubes, are employed. In the last ten years, sensitivities down to the yoctogram range could be realized, corresponding to the mass of a single proton [12–14]. This ultimate sensitivity has been reached with a carbon nanotube resonator oscillating at almost 2 GHz and requires low-temperature operation (4 K) in an ultra-high vacuum environment to prevent adsorption of unwanted molecules [14].

In the future, nanomechanical mass sensors could be employed as low-cost devices for the detection and identification of single molecules or atoms and thus be used for the analysis of gases and aerosols, with possible applications in biology or chemistry.

7.7 Summary

We have fabricated and characterized a circuit nano-electromechanical hybrid system consisting of a superconducting microwave resonator and a pure Si_3N_4 nanomechanical beam with a resonance frequency of 14 MHz. We used the electromechanical coupling to read out the mechanical motion via the microwave resonator. To this end, we monitored the mechanically induced sidebands of the microwave resonator transmission in a homodyne measurement setup. At 550 mK, we observed a mechanical quality factor of 480 000, which

is about one order of magnitude higher than the room temperature quality factor determined by optical interferometry.

For strong external driving forces we observed the transition from the linear to the Duffing regime and used this effect to quantify the mechanical displacement. By fitting the peak values of the measured homodyne power spectra, we determined the mechanical amplitude of the nanobeam motion. This method is complementary to the usually employed calibration via thermal motion [35, 135] and especially useful for systems where the Brownian motion is not straightforwardly detectable. Moreover, the precise knowledge of the motional amplitude allowed us to derive the electromechanical coupling g_0. For our device, we found $g_0/2\pi = 11.5\,\mathrm{mHz}$, which is corroborated by numerical modeling of the device.

The employed coupling scheme is based on dielectric forces between the microwave resonator and the nanobeam. The coupling is therefore about two orders of magnitude smaller than for similar circuit electromechanical systems with a metal/metallized nanobeam resonator. The presented approach, however, allows the realization of particularly high mechanical quality factors which are not limited by dissipation in a metal thin film. Thus, the concept of dielectrically coupling a pure Si_3N_4 nanobeam to a high-Q microwave resonator is promising especially for sensing devices (e. g. for the detection of single molecules) which require high frequency resolution and thus low damping rates. Moreover, this work opens the path for further experimental studies of mechanical losses in silicon nitride at millikelvin temperatures, extending previous work on the damping mechanisms in Si_3N_4 nanomechanical beams [44, 73].

Chapter 8

Circuit nano-electromechanics with an aluminium nanobeam

The integration of metal or metallized mechanical elements into a microwave circuit allows for an efficient electromechanical coupling based on capacitive forces and is therefore the most promising approach towards quantum experiments like the preparation or transfer of non-classical states [24–26, 122]. While in previous experiments at the Walther-Meißner-Institut, a silicon nitride nanobeam covered with a niobium thin film was employed, we here pursue a different approach based on a pure aluminium nanobeam integrated in an aluminium microwave resonator (see also Refs. [18, 109]). First, this scheme reduces the number of fabrication steps as both the microwave resonator and the nanobeam can be fabricated simultaneously. Second, this fabrication process allows for the integration of a standard aluminium transmon qubit as a single photon source. In particular, the direct coupling of a mechanical resonator to a transmon qubit could open the path to a new class of experiments, which we will briefly discuss at the end of this chapter. Besides, aluminium-based nano-electromechanical systems could allow the realization of higher coupling strengths, using e. g. focused ion beam milling as a fabrication technique in order to produce ultra-narrow gaps between the nanobeam and the adjacent ground plane [53].

In this chapter, we show fabrication and characterization of a circuit nano-electromechanical hybrid sample consisting of a pure aluminium nanobeam resonator which is coupled to a superconducting aluminium CPW microwave resonator. We demonstrate sideband cooling of the mechanical resonator and electromechanically induced transparency. Besides, we discuss novel approaches towards experiments in the quantum regime, based on an inductive electromechanical coupling between a microwave and a mechanical resonator, and first steps towards a three-body circuit electromechanical device consisting of a transmon qubit, a microwave resonator and a nanobeam.

The sample fabrication and part of the measurements have been done by Daniel Schwienbacher within the scope of his master's thesis at WMI, which I supervised [136].

8.1 Sample fabrication

Sample #6 consists of a microwave transmission line which is capacitively coupled to eight $\lambda/4$ CPW microwave resonators. Their impedance is $Z_0 = 50\,\Omega$ and their resonance

frequencies are chosen between 6 and 8 GHz. Into six of the microwave resonators, a nanomechanical beam is integrated at the voltage anti-node of the resonator, coupled galvanically to the center line of the microwave resonator. The nanobeam and the adjacent ground plane form a capacitor with capacitance C_g which adds to the capacitance of the bare microwave resonator C_0. Similar to the previous chapter, this results in an electromechanical coupling between the microwave resonator and the nanobeam.

The fabrication process of Sample #6 is schematically shown in Fig. 8.1. Starting with a commercial highly resistive silicon substrate (i), the microwave resonators and the nanobeams are patterned onto the chip simultaneously using e-beam lithography (ii), electron beam evaporation ($t = 100$ nm of aluminium) and lift-off (iii). After annealing the aluminium film at 350 °C for 30 minutes (iv), the chip is covered with a protective resist layer, into which etch windows are patterned around the nanobeam resonators in a second e-beam lithography step (v). The nanobeams are released in a subsequent isotropic reactive ion etching process with an Ar/SF_6 mixture (vi). Finally, the protective resist layer is removed with acetone and the sample is dried in a critical point dryer (vii). This is necessary in order to prevent adhesion of the nanobeams to the adjacent aluminium ground plane caused by strong capillary forces in the solvent and by the comparatively low tensile stress in the aluminium at room temperature.

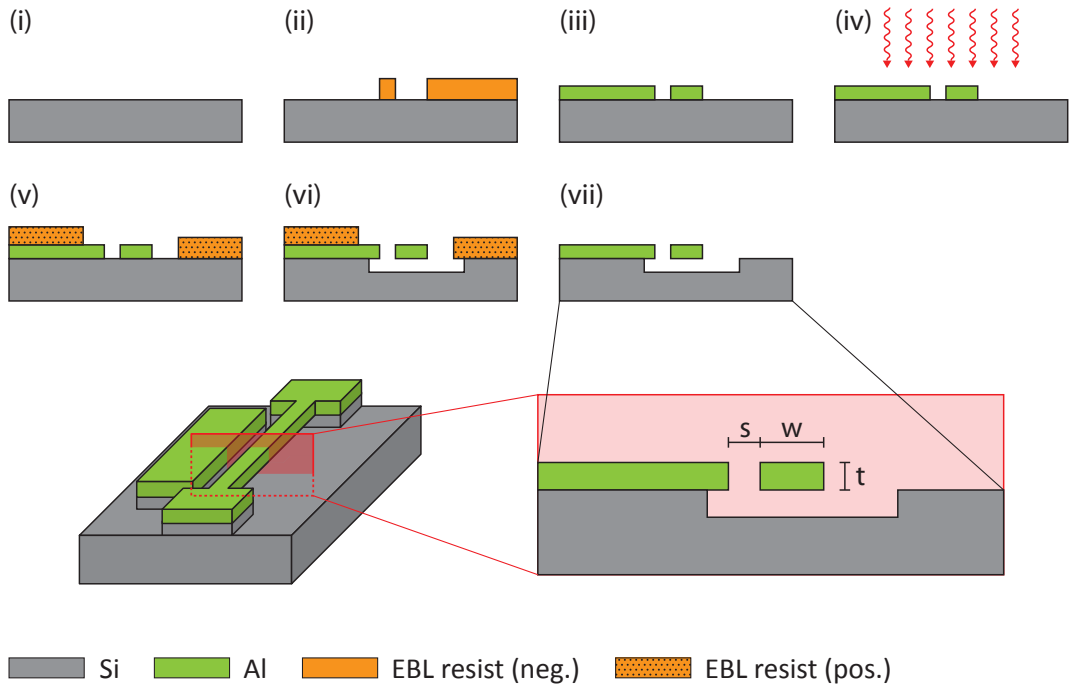

Figure 8.1: Schematic illustration of the fabrication process of Sample #6. The individual steps are explained in the main text.

In the following, we focus on the experimental investigation of microwave resonator #2 (resonance frequency $\omega_c/2\pi = 6.158$ GHz) which is coupled to a $l = 50\,\mu$m long and $w = 120$ nm wide nanobeam (see Fig. 8.2). The gap between the nanobeam and the ground plane is $s = 150$ nm.

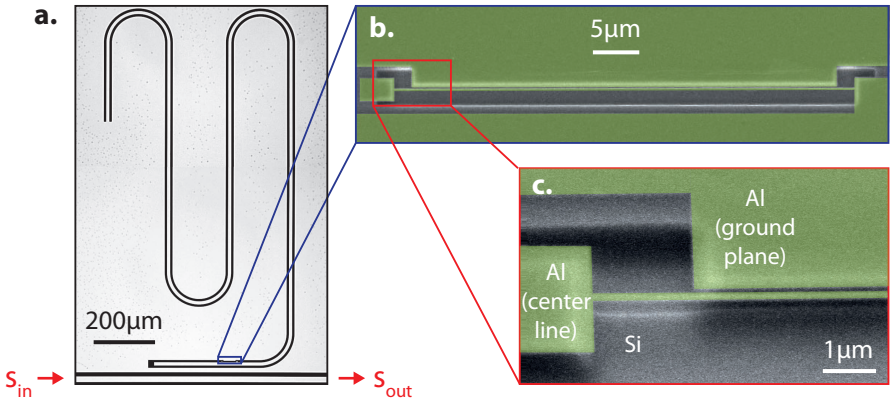

Figure 8.2: **a.** Micrograph of resonator #2 on Sample #6. At the voltage anti-node of the resonator, a nanomechanical beam is integrated. **b.** False-colored SEM image of the nanobeam. **c.** Detailed view of the nanobeam, including one of the clamping pads and the adjacent aluminium ground plane.

8.2 A priori estimation of the electromechanical coupling

To model the electromechanical coupling between microwave cavity and nanobeam resonator, we employ a COMSOL 2D finite element model similar to Sec. 7.2. We use the sample geometry given in the previous section and assume the aluminium to be a perfect conductor. We calculate the electric field distribution, plotted in Fig. 8.3a, and the capacitance between the nanobeam and the adjacent aluminium ground plane as a function of the beam displacement x_0 (see Fig. 8.3b). As the nanobeam is galvanically connected to the center line of the microwave cavity, its capacitance C_g to the ground plane contributes to the total capacitance of the microwave cavity, resulting in a capacitive coupling between microwave and mechanical resonator.

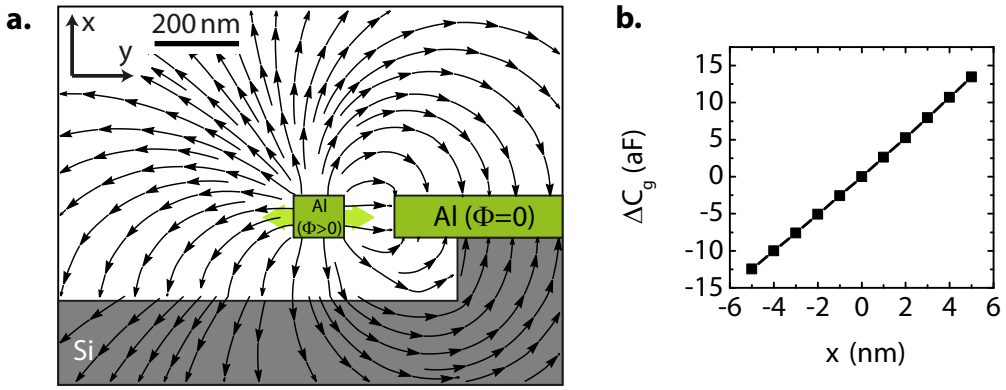

Figure 8.3: **a.** Finite element model of the cross-section of Sample #6 at the position of the nanobeam. **b.** Calculated variation of the capacitance C_g between nanobeam and ground plane as a function of the beam displacement x_0.

From Fig. 8.3b, we estimate $\partial C_g/\partial x = 2.59\,\mathrm{aF/nm}$. With Eq. 6.16, the impedance $Z_0 = 50\,\Omega$ of the microwave cavity and its resonance frequency $\omega_c/2\pi = 6.158\,\mathrm{GHz}$, we calculate the coupling parameter $G/2\pi = 19.6\,\mathrm{kHz/nm}$. Using the effective mass $m_{\mathrm{eff}} = 0.81\,\mathrm{pg}$ and the measured resonance frequency of the nanobeam, $\Omega_m/2\pi = 4.872\,\mathrm{MHz}$ (see

below), we determine the zero-point motion $x_{\mathrm{zpm}} = 46\,\mathrm{fm}$. Thus, the estimated vacuum coupling is $g_0/2\pi = 0.90\,\mathrm{Hz}$.

8.3 Cryogenic setup

To experimentally investigate Sample #6, we use an *Oxford Instruments Triton* dilution refrigerator (*Cryostat #2*), which allows operation down to approximately 35 mK. The microwave circuitry in the fridge is schematically shown in Fig. 8.4. The sample is mounted at the mixing chamber stage of the cryostat and connected to a microwave input and output line. The input line is heavily attenuated to suppress Johnson noise, while the output line is equipped with three circulators (to prevent backscattering of noise photons) and a cold HEMT amplifier (*Low Noise Factory LNC4_8A*), which amplifies the output signal by approximately 38 dB. The DC input line as well as the reference microwave input line are not used in the experiments presented in this chapter.

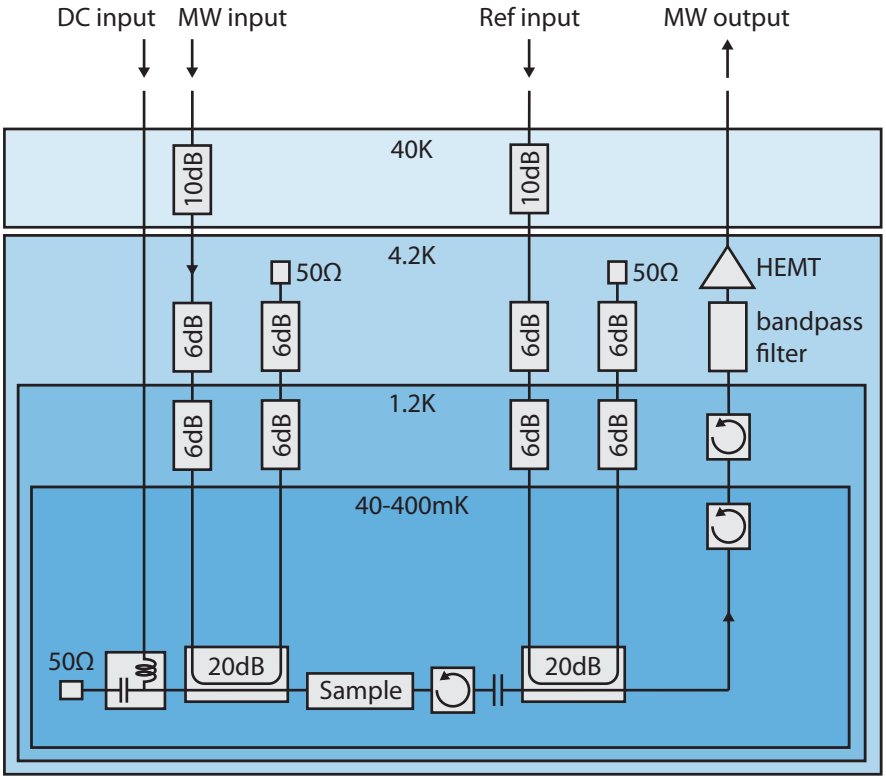

Figure 8.4: Schematic illustration of the microwave circuitry inside Cryostat #2.

8.4 Experimental results

In this section, the experimental results of Sample #6 are presented. First, we show characterization measurements of the relevant microwave resonator as well as the corresponding nanobeam resonator. Next, we calibrate the microwave readout circuit using frequency noise calibration and determine the electromechanical vacuum coupling by homodyne spectroscopy of the thermal motion of the nanobeam. We further demonstrate sideband cooling

of the mechanical motion and electromechanically induced transparency (EMIT) and thus prove the functionality of the circuit nano-electromechanical hybrid device.

8.4.1 Characterization of the microwave resonator

To characterize the microwave circuit of Sample #6, we measure the transmission through the sample as a function of frequency. The measurement is performed at $T = 40\,\mathrm{mK}$ and with a probe power of $P_\mathrm{p} = 0.3\,\mathrm{pW}$ ($-95\,\mathrm{dBm}$) at the sample input. Figure 8.5a shows the transmission spectrum of Sample #6 over a wide frequency range. We observe six distinct resonance dips corresponding to six microwave cavities with frequencies between 6.0 and 7.8 GHz. Two additional microwave resonators are broken.

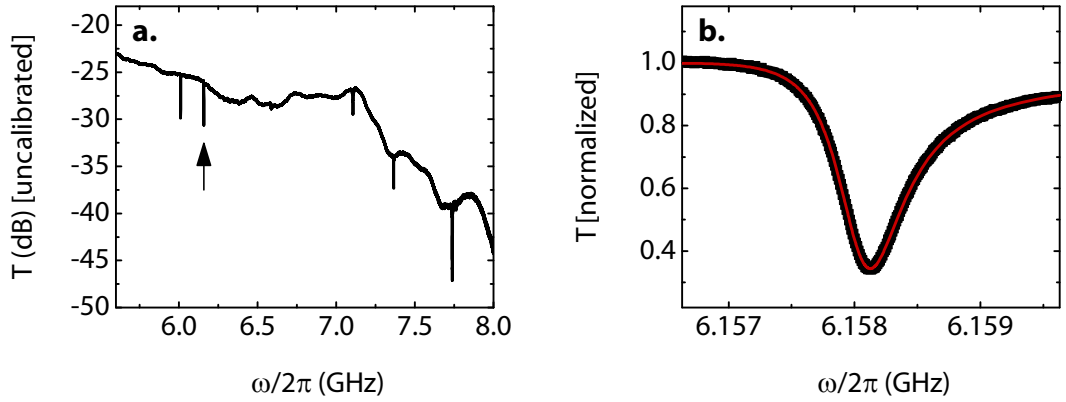

Figure 8.5: **a.** Uncalibrated transmission spectrum of Sample #6. The arrow indicates resonator #2, on which we focus in this chapter. **b.** Detailed view of resonator #2 (resonance frequency $\omega_\mathrm{c}/2\pi = 6.158\,\mathrm{GHz}$) with Lorentzian fit (red line). The probe power applied to the sample input is $P_\mathrm{p} = 0.3\,\mathrm{pW}$ ($-95\,\mathrm{dBm}$).

In the following, we focus on resonator #2, into which a nanomechanical beam with length $l = 50\,\mu\mathrm{m}$ has been integrated. Figure 8.5b shows the absorption spectrum of resonator #2, which has already been normalized so that $T = 1$ far away from resonance. From this spectrum, we extract the resonance frequency $\omega_\mathrm{c}/2\pi = 6.158\,\mathrm{GHz}$ and the linewidth $\kappa/2\pi = 638\,\mathrm{kHz}$, which results in a quality factor of $Q = 9650$. Additionally, the depth of the transmission dip allows extracting the internal and external damping rates[1], $\kappa_\mathrm{in}/2\pi = 404\,\mathrm{kHz}$ and $\kappa_\mathrm{ex}/2\pi = 238\,\mathrm{kHz}$, according to Eq. 6.11.

[1] In some of the measurements with Sample #6 (frequency noise calibration, determination of g_0 and temperature dependence of the mechanical linewidth and resonance frequency), the internal damping rate was significantly higher than the value given here: $\kappa'_\mathrm{in}/2\pi \approx 692\,\mathrm{kHz}$. These measurements have been performed in a first cooldown during which external magnetic fields have been applied to the sample several times. We therefore attribute the increased internal loss rate to magnetic flux pinned in the superconducting aluminium film. During the second cooldown, no intentional magnetic fields have been applied. The external damping rate was found to be equal in both cooldowns; this is expected, as κ_ex only depends on the coupling capacitance between microwave resonator and transmission line, which is not affected by magnetic flux (see Eq. 6.8). For the quantitative evaluation of the experimental data, we therefore use $\kappa'_\mathrm{in}/2\pi = 692\,\mathrm{kHz}$ in Secs. 8.4.3 and 8.4.5 and $\kappa_\mathrm{in}/2\pi = 404\,\mathrm{kHz}$ in Sec. 8.4.4.

8.4.2 Characterization of the nanobeam resonator

To spectroscopically characterize the mechanical resonator integrated in microwave resonator #2, we use the detection scheme illustrated in Fig. 8.6. We drive the microwave

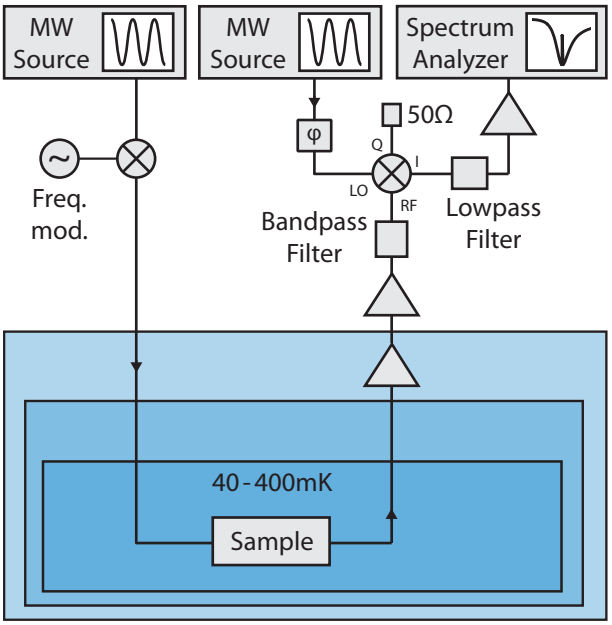

Figure 8.6: Experimental setup used to characterize the mechanical resonator, determine the electromechanical vacuum coupling and demonstrate sideband cooling of mechanical motion. The cryogenic part of the microwave circuitry has been simplified for reasons of clarity.

resonator at its resonance frequency, $\omega_\mathrm{d} = \omega_\mathrm{c}$, with $P_\mathrm{d} = 2.4\,\mathrm{nW}$ ($-56\,\mathrm{dBm}$) at the sample input. The transmitted signal is amplified with a HEMT amplifier at 4 K and a room temperature broadband amplifier (*B&Z BZP110UC1X2*) and down-converted using a *Marki IQ0307LXP I-Q*-demodulator with a local oscillator frequency $\omega_\mathrm{LO} = \omega_\mathrm{d}$. The Stokes and anti-Stokes sidebands arising from the thermal motion of the nanobeam are therefore mapped to the eigenfrequency $\Omega_\mathrm{m}/2\pi$ of the mechanical element. The down-converted signal is measured with a *Rohde&Schwarz FSV* spectrum analyzer and plotted in Fig. 8.7a[2]

Fitting a Lorentzian to the experimental data, we extract the resonance frequency $\Omega_\mathrm{m}/2\pi = 4.872\,\mathrm{MHz}$ and the linewidth $\Gamma_\mathrm{m}/2\pi = 13.2\,\mathrm{Hz}$ of the fundamental in-plane mode of the nanobeam resonator. This corresponds to a quality factor of $Q_\mathrm{m} = 3.69 \times 10^5$ at $T = 50\,\mathrm{mK}$.

With the measured resonance frequency, the length of the beam $l = 50\,\mu\mathrm{m}$ and the density of aluminium $\rho_\mathrm{Al} = 2700\,\mathrm{kg\,m^{-3}}$ [137], we determine the tensile stress in the nanobeam using the relation $\Omega_\mathrm{m} \approx \pi/l\sqrt{\sigma_0/\rho}$ (Eq. 2.3) and obtain $\sigma_0 = 641\,\mathrm{MPa}$. Comparing to the prestress at room temperature, $\sigma_0^\mathrm{RT} = 234\,\mathrm{MPa}$ ($\Omega_\mathrm{m}^\mathrm{RT}/2\pi = 2.95\,\mathrm{MHz}$), we observe an increase by $\Delta\sigma_0 = 407\,\mathrm{MPa}$, which is consistent with estimations based on the thermal expansion coefficient of aluminium (see App. D).

[2]Please note that all measured spectra are single-sided, i. e. S_PP is defined for positive values of Ω only. In the given down-conversion setup, the Stokes and the anti-Stokes peak are therefore mapped to the same frequency $\Omega_\mathrm{m}/2\pi$.

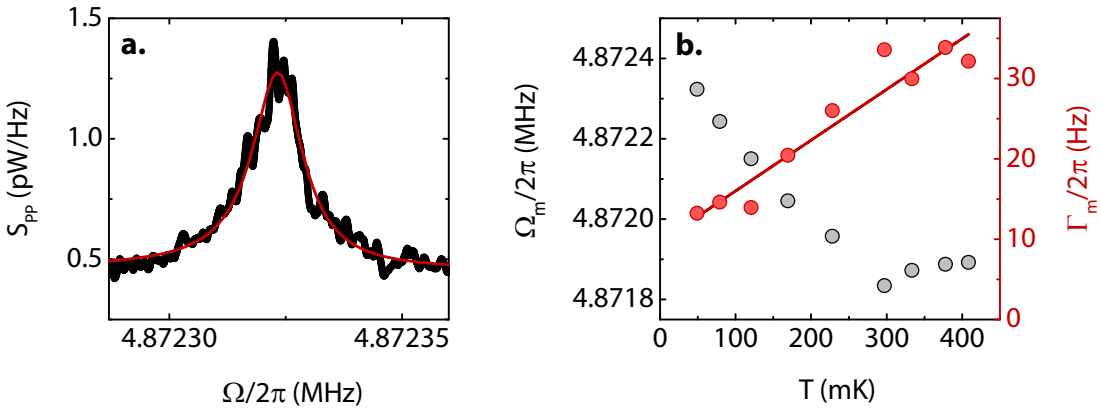

Figure 8.7: **a.** Measured power spectrum of thermal motion of the nanobeam at $T = 50\,\mathrm{mK}$. The red line is a Lorentzian fit to the mechanical response spectrum. **b.** Resonance frequency (black) and linewidth (red, with linear fit) of the fundamental in-plane mode of the nanobeam as a function of temperature.

In Figure 8.7b, resonance frequency and linewidth are plotted as a function of temperature between 50 and 400 mK. We observe an approximately linear temperature dependence of the linewidth, $\Gamma_\mathrm{m}(T) = \Gamma_{\mathrm{m},0} + \gamma\, T$, with $\gamma \approx 66\,\mathrm{Hz/K}$ and an extrapolated linewidth at $T = 0$ of $\Gamma_{\mathrm{m},0}/2\pi \approx 10\,\mathrm{Hz}$. This is consistent with observations reported in literature for pure aluminium nanobeams [52, 53] and Si_3N_4/Nb nanobeams [21]. The linear temperature dependence of $\Gamma_\mathrm{m}(T)$ suggests that coupling of phonons to two-level states (TLS) is the dominating loss mechanism in this type of nanobeam resonator at low temperatures. These TLS can be modeled as a double-well potential whose major damping mechanism is given by tunneling between the potential minima. In a nanobeam resonator, the potential is modulated periodically by the oscillating strain, which couples the TLS to the nanobeam motion. The relaxation rate of the TLS depends on the phonon density and thus on the environment temperature T. As discussed in [21, 52, 53], a T^{-1}-dependence of the damping rate $\Gamma_\mathrm{m}(T)$ is expected for tensile stressed nanobeams. Yet, for a more detailed investigation of the damping of our aluminium nanobeams, ring-down experiments with pulsed excitation would be required, as they allow to separated dissipative and dephasing contributions to the mechanical damping [138].

Regarding the temperature dependence of the resonance frequency, we observe a shift to lower values for increasing temperature. This shift, significantly exceeding the linewidth of the resonance, cannot be attributed to thermal effects, as thermal expansion coefficients vanish at low temperature. The coupling to TLS leads to a temperature-dependent resonance frequency, but the expected frequency shift is one order of magnitude smaller and opposite to our experimental finding (see, e. g., Ref. [21]). A possible explanation for the observed frequency shift could be static charging of the center conductor of the microwave resonator, resulting in a (static) capacitive force between nanobeam and ground plane. With the current sample layout, however, we cannot verify this, as the microwave resonator is not connected galvanically to any DC or microwave line. In future experiments, a design similar to Ref. [139] could allow to apply a voltage or charge bias to the microwave resonator and in this way tune the resonance frequency of the nanobeam as well as increase the electromechanical coupling.

8.4.3 Determination of the electromechanical vacuum coupling

To quantify the electromechanical coupling, we perform frequency noise calibration as described in Sec. 6.3. This data is measured at an elevated temperature of $T = 300\,\mathrm{mK}$ to guarantee the sample to be in thermal equilibrium with its environment. We use the detection scheme illustrated in Fig. 8.6 and modulate the drive tone with a maximum frequency deviation of $\Omega_{\mathrm{dev}}/2\pi = 80\,\mathrm{Hz}$ at $\Omega_{\mathrm{mod}}/2\pi = \Omega_{\mathrm{m}}/2\pi - 100\,\mathrm{Hz}$, i. e. near the mechanical resonance frequency. The measured transmission spectrum, plotted in Fig. 8.8a, shows the calibration peak at Ω_{mod}, resulting from the applied frequency modulation, in addition to the sideband of thermal motion at Ω_{m}, originating from the Stokes and anti-Stokes processes. From the height of this calibration peak, we can determine the transfer function $K(\Omega_{\mathrm{m}}) \approx K(\Omega_{\mathrm{mod}}) = 52\,\mathrm{mW}$ according to Eq. 6.19.

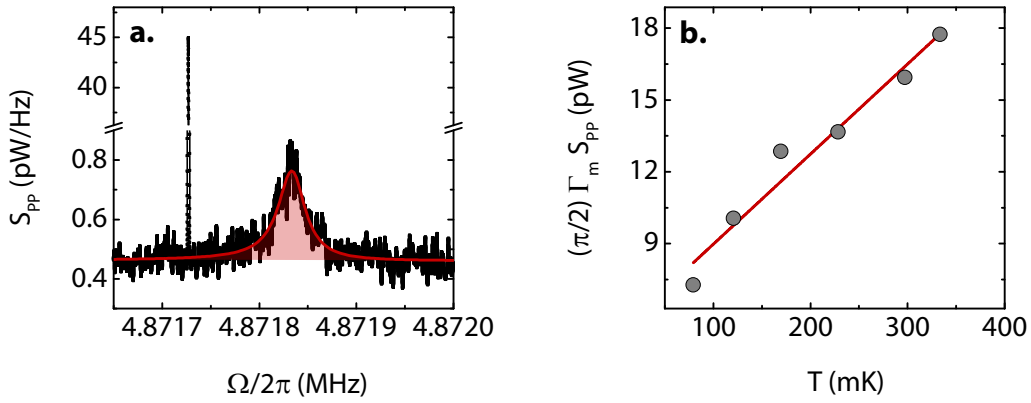

Figure 8.8: **a.** Thermal motion power spectrum of the nanobeam, measured at $T = 300\,\mathrm{mK}$, together with the calibration peak at $\Omega_{\mathrm{mod}}/2\pi = \Omega_{\mathrm{m}}/2\pi - 100\,\mathrm{Hz}$. The red line is a Lorentzian fit to the mechanical response spectrum and the shaded region corresponds to the fitted area under the response spectrum $\mathcal{A} \equiv (\pi/2)\Gamma_{\mathrm{m}} S_{\mathrm{PP}}(\Omega_{\mathrm{m}})$. **b.** Fitted area below the mechanical response spectrum, $\mathcal{A}$, as a function of the cryostat temperature (black circles). The linear fit (red line) allows extracting the coupling g_0 and the backaction-induced temperature offset T_{ba}.

Using Eq. 6.20, the resonance frequency $\Omega_{\mathrm{m}}^{300\,\mathrm{mK}}/2\pi \approx \Omega_{\mathrm{m}}/2\pi = 4.872\,\mathrm{MHz}$, the fitted linewidth at 300 mK, $\Gamma_{\mathrm{m}}^{300\,\mathrm{mK}}/2\pi = 34\,\mathrm{Hz}$, and the thermal phonon number $\bar{n}_{\mathrm{m}}(T = 300\,\mathrm{mK}) = 1282$ (see Eq. 6.17), we calculate the electromechanical vacuum coupling rate $g_0/2\pi = 0.67\,\mathrm{Hz}$.

To experimentally verify the thermalization of the sample and to account for the effects of backaction of cavity photons on the mechanical motion, we exploit the temperature dependence of the mechanical motion spectra. We fit a Lorentzian to all measured spectra and plot the area below the response spectrum $\mathcal{A} = (\pi/2)\Gamma_{\mathrm{m}} S_{\mathrm{PP}}(\Omega_{\mathrm{m}})$ as a function of temperature as shown in Fig. 8.8b. The slope of the fitted straight line in Fig. 8.8b allows to extract the coupling g_0, while the intercept allows to quantify a potential temperature offset caused by backaction effects. To illustrate this, we use Eq. 6.20 and plug in the relation between the thermal phonon number and the sample environment temperature, given by Eq. 6.17. To account for backaction of the microwave drive on the mechanics, we introduce a temperature offset T_{ba}. With this, we obtain

$$\frac{\pi}{2}\Gamma_{\mathrm{m}} S_{\mathrm{PP}}(\Omega_{\mathrm{m}}) = \frac{4\pi k_{\mathrm{B}}}{\hbar \Omega_{\mathrm{m}}^3} g_0^2 K(\Omega_{\mathrm{m}})\,(T + T_{\mathrm{ba}}) \ .$$

Using the transfer function $K(\Omega_\mathrm{m}) = 52\,\mathrm{mW}$, we extract the coupling $g_0/2\pi \approx (0.57 \pm 0.06)\,\mathrm{Hz}$ from the data plotted in Fig. 8.8b. This is in reasonable agreement with the value obtained above. In addition, we find a backaction temperature of $T_\mathrm{ba} \approx 80\,\mathrm{mK}$, caused by the comparatively high drive power used in this measurement [19, 21].

The experimentally determined coupling agrees well with the predicted value $g_0^\mathrm{FEM}/2\pi = 0.90\,\mathrm{Hz}$, which we obtained from a simple finite element model (see Sec. 8.2). Besides, the measured coupling g_0 is consistent with values reported for similar samples [18, 21, 54].

8.4.4 Sideband cooling of mechanical motion

Up to now, we have driven the microwave cavity at its resonance frequency ($\omega_\mathrm{d} = \omega_\mathrm{c}$), which allows to read out the mechanical motion of the nanobeam without backaction on its motion. Employing a red- or blue-detuned drive tone, however, the nanobeam motion can be damped or amplified, resulting in a broadening/narrowing of the linewidth Γ_m and a reduction/increase of the average phonon number $\bar{n}_\mathrm{m}$. At the Walther-Meißner-Institut, these effects have already been demonstrated with a similar device in which a Si_3N_4/Nb bilayer nanobeam is capacitively coupled to a superconducting CPW microwave resonator [21].

Here, we demonstrate that these effects can be reproduced with the present all-aluminium sample. This opens the path for the integration of, e. g., superconducting qubits for quantum experiments with a circuit nano-electromechanical device.

In this section, we demonstrate sideband cooling of the nanobeam motion from the initial thermal occupation number $\bar{n}_\mathrm{m} = 171$ at $T = 40\,\mathrm{mK}$ down to $\bar{n}_\mathrm{m}^\mathrm{min} \approx 10$. We drive the microwave resonator ideally red-detuned ($\Delta = -\Omega_\mathrm{m}$) and monitor the sidebands of mechanical motion in the detection scheme depicted in Fig. 8.6.

Figure 8.9a shows the measured power spectrum $S_\mathrm{PP}(\Omega)$ for three different drive power values $P_\mathrm{source} = 32, 50, 79\,\mathrm{mW}$. For increasing drive power, we observe a decrease of the area $\mathcal{A}$ below the response curve. As $\mathcal{A} \propto \bar{n}_\mathrm{m}$, this indicates a reduction of the phonon number and thus a cooling of the mechanical mode. In addition, the spectrum broadens as expected from the discussion in Sec. 6.1.

We extract the effective linewidth Γ_eff by fitting a Lorentzian to the measured response spectra for various driving strengths between $P_\mathrm{source} = 1.8\,\mathrm{mW}$ and 106 mW, as shown in Fig. 8.9b, and observe the expected linear drive power dependence. Fitting Eq. 6.23 to the measured effective linewidth as a function of the microwave power P_source allows extracting the low-power limit of the mechanical linewidth $\Gamma_\mathrm{m}/2\pi \approx 12.2\,\mathrm{Hz}$ and the attenuation of the input microwave line $\mathrm{Att} \approx 1/331\,\mathrm{k}$ (corresponding to 55 dB). Here, we have used the fact that $\bar{n}_\mathrm{c}$ and the microwave source output power P_source are related via Eqs. 6.12 and 6.13. Therefore, Att can be determined from the slope of the linear fit in Fig. 8.9b using the coupling rate g_0 determined in the previous section.

Having calculated the attenuation along the input microwave line, we can determine the intra-cavity photon number $\bar{n}_\mathrm{c}$ from P_source, as the upper horizontal axis of Fig. 8.9b indicates.

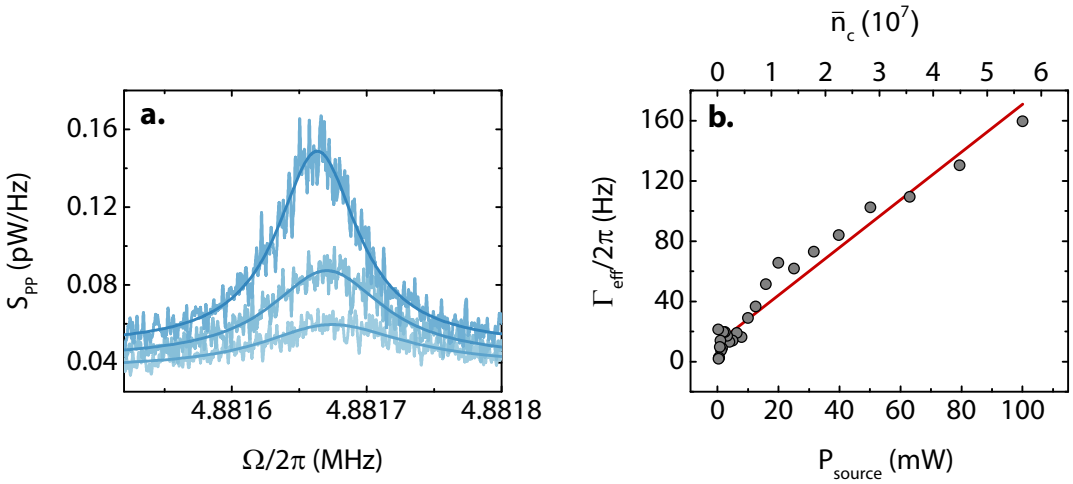

Figure 8.9: a. Measured power spectra of mechanical motion (with Lorentzian fit) for an ideally red-detuned drive and three different cavity photon numbers (corresponding to $P_{\mathrm{source}} = 32, 50$ and $79\,\mathrm{mW}$, dark to light blue). **b.** Effective linewidth of the mechanical resonance as a function of microwave drive power or cavity photon number, respectively.

Figure 8.10 shows the extracted phonon number $\bar{n}_{\mathrm{m}}$ as a function of the cavity photon number $\bar{n}_{\mathrm{c}}$ together with the theoretical prediction given by Eq. 6.22. To determine $\bar{n}_{\mathrm{m}}$ from the measured power spectra of mechanical motion, we use Eq. 6.21.[3]

Starting at a thermal phonon number of $\bar{n}_{\mathrm{m}}^{\mathrm{th}} \approx 171$, we are able to cool down the fundamental in-plane mode of the nanobeam to $\bar{n}_{\mathrm{m}}^{\mathrm{min}} \approx 10$, corresponding to an effective mode temperature of $T_{\mathrm{m}}^{\mathrm{min}} \approx 2.3\,\mathrm{mK}$.

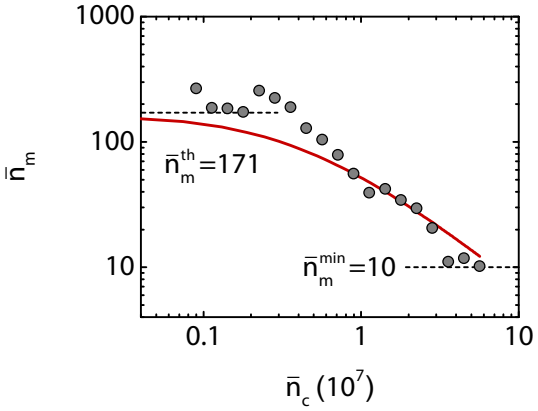

Figure 8.10: Phonon number $\bar{n}_{\mathrm{m}}$ as a function of the cavity photon number $\bar{n}_{\mathrm{c}}$ for an ideally red-detuned drive. The black circles indicate the experimental data, the red line shows the theoretical prediction, given by Eq. 6.22. At the maximum available drive power, we reach a minimum phonon number of 10. The phonon number in thermal equilibrium is $\bar{n}_{\mathrm{m}}^{\mathrm{th}} = 171$.

[3] Technically, the transfer function $K(\Omega)$ is proportional to signal power P_{Sig} at the mixer, which in turn scales linearly with the drive power P_{d} at the sample input [21]. The transfer function thus has to be measured for a single drive power value only, even if the drive is varied during the experiment as shown e. g. in Fig. 8.9. Here, however, large cavity photon numbers are required so that the signal power at the sample output reaches the compression point of the cryogenic amplifier, where the amplification drops significantly. For high drive power, the transfer function is therefore reduced. To account for this, we determine the transfer function for each applied drive power separately using frequency noise calibration. With this, we determine $\bar{n}_{\mathrm{m}}$ from the measured power spectra.

Whereas in previous sideband cooling experiments with a Si_3N_4/Nb sample at WMI [21], the phonon number saturated at high cavity photon numbers ($\bar{n}_c \gtrsim 10^7$) due to sideband noise from the microwave source, this technical issue is not present here. The reason is that thanks to the higher mechanical resonance frequency, the sideband noise (relative to the output power) at the offset frequency $\Omega_m/2\pi$ is significantly reduced [140] compared to Ref. [21]. Instead, our minimum attainable phonon number is limited by the available microwave power $P_{source} \lesssim 100\,\mathrm{mW}$, as the electromechanical coupling of our sample is somewhat smaller than that of the mentioned Si_3N_4/Nb sample [21]. Assuming infinite available drive power, the limit $\bar{n}_m^{min}$ would be given by the nonlinearity of the microwave resonator which starts shifting its eigenfrequency at a cavity photon number of approximately 6×10^7.

The fundamental lower limit of the phonon number for the presented system is $\bar{n}_m^{min} = 0.001$ (see Eq. 6.25). The noise photon number in the cavity is approximately $\bar{n}_c^{noise} \approx 0.2$, where we have taken into account the Johnson noise inside the microwave circuitry and the thermal occupation of the microwave resonator. As $\bar{n}_c^{noise} \ll 1$, we can exclude excitation transfer from the microwave resonator to the nanobeam when driving on the red sideband.

8.4.5 Electromechanically induced transparency

In this section, we investigate Sample #6 via two-tone spectroscopy. In particular, we focus on the effect of electromechanically induced transparency (EMIT) which is similar to optomechanically induced transparency [141–143] and has first been demonstrated in [20].

We apply a strong, continuous red-detuned drive tone to the sample while probing the transmission through the sample around the cavity resonance with a weak probe tone. In this configuration, the drive photons scatter with thermal phonons and generate anti-Stokes photons at $\omega_d + \Omega_m$ which interfere destructively with the probe tone, preventing the probe tone to be coupled into the microwave cavity. Thus, the photon-phonon interaction generates a narrow microwave transmission window around the frequency $\omega_d + \Omega_m$.

To investigate EMIT experimentally, we employ the setup depicted in Fig. 8.11. We apply a strong drive tone at $\omega_d \approx \omega_c - \Omega_m$ and simultaneously measure the microwave cavity transmission spectrum using a weak probe tone with frequency $\omega_p/2\pi$.

In Fig. 8.12a, the resulting transmission spectrum is plotted for a drive power of $P_d = 43\,\mathrm{nW}$ ($-44\,\mathrm{dBm}$) and a probe power of $P_d = 0.3\,\mathrm{pW}$ ($-95\,\mathrm{dBm}$). Within the broad cavity absorption dip, we observe a sharp transmission peak at $\omega_d + \Omega_m$. The height of the transmission peak T_0 as well as its linewidth depend on the drive power P_d, as Fig. 8.12b illustrates. Here, the transmission window around $\omega_d + \Omega_m$ is plotted for various drive power values $P_d \in \{1.7, 3.8, 8.5, 19, 43, 96\}\,\mathrm{nW}$. We observe an increase of the transmission window linewidth with increasing drive power, which can be unterstood in terms of linewidth broadening of the nanobeam resonance for a red-detuned drive as discussed in Sec. 6.1.

Additionally, the transmission maximum increases with the drive power. As derived in Sec. 6.5, we expect the transmission T_0 to converge against unity for a cooperativity $C \gg 1$. Comparing the measured maximum transmission T_0 as a function of the cavity photon number to the theory curve Eq. 6.26 shows excellent agreement, as Fig. 8.13a demonstrates. Note that there are no free parameters here, as all relevant quantities – the

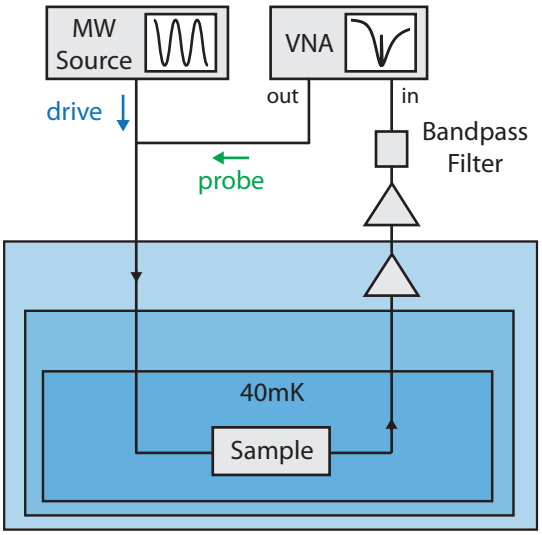

Figure 8.11: Experimental setup used to investigate electromechanically induced transparency. Similar to Fig. 8.6, the cryogenic part of the microwave circuitry has been simplified for reasons of clarity.

vacuum coupling g_0, the microwave attenuation Att and the damping rates of mechanics and microwave resonator, Γ_m, κ_in and κ_ex – have been determined independently before.

In Fig. 8.13b, the $\bar{n}_\mathrm{c}$-dependence of the center frequency and linewidth of the transmission window is plotted. According to Eqs. 6.4 and 6.5, we expect an undeturbed frequency and a linewidth broadening for an ideally red-detuned drive. The latter can be reproduced well in the EMIT measurement. The observed resonance frequency shift is presumably due to a slight deviation of the detuning Δ from the optimally red-detuned case $\Delta = \omega_\mathrm{c} - \Omega_\mathrm{m}$.

8.5 Steps towards circuit electromechanics in the quantum regime

One of the driving forces in cavity opto/electromechanics is the perspective of studying quantum effects in macro/mesoscopic mechanical systems. There are, however, several prerequisites that have to be fulfilled to reach the quantum regime with circuit electromechanical systems:

Ground state cooling of the mechanical resonator: Even at mK temperatures, the thermal population of a mechanical resonator at MHz frequencies significantly exceeds unity. To investigate single phonons in such a system, it is necessary to cool the resonator to the ground state. This can be done by sideband cooling with a red-detuned drive, as shown above, or with other, more elaborate cooling schemes [144–147]. Meanwhile, ground state cooling of MHz mechanical resonators has been demonstrated by several groups [24, 25, 122].

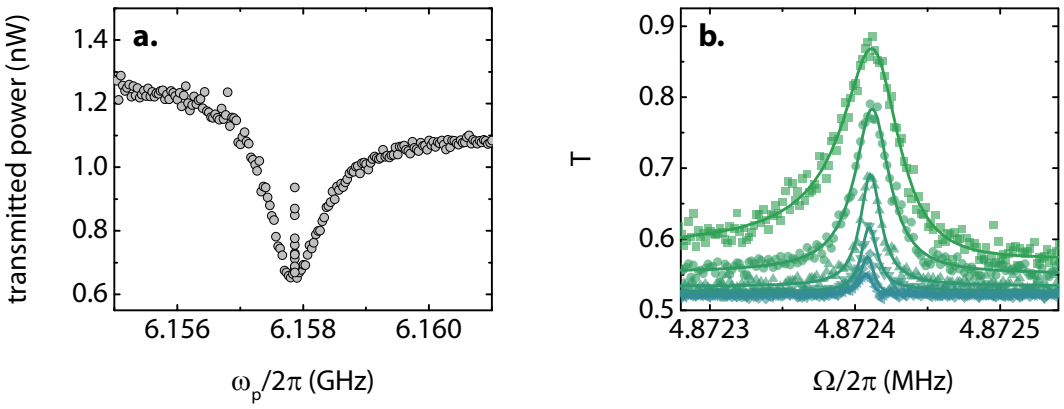

Figure 8.12: **a.** Two-tone spectroscopy of Sample #6 with a strong red-detuned drive tone ($P_\mathrm{d} = 43\,\mathrm{nW}$ [$-44\,\mathrm{dBm}$]). The interaction between electromechanically generated anti-Stokes photons and the probe tone leads to a transmission window at $\omega_\mathrm{p} = \omega_\mathrm{d} + \Omega_\mathrm{m}$ (*electromechanically induced transparency*). **b.** Transmission window for various cavity photon numbers $\bar{n}_\mathrm{c} \in \{0.3, 0.7, 1.7, 3.7, 8.4, 18.8\} \times 10^6$ (blue to green). The lines are Lorentzian fits to the experimental data.

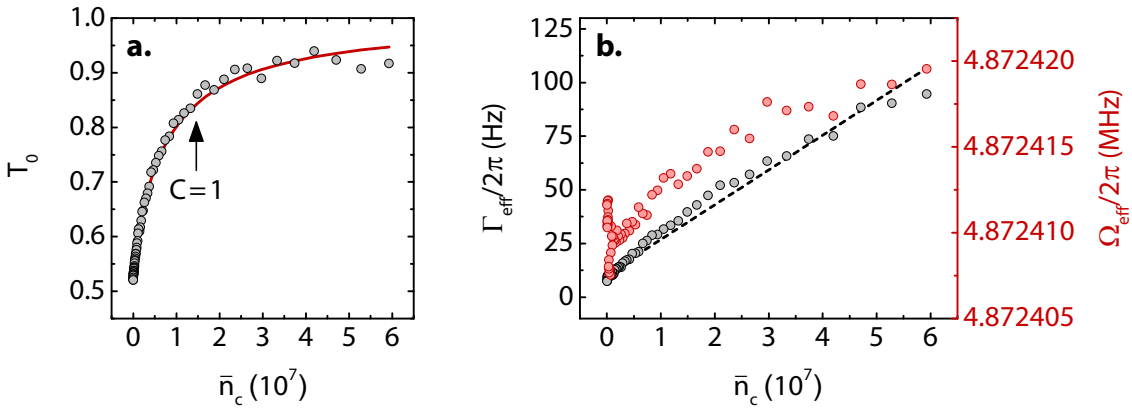

Figure 8.13: **a.** Maximum of the transmission window, T_0, as a function of the cavity photon number $\bar{n}_\mathrm{c}$. The red line is a parameter-free curve, showing the $\bar{n}_\mathrm{c}$-dependence of the transmission T_0 according to Eq. 6.26. **b.** Effective linewidth (black, with linear fit) and resonance frequency (red) as a function of $\bar{n}_\mathrm{c}$. The drive tone is ideally red-detuned ($\Delta = -\Omega_\mathrm{m}$), the probe power is fixed at $P_\mathrm{d} = 0.3\,\mathrm{pW}$ ($-95\,\mathrm{dBm}$).

Preparation of non-classical mechanical or entangled electromechanical states: Driving the microwave resonator on the blue sideband generates entangled photon-phonon pairs and thus allows entangling the states of the mechanical and the microwave resonator [26, 148]. This can be useful for applications in quantum information processing as well as for experiments on fundamental quantum mechanics. Besides, it has been demonstrated recently that a micromechanical resonator can be prepared in a squeezed vacuum state, where one of the quadratures falls below the standard quantum limit [24, 25]. Similar squeezed states can be employed for testing quantum mechanics in macro/mesoscopic systems.

Strong single photon coupling: One of the drawbacks of circuit nano-electromechanical systems is the typically small vacuum coupling. While, e.g., superconducting

qubits can easily be coupled to a CPW microwave resonator with the vacuum coupling exceeding the damping rates of both resonator and qubit [149, 150], this turns out to be complicated for circuit nano-electromechanical systems. O'Connell *et al.* have coupled a piezoelectric sandwich-like resonator to a superconducting qubit, resulting in a coupling strength of $g/2\pi = 62\,\mathrm{MHz}$ [22]. The mechanical quality factor, however, is rather small, which prevents operation in the resolved sideband regime. Apart from piezoelectric mechanical resonators, the highest vacuum coupling strengths reported are in the order of several hundred Hz [20, 26], which is far below the damping rate of the microwave resonator (several hundred kHz). When biasing the microwave cavity with a high average photon number $\bar{n}_\mathrm{c} \gg 1$, however, the effective coupling rate $g = g_0\sqrt{\bar{n}_\mathrm{c}}$ can exceed both the mechanical and microwave damping rate. In the strong coupling regime ($g \gtrsim \Gamma_\mathrm{m}, \kappa$), photons can coherently be converted to phonons, giving rise to, e. g., normal mode splitting or Rabi oscillations [20, 151].

For quantum experiments with single photons/phonons, however, strong *single photon* coupling is required. This means that the vacuum coupling g_0 needs to exceed the damping rates of both microwave and mechanical resonator, $g_0 \gtrsim \Gamma_\mathrm{m}, \kappa$. Strong single photon coupling would allow a coherent transfer of a single photon to a phonon and vice versa within the relevant decay times. Currently, there are no systems satisfying this condition.

Generation of single photonic or phononic excitations: A possible approach for generating single phonons in a circuit electromechanical system is the integration of a qubit into the microwave circuit, serving as a single photon source, and a coherent transfer of this excitation into the mechanical system via a microwave resonator (see, e. g., Ref. [22]). Such a device would strongly extend coupled qubit-resonator systems (see, e. g., Refs. [149, 150, 152]) by a mechanical degree of freedom.

Within the scope of this thesis, first steps in overcoming these challenges have been taken. To increase the electromechanical coupling beyond the current state of the art, we couple a nanobeam to a microwave resonator via a SQUID (superconducting quantum interference device), acting as a tunable inductor. More precisely, the mechanical motion of the nanobeam modulates the inductance of the SQUID and thus changes the resonance frequency of the microwave resonator. The vacuum coupling of this inductively coupled electromechanical hybrid system is expected to reach the mid kHz regime, significantly exceeding the coupling rates of current circuit electromechanical systems. Additionally, the inductive coupling can be tuned via an externally applied magnetic field, allowing to switch the coupling on and off faster than the relevant decay rates of the system.

Second, we have started to integrate a transmon qubit into a circuit electromechanical system consisting of a microwave resonator and a nanobeam. The qubit can serve as a single photon source for future quantum experiments. Besides, this three-body system could open the path for the preparation and investigation of novel quantum states of phonons, photons and qubit excitations.

8.5.1 Inductive coupling between a microwave resonator and a nanobeam

In this section, we estimate the inductive coupling between a nanobeam resonator and a superconducting CPW microwave resonator, mediated by a SQUID, and present first results towards its experimental realization. This work has been pursued together with Friedrich Wulschner [153] and, in particular, Philip Schmidt which I supervised during his master's thesis [40]. Here, we summarize the modeling and the experimental results. For a more detailed description, please see Ref. [40]. Related theoretical and experimental work can be found in Refs. [154–157].

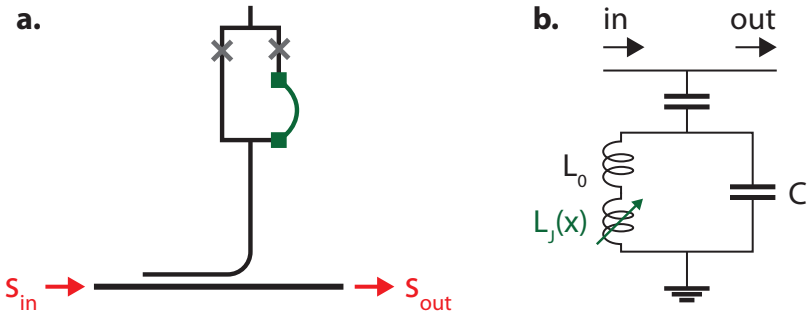

Figure 8.14: **a.** Schematic illustration and **b.** equivalent circuit of an inductively coupled circuit electromechanical hybrid system, in which a mechanical resonator is coupled to a microwave resonator via a dc-SQUID.

We investigate the hybrid system sketched in Fig. 8.14, where a coplanar waveguide, capacitively coupled to a transmission line, is connected to ground via a SQUID, forming a $\lambda/4$ microwave resonator (cf. Ref. [158]). The Josephson inductance L_J of the SQUID adds to the inductance of the bare microwave resonator, L_0, so that the resonance frequency of the microwave resonator is given by

$$\omega_\mathrm{c} = \frac{1}{\sqrt{(L_0 + L_\mathrm{J})C}} \,, \tag{8.1}$$

where C is the effective capacitance of the resonator.

The inductance of the dc-SQUID depends on the applied magnetic flux through the SQUID loop ϕ_ext according to [153]

$$L_J = \frac{\phi_0}{2\pi I_\Sigma |\cos(\pi\phi_\mathrm{ext}/\phi_0)|} \,.$$

Here, $\phi_0 = h/2e$ is the magnetic flux quantum and I_Σ denotes the maximum critical current over both Josephson junctions. Note that L_J can take values between $L_\mathrm{J}^\mathrm{min} = \phi_0/2\pi I_\Sigma$ and infinity, depending on ϕ_ext, so that the resonance frequency of the microwave resonator, given by Eq. 8.1, can be tuned from a maximum value $\omega_\mathrm{c}^\mathrm{max} = 1/\sqrt{(L_0 + L_\mathrm{J}^\mathrm{min})C}$ down to 0.

We introduce a mechanical degree of freedom in this tunable microwave resonator by replacing one of the SQUID arms by a nanobeam resonator as illustrated in Fig. 8.14a.

Thus, the flux through the SQUID loop depends on the displacement of the nanobeam x_0 via

$$\phi(x) = \phi_\mathrm{p} + l_\mathrm{eff} B_\mathrm{ext} x_0 \ ,$$

where ϕ_p is the static flux through the SQUID loop and B_ext denotes the applied magnetic field. The effective length $l_\mathrm{eff} \approx 0.5l$ accounts for the shape of the displaced nanobeam (cf. App. C).

In this system, the electromechanical coupling is given by

$$G = \frac{\partial \omega_\mathrm{c}}{\partial x} = l_\mathrm{eff} B_\mathrm{ext} \frac{\partial \omega_\mathrm{c}}{\partial \phi} \ . \tag{8.2}$$

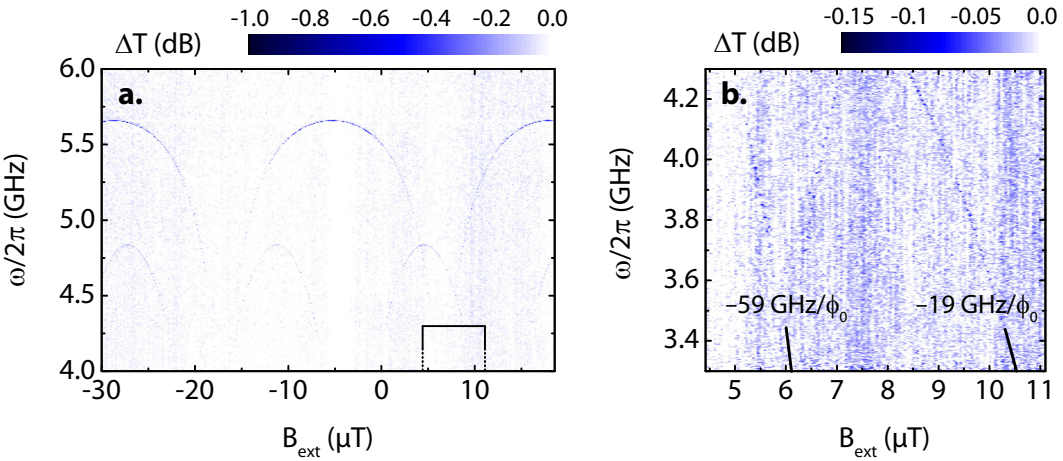

Figure 8.15: Transmission spectrum of the inductively coupled electromechanics sample, containing two tunable microwave resonators, as a function of the external magnetic field. A frequency-dependent background has been subtracted. **a.** Overview spectrum over a broad magnetic field range. **b.** Detailed view around $B_\mathrm{ext} \approx 8\,\mu\mathrm{T}$. At 3.3 GHz, the extracted slope of the resonance frequency versus magnetic field corresponds to $\partial\omega_{\mathrm{c},1}/\partial\phi \approx -2\pi \times 59\,\mathrm{GHz}/\phi_0$ and $\partial\omega_{\mathrm{c},2}/\partial\phi \approx -2\pi \times 19\,\mathrm{GHz}/\phi_0$, respectively.

In a first step, a tunable microwave resonator, consisting of a niobium CPW and an aluminium SQUID with Al/AlOx/Al Josephson junctions, has been fabricated, into which a $l = 50\,\mu\mathrm{m}$ long Si_3N_4/Al nanobeam is integrated. The resonance frequency of the fundamental in-plane mode of the nanobeam is $\Omega_\mathrm{m}^\mathrm{RT}/2\pi = 3.635\,\mathrm{MHz}$ at room temperature. At mK temperatures, we expect $\Omega_\mathrm{m}/2\pi \approx 4.7\,\mathrm{MHz}$ due to the strong thermal contraction of the aluminium film on top of the Si_3N_4 nanobeam [40]. Although the experimental characterization is still in progress, first results already show that the derivative $\partial\omega_\mathrm{c}/\partial\phi$ can reach values up to $2\pi \times 59\,\mathrm{GHz}/\phi_0$ (see Fig. 8.15). With an experimentally determined maximum applicable magnetic field[4] $B_\mathrm{ext}^\mathrm{max} \approx 1\,\mathrm{mT}$, Eq. 8.2 predicts an electromechanical coupling of $G/2\pi = 0.69\,\mathrm{GHz/nm}$. Using the estimated zero-point motion of the nanobeam $x_\mathrm{zpm} \approx 19\,\mathrm{fm}$, we expect the vacuum coupling rate $g_0/2\pi \approx 13\,\mathrm{kHz}$.

To compare the projected coupling to the relevant decay rates of the system, we assume damping rates of $\kappa/2\pi \simeq 2\,\mathrm{MHz}$ for the microwave resonator and $\Gamma_\mathrm{m}/2\pi \simeq 30\,\mathrm{Hz}$ for the

[4]The maximum allowed magnetic field is limited by the critical field of the superconducting thin film and is therefore lower than the critical field of bulk aluminium. Experimentally, we find that at 2.2 mT the superconductivity in the microwave resonator breaks down. We therefore intend to apply a maximum magnetic field $B_\mathrm{ext}^\mathrm{max} \approx 1\,\mathrm{mT}$, which is well below the breakdown field.

mechanical resonator. Hence, we obtain $g_0^2/\Gamma_m\kappa \simeq 2.8$, i. e. we expect to reach strong single-photon cooperativity with such a device.

8.5.2 Coupling of a transmon qubit to a circuit electromechanical hybrid system

As mentioned above, a prerequisite for quantum experiments in a circuit electromechanical hybrid system is the ability of generating single excitations in the microwave and/or mechanical resonator. To this end, we couple a transmon qubit to a hybrid system consisting of an aluminium CPW microwave resonator and an aluminium nanobeam, similar to Sample #6.

The fabrication of such an integrated device, however, is challenging and requires a thorough optimization of the process parameters. Within Daniel Schwienbacher's master's thesis [136], a fabrication process was developed allowing integration of a tensile-stressed aluminium nanobeam into an aluminium CPW microwave resonator which is strongly coupled to a transmon qubit. First experiments show that the qubit parameters (in particular its plasma frequency, anharmonicity and coupling to the microwave resonator) can be controlled in the desired regime with the prospect of using the qubit as a single photon source in future experiments.

For a detailed description of the fabrication process and first experimental results, please see Ref. [136].

8.5.3 Three-body interactions in an electromechanical resonator-qubit hybrid system

In this section, we present the proposal of a novel three-body hybrid system, consisting of a transmon qubit, a microwave resonator and a mechanical resonator. This project, led by Mehdi Abdi (TU Munich), provides some interesting prospects of circuit electromechanics in the quantum regime, featuring, e. g., a three-body polariton-mechanical mode and a strong nonlinear transmon-mechanical interaction. The results have been published in Ref. [147].

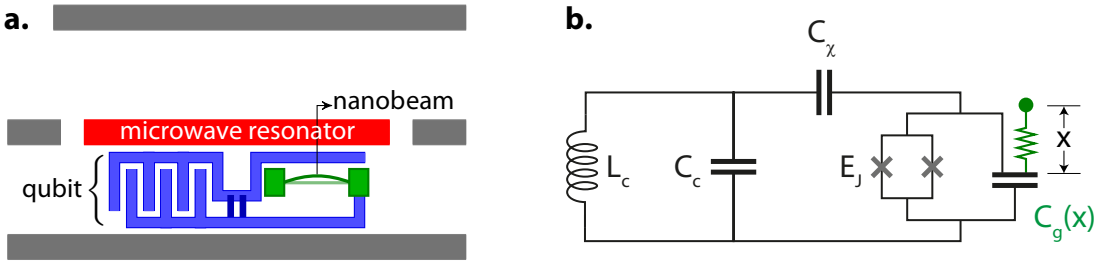

Figure 8.16: **a.** Schematic layout of the proposed three-body hybrid system, consisting of a transmon qubit, a CPW microwave resonator and a nanobeam resonator. **b.** Equivalent circuit diagram.

We investigate the qubit-resonator-nanobeam hybrid system illustrated in Fig. 8.16. The transmon qubit is capacitively coupled to the microwave resonator, with the coupling χ exceeding the damping rates of both qubit and cavity, γ_{tr} and κ, respectively. We

propose to integrate a nanobeam into the shunt capacitance of the transmon and forms a displacement-dependent capacitance $C_\mathrm{g}(x)$, where x denotes the displacement of the mechanical resonator.

A possible realization of the proposed hybrid system uses an $l = 100\,\mu\mathrm{m}$ long aluminium nanobeam with a cross-section of $w \times t = 120 \times 100\,\mathrm{nm}^2$ and a distance of 10 nm to the neighboring aluminium plane. For this geometry, the displacement-dependent change of the capacitance between nanobeam and counterelectrode can reach $\partial C_\mathrm{g}/\partial x \simeq 0.9\,\mathrm{fF/nm}$. The total capacitance of the transmon is given by $C_\mathrm{tr}(x) = C_0 + C_\mathrm{g}(x)$ with the constant shunt capacitance $C_0 \gg C_\mathrm{g}$. The coupling between transmon qubit and nanobeam resonator can be written as

$$G = \frac{\partial \omega_\mathrm{tr}}{\partial x} = \frac{\partial \omega_\mathrm{tr}}{\partial C_\mathrm{g}} \frac{\partial C_\mathrm{g}}{\partial x} \,,$$

where $\omega_\mathrm{tr}/2\pi$ is the plasma frequency of the transmon qubit. As $\omega_\mathrm{tr} \propto C_t^{-1/2}$ [153], the derivative is $\partial\omega_\mathrm{tr}/\partial C_\mathrm{g} = \omega_\mathrm{tr}/2C_t$. Assuming a qubit frequency of $\omega_\mathrm{tr}/2\pi \simeq 10\,\mathrm{GHz}$ and a typical shunt capacitance of $C_0 \simeq 60\,\mathrm{fF}$, we estimate an electromechanical vacuum coupling between qubit and nanobeam of $g_0/2\pi \simeq 2.3\,\mathrm{kHz}$. The effective coupling is given by $g_\mathrm{t} = g_0\sqrt{2\zeta}$ with $\zeta = E_\mathrm{J}/E_\mathrm{C}$ (E_J: Josehpson energy, E_C: charging energy of the transmon qubit).

In addition, we assume a strong capacitive coupling χ between transmon qubit and microwave resonator, dominating the dephasing rates of both qubit and cavity: $\chi \gg \gamma_\mathrm{tr}, \kappa$. In this regime, the qubit-resonator system can be described in terms of dressed state excitations, so-called *polaritons*. Here, the polariton-mechanical mode interaction cannot be linearized, in contrast to standard cavity opto/electromechanical systems. This characteristic allows new prospects for the engineering of quantum states of a mechanical resonator via microwave signals.

First, the presented three-body hybrid system enables ground state cooling of the mechanical resonator via sidebands similar to a standard cavity opto/electromechanical system, which is a prerequisite for quantum experiments. The proposed cooling scheme is based on a large cavity-transmon detuning. In this case, the transmon-like polariton strongly interacts with the mechanical mode (at a rate close to g_t), while the photon-like polariton is nearly decoupled from the mechanical mode. The minimum phonon number that can be achieved with this cooling scheme is determined by the total dephasing time T_2^* of the qubit. For $\Omega_\mathrm{m} T_2^* > 1$, the ground state can be reached (for details see Ref. [147]).

In addition, the system allows the preparation of mechanical Fock states via the strong interaction between polaritons and the mechanical resonator. In order to generate a single-phonon Fock state, the mechanical resonator has to be cooled down to the ground state first, using e. g. sideband cooling as mentioned above. Then, a single polaritonic excitation is created in the cavity-transmon system. Here, we excite the polariton with the higher frequency (ω_+) by applying a properly shaped microwave pulse. In the next step, the transmon is tuned so that the eigenfrequency difference of the polaritons matches the mechanical resonance frequency, $\omega_+ - \omega_- = \Omega_\mathrm{m}$. After an evolution time of $\tau_1 = \pi/2\tilde{g}$ (where $\tilde{g}$ is the effective coupling rate, see Ref. [147]), the higher-energy polariton has been converted to a lower-energy polariton and a phonon. Using another microwave pulse, the lower-energy polariton is annihilated and the system ends up in a single-phonon Fock state. This scheme can easily be repeated to prepare higher number states.

Lastly, a protocol is proposed which allows the generation of tripartite hybrid entanglement between qubit, microwave cavity and mechanical resonator. To describe this protocol, we use the original picture of qubit, cavity and mechanical resonator states instead of dressed states. Again, the mechanical resonator has to be in its ground state at the beginning of the protocol. We apply a $[\pi/2]_{0\leftrightarrow1}$ pulse to the qubit to prepare it in a symmetric superposition of ground state and first excited state. Next, we let the qubit interact with the mechanical resonator for half of the mechanical oscillation period. This interaction leads to a conditional displacement of the state of the mechanics in phase space, depending on the qubit excitation state. In realistic devices, the nanobeam-qubit coupling g_t is significantly smaller than the mechanical resonance frequency Ω_m, so that the displacement of the mechanical resonator is too small to be detected. We can solve this issue by repeating the nanobeam-qubit interaction step several times, each time followed by application of a $[\pi]_{0\leftrightarrow1}$ pulse to the qubit. After N_p steps, the system is in the state[5] $(|0\rangle_\mathrm{t}|0\rangle_\mathrm{c}|\beta\rangle_\mathrm{m}+|1\rangle_\mathrm{t}|0\rangle_\mathrm{c}|-\beta\rangle_\mathrm{m})/\sqrt{2}$ with $\beta=(N_\mathrm{p}+1)g_\mathrm{t}/\Omega_\mathrm{m}$. Here, $|\cdot\rangle_\mathrm{t,c,m}$ denotes the state of the transmon (t), cavity (c) or mechanical resonator (m), respectively. By application of a $[\pi/2]_{0\leftrightarrow1}$ pulse to the qubit, the mechanical resonator can be prepared in a superposition of odd and even cat states, $(|0\rangle_\mathrm{t}|0\rangle_\mathrm{c}|\Psi_+\rangle_\mathrm{m}+|1\rangle_\mathrm{t}|0\rangle_\mathrm{c}|\Psi_-\rangle_\mathrm{m})/2$, where $|\Psi_\pm\rangle\propto(|\beta\rangle\pm|-\beta\rangle)$ is an even-odd cat state. Last, we generate a single photon in the microwave cavity. To this end, we apply a $[\pi]_{1\leftrightarrow2}$ pulse to the transmon and thus flip the qubit from the first to the second excited state. Then we tune the transmon in resonance with the cavity for a time span $\pi/2\sqrt{2}\chi$, so that the second qubit excitation decays by emitting a photon into the cavity. The resulting state of the three-body system is

$$|\Psi_\mathrm{tcm}\rangle=\frac{1}{2}\left(|0\rangle_\mathrm{t}|0\rangle_\mathrm{c}|\Psi_+\rangle_\mathrm{m}+|1\rangle_\mathrm{t}|1\rangle_\mathrm{c}|\Psi_-\rangle_\mathrm{m}\right)\ ,$$

which is a hybrid Greenberger-Horne-Zeilinger (GHZ) state [159].

To account for energy relaxation and dephasing of qubit, mechanical resonator and cavity, the protocols described above are performed numerically by solving the corresponding master equation. These calculations show that for a realistic set of parameters, the single-phonon Fock state as well as the GHZ state can be realized with high fidelity ($\sim 80\%$).[6] Thus we are confident that an experimental implementation of the proposed three-body hybrid system will allow for the realization of the protocols described above and thus provide a tool for quantum state engineering in circuit electromechanics.

8.6 Summary

We have demonstrated the experimental realization of an all-aluminium circuit nano-electromechanical hybrid device consisting of a superconducting CPW microwave resonator into which a tensile-stressed nanobeam resonator is integrated. We observed a mechanical quality factor of 369 k at 50 mK, at a resonance frequency of 4.87 MHz. Using frequency noise calibration and sideband spectroscopy of the thermal nanobeam motion, we determined the electromechanical vacuum coupling rate $g_0/2\pi=0.67$ Hz, which is corroborated by finite element modeling. We demonstrated sideband cooling of the nanobeam motion to

[5] Here, we neglect an irrelevant global phase factor.

[6] For a detailed list of parameters and for the numerical results, please see Ref. [147].

approximately 10 phonons, limited by the available microwave drive power. Besides, we investigated the device with two-tone spectroscopy and showed electromechanically induced transparency, an interference effect between electromechanically generated cavity photons and a weak probe tone. With this, we demonstrated the functionality of the presented circuit electromechanical device.

The all-aluminium architecture employed here provides the basis for future, more complex hybrid devices, combining e. g. a transmon qubit with a nanobeam resonator. This would allow for state preparation and transfer experiments with single photonic/phononic excitations, which are key requirements for quantum information processing. Moreover, a three-body hybrid system consisting of a qubit, a microwave resonator and a nanobeam could open new routes in quantum state engineering due to the expected strong nonlinear polariton-mechanical interaction, which cannot be realized in current cavity opto/electromechanical systems.

Chapter 9

Summary and Outlook

In this thesis, we have investigated nanomechanical resonators integrated in hybrid systems. We have used doubly-clamped nanobeam resonators fabricated from a tensile stressed silicon nitride or aluminium thin film, characterized them and integrated them into magnetomechanical and circuit electromechanical hybrid devices. The presented results can be important for sensing applications and material studies as well as for cavity optomechanical-like experiments and mechanics in the quantum regime.

Based on former work at the Walther-Meißner-Institut and at the chair of Prof. J. Kotthaus (LMU Munich), we have developed processes for the fabrication of various hybrid devices. By optimizing and adapting the individual fabrication steps – electron beam lithography, thin film deposition, lift-off, dry and wet etching techniques and critical point drying – to the respective demands, we have established the processes for the fabrication of magnetomechanical and circuit electromechanical hybrid systems.

In the first part of this thesis, we demonstrated the fabrication and characterization of high-Q nanobeam resonators made from a tensile stressed Si_3N_4 or aluminium film. We determined the two most relevant material parameters, prestress and Young's modulus, which are consistent with literature values. With these results, we developed the basis for the integration of high-Q nanobeam resonators into hybrid devices. For the characterization measurements, we have designed and installed an optical free space laser interferometer into which a microscope is integrated. This setup allows for a fast and easy investigation of the motion of nanomechanical resonators and is also useful for the pre-characterization of electro- or magnetomechanical hybrid devices.

In a second step, we extended our analysis to nanobeams consisting of a stack of two or more layers. The combination of different materials in a nanomechanical beam allows tailoring the system's material properties to meet particular experimental requirements. Besides, multilayer nanobeams allow to combine excellent mechanical properties with efficient coupling to other degrees of freedom of e. g. optical cavities, microwave circuits or magnetic/multiferroic materials. Therefore multilayer nanobeams play a vital role for the realization of nanomechanical hybrid devices. We presented a comprehensive theoretical analysis of the mechanics of multilayer nanobeams. Taking the inhomogenity of a multilayer nanobeam's cross-section into account, we derived the equation of motion describing the vibrational in-plane and out-of-plane modes of the beam. We showed that the motion of multilayer nanobeams can be described similar to the one of a homogeneous beam

when introducing effective material parameters for prestress, Young's modulus and density. These effective parameters can be calculated from the properties of the individual layers, which allows predicting the properties of the multilayer nanobeam or extracting material properties from a spectroscopic investigation of the nanobeam motion. We verified the presented theory by comparing to experimental data of a Si_3N_4/Nb bilayer nanobeam.

Next, we investigated a magnetomechanical hybrid system, where a ferromagnetic thin film (FM) has been deposited on a Si_3N_4 nanobeam. We showed that this platform can be used to probe magnetostriction in thin films. As a proof-of-principle experiment, we studied magnetostriction in a cobalt and a nickel thin film. Due to magnetoelastic coupling in the ferromagnet, an alignment of the magnetization generates stress in the magnetic film. In the presented Si_3N_4/FM bilayer nanobeams, this magnetoelastic stress translates into a resonance frequency shift of the beam's vibrational modes. We measured this frequency shift as a function of an externally applied magnetic field and could thus deduce the magnetostriction constants of the magnetic thin films. Furthermore, we analyzed the measurement sensitivity of this magnetostriction measurement method and showed that the presented approach is promising in particular for the investigation of thin and ultrathin films. As the magnetoelastic interaction results in a frequency shift in the presented device, the magnetostriction constants can easily be determined by a resonance frequency measurement, which does not require a quantitative read-out of the displacement of the nanobeam. Besides, the platform is versatile in the sense that it can be applied to any magnetic thin film that can be deposited via electron beam evaporation, thermal evaporation or sputtering. The presented device layout opens the path for the investigation of magnetostriction in films consisting of few (or even a single) monolayer(s) and thus study of magnetoelastic coupling in (quasi-)2D materials.

In a next step, a similar magnetomechanical hybrid system could be employed to study coherent magnon-phonon coupling. Using a nanobeam with a periodic hole pattern acting as a superlattice, mechanical modes in the GHz regime can be realized, which are efficiently decoupled from the environment [160]. Similarly, the magnons (quantized spin waves) in such a patterned nanobeam covered with a ferromagnetic thin film can be tailored in a way that their resonance frequency matches the mechanical eigenfrequency [161]. In such a system, cooled down to mK temperatures, magnon-phonon interaction in the quantum limit could be studied. Besides, sideband coupling of the MHz fundamental vibrational mode of the nanobeam to the magnetic degrees of freedom could allow to transfer the field of cavity opto/electromechanics to magnetism (cf. Refs. [162, 163]).

Turning to circuit electromechanics, we presented two devices with a tensile stressed nanobeam coupled to a superconducting coplanar waveguide (CPW) microwave resonator. In the first realization, we used a pure Si_3N_4 nanobeam integrated into a niobium microwave cavity. Thus we extended previous work on the dielectric actuation and read-out of nanomechanical resonators by using the superconducting high-Q microwave resonator to detect the motion of the nanobeam. We characterized the system and determined the electromechanical coupling between the nanobeam and the microwave resonator. Even if the coupling rate is small compared to typical circuit electromechanical devices, the presented sample layout enables particularly high mechanical quality factors as it avoids additional damping contributions caused by a metallization of the nanobeam. This approach is therefore well-suited to study mechanical damping in silicon nitride at low temperatures. In particular, analyzing the temperature dependence of the damping rate could allow to

identify damping mechanisms and thus contribute to the understanding of the relevant damping channels on a microscopic level. High mechanical quality factors are required especially for sensing devices and therefore the precise investigation and elimination of loss contributions is currently subject to extensive research [71, 73, 164]. The presented platform allows access to the temperature range below 4 K, which could not be investigated so far. In the long term, magnetic and multiferroic materials can be integrated into the Si_3N_4 nanobeam, enabling new ways of static and dynamic control of the mechanical properties.

In addition, we have developed the fabrication of tensile stressed aluminium nanobeams which we have integrated into a superconducting aluminium CPW microwave resonator. With this approach, we continued previous work at the Walther-Meißner-Institut on circuit electromechanics with a Si_3N_4/Nb bilayer beam coupled to a niobium microwave resonator. We transfered this idea to an all-aluminium basis, which allows for the direct integration of, e. g., SQUIDs (superconducting interference devices) or transmon qubits, based on Al/AlOx/Al Josephson junctions. We demonstrated the functionality of the aluminium circuit electromechanical hybrid device and characterized the microwave resonator as well as the nanobeam resonator. This allowed us to determine the prestress in the aluminium film at mK temperatures and analyze the damping rate as a function of temperature. Besides, we demonstrated sideband cooling of the fundamental vibrational mode of the nanobeam to a phonon number of approximately ten. Using the example of electromechanically induced transparency, we showed the effects of mechanical backaction on the microwave circuit.

The presented all-aluminium design is promising with respect to the realization of circuit electromechanics in the quantum regime. First, by introducing e. g. focused ion beam milling in order to separate the nanobeam from the adjacent ground plane [53], the gap between beam and ground plane could be reduced by approximately one order of magnitude, resulting in a coupling enhancement by a factor of ten. Second, the electromechanical coupling can be increased further by replacing the CPW microwave resonator with a high-impedance lumped element resonator (see, e. g., Refs. [20, 24, 25]). The projected coupling is then comparable to the one reached with drum-like aluminium mechanical resonators, coupled to a lumped element microwave cavity [20, 24, 25]. Compared to membrane resonators, tensile stressed nanobeams feature particularly small masses and therefore large zero-point motion. This is beneficial for sensing applications as well as for fundamental quantum mechanics experiments below the standard quantum limit.

Furthermore, the realization of the all-aluminium circuit electromechanical hybrid device opens the path for the integration of a transmon qubit as a single photon source. This allows, e. g., the preparation of Fock states in the mechanical resonator [23]. Besides, the nanobeam can be integrated directly into the shunt capacitor of the transmon qubit. This system has been proposed for the generation of mechanical Fock and cat states and hybrid tripartite entangled states. Furthermore, it features intrinsically strong nonlinear interactions between the transmon and the nanobeam resonator, which is qualitatively different from standard cavity opto/electromechanical systems [147].

As an alternative approach towards strong electromechanical coupling, we have designed an inductively coupled nanobeam-microwave resonator hybrid system, in which the electromechanical interaction is mediated via a SQUID. The vacuum coupling is expected to exceed the one of the presented (capacitively coupled) all-aluminium device by about

three orders of magnitude and thus reach the single photon strong coupling limit. Moreover, the inductive coupling can be switched on and off faster than the relevant decoherence times of the system, allowing e. g. novel state preparation protocols.

Thinking one step ahead, the combination of high-Q nanomechanical resonators with superconducting qubits may open a door towards the realization of quantum computing architectures. This idea has been subject to extensive theoretical investigation and formulated in various proposals, of which we want to mention two. Rips *et al.* studied a network of mechanical qubits formed by the two lowest excitation states of a strongly anharmonic resonator [165]. In this system, single qubit rotations are performed by application of RF electrical fields. A coherent optical photon field couples the mechanical qubits to each other and allows the realization of two-qubit gates. Zou *et al.* investigated an electromechanical network of Josephson charge qubits [166]. Here, a MHz mechanical resonator is coupled to charge qubits via electrostatic forces and serves as a bus for quantum information. The authors show the feasibility of quantum phase gates and the generation of maximally entangled states in the presented system. The realization of these proposals on the basis of the all-aluminium platform would constitute an important step towards quantum information processing with nanomechanical elements.

One particular aspect of quantum effects in mechanical systems is the realization of a phonon blockade, which means that a single phonon in a mechanical resonator can block the excitation of a second one. This purely quantum mechanical effect is considered an important step towards single phonon generation and detection, and thus constitutes a crucial resource for quantum information processing with phonons [167,168]. Theory work suggests a realization, e. g., by coupling a mechanical resonator to a charge qubit [169] or by exploiting Kerr-type nonlinearities [170,171]. From the perspective of sample fabrication, the first approach is close to the systems realized in the scope of this thesis and could therefore be the next step towards nanomechanics in the quantum regime.

In conclusion, we have realized nanomechanical hybrid systems which combine the specific features of tensile stressed nanobeams (high quality factors, small effective masses, frequencies in the MHz regime) with magnetic and electrical degrees of freedom. This is relevant for sensing applications as well as for fundamental quantum mechanics and quantum information processing and storage.

Appendix A

Analytical approximation of the resonance frequency of a tensile stressed nanobeam including bending effects

In Sec. 4.1.5, we have demonstrated that the resonance frequency of our typical tensile stressed nanobeam resonators cannot be reproduced very precisely using the approximation of a highly tensile stressed (HTS) nanostring (Eq. 4.18). We therefore derive an approximation which includes the contribution of bending in a tensile stressed nanobeam to first order. This new expression, which can be regarded as a first order correction of the HTS formula, reduces the error of the predicted resonance frequency by about one order of magnitude (relative to the exact numerical solution) and can still be written in a handy analytical form.

We start with the determinant of the system of linear equations, which we derive by substituting the general solution of the Equation of motion 4.9

$$v(x) = c_1 \exp(\alpha x) + c_2 \exp(-\alpha x) + c_3 \sin(\beta x) + c_4 \cos(\beta x)$$

with

$$\mu_{\pm} = \frac{\sigma_0 A \pm \sqrt{\sigma_0^2 A^2 + 4EI\rho A\Omega^2}}{2EI} , \tag{A.1}$$

$$I = \frac{wt^3}{12} ,$$

$$\alpha = \sqrt{\mu_+} > 0 \text{ , and} \tag{A.2}$$

$$\beta = -\imath\sqrt{\mu_-} > 0 \tag{A.3}$$

into the set of boundary conditions (Eq. 4.11)

$$\begin{aligned} v(x = -l/2) &= 0 \\ v(x = l/2) &= 0 \\ \partial v(x = -l/2)/\partial x &= 0 \\ \partial v(x = +l/2)/\partial x &= 0 \, . \end{aligned}$$

The determinant has to vanish to allow non-trivial solutions (i. e. solutions with at least one non-vanishing coefficient c_j, $j = 1, .., 4$):

$$e^{-\alpha l}\left[\left(\alpha^2-\beta^2\right)\left(e^{2\alpha l}-1\right)\sin(\beta l)+4\alpha\beta e^{\alpha l}-2\alpha\beta\left(e^{2\alpha l}+1\right)\cos(\beta l)\right]=0 \tag{A.4}$$

For typical tensile stressed nanobeams, $4EI\rho A\Omega^2 \ll \sigma_0^2 A^2$. We can therefore expand the square root in A.1 to first order and obtain

$$\mu_\pm \approx \frac{\sigma_0 A}{2EI}\left[1\pm\left(1+\frac{2EI\rho A\Omega^2}{\sigma_0^2 A^2}\right)\right] .$$

With Eqs. A.2 and A.3, we get

$$\alpha \approx \alpha_0 := \sqrt{\frac{\sigma_0 A}{EI}} \quad \text{and} \tag{A.5}$$

$$\beta \approx \sqrt{\frac{\rho}{\sigma_0}}\Omega . \tag{A.6}$$

In the HTS approximation (where bending effects are neglected), the resonance frequency of the n-th order mode is given by $\Omega_{n,\mathrm{HTS}} = n\pi/l\sqrt{\sigma_0/\rho}$ (see Eq. 4.18). We substitute this into Eq. A.6 and obtain

$$\beta l = \sqrt{\frac{\rho}{\sigma_0}}\Omega l \approx n\pi \tag{A.7}$$

and therefore

$$\cos(\beta l) \approx (-1)^n .$$

With this, we can simplify Eq. A.4 to

$$\left(\alpha_0^2-\beta^2\right)\left(e^{2\alpha_0 l}-1\right)\sin(\beta l)+2\alpha_0\beta\left[2e^{\alpha_0 l}-(-1)^n e^{2\alpha_0 l}+(-1)^n\right]=0 . \tag{A.8}$$

Applying typical geometry and material parameters (as given, e. g., in Chap. 3), we notice that $\alpha_0 \gtrsim 10\beta$ with $\beta l \approx n\pi > 1$. We can therefore safely assume $e^{\alpha_0 l} \gg 1$ and reduce Eq. A.8 to

$$(\alpha_0^2-\beta^2)\sin(\beta l)-(-1)^n 2\alpha_0\beta = 0 .$$

Approximating $\alpha \gg \beta$, we obtain

$$\alpha_0 \sin(\beta l)-(-1)^n 2\beta = 0 . \tag{A.9}$$

In order to solve this for β, we employ Eq. A.7 and expand $\sin(\beta l)$ around $n\pi$:

$$\sin(\beta l) \approx (-1)^n(\beta l - n\pi)$$

Substituting this into Eq. A.9, we get

$$\beta = \frac{n\alpha_0\pi}{\alpha_0 l - 2} .$$

Finally, we use Eqs. A.5 and A.6 to replace α_0 and β by the geometry and material parameters σ_0, A, E, I and ρ and the resonance frequency $\Omega_n/2\pi$. Solving for Ω_n yields

$$\Omega_{n,\mathrm{TS}} = \frac{n\sigma_0\pi\sqrt{A/\rho}}{\sqrt{\sigma_0 A}\,l-2\sqrt{EI}} = \Omega_{n,\mathrm{HTS}}\frac{\sqrt{\sigma_0 A}\,l}{\sqrt{\sigma_0 A}\,l-2\sqrt{EI}} . \tag{A.10}$$

Equation A.10 illustrates that the derived expression is a first order correction to the approximation of a highly tensile stressed beam. Obviously, $\Omega_{n,\mathrm{TS}} > \Omega_{n,\mathrm{HTS}}$. This can easily be understood as the bending contribution to the total energy of the vibrating nanobeam leads to an effective stiffening of the resonator, resulting in an increased eigenfrequency.

Appendix B

Lorentzian response spectrum with complex background

In experiments, the transmission spectroscopy of microwave resonators often shows significant deviations from the ideal Lorentzian lineshape (Eq. 6.7 resp. 6.10). These deviations can be attributed to impedance mismatches and discontinuities in the microwave lines [118–120]. We therefore fit a modified Lorentzian to the experimental data, which phenomenologically covers these effects by introducing a constant complex background.

We start with the complex voltage transmission of a $\lambda/2$ microwave resonator, coupled to an input and output line as shown in Fig. 6.5a, which is given by [115, 116]

$$t(\omega) = \frac{\sqrt{\kappa_{\mathrm{ex}}\kappa}/2}{\kappa/2 + i(\omega - \omega_{\mathrm{c}})} ,$$

where κ_{in} and κ_{ex} denote the internal and external damping rate, respectively, and $\kappa = \kappa_{\mathrm{in}} + \kappa_{\mathrm{ex}}$ is the total damping rate.

We introduce a complex background ic_1 that modifies the measured voltage transmission as

$$t^{\mathrm{meas}}(\omega) = t(\omega) + ic_1 .$$

The power transmission spectrum of the resonator can then be written as

$$T^{\mathrm{meas}}(\omega) = |t^{\mathrm{meas}}(\omega)|^2 = \left| ic_1 + \frac{\sqrt{\kappa_{\mathrm{ex}}\kappa}/2}{\kappa/2 + i(\omega - \omega_{\mathrm{c}})} \right|^2 + c_2 , \tag{B.1}$$

where c_2 accounts for a constant real background due to amplifier noise, for instance.

Analogously, we can write the transmission of a $\lambda/4$ microwave resonator, coupled to a transmission line as depicted in Fig. 6.5b, as

$$T^{\mathrm{meas}}(\omega) = 1 - \left| ic_1 + \frac{\sqrt{\kappa_{\mathrm{ex}}\kappa}/2}{\kappa/2 + i(\omega - \omega_{\mathrm{c}})} \right|^2 + c_2 . \tag{B.2}$$

Within this thesis, we use Eqs. B.1 and B.2 to fit the measured power transmission spectra of our microwave resonators and determine ω_{c}, κ_{in} and κ_{ex} from the experimental data.

Appendix C

Effective length of a nanobeam integrated in a CPW microwave resonator

For an *a priori* estimation of the electromechanical coupling between the nanobeam and the superconducting microwave resonator of Sample #5 and #6, we employ a COMSOL finite element model that allows to determine the change of the capacitance C_g as a function of the displacement of the nanobeam $v_0 \equiv x_0$[1]. To save computing power, we use a 2D model representing the cross-section of the devices at the position of the nanobeam, as illustrated in Figs. 7.3 and 8.3, respectively. With this, we can calculated the derivative $\partial c_g/\partial v_0$, where c_g is the capacitance per length between the electrodes. When calculating the total capacitance from c_g, we have to take into account that the nanobeam displacement is not uniform over the length of the nanobeam, i. e. the mechanical displacement and thus its effect on the capacitance is maximal at the center of the beam.

Considering that the displacement v is a function of the position x along the beam, the capacitance variation δC_g induced by a displacement $v(x)$ is given by

$$\delta C_g = \frac{\partial c_g}{\partial v} \int_{-l/2}^{l/2} \mathrm{d}x \, v(x) \, .$$

In linear approximation, we write

$$\frac{\partial C_g}{\partial v_0} \approx \frac{\delta C_g}{v_0} = \frac{\partial c_g}{\partial v} \int_{-l/2}^{l/2} \mathrm{d}x \, \frac{v(x)}{v_0} \, .$$

The integral can be solved numerically using the beam shape calculated in Sec. 4.1.5, or approximated analytically using $v(x) = v_0 \cos(\pi x/l)$ (which is the exact solution for the fundamental mode of a highly tensile stressed nanobeam). In the latter case, we obtain

$$\int_{-l/2}^{l/2} \mathrm{d}x \, \frac{v(x)}{v_0} = \frac{2l}{\pi} \, .$$

Thus, we define

$$\frac{\partial C_g}{\partial v_0} = \frac{\partial c_g}{\partial v} \cdot l_{\mathrm{eff}} \, ,$$

[1] Similar to Chap. 4, we denominate the displacement of the beam $v(x)$, where x is the coordinate along the beam axis. The displacement at the center of the beam, at $x = 0$, is denoted v_0.

where $l_{\mathrm{eff}} := 2l/\pi \approx 0.637\,l$ is the *effective length* of the beam.

In Ref. [128], we have calculated the beam shape of the fundamental out-of-plane mode of the tensile stressed Si_3N_4 nanobeam integrated in Sample #5 and found

$$\int_{-l/2}^{l/2} \mathrm{d}x\, \frac{v(x)}{v_0} \approx 0.613\,l\ ,$$

corresponding to an effective length $l_{\mathrm{eff}}^{\mathrm{S}\,\#5} \approx 0.613\,l$.

Appendix D

Temperature dependence of the resonance frequency of a tensile stressed nanobeam

We assume a tensile stressed nanobeam resonator, fabricated on a thick single-crystalline silicon substrate, as illustrated e. g. in Fig. 2.1 [left-hand side]. Typically, the resonance frequency of such a nanobeam depends on temperature, which is caused by different thermal expansion coefficients of the nanobeam material and the substrate.

In this section, we derive the thermally induced stress and the resulting resonance frequency shift for a given temperature change ΔT as a function of the relevant material parameters. We use this to estimate the stress in annealed aluminium nanobeams at room temperature and at mK temperatures.

When applying a temperature change ΔT, an *unclamped* nanobeam with a room-temperature length l_0 would elongate according to [85]

$$l' = l_0 \alpha_{\mathrm{beam}} \Delta T \, .$$

Similarly, the silicon substrate changes its dimensions according to

$$l'' = l_0 \alpha_{\mathrm{Si}} \Delta T \, .$$

The thermal expansion of the beam relative to the substrate is therefore

$$\Delta l = l' - l'' = l_0 \left(\alpha_{\mathrm{beam}} - \alpha_{\mathrm{Si}} \right) \Delta T \, .$$

In case of a doubly-clamped nanobeam, the length of the beam is given by the distance between the clamping points. The different thermal expansion coefficients of beam and substrate therefore result in a thermal stress along the beam axis [85]

$$\Delta\sigma = E_{\mathrm{beam}} \frac{\Delta l}{l_0} = E_{\mathrm{beam}} \left(\alpha_{\mathrm{beam}} - \alpha_{\mathrm{Si}} \right) \Delta T \, . \tag{D.1}$$

To calculate the impact on the resonance frequency, we use Eq. 2.3 and obtain

$$\Omega_{\mathrm{m}}' = \frac{\pi}{l'} \sqrt{\frac{\sigma_0 + \Delta\sigma}{\rho}} \approx \frac{\pi}{l_0} \sqrt{\frac{\sigma_0}{\rho_0}} \sqrt{1 + \frac{\Delta\sigma}{\sigma_0}} \approx \Omega_{\mathrm{m}} \left(1 + \frac{\Delta\sigma}{2\sigma_0} \right) \, .$$

With Eq. D.1, we find for the relative resonance frequency shift

$$\frac{\Delta\Omega_{\mathrm{m}}}{\Omega_{\mathrm{m}}} := \frac{\Omega_{\mathrm{m}}' - \Omega_{\mathrm{m}}}{\Omega_{\mathrm{m}}} \approx \frac{\Delta\sigma}{2\sigma_0} = \frac{\alpha_{\mathrm{beam}} - \alpha_{\mathrm{Si}}}{2\sigma_0} E_{\mathrm{beam}} \Delta T \, .$$

In the following, we estimate the expected thermal stress and relative frequency shift for two cases relevant within this thesis.

D.1 Annealing of an aluminium beam

As mentioned in Sec. 3.1.2, we use an annealing step (30 min at 350 °C) after the aluminium evaporation to generate a tensile stress σ_0 in the aluminium thin film. To estimate the resulting stress, we use the thermal expansion coefficients of aluminium and silicon at room temperature, $\alpha_{\mathrm{Al}} = 23.1 \times 10^{-6}\,\mathrm{K}^{-1}$ [96] and $\alpha_{\mathrm{Si}} = 3.3 \times 10^{-6}\,\mathrm{K}^{-1}$ [172] and Young's modulus of aluminium, $E_{\mathrm{Al}} = 70\,\mathrm{GPa}$ [137]. With $\Delta T \approx 330\,\mathrm{K}$, we obtain $\sigma_0 \equiv \Delta\sigma = 460\,\mathrm{MPa}$. This clearly exceeds the experimentally determined values $\sigma_0 = 159\,\mathrm{MPa}$ (Sample #2) and $\sigma_0 = 243\,\mathrm{MPa}$ (Sample #6), respectively. We thus conclude that the aluminium thin film consolidates at a temperature significantly below 350 °C and therefore releases part of the expected strain during the cooldown process.

D.2 Cooling an aluminium beam to mK temperatures

When cooling a tensile stressed aluminium nanobeam to mK temperatures, the stress will increase further. To estimate this stress contribution, we have to consider that the thermal expansion coefficients of most materials vanish at low temperature. To account for this, we average the temperature-dependent thermal expansion coefficients for aluminium and silicon, given in [173], over the temperature range between 0 and 300 K and obtain $\alpha_{\mathrm{Al}}^{\mathrm{mean}} = 15.3 \times 10^{-6}\,\mathrm{K}^{-1}$ and $\alpha_{\mathrm{Si}}^{\mathrm{mean}} = 0.9 \times 10^{-6}\,\mathrm{K}^{-1}$. Together with $E_{\mathrm{Al}} = 70\,\mathrm{GPa}$ (we neglect the slight increase of E_{Al} at low temperatures [174]), we obtain $\Delta\sigma = 295\,\mathrm{MPa}$, corresponding to a relative frequency shift of $\Delta\Omega_{\mathrm{m}}/\Omega_{\mathrm{m}} \approx 0.63$ for Sample #6. This agrees roughly with the value $\Delta\sigma^{\mathrm{exp}} = 407\,\mathrm{MPa}$, experimentally determined for Sample #6. The deviations are due to the fact that we do not know the precise material constants for our thin films and have therefore used literature bulk values.

Bibliography

[1] N. P. Mahalik, *Micromanufacturing and Nanotechnology* (Springer, 2006).

[2] R. Bogue, Sensor Review **33:4**, 300 (2013).

[3] M. Perlmutter and L. Robin, *Position Location and Navigation Symposium (PLANS), 2012 IEEE/ION*, 225 (2012).

[4] J. Marek, *2010 IEEE International Solid-State Circuits Conference (ISSCC)*, 9 (2010).

[5] P. Vogt and J. Kuhn, The Physics Teacher **50**, 182 (2012).

[6] J. B. Angell, P. W. Barth, and S. C. Terry, Scientific American **248**, 44 (1983).

[7] D. S. Eddy and D. R. Sparks, Proceedings of the IEEE **86**, 1747 (1998).

[8] S. N. Magonov and M.-H. Whangbo, *Surface Analysis with STM and AFM* (VCH Weinheim, 1996).

[9] S. Hong, M. S. Grinolds, P. Maletinsky, R. L. Walsworth, M. D. Lukin, and A. Yacoby, Nano Letters **12**, 3920 (2012).

[10] C. L. Degen, M. Poggio, H. J. Mamin, C. T. Rettner, and D. Rugar, Proceedings of the National Academy of Sciences **106**, 1313 (2009).

[11] E. M. Puchner and H. E. Gaub, Current Opinion in Structural Biology **19**, 605 (2009).

[12] Y. T. Yang, C. Callegari, X. L. Feng, K. L. Ekinci, and M. L. Roukes, Nano Letters **6**, 583 (2006).

[13] B. Lassagne, D. Garcia-Sanchez, A. Aguasca, and A. Bachtold, Nano Letters **8**, 3735 (2008).

[14] J. Chaste, A. Eichler, J. Moser, G. Ceballos, R. Rurali, and A. Bachtold, Nature Nanotechnology **7**, 301 (2012).

[15] K. Eom, H. S. Park, D. S. Yoon, and T. Kwon, Physics Reports **503**, 115 (2011).

[16] B. Arash, J.-W. Jiang, and T. Rabczuk, Applied Physics Reviews **2**, 021301 (2015).

[17] A. Boisen, S. Dohn, S. S. Keller, S. Schmid, and M. Tenje, Reports on Progress in Physics **74**, 036101 (2011).

[18] C. A. Regal, J. D. Teufel, and K. W. Lehnert, Nature Physics **4**, 555 (2008).

[19] M. Aspelmeyer, T. J. Kippenberg, and F. Marquardt, Reviews of Modern Physics **86**, 1391 (2014).

[20] J. D. Teufel, D. Li, M. S. Allman, K. Cicak, A. J. Sirois, J. D. Whittaker, and R. W. Simmonds, Nature **471**, 204 (2011).

[21] F. Hocke, *Microwave circuit-electromechanics in a nanomechanical hybrid system*, Ph.D. thesis, Walther-Meißner-Institut and Technische Universität München (2013).

[22] A. D. O'Connell, M. Hofheinz, M. Ansmann, R. C. Bialczak, M. Lenander, E. Lucero, M. Neeley, D. Sank, H. Wang, M. Weides, J. Wenner, J. M. Martinis, and A. N. Cleland, Nature **464**, 697 (2010).

[23] J.-M. Pirkkalainen, S. U. Cho, J. Li, G. S. Paraoanu, P. J. Hakonen, and M. A. Sillanpää, Nature **494**, 211 (2013).

[24] J.-M. Pirkkalainen, E. Damskägg, M. Brandt, F. Massel, and M. A. Sillanpää, Physical Review Letters **115**, 243601 (2015).

[25] E. E. Wollman, C. U. Lei, A. J. Weinstein, J. Suh, A. Kronwald, F. Marquardt, A. A. Clerk, and K. C. Schwab, Science **349**, 952 (2015).

[26] T. A. Palomaki, J. D. Teufel, R. W. Simmonds, and K. W. Lehnert, Science **342**, 710 (2013).

[27] S. A. McGee, D. Meiser, C. A. Regal, K. W. Lehnert, and M. J. Holland, Physical Review A **87**, 053818 (2013).

[28] J. Bochmann, A. Vainsencher, D. D. Awschalom, and A. N. Cleland, Nature Physics **9**, 712 (2013).

[29] K. C. Balram, M. I. Davanço, J. D. Song, and K. Srinivasan, Nature Photonics **advance online publication** (2016).

[30] S. S. Verbridge, J. M. Parpia, R. B. Reichenbach, L. M. Bellan, and H. G. Craighead, Journal of Applied Physics **99**, 124304 (2006).

[31] J. M. Gere and S. Timoshenko, *Mechanics of materials* (PWS-KENT Pub. Co., 1990).

[32] A. N. Cleland, *Foundations of Nanomechanics* (Springer, 2003).

[33] L. Boltzmann, Wiener Berichte **63**, 679 (1871).

[34] P. R. Saulson, Physical Review D **42**, 2437 (1990).

[35] M. L. Gorodetsky, A. Schliesser, G. Anetsberger, S. Deleglise, and T. J. Kippenberg, Optics Express **18**, 23236 (2010).

[36] S. Timoshenko, *Vibration Problems in Engineering* (D. Van Nostrand Company, Inc., 1937).

[37] Q. P. Unterreithmeier, *Gradient Field Transduction of Nanomechanical Resonators*, Ph.D. thesis, Ludwig-Maximilians-Universität München (2010).

[38] A. H. Nayfeh and D. T. Mook, *Nonlinear Oscillations* (John Wiley & Sons, New York, 1979).

[39] Q. P. Unterreithmeier, S. Manus, and J. P. Kotthaus, Applied Physics Letters **94**, 263104 (2009).

[40] P. Schmidt, *Inductive switchable cavity electromechanics*, Master's thesis, Walther-Meißner-Institut and Technische Universität München (2015).

[41] A. N. Cleland and M. L. Roukes, Applied Physics Letters **69**, 2653 (1996).

[42] S. S. Verbridge, H. G. Craighead, and J. M. Parpia, Applied Physics Letters **92**, 013112 (2008).

[43] M. Mühlbacher, *Interferometrische Detektion nanomechanischer Bewegung bei Raumdruck*, Bachelor's thesis, Ludwig-Maximilians-Universität München (2011).

[44] Q. P. Unterreithmeier, T. Faust, and J. P. Kotthaus, Physical Review Letters **105**, 027205 (2010).

[45] M. Gad-el Hak, *The MEMS Handbook* (CRC Press, 2001).

[46] T. Faust, P. Krenn, S. Manus, J. P. Kotthaus, and E. M. Weig, Nature Communications **3**, 728 (2012).

[47] M. Jung, *Charakterisierung nanomechanischer Balken mittels optischer Interferometrie*, Bachelor's thesis, Walther-Meißner-Institut and Technische Universität München (2013).

[48] M. Chinmulgund, R. B. Inturi, and J. A. Barnard, Thin Solid Films **270**, 260 (1995).

[49] A. Reddy, H. Kahn, and A. Heuer, Journal of Microelectromechanical Systems **16**, 650 (2007).

[50] P.-L. Yu, T. P. Purdy, and C. A. Regal, Physical Review Letters **108**, 083603 (2012).

[51] M. J. Seitner, K. Gajo, and E. M. Weig, Applied Physics Letters **105**, 213101 (2014).

[52] F. Hoehne, Y. A. Pashkin, O. Astafiev, L. Faoro, L. B. Ioffe, Y. Nakamura, and J. S. Tsai, Physical Review B **81**, 184112 (2010).

[53] J. Sulkko, M. A. Sillanpää, P. Häkkinen, L. Lechner, M. Helle, A. Fefferman, J. Parpia, and P. J. Hakonen, Nano Letters **10**, 4884 (2010).

[54] X. Zhou, F. Hocke, A. Schliesser, A. Marx, H. Huebl, R. Gross, and T. J. Kippenberg, Nature Physics **9**, 179 (2013).

[55] J. A. Burgess, A. E. Fraser, F. F. Sani, D. Vick, B. D. Hauer, J. P. Davis, and M. R. Freeman, Science **339**, 1051 (2013).

[56] P. Mohanty, G. Zolfagharkhani, S. Kettemann, and P. Fulde, Physical Review B **70**, 195301 (2004).

[57] F. Hocke, M. Pernpeintner, X. Zhou, A. Schliesser, T. J. Kippenberg, H. Huebl, and R. Gross, Applied Physics Letters **105**, 133102 (2014).

[58] W. Weaver, Jr., S. P. Timoshenko, and D. H. Young, *Vibration Problems in Engineering* (Wiley, 1990).

[59] W. Demtröder, *Experimentalphysik 1 - Mechanik und Wärme* (Springer, 2005).

[60] J. R. Rice, *Solid Mechanics* (Harvard University, Cambridge, 2010).

[61] G. Duffing, *Erzwungene Schwingungen bei veränderlicher Eigenfrequenz* (Vieweg, 1918).

[62] D. Kleppner and R. Kolenkow, *An introduction to mechanics* (McGraw-Hill, 1973).

[63] X. Zhou, *Superconducting Cavity Nanoelectromechanics*, Ph.D. thesis, École polytechnique fédérale de Lausanne (2013).

[64] N. N. Greenwood and A. Earnshaw, *Chemie der Elemente* (Wiley-VCH Weinheim, 1988).

[65] T. Imamura, T. Shiota, and S. Hasuo, IEEE Transactions on Applied Superconductivity **2**, 1 (1992).

[66] M. Bauccio (ed.), *ASM Engineered Materials Reference Book* (ASM International, 1994).

[67] J. L. Arlett, E. B. Myers, and M. L. Roukes, Nature Nanotechnology **6**, 203 (2011).

[68] J. Moser, J. Güttinger, A. Eichler, M. J. Esplandiu, D. E. Liu, M. I. Dykman, and A. Bachtold, Nature Nanotechnology **8**, 493 (2013).

[69] R. Mukhopadhyay, M. Lorentzen, J. Kjems, and F. Besenbacher, Langmuir **21**, 8400 (2005).

[70] P. A. Greaney and J. C. Grossman, Nano Letters **8**, 2648 (2008).

[71] S. Schmid, K. D. Jensen, K. H. Nielsen, and A. Boisen, Physical Review B **84**, 165307 (2011).

[72] R. B. Karabalin, L. G. Villanueva, M. H. Matheny, J. E. Sader, and M. L. Roukes, Physical Review Letters **108**, 236101 (2012).

[73] T. Faust, J. Rieger, M. J. Seitner, J. P. Kotthaus, and E. M. Weig, Physical Review B **89**, 100102 (2014).

[74] A. J. Sorensen, Physical Review **24**, 658 (1924).

[75] F. Richter, *Mechanical properties of solid bulk materials and thin films* (Technische Universität Chemnitz, 2010).

[76] N. A. Spaldin and M. Fiebig, Science **309**, 391 (2005).

[77] S. C. Masmanidis, H. X. Tang, E. B. Myers, M. Li, K. de Greve, G. Vermeulen, W. van Roy, and M. L. Roukes, Physical Review Letters **95**, 187206 (2005).

[78] M. Pernpeintner, R. B. Holländer, M. J. Seitner, E. M. Weig, R. Gross, S. T. B. Goennenwein, and H. Huebl, Journal of Applied Physics **119**, 093901 (2016).

[79] R. Holländer, *Räumliche Untersuchung nanomechanischer Objekte mit Interferometrie*, Bachelor's thesis, Walther-Meißner-Institut and Technische Universität München (2011).

[80] P. Jörg, *Aufbau eines Freistrahl-Interferometers zur Untersuchung nanomechanischer Resonatoren im Magnetfeld*, Bachelor's thesis, Walther-Meißner-Institut and Technische Universität München (2015).

[81] J. Wildmann, *Tailoring of Quantum dot Nanostructures*, Diploma thesis, Walther Schottky Institut, Technische Universität München (2012).

[82] J. Kerr, Philosophical Magazine Series V **3:19**, 321 (1877).

[83] N. O. Azak, M. Y. Shagam, D. M. Karabacak, K. L. Ekinci, D. H. Kim, and D. Y. Jang, Applied Physics Letters **91**, 093112 (2007).

[84] S. Chikazumi, *Physics of Ferromagnetism* (Oxford University Press, 1997).

[85] R. Gross and A. Marx, *Festkörperphysik* (Oldenbourg, 2012).

[86] S. Hunklinger, *Festkörperphysik* (Oldenbourg, 2009).

[87] H. Masumoto, H. Saito, and M. Kikuchi, Science reports of the Research Institutes, Tohoku University Series A **19**, 172 (1967).

[88] W. P. Mason, Physical Review **96**, 302 (1954).

[89] E. Klokholm, IEEE Transactions on Magnetics **12**, 819 (1976).

[90] A. C. Tam and H. Schroeder, Journal of Applied Physics **64**, 5422 (1988).

[91] E. du Trémolet de Lacheisserie and J. C. Peuzin, Journal of Magnetism and Magnetic Materials **136**, 189 (1994).

[92] M. Weber, R. Koch, and K. H. Rieder, Physical Review Letters **73**, 1166 (1994).

[93] A. H. Morrish, *The physical principles of magnetism* (Wiley, 2001).

[94] A. Brandlmaier, *Magnetische Anisotropie in dünnen Schichten aus Magnetit*, Master's thesis, Walther-Meißner-Institut and Technische Universität München (2006).

[95] M. Weiler, A. Brandlmaier, S. Geprägs, M. Althammer, M. Opel, C. Bihler, H. Huebl, M. S. Brandt, R. Gross, and S. T. B. Goennenwein, New Journal of Physics **11**, 013021 (2009).

[96] D. R. Lide (ed.), *CRC Handbook of Chemistry and Physics, 84th edition* (CRC Press, 2003).

[97] E. A. Brandes and G. B. Brook, editors, *Smithells Metals Reference Book, 7th edition* (Butterworth-Heinemann Ltd, 1992).

[98] E. Klokholm and J. Aboaf, Journal of Applied Physics **53**, 2661 (1982).

[99] M. Pernpeintner, *Magnon-Phonon Coupling in Ferromagnetic Thin Films*, Diploma thesis, Walther-Meißner-Institut and Technische Universität München (2012).

[100] C. A. Neugebauer, Physical Review **116**, 1441 (1959).

[101] D. C. Hurley, R. H. Geiss, M. Kopycinska-Müller, J. Müller, D. T. Read, J. E. Wright, N. M. Jennett, and A. S. Maxwell, Journal of Materials Research **20**, 1186 (2005).

[102] J. K. Luo, A. J. Flewitt, S. M. Spearing, N. A. Fleck, and W. I. Milne, Materials Letters **58**, 2306 (2004).

[103] A. Kamra, private communication.

[104] L. Dreher, M. Weiler, M. Pernpeintner, H. Huebl, R. Gross, M. S. Brandt, and S. T. B. Goennenwein, Physical Review B **86**, 134415 (2012).

[105] A. Kamra, Magnetic field dependence of the quality factor in torque differential magnetometry (2014), unpublished.

[106] T. J. Kippenberg and K. J. Vahala, Science **321**, 1172 (2008).

[107] M. Aspelmeyer, T. J. Kippenberg, and F. Marquart (eds.), *Cavity Optomechanics* (Springer, 2014).

[108] M. Aspelmeyer, P. Meystre, and K. Schwab, Physics Today **65**, 29 (2012).

[109] F. Massel, T. T. Heikkilä, J.-M. Pirkkalainen, S. U. Cho, H. Saloniemi, P. J. Hakonen, and M. A. Sillanpää, Nature **480**, 351 (2011).

[110] M. Yuan, V. Singh, Y. M. Blanter, and G. A. Steele, Nature Communications **6**, 8491 (2015).

[111] V. Singh, S. J. Bosman, B. H. Schneider, Y. M. Blanter, A. Castellanos-Gomez, and G. A. Steele, Nature Nanotechnology **9**, 820 (2014).

[112] F. Hocke, X. Zhou, A. Schliesser, T. J. Kippenberg, H. Huebl, and R. Gross, New Journal of Physics **14**, 123037 (2012).

[113] I. Mahboob, K. Nishiguchi, A. Fujiwara, and H. Yamaguchi, Physical Review Letters **110**, 127202 (2013).

[114] M. Göppl, A. Fragner, M. Baur, R. Bianchetti, S. Filipp, J. M. Fink, P. J. Leek, G. Puebla, L. Steffen, and A. Wallraff, Journal of Applied Physics **104**, 113904 (2008).

[115] D. M. Pozar, *Microwave engineering* (Wiley, 2012).

[116] B. A. Mazin, *Microwave Kinetic Inductance Detectors*, Ph.D. thesis, California Institute of Technology (2004).

[117] J. Goetz, F. Deppe, M. Haeberlein, F. Wulschner, C. W. Zollitsch, S. Meier, M. Fischer, P. Eder, E. Xie, K. G. Fedorov, E. P. Menzel, A. Marx, and R. Gross, Journal of Applied Physics **119**, 015304 (2016).

[118] A. Megrant, C. Neill, R. Barends, B. Chiaro, Y. Chen, L. Feigl, J. Kelly, E. Lucero, M. Mariantoni, P. J. J. O'Malley, D. Sank, A. Vainsencher, J. Wenner, T. C. White, Y. Yin, J. Zhao, C. J. Palmstrøm, J. M. Martinis, and A. N. Cleland, Applied Physics Letters **100**, 113510 (2012).

[119] M. S. Khalil, M. J. A. Stoutimore, F. C. Wellstood, and K. D. Osborn, Journal of Applied Physics **111**, 054510 (2012).

[120] C. Deng, M. Otto, and A. Lupascu, Journal of Applied Physics **114**, 054504 (2013).

[121] C. Genes, D. Vitali, P. Tombesi, S. Gigan, and M. Aspelmeyer, Physical Review A **77**, 033804 (2008).

[122] J. D. Teufel, T. Donner, D. Li, J. W. Harlow, M. S. Allman, K. Cicak, A. J. Sirois, J. D. Whittaker, K. W. Lehnert, and R. W. Simmonds, Nature **475**, 359 (2011).

[123] F. W. Beil, R. H. Blick, A. Wixforth, W. Wegscheider, D. Schuh, and M. Bichler, Europhysics Letters **76**, 1207 (2006).

[124] E. Collin, J. Kofler, S. Lakhloufi, S. Pairis, Y. M. Bunkov, and H. Godfrin, Journal of Applied Physics **107**, 114905 (2010).

[125] K. Das, G. Sosale, and S. Vengallatore, Nanotechnology **23**, 505703 (2012).

[126] Q. P. Unterreithmeier, E. M. Weig, and J. P. Kotthaus, Nature **458**, 1001 (2009).

[127] J. Rieger, T. Faust, M. J. Seitner, J. P. Kotthaus, and E. M. Weig, Applied Physics Letters **101**, 103110 (2012).

[128] M. Pernpeintner, T. Faust, F. Hocke, J. P. Kotthaus, E. M. Weig, H. Huebl, and R. Gross, Applied Physics Letters **105**, 123106 (2014).

[129] Ioffe Institute, St. Petersburg, *Basic Properties of Silicon*, URL: http://www.ioffe.ru/SVA/NSM/Semicond/Si/basic.html.

[130] Virginia Semiconductor, Fredericksburg, *The General Properties of Si, Ge, SiGe, SiO_2 and Si_3N_4*,
URL: http://www.virginiasemi.com/pdf/generalpropertiesSi62002.pdf.

[131] K. Y. Fong, W. H. P. Pernice, and H. X. Tang, Physical Review B **85**, 161410 (2012).

[132] C. Seoánez, F. Guinea, and A. H. Castro Neto, Physical Review B **77**, 125107 (2008).

[133] A. Venkatesan, K. J. Lulla, M. J. Patton, A. D. Armour, C. J. Mellor, and J. R. Owers-Bradley, Physical Review B **81**, 073410 (2010).

[134] L. G. Villanueva and S. Schmid, Physical Review Letters **113**, 227201 (2014).

[135] B. D. Hauer, C. Doolin, K. S. D. Beach, and J. P. Davis, Annals of Physics **339**, 181 (2013).

[136] D. Schwienbacher, *Circuit nano-electromechanics: transmon qubits, nano-strings and resonators*, Master's thesis, Walther-Meißner-Institut and Technische Universität München (2016).

[137] Mark Winter (The University of Sheffield and WebElements Ltd, UK), *Aluminium, Physical properties*, URL: http://www.webelements.com/aluminium.

[138] B. H. Schneider, V. Singh, W. J. Venstra, H. B. Meerwaldt, and G. A. Steele, Nature Communications **5**, 5819 (2014).

[139] Y. Hao, F. Rouxinol, and M. D. LaHaye, Applied Physics Letters **105**, 222603 (2014).

[140] Rohde&Schwarz GmbH&Co. KG, *R&S SMF100A Microwave Signal Generator Specifications* (2009).

[141] A. Schliesser, *Cavity Optomechanics and Optical Frequency Comb Generation with Silica Whispering-Gallery-Mode Microresonators*, Ph.D. thesis, Ludwig-Maximilians-Universität München (2009).

[142] G. S. Agarwal and S. Huang, Physical Review A **81**, 041803 (2010).

[143] S. Weis, R. Rivière, S. Deléglise, E. Gavartin, O. Arcizet, A. Schliesser, and T. J. Kippenberg, Science **330**, 1520 (2010).

[144] M. Grajcar, S. H. W. van der Ploeg, A. Izmalkov, E. Il'ichev, H.-G. Meyer, A. Fedorov, A. Shnirman, and G. Schön, Nature Physics **4**, 612 (2008).

[145] K. Jaehne, K. Hammerer, and M. Wallquist, New Journal of Physics **10**, 095019 (2008).

[146] K. Xia and J. Evers, Physical Review Letters **103**, 227203 (2009).

[147] M. Abdi, M. Pernpeintner, R. Gross, H. Huebl, and M. J. Hartmann, Physical Review Letters **114**, 173602 (2015).

[148] S. G. Hofer, W. Wieczorek, M. Aspelmeyer, and K. Hammerer, Physical Review A **84**, 052327 (2011).

[149] A. Wallraff, D. I. Schuster, A. Blais, L. Frunzio, R.-S. Huang, J. Majer, S. Kumar, S. M. Girvin, and R. J. Schoelkopf, Nature **431**, 162 (2004).

[150] T. Niemczyk, F. Deppe, H. Huebl, E. P. Menzel, F. Hocke, M. J. Schwarz, J. J. Garcia-Ripoll, D. Zueco, T. Hümmer, E. Solano, A. Marx, and R. Gross, Nature Physics **6**, 772 (2010).

[151] T. A. Palomaki, J. W. Harlow, J. D. Teufel, R. W. Simmonds, and K. W. Lehnert, Nature **495**, 210 (2013).

[152] A. Blais, R.-S. Huang, A. Wallraff, S. M. Girvin, and R. J. Schoelkopf, Physical Review A **69**, 062320 (2004).

[153] K. F. Wulschner, *Interactions of harmonic and anharmonic macroscopic quantum oscillators in superconducting circuits*, Ph.D. thesis, Walther-Meißner-Institut and Technische Universität München (2016).

[154] M. P. Blencowe and E. Buks, Physical Review B **76**, 014511 (2007).

[155] E. Buks, E. Segev, S. Zaitsev, B. Abdo, and M. P. Blencowe, EPL (Europhysics Letters) **81**, 10001 (2008).

[156] S. Etaki, M. Poot, I. Mahboob, K. Onomitsu, H. Yamaguchi, and H. S. J. van der Zant, Nature Physics **4**, 785 (2008).

[157] P. D. Nation, M. P. Blencowe, and E. Buks, Physical Review B **78**, 104516 (2008).

[158] M. Sandberg, C. M. Wilson, F. Persson, T. Bauch, G. Johansson, V. Shumeiko, T. Duty, and P. Delsing, Applied Physics Letters **92**, 203501 (2008).

[159] D. M. Greenberger, M. A. Horne, and A. Zeilinger, *Going Beyond Bell's Theorem*, in: M. Kafatos (ed.), *Fundamental Theories of Physics, vol. 37: Bell's Theorem, Quantum Theory and Conceptions of the Universe* (Springer, 1989).

[160] M. Eichenfield, J. Chan, R. M. Camacho, K. J. Vahala, and O. Painter, Nature **462**, 78 (2009).

[161] S. Neusser, *Spin Waves in Antidot Lattices: From Quantization to Magnonic Crystals*, Ph.D. thesis, Technische Universität München (2011).

[162] X. Zhang, C.-L. Zou, L. Jiang, and H. X. Tang, arXiv:1511.03680 (2015).

[163] O. Romero-Isart, L. Clemente, C. Navau, A. Sanchez, and J. I. Cirac, Physical Review Letters **109**, 147205 (2012).

[164] J. Rieger, A. Isacsson, M. J. Seitner, J. P. Kotthaus, and E. M. Weig, Nature Communications **5** (2014).

[165] S. Rips and M. J. Hartmann, Physical Review Letters **110**, 120503 (2013).

[166] X. Zou and W. Mathis, Physics Letters A **324**, 484 (2004).

[167] Y.-X. Liu, A. Miranowicz, Y. B. Gao, J. Bajer, C. P. Sun, and F. Nori, Physical Review A **82**, 032101 (2010).

[168] T. Ramos, V. Sudhir, K. Stannigel, P. Zoller, and T. J. Kippenberg, Physical Review Letters **110**, 193602 (2013).

[169] X. Wang, A. Miranowicz, H.-R. Li, and F. Nori, arXiv:1603.07546 (2016).

[170] N. Didier, S. Pugnetti, Y. M. Blanter, and R. Fazio, Physical Review B **84** (2011).

[171] A. Miranowicz, J. Bajer, N. Lambert, Y.-X. Liu, and F. Nori, Physical Review A **93**, 013808 (2016).

[172] Accuratus Corporation, Phillipsburg, *Silicon Nitride Ceramic Properties*, URL: http://accuratus.com/silinit.html.

[173] D. F. Gibbons, Physical Review **112**, 136 (1958).

[174] P. M. Sutton, Physical Review **91**, 816 (1953).

List of Publications

- L. Dreher, M. Weiler, M. Pernpeintner, H. Huebl, R. Gross, M. S. Brandt, and S. T. B. Goennenwein. Surface acoustic wave driven ferromagnetic resonance in nickel thin films: Theory and experiment. *Phys. Rev. B* **86**, 134415 (2012); doi: 10.1103/PhysRevB.86.134415
- M. Weiler, M. Althammer, M. Schreier, J. Lotze, M. Pernpeintner, S. Meyer, H. Huebl, R. Gross, A. Kamra, J. Xiao, Y.-T. Chen, H. J. Jiao, G. E. W. Bauer, and S. T. B. Goennenwein. Experimental Test of the Spin Mixing Interface Conductivity Concept. *Phys. Rev. Lett.* **111**, 176601 (2013); doi: 10.1103/PhysRevLett.111.176601
- F. Hocke, M. Pernpeintner, X. Zhou, A. Schliesser, T. J. Kippenberg, H. Huebl, and R. Gross. Determination of effective mechanical properties of a double-layer beam by means of a nano-electromechanical transducer. *Appl. Phys. Lett.* **105**, 133102 (2014); doi: 10.1063/1.4896785
- M. Pernpeintner, T. Faust, F. Hocke, J. P. Kotthaus, E. M. Weig, H. Huebl, and R. Gross. Circuit electromechanics with a non-metallized nanobeam. *Appl. Phys. Lett.* **105**, 123106 (2014); doi: 10.1063/1.4896419
- M. Abdi, M. Pernpeintner, R. Gross, H. Huebl, and M. J. Hartmann. Quantum State Engineering with Circuit Electromechanical Three-Body Interactions. *Phys. Rev. Lett.* **114**, 173602 (2015); doi: 10.1103/PhysRevLett.114.173602
- F. Wulschner, J. Goetz, F. R. Koessel, E. Hoffmann, A. Baust, P. Eder, M. Fischer, M. Haeberlein, M. J. Schwarz, M. Pernpeintner, E. Xie, L. Zhong, C. W. Zollitsch, B. Peropadre, J.-J. Garcia Ripoll, E. Solano, K. Fedorov, E. P. Menzel, F. Deppe, A. Marx, and R. Gross. Tunable coupling of transmission-line microwave resonators mediated by an rf SQUID. arXiv:1508.06758 (2015)
- S. T. B. Goennenwein, R. Schlitz, M. Pernpeintner, K. Ganzhorn, M. Althammer, R. Gross, and H. Huebl. Non-local magnetoresistance in YIG/Pt nanostructures. *Appl. Phys. Lett.* **107**, 172405 (2015); doi: 10.1063/1.4935074
- M. Pernpeintner, R. B. Holländer, M. J. Seitner, E. M. Weig, R. Gross, S. T. B. Goennenwein, and H. Huebl. A versatile platform for magnetostriction measurements in thin films. *Journal of Applied Physics* **119**, 093901 (2016); doi: 10.1063/1.4942531

Acknowledgments

There are several people without whom this thesis would not have been possible. In particular, I would like to thank:

Prof. Dr. Rudolf Gross, for giving me the opportunity to write my PhD thesis at the Walther-Meißner-Institut, for various fruitful discussions and for valuable support in every situation.

Dr. Hans Hübl, my supervisor, who convinced me to join the field of nanomechanics, for invaluable support regarding sample fabrication, experiments and data evaluation, for sharing his excellent knowledge on microwave spectroscopy and for carefully proofreading this thesis. Besides, I am grateful for his encouragement and personal support in many situations.

Dr. Fredrik Hocke, for introducing me to the field of circuit electromechanics, for sharing his expertise with me and for preparing the dielectrically coupled electromechanics project together with Thomas Faust and Eva Weig.

Dr. Thomas Faust, for introducing me to nanofabrication in the cleanroom of the Kotthaus chair, for his patience and the time he spend on explanations and on solving fabrication problems. This helped me a lot at the beginning of my work on nanomechanics fabrication.

Prof. Dr. Eva Weig, for supporting the Si_3N_4 circuit electromechanics project, for sharing her broad knowledge on nanomechanics with me and for very helpful discussions and comments regarding the magnetomechanics project.

Prof. Dr. Jörg Kotthaus, for giving me the opportunity to work in his cleanroom and for valuable comments regarding the Si_3N_4 circuit electromechanics project.

Dr. Sebastian Gönnenwein, for several helpful discussions about spin mechanics and for supporting the magnetomechanics project.

Maximilian Seitner, for several fruitful discussions and valuable comments and for his contributions to the magnetomechanics project.

Dr. Mehdi Abdi and Prof. Dr. Michael Hartmann, for inspiring discussions about circuit electromechanics with transmon qubits, for sharing their excellent knowledge and their ideas with us experimentalists, and in particular for their great effort in working out the proposal on three-body hybrid systems.

Dr. Akashdeep Kamra, for various inspiring discussions about spin mechanics and for his calculations regarding spin accumulation in thin films and damping in magnetomechanical systems.

Dr. Hiroshi Yamaguchi, for giving me the chance to work in his group at NTT Basic Research Laboratories for three months, and Dr. Imran Mahboob, for his enthusiasm, support and the time he spent with me searching for mechanically detected NMR.

Prof. Dr. Albert Schliesser, Dr. Xiaoqing Zhou and Prof. Dr. Tobias Kippenberg for their contributions to the fruitful WMI-EPFL collaboration.

Prof. Dr. Martin Brandt, for being my mentor not only during my studies, for valuable advice and for several invitations to barbecue evenings in his garden.

My master students, Rasmus Holländer, Anh Tu Bohn, Philip Schmidt and Daniel Schwienbacher, for joining the nanomechanics group at the WMI, for the effort they made in sample fabrication and characterization and for the indispensable results they contributed to this thesis.

My bachelor students, Moritz Jung, Lisa Rosenzweig and Peter Jörg, for improving and characterizing the optical interferometry setup and the nanobeam samples.

My office colleagues Dr. Sibylle Meyer, Michael Schreier and Christoph Zollitsch, for a great time together at the WMI, for innumerable discussions about physical and unphysical topics and for assistance regarding all kinds of problems.

Friedrich Wulschner, for his valuable support in reconstructing the "Kermit" cryostat, for sharing his knowledge about design and fabrication of SQUIDs and transmon qubits, and for various discussions about tunable resonators and circuit electromechanics with transmon qubits.

Thomas Brenninger, for his remarkable and constant effort to maintain and develop the thin film and nanofabrication facilities at the WMI, in particular the aluminium and magnetics evap, the sputtering chamber, the RIE, the SEM and the *Nanobeam* e-beam writer.

Sebastian Kammerer, for assistance in the cleanroom and for preparing the vacuum chamber of the free space interferometer.

Sonja Matich and Peter Weiser, for introducing me to FIB and SEM at the ZNN.

Dr. Karl Neumaier, for sharing his knowledge on dilution fridges with me and for support in solving technical problems at the cryostat.

The qubit and the magnetism group, for sharing experimental equipment, support in case of technical problems and for a lot of helpful discussions. In particular Dr. Stephan Geprägs and Dr. Matthias Althammer, for taking care of the magnetism evap and for SQUID and x-ray measurements.

The chemical-technical assistants, Karen Helm-Knapp and Astrid Habel, for advice regarding wet etching, for gold plating a microwave filter cavity and for a lot of help regarding cleanroom clothes, chemicals and consumables.

The WMI workshop, Helmut Thies, Julius Klaus, Georg Nitschke, Christian Reichlmeier and Alexander Rößl, for fabricating components for the ”Kermit” cryostat and the interferometry setups and for support regarding several technical problems.

The ”Helium Halle”, Peter Binkert, Jan Naundorf and Harald Schwaiger, for providing liquid helium for my low temperature experiments.

The secretary and administration, Emel Dönertas and Ludwig Ossiander, for taking over most of the administrative work so that I could always focus on physics.

My friends and my family, for supporting me during my studies and my PhD thesis and for reminding me of a life apart from physics.

My wife Carla, for constant support, unreserved encouragement and understanding in all situations.